UNCLASSIFIED

AD NUMBER

AD404618

NEW LIMITATION CHANGE

TO

Approved for public release, distribution unlimited

FROM

Distribution authorized to U.S. Gov't. agencies and their contractors; Administrative/Operational Use; FEB 1963. Other requests shall be referred to Army Signal Command, Washington, DC 20310.

AUTHORITY

nba ltr, 9 mar 1965

THIS PAGE IS UNCLASSIFIED

UNCLASSIFIED

AD 404 618

Reproduced
by the

DEFENSE DOCUMENTATION CENTER

FOR

SCIENTIFIC AND TECHNICAL INFORMATION

CAMERON STATION ALEXANDRIA, VIRGINIA

UNCLASSIFIED

NOTICE: When government or other drawings, specifications or other data are used for any purpose other than in connection with a definitely related government procurement operation, the U. S. Government thereby incurs no responsibility, nor any obligation whatsoever; and the fact that the Government may have formulated, furnished, or in any way supplied the said drawings, specifications, or other data is not to be regarded by implication or otherwise as in any manner licensing the holder or any other person or corporation, or conveying any rights or permission to manufacture, use or sell any patented invention that may in any way be related thereto.

404618

SEL-62-151

Cyclotron-Wave Amplification Using Simultaneous RF Coupling and DC Pumping

CATALOGED BY ASTIA
AS AD No.

by
Shing Mao

February 1963

DDC
MAY 3 1963
TISIA A

Technical Report No. 159-2

Prepared under
Signal Corps Contract DA 36-039 SC-85387

404 618

ELECTRON DEVICES LABORATORY
STANFORD ELECTRONICS LABORATORIES
STANFORD UNIVERSITY · STANFORD, CALIFORNIA

NO OTS

Best
Available
Copy

ASTIA AVAILABILITY NOTICE

Qualified requesters may obtain copies of this report from ASTIA. Foreign announcements and dissemination of this report by ASTIA is limited. ASTIA release to OTS not authorized.

SEL-62-151

CYCLOTRON-WAVE AMPLIFICATION USING SIMULTANEOUS RF COUPLING AND DC PUMPING

by

Shing Mao

February 1963

Reproduction in whole or in part is permitted for any purpose of the United States Government.

Technical Report No. 159-2

Prepared under
Signal Corps Contract DA 36-039 SC-85387

Electron Devices Laboratory
Stanford Electronics Laboratories
Stanford University Stanford, California

ABSTRACT

This report presents a new wideband cyclotron-wave amplifier using simultaneous rf coupling and dc pumping. A single quadrifilar helix is operated so that its -1 mode is synchronous with the fast cyclotron wave over the full helix passband ($ka = 1$ at $\omega = \omega_c$). This coincides with the condition for dc pumping when quadrupolar dc voltages are applied to the four helix wires. The one helix then serves simultaneously as dc pump structure and as slow-wave structure to couple rf energy into and out of the beam waves.

A detailed analysis of simultaneous pumping and coupling is developed, using appropriate coupled-mode equations. Expressions for gain, bandwidth, and noise figure are presented in terms of practical tube parameters, especially for the case of a hollow beam in a helix with concentric inner conductor. For the latter case, when the frequency dependence of all parameters is taken into account, the gain is found to vary by less than 3 db over a frequency range in excess of 4:1. Since the amplification process involves both the slow and fast cyclotron waves, its noise figure depends in part on cathode temperature and is not extremely low.

An experimental tube in S-band using a 1-in.-diameter by 5-in.-long helix and an (intended) 300-v, 100-ma beam was built and tested. An unduly large helix-to-center-conductor gap (0.100 in.) was used because of an erroneous early approximation for the dc pumping fields. As a result of this and of spurious gun oscillations at currents above a few ma, high-gain operation was not obtained. However, the dependence of the low-gain behavior on all available parameters was closely examined and found to be in excellent agreement with computations based on the analysis. Moreover, the broadband nature of the gain was verified with the observation of $\sim$ 5-db gain over a 4:1 frequency range with all tube parameters fixed.

Certain unexpected high-gain operating modes were also observed with different tube parameters, particularly with different dc-pump-voltage configurations. These are not fully understood as yet. They form an interesting possible future extension for this work, in addition to further development of the simultaneous pumping/coupling concept.

CONTENTS

		Page
I.	Introduction	1
II.	General Theory of dc Pumping and rf Coupling	8
	A. Cyclotron-Wave Amplification by Twisted dc-Pumping Field	8
	1. Complete Analysis from a Wave Point of View	8
	2. Small-Signal Analysis from a Ballistic Point of View	26
	3. Perturbation of Small-Signal Analysis from a Ballistic Point of View	34
	4. Conditions Required for Amplification due to dc Pumping	37
	B. RF Coupling in the Quadrifilar Helix	41
	1. Normal Modes of the Quadrifilar Helix	41
	2. Normal Modes of the Transverse Beam Waves Carried by the Confined Electron Beam	44
	3. Conditions Required for Coupling between the Circuit Waves and the Beam Waves	47
	4. Mode Excitation of the Circuit Waves on the Quadrifilar Helix	50
III.	Theory of the Amplifier using Simultaneous Pumping and Coupling	52
	A. Coupled-Mode Theory	52
	B. Physical Interpretation of the Operation	56
	C. Gain and Bandwidth of the Amplifier	69
	D. Noise Performance	80
IV.	Design Criterion and the Construction of an Experimental Tube	89
	A. Design of the Quadrifilar Helix	89
	B. Design of the electron gun	98
	C. Construction of an Experimental Tube	105
V.	Experimental Results and Interpretation	111
	A. Cold Tests on the Helix	111
	1. Mode Excitation on the Quadrifilar Helix	111
	2. Circuit Matching Measurement and Insertion Loss	120
	3. Cold Measurement of the ω-β Diagram of the Quadrifilar Helix	120
	B. DC Beam Tests	124
	1. Tests on the Electron Gun	125
	2. Tests on the Current Transmission Through the Helix	127
	C. RF Tests of the Tube	129
	1. Interactions of the Beam Waves and the Circuit Waves	129
	2. Measurement of the ω-β Diagram of the Circuit by the Interaction with the Beam Waves	135
	3. Measurement of the Coupling Coefficient and the Transverse Impedance	137
	4. Measurements of the Operation of Simultaneous rf Coupling and dc Pumping on Cyclotron Waves	141
	5. Measured Gain and Bandwidth	144
	6. Sensitivity to dc Beam Voltage, Magnetic Field, and the Lens Effect	144
	7. Observation of High-Gain Operation under other Arrangements	145

CONTENTS (Cont'd)

	Page
VI. Conclusions and Recommendations for Further Study	148
Appendix A. The Potential Distribution Inside the Quadrifilar Helix with Axially Symmetrical dc Pumping	149
Appendix B. Four-Wave Analysis	150
Appendix C. The Transverse Impedance of Helices with Center Conductor	156
Appendix D. The Pumping Coefficient of a Quadrifilar Helix with Center Conducting Rod	160
References	164

TABLES

Table		Page
1	Transverse beam waves	9
2	Circuit waves on a quadrifilar helix	42

ILLUSTRATIONS

Figure		Page
1	The ω-β diagram of an rf-pumped fast-cyclotron-wave parametric amplifier	1
2	The ω-β diagram of a dc-pumped cyclotron-wave quasi-parametric amplifier	3
3	Cyclotron-wave amplification using simultaneous rf coupling and dc pumping	4
4	A comparison between the conventional beam-type parametric amplifier and the simultaneous coupling and pumping amplifier	5
5	The helical trajectory of an electron with transverse energy and constant axial velocity immersed in an axial magnetic field	8
6	The axially symmetrical dc electric field set up by a quadrifilar helix	11
7	The ω-β diagram of the space sidebands of the fast cyclotron wave under active pumping	18
8	The ω-β diagram of the space sidebands of the slow cyclotron wave under active pumping	18
9	The wave amplitude along the beam under active dc pumping	19
10	The ω-β diagram of the four space sidebands of the slow cyclotron wave under passive pumping	22
11	The ω-β diagram of the four space sidebands of the perturbed second synchronous wave under passive pumping	22
12	The ω-β diagram, showing the shift on phase constant	23

ILLUSTRATIONS (Cont'd)

Figure		Page
13	The ω-β diagram, showing the shift in phase constant due to the coupling between the fast cyclotron wave and the first synchronous wave	24
14	The space sidebands of the synchronous waves under active pumping	26
15	The rotating and moving frame x', y', z' and its relation to the stationary frame x, y, z	28
16	Potential distribution in the transverse plane of the quadrifilar helix	29
17	The trajectory of the electron entering the input plane of the helix on the x-axis	32
18	The trajectory of the electron entering the input plane of the helix on the y-axis	33
19	The amplifying condition for the cyclotron-wave amplification	38
20	The tuning curves of the accelerating voltage and the magnetic field for active dc pumping on cyclotron waves using helix pitch as a parameter	40
21	Nomograph of active pumping conditions on cyclotron waves	41
22	The methods of exciting the four independent modes on the quadrifilar helix	43
23	The characteristics of the fundamental waves of the four independent excitable modes on a quadrifilar helix	44
24	The characteristics of the transverse waves carried by an electron beam confined in a longitudinal dc magnetic field	45
25	Electron-beam motion in a dc magnetic field directed perpendicularly into the paper	46
26	The radius of the quadrifilar helix as a function of magnetic field for wideband coupling	49
27	The radius of the helix as a function of cyclotron frequency for wideband coupling	49
28	The operation of the cyclotron-wave amplification using simultaneous rf coupling and dc pumping	50
29	The amplitude of various waves growing along the z-direction in the quadrifilar helix when both the rf coupling and dc pumping are applied simultaneously	58
30	Universal curve for the dependence on frequency of the critical length	60
31	Universal curve for the dependence on pump voltage of the critical length	60

ILLUSTRATIONS (Cont'd)

Figure		Page
32	The pumping effect on the circuit wave carried by an infinitely long helix originally coupled with the fast cyclotron beam wave	61
33	The circuit outputs of a helix with finite length as functions of the pumping coefficient with the coupling coefficient as the parameter	63
34	The number of nulls in the circuit output as a function of the coupling coefficient and the circuit length . .	64
35	The coupling effect on the circuit wave carried by an infinitely long helix with the pumping coefficient as a parameter	65
36	The circuit outputs of a helix with finite length as functions of the coupling coefficient with the pumping coefficient as the parameter	67
37	The power carried by various waves along z-direction in the quadrifilar helix when both the rf coupling and the dc pumping are applied simultaneously	68
38	Power gain as a function of $\tau = k_-/k_p$ using G_{po} as a parameter	70
39	Power gain as a function of $\tau = k_-/_p$ for high pump levels	71
40	Universal curve of the pump parameter G_{po} vs k_pL . .	72
41	The frequency parameter as a function of ka for $I_o = 10$ ma and $\cot \psi = 12$	73
42	The frequency parameter of the quadrifilar helix with center conductor for $I_o = 0.10$ amp	75
43	The frequency parameter τ of the quadrifilar helix with center conductor for $I_o = 0.05$ amp	76
44	The frequency parameter τ of the quadrifilar helix with center conductor for $I_o = 0.03$ amp	76
45	The value of τ at which maximum gain occurs as a function of pump level	77
46	Bandwidth characteristic curve as a function of pump level of the cyclotron-wave amplifier using a quadrifilar helix with center conductor as a simultaneous coupling and pumping structure	77
47	Frequency response of the gain	79
48	Noise characteristic of various pump levels as a function of the frequency parameter τ	84
49	The noise ratio ξ at the value of τ where maximum gain occurs, as a function of pump level	85
50	Noise figure in decibels assuming $T_c = 870^oK$, as a function of pump level for various frequencies	85

ILLUSTRATIONS (Cont'd)

Figure		Page
51	The noise ratio ξ as a function of the value of τ at which the maximum gain occurs	86
52	The noise temperature as a function of frequency for various conditions using cathode temperature as a parameter	87
53	Noise in decibels as a function of noise temperature	87
54	The ratio $\sinh 2\beta_c(r_o - b)/\sinh 2\beta_c(a - b)$ of a quadrifilar helix as a function of $r_o - b/a - b$ with $(a - b)$ as a parameter	92
55	The current density and the current limit under brillouin condition for flat beam	95
56	The nomograph for helix design	97
57	The two-anode confined-flow strip beam gun	100
58	The curves showing the condition for perfect cancellation of the lens effect at the two anodes	102
59	Nomograph of Childs law	103
60	The quadrifilar helix supported by four sapphire rods	107
61	Hollow-beam gun for the quadrifilar dc-pumped traveling-wave tube with beam current 100 ma and accelerating voltage 375 v	107
62	The actual experimental tube	108
63	Waveguide balun for dividing the signal into two branches with equal magnitude but opposite phase	111
64	The exterior and the interior of the double-ridged waveguide	112
65	The arrangement for equal power division into four successive branches with 90 deg phase difference	113
66	The actual assembly of the input or the output circuit	114
67	The measured power ratio and phase difference of the two outputs of the input waveguide balun	115
68	The measured power ratio and phase difference of the two outputs of the output waveguide balun	116
69	The output of the quadrifilar helix with -1 mode excitation	118
70	The output of the quadrifilar helix with +1 mode excitation	119
71	The quadrifilar helix with center conductor assembled for cold testing	121
72	Block diagram for the measurement of the propagation characteristic along the helix	122
73	The standing wave pattern along the helix for f = 3200 Mc	123

ILLUSTRATIONS (Cont'd)

Figure		Page
32	The pumping effect on the circuit wave carried by an infinitely long helix originally coupled with the fast cyclotron beam wave	61
33	The circuit outputs of a helix with finite length as functions of the pumping coefficient with the coupling coefficient as the parameter	63
34	The number of nulls in the circuit output as a function of the coupling coefficient and the circuit length . .	64
35	The coupling effect on the circuit wave carried by an infinitely long helix with the pumping coefficient as a parameter	65
36	The circuit outputs of a helix with finite length as functions of the coupling coefficient with the pumping coefficient as the parameter	67
37	The power carried by various waves along z-direction in the quadrifilar helix when both the rf coupling and the dc pumping are applied simultaneously	68
38	Power gain as a function of $\tau = k_{-}/k_p$ using G_{po} as a parameter	70
39	Power gain as a function of $\tau = k_{-}/_p$ for high pump levels	71
40	Universal curve of the pump parameter G_{po} vs k_pL . .	72
41	The frequency parameter as a function of ka for I_o = 10 ma and cot ψ = 12	73
42	The frequency parameter of the quadrifilar helix with center conductor for I_o = 0.10 amp	75
43	The frequency parameter τ of the quadrifilar helix with center conductor for I_o = 0.05 amp	76
44	The frequency parameter τ of the quadrifilar helix with center conductor for I_o = 0.03 amp	76
45	The value of τ at which maximum gain occurs as a function of pump level	77
46	Bandwidth characteristic curve as a function of pump level of the cyclotron-wave amplifier using a quadrifilar helix with center conductor as a simultaneous coupling and pumping structure	77
47	Frequency response of the gain	79
48	Noise characteristic of various pump levels as a function of the frequency parameter τ	84
49	The noise ratio ξ at the value of τ where maximum gain occurs, as a function of pump level	85
50	Noise figure in decibels assuming T_c = 870°K, as a function of pump level for various frequencies	85

ILLUSTRATIONS (Cont'd)

Figure		Page
74	The measured ω-β propagation characteristics of -1 mode helix wave	123
75	Schematic diagram of the quadrifilar helix tube	124
76	Test setup for testing the electron gun	125
77	The temperature-limited cathode emission current as a function of heater power	126
78	The cathode emission current as a function of first anode voltage for various heater powers	126
79	Test setup for measuring the transmission of the beam	127
80	The percent of beam current transmitted to the collector	128
81	The couplings between beam waves and the 0 mode circuit wave at f = 1.2 kMc	131
82	The co-flow coupling between the fast cyclotron wave and the -1 mode circuit wave	132
83	The contra-flow coupling between the fast cyclotron wave and the -1 mode circuit wave	133
84	The fast wave interaction with the -1 mode circuit wave, with beam voltage fixed at 100 v	134
85	The beam voltage at which longitudinal interaction occurs, as a function of frequency	135
86	The ω-β diagram of the circuit measured by the interaction with beam waves	136
87	The measured $(\cos^{-1}\sqrt{P_c/P})^2$ of the -1 mode vs I_o for various frequencies	138
88	The measured $(\cos^{-1}\sqrt{P_c/P})^2$ of the 0 mode vs I_o for various frequencies	139
89	The measured transverse impedance vs (ka +n) in comparison with the theoretical value	140
90	The pumped gain of the circuit wave	141
91	The output as a function of pumping voltage at f = 3700 Mc with beam current as a parameter	142
92	The comparison of the observed and calculated output vs pumping voltage	143
93	The measured gain at various frequencies for synchronous electron beam under + - + - dc pumping	144
94	The sensitivity of the operation to dc beam voltage, magnetic field, and the lens effect	145
95	The operation with slowed electron beam under + - + - dc pumping	146
96	The operation with synchronous electron beam under + + - - dc pumping	146

ILLUSTRATIONS (Cont'd)

Figure		Page
97	The gains of the circuit waves plotted as functions of τ at pump level G_{po} = 20 db	154
98	The gains of the circuit waves plotted as functions of τ at pump level G_{po} = 40 db	155
99	The gains of the circuit waves plotted as functions of τ at pump level G_{po} = 60 db	155
100	The dimensions of a quadrifilar helix with center conductor	157
101	A developed quadrifilar helix with center conductor close to the helix	160

ACKNOWLEDGMENT

The author wishes to express his sincere gratitude to his adviser, Dr. A. E. Siegman, for his guidance, encouragement, and valuable criticism given during this research. Thanks are also due to Dr. T. Wessel-Berg for his many helpful suggestions and comments. The author is also grateful to his colleagues on the staff at Stanford Electronics Laboratories and the Microwave Laboratory for numerous beneficial discussions.

This research was supported by the U. S. Signal Corps under contracts DA 36-039 SC-73178 and DA 36-039 SC-85387. The author also appreciated financial support from the C. T. Loo Fellowship grant.

I. INTRODUCTION

Parametric amplification using an electron beam as a parametric medium has been studied by many researchers in the past few years. Both longitudinal beam waves [Ref. 1] and transverse beam waves [Ref. 2] have been utilized. Only the transverse cyclotron waves have so far provided good performance.

The fast space-charge wave was studied by Louisell, Quate, Ashkin, and others [Refs. 3,4,5,6]. Ashkin carried out an experimental investigation, and poor performance of the fast space-charge-wave parametric amplifier was found. The reason is that the ratio of plasma frequency to operating frequency typically is a small number, so that the space-charge waves are essentially of a nondispersive nature. As a consequence, those space-charge waves at frequencies $n\omega_p \pm \omega_s$ which have the proper velocity synchronism will beat with the pump field or its harmonics, thereby transferring their excitation to the signal frequency wave at ω_s.

The fast cyclotron wave was sucessfully used by Adler, Hrbek, and Wade [Refs. 7,8]. In this operation the magnetic field plays an important role in addition to that of focusing the beam. The signal mode is a fast cyclotron wave on the beam. It is actively coupled to an idler mode, which is also a fast cyclotron wave, by the pumping action of a high-frequency, transverse, electric quadrupole field which oscillates at twice the cyclotron frequency. This operation can be clearly shown as a vector relation in the ω-β space in Fig. 1.

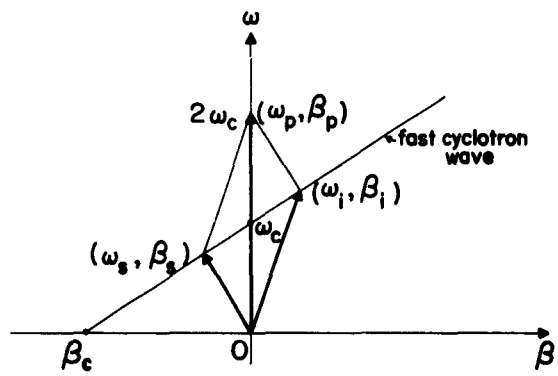

FIG. 1. THE ω-β DIAGRAM OF AN RF-PUMPED FAST-CYCLOTRON-WAVE PARAMETRIC AMPLIFIER.

In matrix form:

$$\begin{bmatrix} \omega_p \\ \beta_p \end{bmatrix} = \begin{bmatrix} \omega_s \\ \beta_s \end{bmatrix} + \begin{bmatrix} \omega_i \\ \beta_i \end{bmatrix} = \begin{bmatrix} 2\omega_c \\ 0 \end{bmatrix}$$

Since the wave number of the pumping field is zero, the pumping structure is a quadrupole with four straight bars. Input and output coupling to the signal and idler modes is accomplished via the use of a fast-wave circuit, such as a resonant cavity or Cuccia coupler, which provides a transverse electric field. The low-noise advantage of this type of tube arises because both interacting modes are fast waves carrying positive energy, so that the initial noise can be stripped off by the same coupler. Both modes increase their energy exponentially in the rf pumping field. The experimental tubes described in Refs. 7 and 8 showed excellent performance, with 20-db gain and a double-channel noise temperature of 40°K (the noise figure 0.53 db) in the range of 400 to 1000 Mc. Ashkin also built a tube operating successfully at 4137 Mc with 19-db gain and a noise figure of 0.79 db (noise temperature 55°K) [Ref. 9]. The space-charge effects on this type of operation were studied by Everhart [Ref. 10]. The causes of noise in the transverse beam waves were studied by Lee-Wilson and Gordon [Refs. 11 and 12]. Methods of discriminating the beam noise were studied by Robinson, Hart, and others [Refs. 13,14,15].

Cyclotron waves can also be amplified by dc field pumping, as pointed out by Gordon and others [Refs. 16 and 17]. A wave analysis describing the processes occurring in these devices was introduced by Siegman [Refs. 18 and 19]. The signal mode in the dc-pumped case is a fast cyclotron wave as in the Adler-Wade tube. But, the signal mode is actively coupled to a slow cyclotron idler mode by the pumping action of a dc transverse electric quadrupole field. This operation can also be represented as a vector relation in the ω-β space as shown in Fig. 2. In matrix form:

$$\begin{bmatrix} \omega_p \\ \beta_p \end{bmatrix} = \begin{bmatrix} \omega_s \\ \beta_s \end{bmatrix} - \begin{bmatrix} \omega_i \\ \beta_i \end{bmatrix} = \begin{bmatrix} 0 \\ -2\beta_c \end{bmatrix}$$

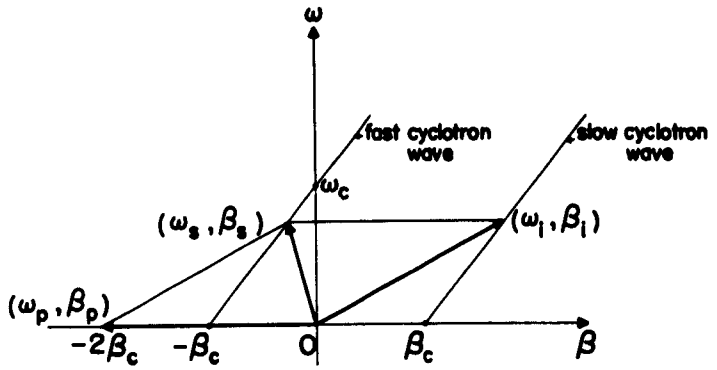

FIG. 2. THE ω-β DIAGRAM OF A DC-PUMPED CYCLOTRON-WAVE QUASI-PARAMETRIC AMPLIFIER.

The use of dc fields rather than rf fields for pumping requires either a series of successively rotated quadrupole segments or a continuously twisted quadrifilar helical structure in order to provide the proper wave number $\beta_p = -2\beta_c$ of the pumping field. Though the dc-pumped quadrupole amplifier in many respects is similar to the rf-pumped quadrupole amplifier, it possesses quite different characteristics in performance and operation. Two significant differences are:

1. In the dc case the signal and the idler modes are not actually "pumped" by the quadrupole fields, since no energy is delivered to the beam from the dc field. The quadrupole field is merely acting as a linking mechanism to achieve active coupling between the signal and the idler modes;
2. Due to the fact that the idler mode is a slow cyclotron wave carrying negative energy, the dc-pumped amplifier does not exhibit the same low-noise performance as the rf-pumped amplifier.

Recently, Wessel-Berg proposed a magnetic field reversal to convert cyclotron waves to synchronous waves and vice versa [Ref. 20]. He and Blötekjaer also studied the coupling between cyclotron waves and synchronous waves by axially symmetric and spatially periodic electrostatic or magnetostatic fields, plus the coupling between two synchronous waves by straight quadrupoles [Refs. 21 and 22]. Bass tested the electrostatic ring structure, with about 12 to 18 db electronic gain [Refs. 23 and 24].

All of these devices consist of three important parts, namely: the input coupler, the pumping section, and the output coupler. Although their bandwidth is considerably broader than the solid-state parametric amplifier, it is still limited in most cases by the relatively narrow frequency response of the input and output couplers.

The present report is a detailed study, both theoretical and experimental, of the possible wideband operation of a cyclotron-wave amplifier using *simultaneous* rf coupling and dc pumping in a single structure, as first proposed by A. E. Siegman [unpublished]. In this operation a single circuit such as a quadrifilar helix is used to provide the coupling of a signal into and out of the fast cyclotron wave, and also to provide the proper twisted dc electrostatic field to pump the cyclotron waves. Due to the elimination of the frequency-sensitive input and output couplers encountered in the conventional cyclotron-wave amplifier, the bandwidth can be considerably broadened, since the pump coefficient itself is independent of signal frequency and the coupling coefficient can be made fairly insensitive to the signal frequency. This operation can also be clearly illustrated in an ω-β diagram, as shown in Fig. 3. A circuit wave having the same phase velocity as the fast cyclotron wave over a wide band of frequencies is used to provide the coupling, as in conventional traveling-wave tubes. The coupling helix structure is also used to provide the dc pumping fields that couple the fast and the slow cyclotron waves, causing amplification. (There is also an alternate mode of operation which couples one of the synchronous waves to the fast cyclotron wave to give similar results.) Figure 4 shows the structural differences between the conventional parametric amplifier and the present amplifier reported.

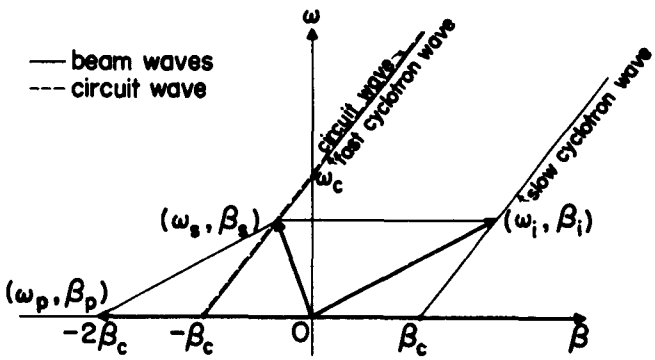

FIG. 3. CYCLOTRON-WAVE AMPLIFICATION USING SIMULTANEOUS RF COUPLING AND DC PUMPING.
Interaction is possible anywhere along the circuit wave line with fixed beam voltage and magnetic field.

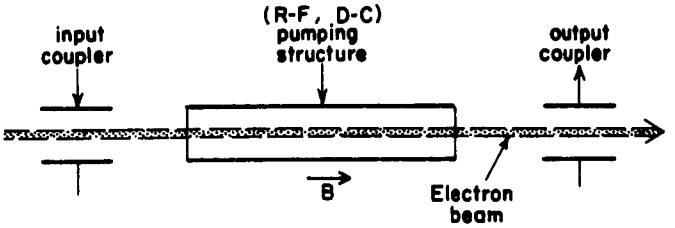

a. Conventional beam-type parametric amplifier

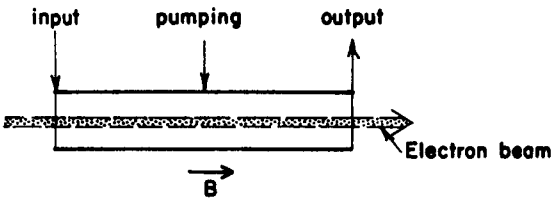

b. Simultaneous coupling and pumping amplifier

FIG. 4. A COMPARISON BETWEEN THE CONVENTIONAL BEAM-TYPE PARAMETRIC AMPLIFIER AND THE SIMULTANEOUS COUPLING AND PUMPING AMPLIFIER.

This report can be broken into two parts: 1) theoretical study and analysis of the physical details and processes of the operation; and 2) experimental design, tests, measurements, and comparison between theory and experimental results. Chapters II and III cover the theoretical aspects of dc pumping, rf coupling, and their combination, as well as theoretical gain, bandwidth, and noise characteristics. Chapters IV and V cover the design aspect, the construction of experimental tubes, the experimental arrangements, and the results from the measurements.

In Chapter II the detailed analysis of dc pumping and rf coupling using a quadrifilar helix is reviewed. The dc pumping includes a complete wave analysis following the Eulerian approach with the assumption of small pumping strength. The analysis provides physical understanding of the interaction phenomena under various pumping conditions. The chapter further contains a large-signal perturbation analysis following the Lagrangian approach for the case of cyclotron-wave amplification. The expression for the pumping coefficient found from this analysis is in

agreement with that obtained from the wave analysis, and the slowing down in the dc beam velocity for the amplifying electrons is confirmed. Conditions required on the helix pitch, beam voltage, magnetic field, etc., for the amplification of cyclotron waves are discussed. The rf coupling includes a discussion of the normal modes of circuit waves and transverse beam waves; their excitation and dependence on beam voltage, magnetic field, and helix structure, etc.; and conditions required for the proper coupling leading to interchange of energy between circuit and beam waves. These analyses are generally similar to analyses carried out previously by other workers.

In Chapter III coupled-mode theory is used to study the novel mode of operation with simultaneous rf coupling between the circuit and the beam, and active dc pumping on the beam. Energy flow and power conservation is explained and the physical processes of operation are interpreted. From the results of the coupled-mode analysis, the gain and bandwidth as a function of the ratio τ of the coupling coefficient to the pumping coefficient is studied. This provides the basis for practical designs operating in the same scheme. Bandwidths of more than 100 percent are found possible for this type of operation. Although low-noise operation is not an aim of this study, due to the existence of the slow cyclotron wave, the noise characteristic of the tube is calculated as a function of τ assuming that there is no refrigeration of the beam. If the beam is cooled down by a collimator as proposed by Wade [Ref. 25] or by parametric refrigeration as proposed by Sturrock [Ref. 26] or by some other means unknown at present, this tube can be operated as a low-noise amplifier.

Chapter IV is devoted to the design and actual construction of an experimental tube to test the preceding theory of simultaneous rf coupling and dc pumping. In designing a quadrifilar helix to operate under this scheme we have to meet both the pumping conditions and the coupling conditions. The design procedure is to assume a specified frequency range and from this to determine the corresponding radius and pitch of the helix. At this point practical construction techniques are brought into consideration, from which the size and the shape of the wire as well as the material are decided. In designing the electron gun the simplest type would be the immersed flow gun. Cancellation of lens effects is considered in detail. The possibility of controlling the beam current is also a consideration. Design procedures for the complete tube are outlined and several tentative designs for various frequency bands are

tabulated. An experimental tube in S-band, using a quadrifilar helix with center conductor and a hollow beam gun, was designed and constructed in this laboratory. The special technique developed in our tube shop in manufacturing the fine-wire large-radius quadrifilar helix is included.

In Chapter V the experimental data and results of the experimental tube are presented and compared with theory. The fast cyclotron-wave interaction is also found useful in measuring the ω-β characteristics of the circuit structure especially for the -1 mode.

Finally in Chapter VI, the work is summarized, with recommendations for further research into the problems of other possible coupling, pumping, and noise-reduction schemes, as well as efficiency, power capability, and frequency limitations.

II. GENERAL THEORY OF DC PUMPING AND RF COUPLING

This chapter contains two parts; the first part develops the detailed study of dc pumping using both a Eulerian (wave) and a Lagrangian (ballistic) approach; the second part deals with the possible rf coupling between the circuit waves in the quadrifilar helix and the transverse waves in the electron beam. The conditions for active pumping of the fast and slow cyclotron waves and the conditions for wideband rf coupling between the fast cyclotron beam wave and the -1 mode circuit wave are specified. It is found that both conditions can be simultaneously obtained by proper design of the helix and the beam.

A. CYCLOTRON-WAVE AMPLIFICATION BY TWISTED DC-PUMPING FIELDS

1. Complete Analysis from a Wave Point of View

Transverse modulation on an electron beam confined in a longitudinal dc magnetic field will make the individual electrons rotate in the transverse direction. The rate of rotation is determined by the dc magnetic field and is called the cyclotron frequency, $\omega_c = B\ e/m$, which is about 2.8 Mc for each gauss of magnetic field. Assume that the beam has a constant velocity in the longitudinal direction; then due to the transverse rotation, the electron will perform a helical trajectory as shown in Fig. 5.

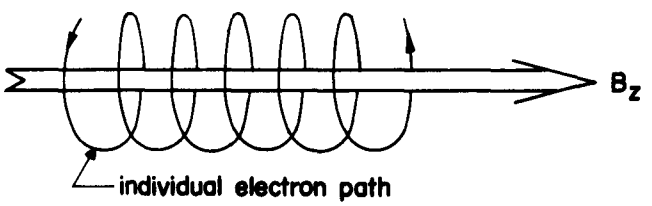

FIG. 5. THE HELICAL TRAJECTORY OF AN ELECTRON WITH TRANSVERSE ENERGY AND CONSTANT AXIAL VELOCITY IMMERSED IN AN AXIAL MAGNETIC FIELD.

This combination of rotational and translational motion of the electrons can be considered as a wave motion. Since there are four independent transverse mechanical modulations (namely, v_x, v_y, x and y) on the electron beam, it is logical that the beam should carry four transverse normal modes or waves which span the four-dimensional space in

the transverse plane. These waves have been discussed by Siegman [Ref. 2] and others, and their important properties are summarized in Table 1.

TABLE 1. TRANSVERSE BEAM WAVES

Symbol	Type	Wave Number*	AC Energy	Polarization
A_f	Fast Cyclotron Wave	$\beta_e - \beta_c$	+	right hand
A_s	Slow Cyclotron Wave	$\beta_e + \beta_c$	-	left hand
A_1	First Synchronous Wave	β_e	+	left hand
A_2	Second Synchronous Wave	β_e	-	right hand

*$\beta_e = \frac{\omega}{u_o}$, $\beta_c = \frac{\omega_c}{u_o}$, ω_c = cyclotron frequency, and u_o = dc beam velocity.

The normalized mode amplitudes of the four waves are a linear combination of the four independent transverse modulations on the electron beam. This relation can be expressed clearly in matrix form:

$$\begin{bmatrix} \tilde{A}_f \\ \tilde{A}_s \\ \tilde{A}_1 \\ \tilde{A}_2 \end{bmatrix} = j\,\frac{k}{2} \begin{bmatrix} 1 & +j & 0 & 0 \\ 1 & -j & 0 & 0 \\ 1 & -j & j\omega_c & \omega_c \\ 1 & +j & -j\omega_c & \omega_c \end{bmatrix} \begin{bmatrix} v_x \\ v_y \\ x \\ y \end{bmatrix} \tag{2.1}$$

where

$$k = \sqrt{\frac{I_o\,\omega}{2\pi\omega_c}}$$

$$\begin{aligned} \tilde{A}_f &= A_f \exp\{j[\omega t - (\beta_e - \beta_c)z]\} \\ \tilde{A}_s &= A_s \exp\{j[\omega t - (\beta_e + \beta_c)z]\} \\ \tilde{A}_1 &= A_1 \exp\{j[\omega t - \beta_e z]\} \\ \tilde{A}_2 &= A_2 \exp\{j[\omega t - \beta_e z]\} \end{aligned} \tag{2.2}$$

and

A_f = fast cyclotron-wave amplitude

A_s = slow cyclotron-wave amplitude

A_1 = first synchronous-wave amplitude

A_2 = second synchronous-wave amplitude

Conversely, the transverse rf modulation of the beam is a linear combination of the waves,

$$\begin{bmatrix} v_x \\ v_y \\ \\ x \\ y \end{bmatrix} = \frac{e^{j(\omega t-\beta_e z)}}{k\omega_c} \begin{bmatrix} -j\omega_c & -j\omega_c & 0 & 0 \\ -\omega_c & \omega_c & 0 & 0 \\ \\ -1 & 1 & -1 & 1 \\ j & j & -j & -j \end{bmatrix} \begin{bmatrix} A_f\, e^{+j\beta_c z} \\ A_s\, e^{-j\beta_c z} \\ \\ A_1 \\ A_2 \end{bmatrix} \tag{2.3}$$

All the amplitudes of the waves are constant along the z-direction provided there is no influence from external fields (except the longitudinal dc magnetic field). But, they will be a function of z if there are either transverse electric or magnetic fields in the beam region. They may be verying sinusoidally or exponentially or in arbitrary fashion depending upon the type of field.

Now let us consider the dc-twisted electric field set up by a quadrifilar helix as shown in Fig. 6. The potential distribution inside the quadrifilar helix can be expressed approximately as

$$V = \frac{1}{2} K[2xy \cos 2\beta_q z - (x^2 - y^2) \sin 2\beta_q z] \tag{2.4}$$

The derivation of this equation is shown in Appendix A. In this equation, K is proportional to the dc pumping voltage and inversely proportional to the square of the diameter of the helix; and β_q is equal to $2\pi/p$ where p is the pitch of the quadrifilar helix. The phase number of the pumping field is then $\beta_p = 2\beta_q$.

This twisted dc potential provides a transverse electric field as follows:

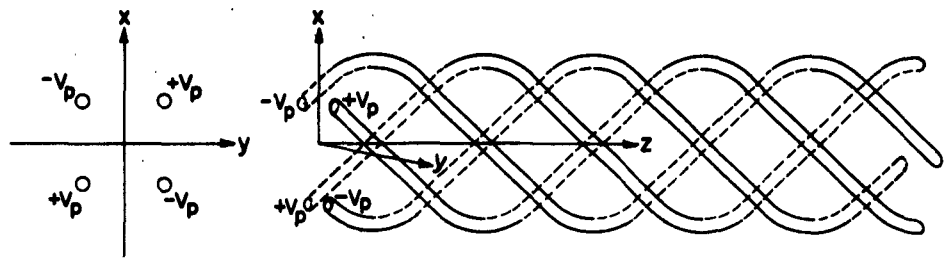

a. Transverse plane at $z = 0$

b. The quadrifilar helix

FIG. 6. THE AXIALLY SYMMETRICAL DC ELECTRIC FIELD SET UP BY A QUADRIFILAR HELIX.

$$E_x = -\frac{\partial V}{\partial x} = -K\,(y \cos 2\beta_q z - x \sin 2\beta_q z) \tag{2.5}$$

$$E_y = -\frac{\partial V}{\partial y} = -K\,(x \cos 2\beta_q z + y \sin 2\beta_q z) \tag{2.6}$$

We now proceed to investigate how these transverse electric fields influence the electronic motion from a wave point of view. In order to formulate the problem, we start from the equations of motion.

$$\frac{d^2x}{dt^2} + \omega_c \frac{dy}{dt} + \eta E_x = 0 \tag{2.7}$$

$$\frac{d^2y}{dt^2} - \omega_c \frac{dx}{dt} + \eta E_y = 0 \tag{2.8}$$

Since the transverse electron motion in a magnetic field has rotational character, it is convenient to use circularly polarized components rather than linearly polarized components. The relation between circularly polarized components and linearly polarized components of a transverse vector $\vec{F}$ is

$$\begin{bmatrix} F_+ \\ F_- \end{bmatrix} = \frac{1}{2} \begin{bmatrix} 1 & -j \\ 1 & j \end{bmatrix} \begin{bmatrix} F_x \\ F_y \end{bmatrix} \tag{2.9}$$

and inversely

$$\begin{bmatrix} F_x \\ F_y \end{bmatrix} = \begin{bmatrix} 1 & 1 \\ j & -j \end{bmatrix} \begin{bmatrix} F_+ \\ F_- \end{bmatrix} \tag{2.10}$$

where the subscript (-) represents the right-hand circularly polarized component, for which the sense of rotation corresponds to the rotation of electrons or particles carrying negative charge in the longitudinal dc magnetic field; and the subscript (+) represents the left-hand circularly polarized component with opposite sense of rotation, which corresponds to the rotation of particles carrying positive charge in the same magnetic field. The subscripts x and y represent the linearly polarized components in the x- and y-directions, respectively. Then, the circularly polarized components of the position of electrons can be found from Eq. (2.9) as follows:

$$\begin{aligned} r_+ &= \frac{1}{2}(x - jy) \\ r_- &= \frac{1}{2}(x + jy) \end{aligned} \tag{2.11}$$

and the potential in the quadrifilar h(ix as shown in Eq. (2.4) can be expressed as:

$$V = jK\left(r_+^2\, e^{j2\beta_q z} - r_-^2\, e^{-j2\beta_q z}\right) \tag{2.12}$$

It can be easily proved that

$$E_+ = \frac{1}{2}(E_x - jEy) = -\frac{1}{2}\frac{\partial V}{\partial r_-}$$

and

$$E_- = \frac{1}{2}(E_x + jE_y) = -\frac{1}{2}\frac{\partial V}{\partial r_+}$$

and the equations of motion become:

$$\frac{d^2 r_+}{dt^2} + j\omega_c \frac{dr_+}{dt} + j\eta K\, r_-\, e^{-j2\beta_q z} = 0 \tag{2.13}$$

$$\frac{d^2 r_-}{dt^2} - j\omega_c \frac{dr_-}{dt} - j\eta K\, r_+\, e^{+j2\beta_q z} = 0 \tag{2.14}$$

Note the vital point that the field components E must be evaluated at the electron position in writing the equations of motion. From Eqs. (2.3) and (2.11) we have the wave expression for the circularly polarized rf modulation as

$$r_+ = \frac{1}{k\omega_c}\left(A_s\, e^{-j\beta_c z} - A_1\right) e^{j(\omega t - \beta_e z)} \tag{2.15}$$

$$r_- = \frac{-1}{k\omega_c}\left(A_f\, e^{+j\beta_c z} - A_2\right) e^{j(\omega t - \beta_e z)} \tag{2.16}$$

Due to the influence of the twisted dc field, the amplitude of the waves is no longer constant along the direction of the beam. Consider a wave quantity of the form:

$$\tilde{C} = C(z)\, e^{j(\omega t - \beta_e z)} \tag{2.17}$$

Assuming small modulation, the longitudinal beam velocity u_o is approximately a constant, and therefore:

$$\frac{d}{dt}\tilde{C} = \frac{\partial}{\partial t}\tilde{C} + u_o \frac{\partial}{\partial z}\tilde{C}$$

from which we obtain a useful equation:

$$\frac{d}{dt}\left[C(z)\, e^{j(\omega t - \beta_e z)}\right] = e^{j(\omega t - \beta_e z)} \frac{d}{d\left(\frac{z}{u_o}\right)} C(z) \tag{2.18}$$

This says the total derivative with respect to time of a product of the function of z and a complex phase factor $\exp[j(\omega t - \beta_e z)]$ is equal to the product of the phase factor and the total derivative with respect to z/u_o of the said function of z. With the phase factor $\exp[j(\omega t - \beta_e z)]$ understood and kept in mind, we can simplify our writing as

$$\frac{d}{dt} C = u_o \frac{d}{dz} C \tag{2.18a}$$

to represent Eq. (2.18).

From Eqs. (2.15) and (2.16) and using the relation we just obtained, we can easily obtain the derivatives of the circularly polarized components in terms of normalized waves with the factor $\exp[j(\omega t - \beta_e z)]$ understood:

$$\frac{dr_+}{dt} = \frac{u_o}{k\omega_c}\left(\frac{dA_s}{dz} - j\beta_c A_s\right) e^{-j\beta_c z} - \frac{u_o}{k\omega_c}\frac{dA_1}{dz} \tag{2.19}$$

$$\frac{dr_-}{dt} = -\frac{u_o}{k\omega_c}\left(\frac{dA_f}{dz} + j\beta_c A_f\right) e^{+j\beta_c z} + \frac{u_o}{k\omega_c}\frac{dA_2}{dz} \tag{2.20}$$

$$\frac{d^2r_+}{dt^2} = \frac{u_o^2}{k\omega_c}\left(\frac{d^2A_s}{dz^2} - j2\beta_c\frac{dA_s}{dz} - \beta_c^2 A_s\right) e^{-j\beta_c z} - \frac{u_o^2}{k\omega_c}\frac{d^2A_1}{dz^2} \tag{2.21}$$

$$\frac{d^2r_-}{dt^2} = -\frac{u_o^2}{k\omega_c}\left(\frac{d^2A_f}{dz^2} + j2\beta_c\frac{dA_f}{dz} - \beta_c^2 A_f\right) e^{+j\beta_c z} + \frac{u_o^2}{k\omega_c}\frac{d^2A_2}{dz^2} \tag{2.22}$$

Substituting these equations into the equations of motion (2.13) and (2.14), we obtain the desired key equations which describe the influence of the twisted dc field on the four beam waves:

$$\left(\frac{d^2A_s}{dz^2} - j\beta_c\frac{dA_s}{dz}\right) e^{-j\beta_c z} - \left(\frac{d^2A_1}{dz^2} + j\beta_c\frac{dA_1}{dz}\right) = j\beta_c\, k_p\left(A_s\, e^{+j\beta_c z} - A_2\right) e^{-j2\beta_q z} \tag{2.23}$$

$$\left(\frac{d^2A_f}{dz^2} + j\beta_c\frac{dA_f}{dz}\right) e^{+j\beta_c z} - \left(\frac{d^2A_2}{dz^2} - j\beta_c\frac{dA_2}{dz}\right) = -j\beta_c\, k_p\left(A_s\, e^{-j\beta_c z} - A_1\right) e^{+j2\beta_q z} \tag{2.24}$$

where

$$k_p = \frac{K}{\eta B^2}\beta_c = \frac{K}{Bu_o} = \left(\frac{\lambda_c}{2\pi a}\right)^2 \frac{V_p}{2V_o}\beta_c \tag{2.25}$$

is defined as a pump factor since it is proportional to the dc pump potential on the quadrifilar helix.

It should be noted that Eqs. (2.23) and (2.24) are obtained without specifying the pitch of the helix. It is found that we can choose the proper pitch of the quadrifilar helix to achieve three different operating conditions of the dc pump:

1. Both the fast and slow cyclotron wave will be actively pumped by the field if $\beta_p = 2\beta_c$, i.e., $p = \lambda_c = u_o/f_c$ or $\beta_q = \beta_c$. Growing cyclotron waves are obtained.
2. One cyclotron wave and one synchronous wave with the same parity matrix element [Ref. 27] (i.e., they carry the same sign of ac energy) will be passively pumped by the field if $\beta_p = \beta_c$, i.e., $p = 2\lambda_c$ or $\beta_q = 1/2\ \beta_c$. Energy-beating phenomena and sinusoidal energy transfer between the waves are obtained at small pump levels.
3. The first and second synchronous waves will be actively pumped by the field if $\beta_p = 0$, i.e., $p = \infty$ or $\beta_q = 0$, or, in other words, the field is no longer twisted. Growing synchronous waves will be obtained.

The following paragraphs will discuss these three cases in detail, with the assumption of small pumping strength. First it is assumed that the solutions of the wave amplitudes of Eqs. (2.23) and (2.24) are of Floquet form consisting of an infinite series of exponentials. Then, equating the terms with the same z periodicity on both sides of the equations leads to an infinite set of algebraic equations. However, with the assumption of small pumping strength one can then neglect all the equations containing higher order terms of the pumping coefficient and leave only the equations of first order of the pumping coefficient for further investigation.

a. Active Pumping on Both Cyclotron Waves (Case 1)

If we design the helix to be twisted at the same rate as the electron rotates, so that the pitch of the helix is made equal to the cyclotron wavelength traveling at the dc beam velocity, then we have $\beta_q = \beta_c$. Substituting this relation into Eqs. (2.23) and (2.24) and equating the terms with the same z periodicity on both sides to the first order of pumping only, as mentioned previously, we obtain

$$\frac{d^2A_s}{dz^2} - j\beta_c \frac{dA_s}{dz} = j\beta_c\ k_p\ A_f \tag{2.26}$$

$$\frac{d^2A_f}{dz^2} + j\beta_c \frac{dA_f}{dz} = -j\beta_c\ k_p\ A_s \tag{2.27}$$

It is clear that both the fast and slow cyclotron waves are pumped by the twisted dc field, while the two synchronous waves are not. In order to solve this set of differential equations, we can assume the exponential form $A \sim C\, e^{\nu z}$, where both the C's and ν's are constants. The C's are determined by the initial condition at $z = 0$, and the ν's are the eigenvalues of Eqs. (2.26) and (2.27).

To find the eigenvalues, we first substitute the exponential form of the solution into Eqs. (2.26) and (2.27) to transform the differential equations to homogeneous algebraic equations. In order that there exist nontrivial solutions for the C's, the determinant of their coefficients should be zero, i.e.,

$$\begin{vmatrix} \nu^2 - j\beta_c\nu & -j\beta_c\, k_p \\ j\beta_c\, k_p & \nu^2 + j\beta_c\nu \end{vmatrix} = 0 \tag{2.28}$$

or

$$\nu^4 - \beta_c^2\, \nu^2 - \beta_c^2\, k_p^2 = 0 \tag{2.29}$$

The solutions are

$$\begin{matrix} \nu_1 \\ \\ \nu_2 \end{matrix} = \pm\alpha \tag{2.30}$$

where

$$\alpha = \frac{\beta_c}{\sqrt{2}}\left(\sqrt{1 + \frac{4k_p^2}{\beta_c^2}} - 1\right)^{1/2} \cong k_p$$

$$\begin{matrix} \nu_3 \\ \\ \nu_4 \end{matrix} = \pm j\beta \tag{2.31}$$

where

$$\beta = \frac{\beta_c}{\sqrt{2}}\left(\sqrt{1 + \frac{4k_p^2}{\beta^2}} + 1\right)^{1/2} \cong \beta_c\left[1 + \frac{1}{2}\,\frac{k_p^2}{\beta_c^2}\right]$$

It is evident that there will be four components associated with each wave due to the properly twisted dc field. There is one exponentially growing component and one exponentially decaying component along the z-direction. The other two components have a shift in phase number from the original wave, and can be considered as space sidebands in a fashion similar to the frequency sidebands in amplitude or frequency modulation. Each space sideband possesses a different phase velocity: one of them is slower and the other is faster than the original unperturbed wave. These four components of the fast cyclotron wave are shown explicitly in the phase plane ω-β diagram in Fig. 7 and those of the slow cyclotron wave are shown in Fig. 8. The analytic expression for the waves perturbed by the dc pumping field are:

$$\tilde{A}_f = \left[A_{f1}\, e^{k_p z} + A_{f2}\, e^{-k_p z} + A_{f3}\, e^{j\beta z} + A_{f4}\, e^{-j\beta z}\right] \exp\{j[\omega t-(\beta_e-\beta_c)z]\} \tag{2.32}$$

$$\tilde{A}_s = \left[A_{s1}\, e^{k_p z} + A_{s2}\, e^{-k_p z} + A_{s3}\, e^{j\beta z} + A_{s4}\, e^{-j\beta z}\right] \exp\{j[\omega t-(\beta_e+\beta_c)z]\} \tag{2.33}$$

These can be expressed alternatively as:

$$\tilde{A}_f = [B_{f1} \cosh (k_p z+\phi_f) + B_{f2} \cos (\beta z + \theta_f)]\, e^{j[\omega t-(\beta_e-\beta_c)z]} \tag{2.32a}$$

$$\tilde{A}_s = [B_{s1} \cosh (k_p z+\phi_s) + B_{s2} \cos (\beta z + \theta_s)]\, e^{j[\omega t-(\beta_e+\beta_c)z]} \tag{2.33a}$$

where B's, ϕ's, and θ's are all constants determined by the initial conditions. From Eqs. (2.32a) and (2.33a) one obtains a clear physical picture for this dc-pumped active coupling. The effect due to this coupling is an amplitude variation along the beam consisting of exponential growth on which a sinusoidal variation is superimposed. Both the fast and the slow cyclotron waves will grow at the same rate, with a superimposed sinusoidal variation at the same space frequency. The latter variation can be neglected after sufficient growth in magnitude along the beam. The amplitudes along the beam due to this pumping are shown in Fig. 9. Since the fast cyclotron wave carries positive power and the slow cyclotron wave carries negative power, the energy will flow from the negative-power-carrying wave to the positive-power-carrying wave. Because of this interaction growing waves result, although the total energy carried by both waves is unchanged.

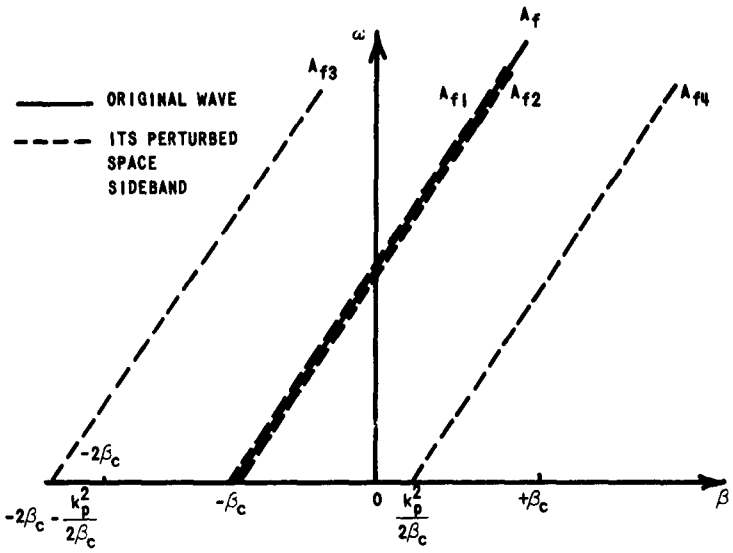

FIG. 7. ω-β DIAGRAM OF THE SPACE SIDEBANDS OF THE FAST CYCLOTRON WAVE UNDER ACTIVE PUMPING.

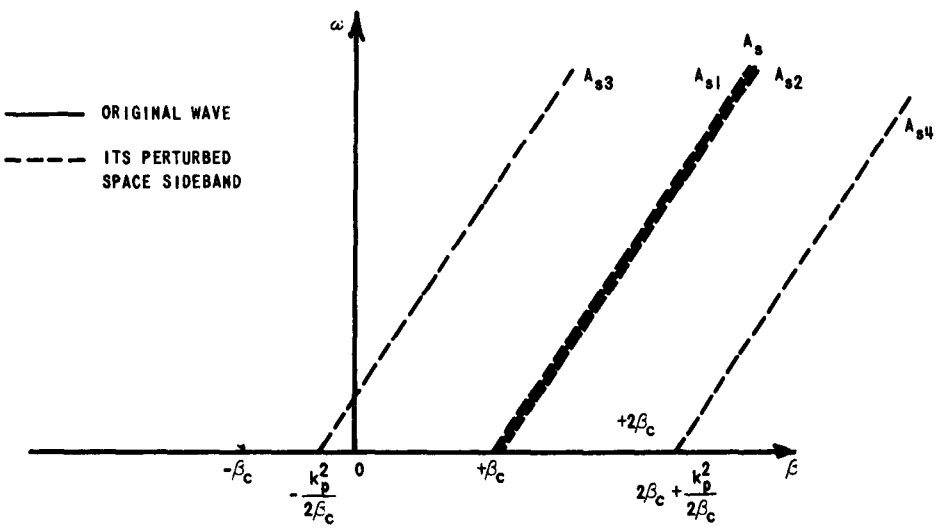

FIG. 8. ω-β DIAGRAM OF THE SPACE SIDEBANDS OF THE SLOW CYCLOTRON WAVE UNDER ACTIVE PUMPING.

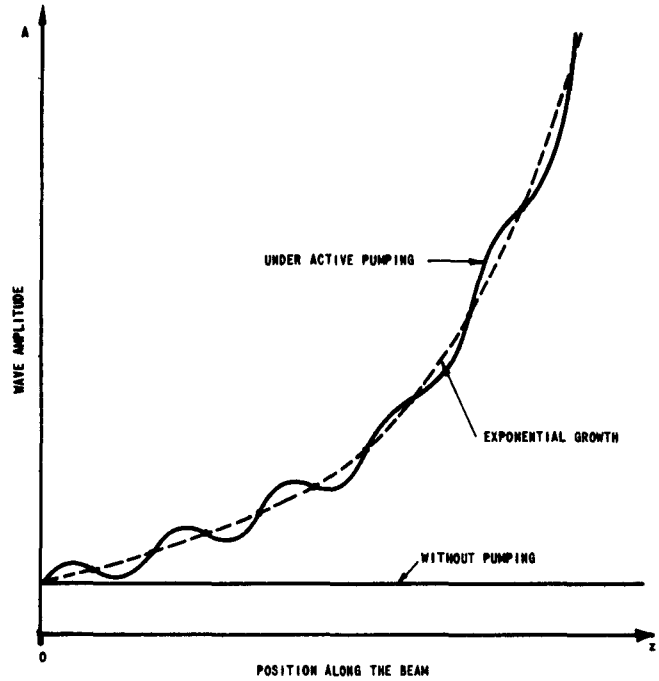

FIG. 9. THE WAVE AMPLITUDE ALONG THE BEAM UNDER ACTIVE DC PUMPING.

b. Passive Pumping of one Cyclotron Wave and one Synchronous Wave (Case 2)

If one designs the helix to be twisted at only one-half of the beam rate, then the pitch of the helix is twice the cyclotron wavelength traveling at the beam dc velocity. This case corresponds to putting $\beta_q = 1/2\ \beta_c$. Substituting this relation of wave constants into Eqs. (2.23) and (2.24) and then equating the terms with the same z-dependence on both sides of the equations, one obtains the following two sets of equations under the assumption of small pumping coefficient:

$$\left.\begin{aligned} \frac{d^2A_s}{dz^2} - j\beta_c \frac{dA_s}{dz} &= -j\beta_c\ k_p\ A_2 \\ \frac{d^2A_2}{dz^2} - j\beta_c \frac{dA_2}{dz} &= j\beta_c\ k_p\ A_s \end{aligned}\right\} \qquad (2.34)$$

and

$$\left.\begin{aligned} \frac{d^2A_f}{dz^2} + j\beta_c \frac{dA_f}{dz} &= +j\beta_c\, k_p\, A_1 \\ \frac{d^2A_1}{dz^2} + j\beta_c \frac{dA_1}{dz} &= -j\beta_c\, k_p\, A_f \end{aligned}\right\} \tag{2.35}$$

The first set of equations evidently shows that the slow cyclotron wave is coupled with the second synchronous wave. They both carry negative ac energy and have the same group velocity, so this coupling is a passive one. The second set of equations shows that the fast cyclotron wave is coupled with the first synchronous wave. This coupling is also a passive one since both of the associated waves carry positive ac power and have the same group velocity. A quantitative analysis is done following the same method as used in Case 1 by assuming that all the wave amplitudes vary exponentially in the z-direction. It is worthwhile to note that Eqs. (2.35) are exactly the same form as Eqs. (2.34) if one substitutes (β_c) for ($-\beta_c$) in the equations of (2.35). So, we can solve Eqs. (2.34) and, simultaneously, Eqs. (2.35) are solved.

Assuming the exponential form to be $C\, e^{\nu z}$ for the amplitudes of the waves, we then have from Eqs. (2.34)

$$\begin{vmatrix} \nu^2 - j\beta_c\nu & +j\beta_c\, k_p \\ -j\beta_c\, k_p & \nu^2 - j\beta_c\nu \end{vmatrix} = 0 \tag{2.36}$$

Hence the solutions are:

$$\begin{aligned} \nu_1 \\ \nu_2 \end{aligned} = +\frac{j\beta_c}{2}\left(1 \pm \sqrt{1 + \frac{4k_p}{\beta_c}}\right) \cong \begin{cases} +j(\beta_c + k_p) \\ -j\, k_p \end{cases}$$

$$\begin{aligned} \nu_3 \\ \nu_4 \end{aligned} = +\frac{j\beta_c}{2}\left(1 \pm \sqrt{1 - \frac{4k_p}{\beta_c}}\right) \cong \begin{cases} +j(\beta_c - k_p) \\ +j\, k_p \end{cases} \tag{2.37}$$

It is clear that the solutions contain four components; each has a different wave constant which is perturbed from its original wave number by a definite amount determined by the pump coefficient. This can be interpreted as each original wave being split into four space components in a fashion similar to the sideband frequencies split from amplitude or frequency modulation in the time domain. Each space sideband possesses a different phase velocity; one of them is slower and the other three are faster than the original unperturbed wave. The four space sidebands of the slow cyclotron wave can be shown in a more realistic way by plotting the phase plane ω-β diagram as shown in Fig. 10. The four space sidebands of the second synchronous wave are shown in the diagram of Fig. 11. The analytic expressions for the perturbed waves are:

$$\tilde{A}_s = \left[A_{s1}\, e^{j(\beta_c+k_p)z} + A_{s2}\, e^{-jk_p z} + A_{s3}\, e^{j(\beta_c-k_p)z} + A_{s4}\, e^{jk_p z}\right] e^{j[\omega t-(\beta_e+\beta_c)z]} \tag{2.38}$$

$$\tilde{A}_2 = \left[A_{21}\, e^{j(\beta_c+k_p)z} + A_{22}\, e^{-jk_p z} + A_{23}\, e^{j(\beta_c-k_p)z} + A_{24}\, e^{jk_p z}\right] e^{j[\omega t-\beta_e z]} \tag{2.39}$$

These can be expressed alternatively as:

$$\tilde{A}_s = \left[B_{s1} \cos(\beta_1 z+\phi_s) + B_{s2} \cos(\beta_2 z+\theta_s)\right] \exp\left\{j\left[\omega t - \left(\beta_e + \frac{1}{2}\beta_c\right)z\right]\right. \tag{2.40}$$

$$\tilde{A}_2 = \left[B_{21} \cos(\beta_1 z+\phi_2) + \beta_{22} \cos(\beta_2 z+\theta_2)\right] \exp\left\{j\left[\omega t - \left(\beta_e - \frac{1}{2}\beta_c\right)z\right]\right. \tag{2.41}$$

where B, ϕ, and θ are all constants, and

$$\begin{aligned} \beta_1 &= \frac{\beta_c}{2}\sqrt{1+\frac{4k_p}{\beta_c}} \cong \frac{\beta_c}{2} + k_p \\ \beta_2 &= \frac{\beta_c}{2}\sqrt{1-\frac{4k_p}{\beta_c}} \cong \frac{\beta_c}{2} - k_p \end{aligned} \tag{2.42}$$

From Eqs. (2.40) and (2.42), we obtain a very clear physical interpretation for this type of pumped passive coupling. The results due to this coupling are the shifting of the original phase constant by $-1/2\ \beta_c$, and the adding of two different amplitude modulations on the original waves along the space (z) domain with space frequencies $1/2\ \beta_c \pm k_p$. The

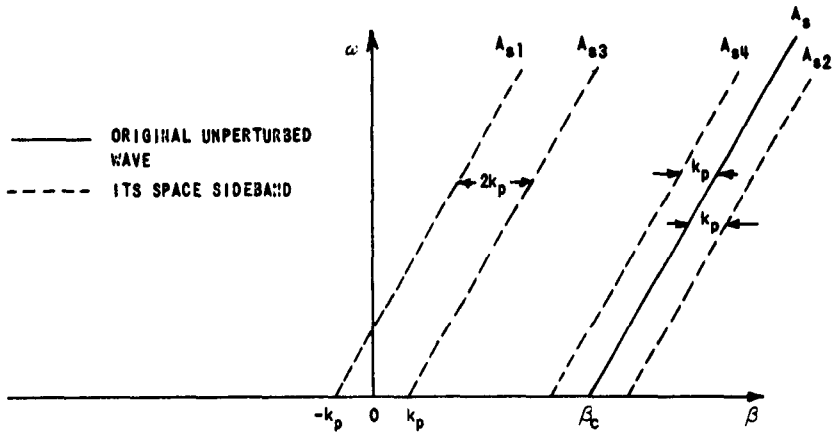

FIG. 10. THE ω-β DIAGRAM OF THE FOUR SPACE SIDEBANDS OF THE SLOW CYCLOTRON WAVE UNDER PASSIVE PUMPING.

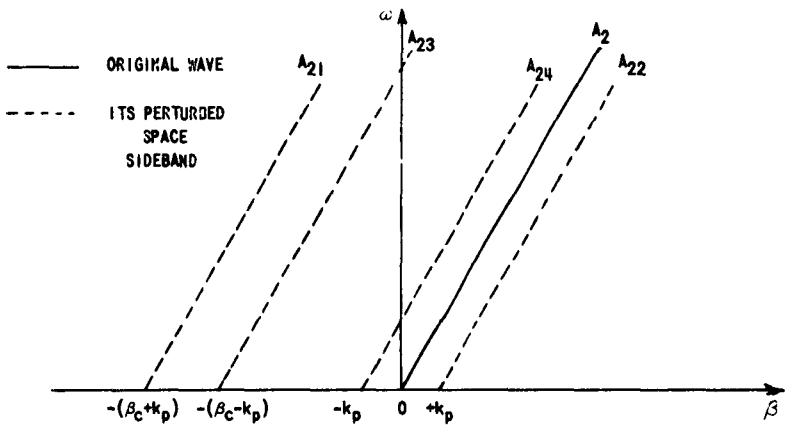

FIG. 11. THE ω-β DIAGRAM OF THE FOUR SPACE SIDEBANDS OF THE PERTURBED SECOND SYNCHRONOUS WAVE UNDER PASSIVE PUMPING.

shifting effect can be shown in Fig. 12. The phase velocities of the perturbed waves are increased due to the shifting in phase constants. The wave amplitudes have two components; both vary sinusoidally along the z-direction with different rates. The constants B, ϕ, and θ are determined by the input conditions.

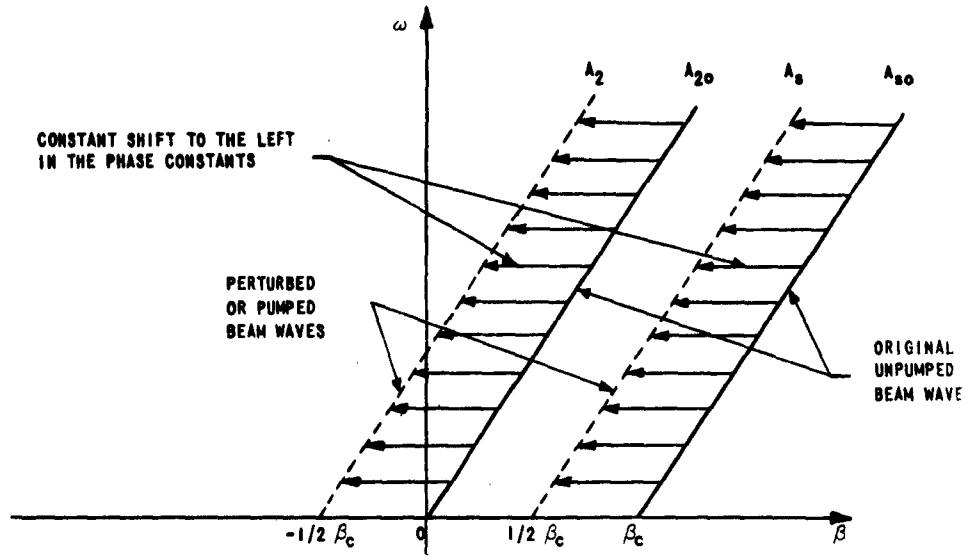

FIG. 12. THE ω-β DIAGRAM, SHOWING THE SHIFT ON PHASE CONSTANT.

Similar results can be obtained for the coupling between the fast cyclotron wave and the first synchronous wave from the set of Eqs. (2.35). The eigenvalues of ν are:

$$\begin{matrix}\nu_1 \\ \nu_2\end{matrix} = -\frac{j\beta_c}{2}\left(1 \pm \sqrt{1 - \frac{4k_p}{\beta_c}}\right) \cong \begin{cases} -j(\beta_c - k_p) \\ -j\ k_p \end{cases}$$

$$\begin{matrix}\nu_3 \\ \nu_4\end{matrix} = -\frac{j\beta_c}{2}\left(1 \pm \sqrt{1 + \frac{4k_p}{\beta_c}}\right) \cong \begin{cases} -j(\beta_c + k_p) \\ +j\ k_p \end{cases} \tag{2.43}$$

From these one can conclude, following the previous analysis, that the perturbed wave has its phase constant shifted by $\beta_c/2$, and its amplitude consists of two sinusoidal modulations along the z-direction. Their analytic solutions should have the following form

$$\tilde{A}_f = [B_{f1} \cos(\beta_1 z + \phi_f) + B_{f2} \cos(\beta_2 z + \theta_f)] \exp\{j[\omega t - (\beta_e - \tfrac{1}{2}\beta_c)z]\}$$

$$\tilde{A}_1 = [B_{11} \cos(\beta_1 z + \phi_1) + B_{12} \cos(\beta_2 z + \theta_2)] \exp\{j[\omega t - (\beta_e + \tfrac{1}{2}\beta_c)z]\}$$

where B's, ϕ's, and θ's are constants determined by initial conditions and:

$$\beta_1 = \frac{\beta_c}{2}\sqrt{1 - \frac{4k_p}{\beta_c}} \simeq \frac{\beta_c}{2} - k_p$$

$$\beta_2 = \frac{\beta_c}{2}\sqrt{1 + \frac{4k_p}{\beta_c}} \simeq \frac{\beta_c}{2} + k_p \qquad (2.44)$$

The shift in phase constant is shown in Fig. 13.

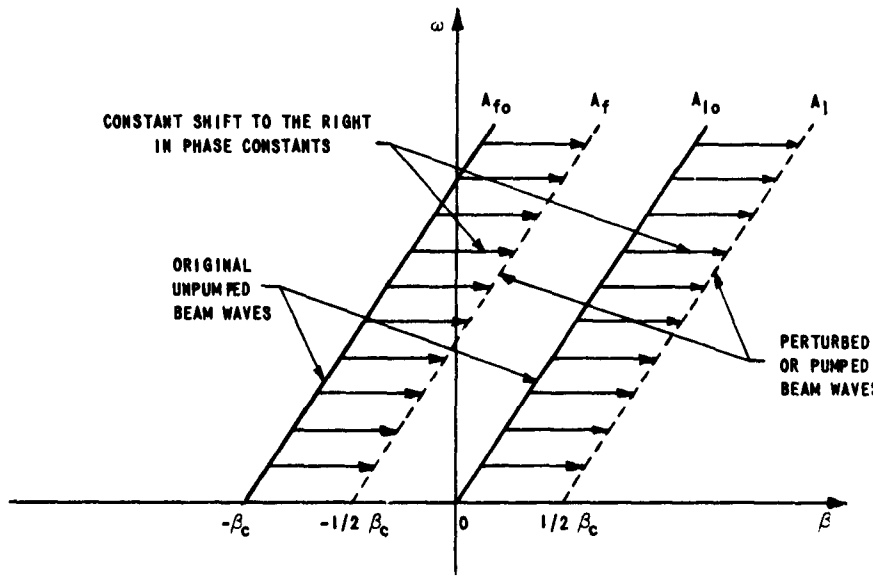

FIG. 13. THE ω-β DIAGRAM, SHOWING THE SHIFT IN PHASE CONSTANT DUE TO THE COUPLING BETWEEN THE FAST CYCLOTRON WAVE AND THE FIRST SYNCHRONOUS WAVE.

c. Active Pumping on Both Synchronous Waves (Case 3)

If one designs a helix with infinite pitch, there will be just four straight conductors equally spaced on an imaginary cylinder. Then the two synchronous waves in the beam will be actively coupled together. This case corresponds to setting the helix wave number $\beta_q = 0$. Substituting this into Eqs. (2.23) and (2.24) and then equating the terms with the same z-dependence in both sides of the equations under assumption of small pumping level, one obtains:

$$\frac{d^2A_1}{dz^2} + j\beta_c \frac{dA_1}{dz} = j\beta_c\, k_p\, A_2 \tag{2.45}$$

$$\frac{d^2A_2}{dz^2} - j\beta_c \frac{dA_2}{dz} = -j\beta_c\, k_p\, A_1 \tag{2.46}$$

These equations are in exactly the same form as Eqs. (2.25) and (2.26) in Case 1 for the active coupling between the two cyclotron waves, if one substitutes $(-k_p)$ for k_p into the above equations. The eigenvalues of Eqs. (2.25) and (2.26), as shown in Eqs. (2.29) and (2.30), are dependent on k_p^2 only; therefore, Eqs. (2.45) and (2.46) should have exactly the same eigenvalues. The results obtained in Case 1 are equally applicable in this case, except that the associated waves are different. The eigenvalues are:

$$\begin{matrix}\nu_1 \\ \\ \nu_2\end{matrix} = \pm\alpha \qquad \begin{matrix}\nu_3 \\ \\ \nu_4\end{matrix} = \pm j\beta$$

where

$$\begin{matrix}\alpha \\ \\ \beta\end{matrix} = \frac{\beta_c}{\sqrt{2}}\left(\sqrt{1 + \frac{4k_p^2}{\beta_c^2}} \pm 1\right)^{1/2} \cong \begin{matrix}k_p \\ \\ \beta_c\left(1 + \frac{1}{2}\frac{k_p^2}{\beta_c^2}\right)\end{matrix}$$

The wave solution is of the form:

$$A_1 = [B_{11} \cosh(\alpha z + \phi_1) + B_{12} \cos(\beta z + \theta_1)] \exp[j(\omega t - \beta_e z)] \tag{2.47}$$

$$A_2 = [B_{21} \cosh(\alpha z + \phi_2) + B_{22} \cos(\beta z + \theta_2)] \exp[j(\omega t - \beta_e z)] \tag{2.48}$$

where B's, ϕ's, and θ's are constants determined by the initial conditions. The space sidebands that split from the original unperturbed waves due to this pumping are shown in Fig. 14.

Due to the coupling, both the first and second synchronous waves will grow at the same rate. Since one carries positive ac power

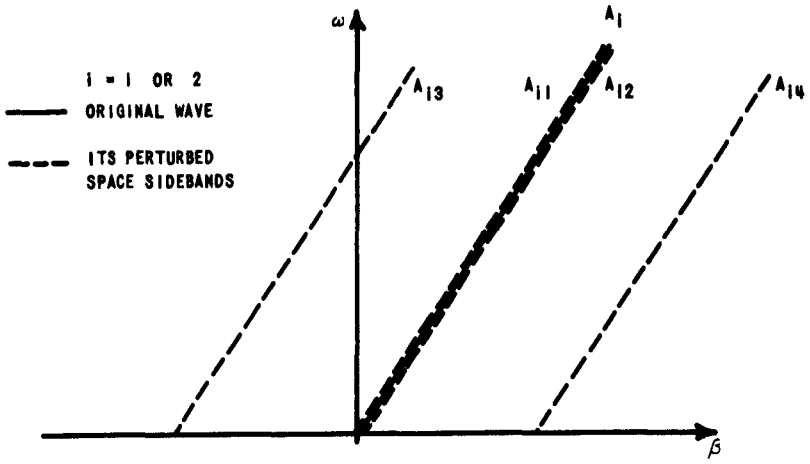

FIG. 14. THE SPACE SIDEBANDS OF THE SYNCHRONOUS WAVES UNDER ACTIVE PUMPING.

and one carries negative ac power, the energy will flow from the negative-power-carrying wave to the positive-power-carrying wave, due to their active coupling. But the total energy carried by both waves is unchanged.

2. Small-Signal Analysis from a Ballistic Point of View

In this section, the trajectory of a single electron within the quadrifilar helix will be examined. Only the case where the two cyclotron waves are actively coupled together is presented, since this is the case we are going to use for amplification. As shown in the previous section, in order to achieve active coupling between the fast cyclotron wave and the slow cyclotron wave, the pitch of the quadrifilar helix should be equal to the cyclotron wavelength of an electron traveling at dc beam velocity if the proper twisted dc field is to be established. This is equivalent to saying that the helix should be twisted at the same rate that the electrons rotate in the magnetic field. In the small-signal analysis, the following assumptions are made:

1. Space charge effects are negligible.
2. The axial velocity of the electron is a constant, and is uniquely determined by the beam voltage.
3. The angular velocity of the electron is a constant, and is uniquely determined by the magnetic field.

In order to simplify the mathematical presentation, a frame that rotates and moves axially with respect to the stationary frame can be used.

Since the quadrifilar helix rotates at the same rate as the electron does, this suggests that the simplest way is to choose a frame in synchronism with both the helix and the electrons. To state this more precisely, a frame is used which rotates at the cyclotron angular frequency and moves at the beam velocity in the same direction as the motion of the electrons. As shown in Fig. 15, the relation between this rotating and moving frame and the stationary frame is

$$\begin{aligned} x' &= x \cos \omega_c t + y \sin \omega_c t \\ y' &= y \cos \omega_c t - x \sin \omega_c t \\ z' &= z - u_o t \end{aligned} \tag{2.49}$$

and inversely,

$$\begin{aligned} x &= x' \cos \omega_c t - y' \sin \omega_c t \\ y &= y' \cos \omega_c t + x' \sin \omega_c t \\ z &= z' + u_o t \end{aligned} \tag{2.50}$$

where ω_c is the cyclotron angular frequency,

u_o is the dc beam axial velocity,

x, y, z are the coordinates in the stationary frame (abbreviated as the S frame), and

x', y', z' are the coordinates in the frame which rotates around the z-z' axis with ω_c and moves along the z-axis with velocity u_o (abbreviated as the RT frame).

Here we also assume that the dc beam velocity u_o is much less than the velocity of light, so that relativistic effects can be neglected.

If an observer in the RT frame sees an electron stationary at (a, 0.0) in its frame, the electron is then actually rotating around the z-axis with radius a and angular velocity ω_c, and also moving along the z-direction with axial velocity u_o in the stationary frame. This means that a stationary electron in the rotating and moving frame traces a helical trajectory in the stationary frame, and this is the actual case for electrons with constant transverse velocity immersed in a dc magnetic field. By adding the transverse twisted dc electric field, the trajectory of the electron would be perturbed. It is the new trajectory of the electron that will be found under the assumptions of small-signal analysis.

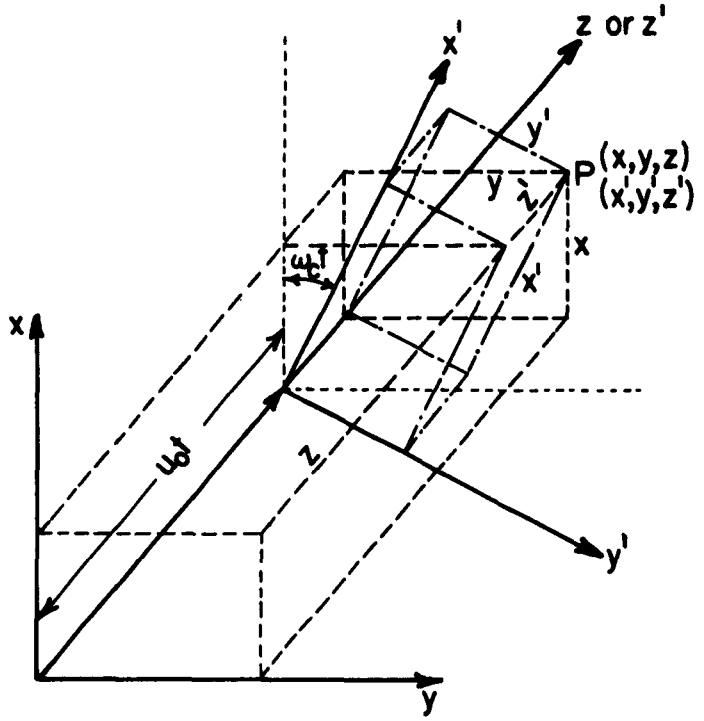

FIG. 15. THE ROTATING AND MOVING FRAME x', y', z', AND ITS RELATION TO STATIONARY FRAME x, y, z.

The potential distribution within the quadrifiliar helix with $\beta_q = \beta_c$ in the stationary frame is, from Eq. (2.4),

$$V = \frac{K}{2}\,[2xy \cos 2\beta_c z - (x^2 - y^2) \sin 2\beta_c z] \tag{2.51}$$

One can then obtain the potential distribution at the plane $z' = 0$ in the rotating and moving frame by substituting the transformation Eq. (2.50) into Eq. (2.51), giving

$$V = Kx'y' \tag{2.52}$$

which is much simpler than Eq. (2.51) in the stationary frame. The potential distribution in the transverse plane $z' = 0$ is shown in Fig. 16. This plane actually represents any transverse plane in the stationary frame corresponding to the specified time.

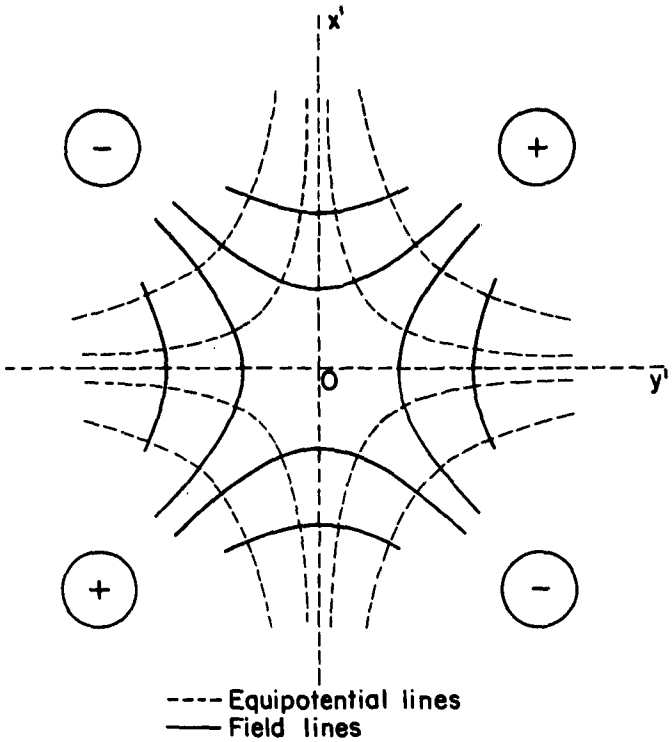

FIG. 16. POTENTIAL DISTRIBUTION IN THE TRANSVERSE PLANE OF THE QUADRIFILAR HELIX.

The transverse electric fields are then:

$$\left.\begin{aligned} E_{x'} &= -Ky' \\ E_{y'} &= -Kx' \end{aligned}\right\} \qquad (2.53)$$

As stated in the previous section the cyclotron waves are proportional to the transverse velocity of the electrons

$$\left.\begin{aligned} A_f &\propto |v_x + jv_y| = v_t \\ A_s &\propto |v_x - jv_y| = v_t \end{aligned}\right\} \qquad (2.54)$$

If one can show that the electron transverse velocity in a certain field grows, this means that both the fast and the slow cyclotron-wave amplitudes grow in similar fashion.

Now consider electrons entering the input plane of the quadrifilar helix at $(x_o, y_o, 0)$ with angular rotation ω_c and axial velocity u_o. Due to the transverse dc electric fields, these electrons are no longer stationary in the rotating and transposing frame. Their motion, however, is uniquely determined by the fields and the initial conditions. Since the angular and axial velocity is assumed unchanged for small-signal analysis, then the motion of the electron in the rotating and moving frame would be along a straight line connecting the origin and its entering point at the input plane. This line can be expressed mathematically as

$$y_o x' - x_o y' = 0 \tag{2.55}$$

for the electron entering at $(x_o, y_o, 0)$.

Let us consider two special electrons, one entering exactly on the x-axis and the other on the y-axis, with a distance r_o from the origin. Under small-signal conditions all other electrons will have trajectories which are linear combinations of those of the two special electrons.

1. Electron enters on x axis, or $(r_o, 0, 0)$: From Eq. (2.55) the motion of this electron is restricted to the line $y' = 0$ in the RT frame, i.e., along the x' axis. This electron will experience a transverse electric field

$$E_{x'} = 0, \qquad E_{y'} = -Kx'$$

all the way along its path through the helix. This field will produce a force on the electron in the same direction as its transverse velocity. It is due to this force that the transverse velocity of the electron will increase. However, the increase in transverse velocity will result in an increase in the rotating radius due to the dc magnetic field, given by:

$$r = \frac{v_t}{\omega_c} \tag{2.56}$$

The growing form of the transverse velocity can be obtained from the equation of motion

$$m \frac{dv_t}{dt} = -eE = eKx' \tag{2.57}$$

Substituting r in Eq. (2.56) for x' in Eq. (2.57), one obtains

$$\frac{dv_t}{dt} = \frac{\eta K}{\omega_c} v_t \tag{2.58}$$

The solution of Eq. (2.58) in exponential form is

$$v_t = v_o e^{(\eta K/\omega_c)t} = v_o e^{\alpha_o z} \tag{2.59}$$

where

$$\alpha_o = \frac{\eta K}{\omega_c u_o} = \frac{\eta K}{\omega_c^2} \beta_c \tag{2.60}$$

This solution says that the transverse velocity is growing exponentially with a growth factor α_o as defined in Eq. (2.60). Alternatively, both the fast and slow cyclotron waves will grow in a similar fashion. It should be pointed out that this solution is in agreement with the solution obtained in the wave analysis. Comparing Eq. (2.60) with Eq. (2.24a), one will notice

$$\alpha_o = k_p$$

Therefore, this electron corresponds to the exponential growth component of the cyclotron waves. The trajectory of this electron is along the x'-axis, growing exponentially as:

$$x' = r_o e^{(K/B)t}$$

in the RT frame, and is of the form

$$\left.\begin{aligned} x &= r_o e^{(K/B)t} \cos \omega_c t \\ y &= r_o e^{(K/B)t} \sin \omega_c t \\ z &= u_o t \end{aligned}\right\} \tag{2.61}$$

in the stationary frame. This is a helical cone path with radius growing exponentially as shown in Fig. 17.

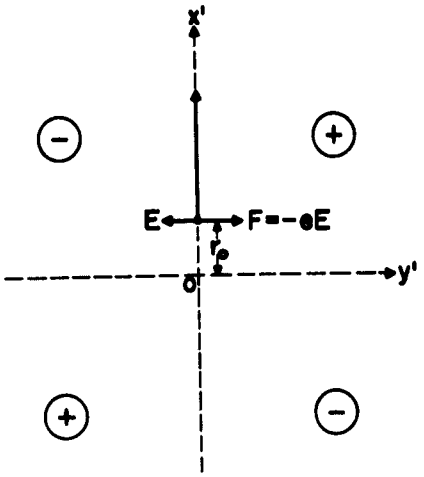

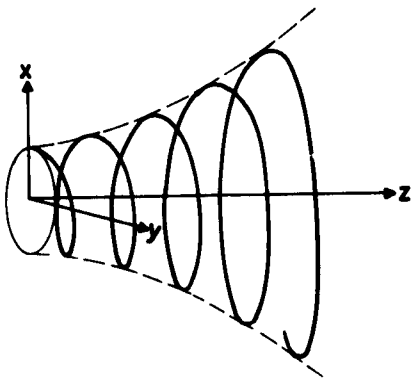

FIG. 17. THE TRAJECTORY OF THE ELECTRON ENTERING THE INPUT PLANE OF THE HELIX ON THE x-AXIS.

2. Electron enters on y-axis, or $(0, r_o, 0)$: Then from Eq. (2.55), the motion of the electron is restricted to the line $x' = 0$ in the RT frame, i.e., along the y'-axis. This electron will experience a transverse electric field

$$E_{x'} = -Ky', \quad E_{y'} = 0$$

all the way along its path within the helix. This field will produce a force on the electron in the reverse direction to its motion in the transverse plane. Therefore its transverse velocity will decrease due to this force. The equation of motion for this electron is then:

$$\frac{dv_t}{dt} = -\eta Ky' = -\frac{\eta K}{\omega_c} v_t \tag{2.62}$$

The solution shows that the transverse velocity of this electron decays exponentially as

$$v_t = v_o\, e^{-(\eta K/\omega_c)t} = v_o\, e^{-\alpha_o z} \tag{2.63}$$

and the decay factor is found to be the same as the growth factor for those electrons entering on the x-axis. Since both cyclotron-wave amplitudes are proportional to the transverse velocity of electrons, the electrons entering on the y-axis correspond to the decay component of the cyclotron waves. The trajectory of this electron is along the y-axis, decaying exponentially as

$$y' = r_o\, e^{-(K/B)t}$$

in the RT frame, and is a shrinking helical path of the form

$$\left.\begin{aligned} x &= -r_o\, e^{-(K/B)t} \sin \omega_c t \\ y &= r_o\, e^{-(K/B)t} \cos \omega_c t \\ z &= u_o t \end{aligned}\right\} \tag{2.64}$$

with a radius of the helix decaying exponentially as shown in Fig. 18.

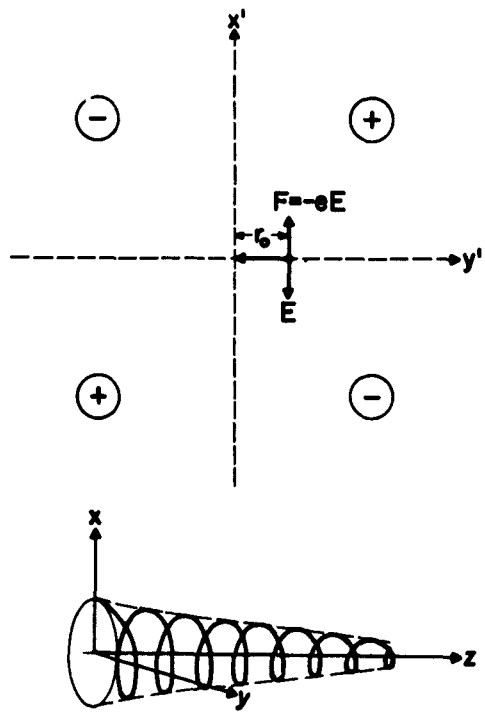

FIG. 18. THE TRAJECTORY OF THE ELECTRON ENTERING THE INPUT PLANE OF THE HELIX ON THE y- AXIS.

It is seen that the small-signal analysis from a ballistic point of view gives the same result as obtained from the complete wave analysis. The amplitudes of both the fast and slow cyclotron waves have an exponentially growing component and an exponentially decaying component in the twisted dc electric field supplied by the helix with $p = \lambda_c$. The exponential factor found in the ballistic point of view, $\alpha_o = k_p$, is exactly the same as the factor found in the wave point of view.

3. Perturbation of Small-Signal Analysis from a Ballistic Point of View - the Lagrangian Approach

In this section, the Lagrangian approach will be used to formulate the three-dimensional equations of motion of the electron within the quadrifilar helix. However, the complete solution of these equations is found to be too complicated to be realizable. An alternative method is used to find the first-order deviation from small-signal solutions.

The equation of motion of the electrons is:

$$\frac{d^2\vec{r}}{dt^2} = -\eta\left(\vec{E} + \frac{d\vec{r}}{dt} x\vec{B}\right) \tag{2.65}$$

in the electric field $\vec{E}$ and the magnetic field $\vec{B}$, where $\vec{r}$ is the position vector of the electron and η is the charge-to-mass ratio for the electron. The fields inside the quadrifilar helix in rectangular coordinates are

$$\vec{E} = (E_x, E_y, E_z), \ \vec{B} = (B_x, B_y, B_z) \tag{2.66}$$

where from Eq. (2.51)

$$E_x = -\frac{\partial V}{\partial x} = -K[y \cos 2\beta_c z - x \sin 2\beta_c z]$$

$$E_y = -\frac{\partial V}{\partial y} = -K[x \cos 2\beta_c z + y \sin 2\beta_c z]$$

$$E_z = -\frac{\partial V}{\partial z} = \beta_c K[2xy \sin 2\beta_c z + (x^2 - y^2) \cos 2\beta_c z]$$

and

$$B_x = 0$$

$$B_y = 0$$

$B_z = B =$ constant dc axial magnetic field.

Substituting these fields into Eq. (2.65) one obtains the equations of motion for three dimensions in rectangular coordinates:

$$\left.\begin{aligned}
\frac{d^2x}{dt^2} &= \eta K[y \cos 2\beta_c z - x \sin 2\beta_c z] - \eta B \frac{dy}{dt} \\
\frac{d^2y}{dt^2} &= \eta K[x \cos 2\beta_c z - y \sin 2\beta_c z] + \eta B \frac{dx}{dt} \\
\frac{d^2z}{dt^2} &= -\eta K\beta_c[2xy \sin 2\beta_c z + (x^2 - y^2) \cos 2\beta_c z]
\end{aligned}\right\} \qquad (2.67)$$

These are three differential equations with three unknowns, namely, x, y, z. If the initial conditions are specified, one should be able to determine the successive positions of the electron completely. However, since these are a set of simultaneous linear second-order differential equations with periodic coefficients, explicit solutions for the three unknowns are not easy to find. Since we are sure their first-order solutions are of the form obtained in the small-signal analysis, it would be convenient and reasonable to find the deviation from the small-signal solutions. It is found that the mathematical manipulation is much simpler if we consider the deviation in the rotating and moving reference frame used in the previous section. Since we are mostly interested in the growing components, we then will consider those electrons entering on the x-axis at the input transverse plane of the helix only. If the deviations from the small-signal solutions are defined as $\delta x'$, $\delta y'$, $\delta z'$ in the RT-frame, then the solution of the equations of motion (2.67) is of the form

$$\begin{aligned}
x' &= x_1' + \delta x' \\
y' &= y_1' + \delta y' \\
z' &= z_1' + \delta z'
\end{aligned} \qquad (2.68)$$

where x_1', y_1', and z_1', are the small-signal solutions, namely:

$$\begin{aligned}
x_1' &= r_o\, e^{(K/B)t} \\
y_1' &= 0 \\
z_1' &= 0
\end{aligned} \qquad (2.69)$$

for the electrons entering on the x-axis.

Transferring Eq. (2.68) into the S-frame by using the transformation Eqs. (2.49), one obtains the form of solution for the electron trajectory in the stationary frame as

$$\left.\begin{aligned} x &= \left[r_o\, e^{(K/B)t} + \delta x'\right] \cos \omega_c t - \delta y' \sin \omega_c t \\ y &= \delta y' \cos \omega_c t + \left[r_o\, e^{(K/B)t} + \delta x'\right] \sin \omega_c t \\ z &= u_o t + \delta z \end{aligned}\right\} \qquad (2.70)$$

In order to find the δ's, one can substitute Eq. (2.70) into the equations of motion of (2.67). Neglecting higher order terms of the δ's, one obtains the following set of differential equations for the δ's

$$\begin{aligned} \frac{d\delta x'}{dt} - \frac{\eta K}{\omega_c}\, \delta x' &= 0 \\ \frac{d\delta y'}{dt} + \frac{\eta K}{\omega_c}\, \delta y' &= 2\, \frac{\eta K}{\omega_c}\, r_o\, e^{(K/B)t} \left[\beta_q\, \delta z' + \frac{K/B}{2\omega_c}\right] \\ \frac{d^2\delta z'}{dt^2} &= -\eta K \beta_c\, r_o\, e^{(K/B)t} \left[r_o\, e^{(K/B)t} + 2\delta x'\right] \end{aligned} \qquad (2.71)$$

The solutions of Eq. (2.71) are readily found with initial condition at $t = 0$

$$\delta x' = \delta y' = \delta z' = 0 \quad \text{and} \quad \frac{dz}{dt} = u_o$$

as

$$\begin{aligned} \delta x' &= 0 \\ \delta y' &= \frac{r_o}{2}\left[\left(\frac{K/B}{\omega_c} + \beta_c^2\, r_o^2\, \omega_c t\right) e^{(K/B)t} - \frac{1}{4}\,(\beta_c r_o)^2\, \frac{\omega_c}{K/B}\, e^{3(K/B)t}\right] \\ \delta z' &= -\frac{u_o \beta_c^2\, r_o^2}{4\, K/B}\left[e^{2(K/B)t} - 2\,\frac{K}{B}\, t - 1\right] \end{aligned} \qquad (2.72)$$

This solution shows that the deviation along the x'-axis is zero, i.e., the transverse-wave amplitude grows according to the small-signal analysis. The deviation in the y'-direction grows as $e^{3(K/B)t}$, and that in the z'-direction as $-e^{2(K/B)t}$.

This solution is for the most favorable electrons only. The deviation in position from the small-signal solutions along the z-direction evidently shows that their axial velocity is decreased. The amount by which the beam axial velocity is slowed down is:

$$\delta v_z = \frac{d\delta z'}{dt} = -\frac{1}{2} u_o \beta_c^2 r_o^2 \left[e^{2(K/B)t} - 1\right]$$

The lagging in position lowers the potential energy of the electrons because they move to a position with higher electrostatic potential; on the other hand, the slowing of the axial velocity decreases their longitudinal kinetic energy. The loss in both the kinetic and the potential energy compensates the gain occurring in the transverse waves.

As the electrons are gradually slowed down, they will gradually drift out of the synchronous position for optimum transverse-wave growth. Once the electrons are completely out of step, further growth is impossible. Therefore, the transverse-wave gain will reach saturation when $\delta z' = 1/2\ (w + g)$, where w is the width of the helix wire and g is the gap between successive helices. This saturation in gain should be compared with another gain saturation set up by the electrons intercepting the finite-diameter helix structure. The lower saturation value will be the actual gain saturation level of the tube.

4. Conditions Required for Amplification due to dc Pumping

As shown in the complete wave analysis as well as in the ballistic analysis, active coupling between the fast and the slow cyclotron waves will be obtained if the wave number of the helix defined as $\beta_q = 2\pi/p$ is equal to the cyclotron-wave number in the beam, i.e.:

$$\beta_q = \beta_c \tag{2.73}$$

This condition can be interpreted in various ways. One point is that the pitch of the helix should be designed to be equal to the cyclotron wavelength at the dc beam velocity:

$$p = \lambda_c = \frac{u_o}{f_c} \tag{2.74}$$

where p is the pitch of the helix, f_c is the cyclotron frequency of the beam, and u_o is the dc axial velocity of the beam. This amplifying condition is plotted in Fig. 19 where the pitch of the helix is shown as a function of the cyclotron frequency using the slowing factor u_o/c as a parameter. These curves can be used as design curves for an

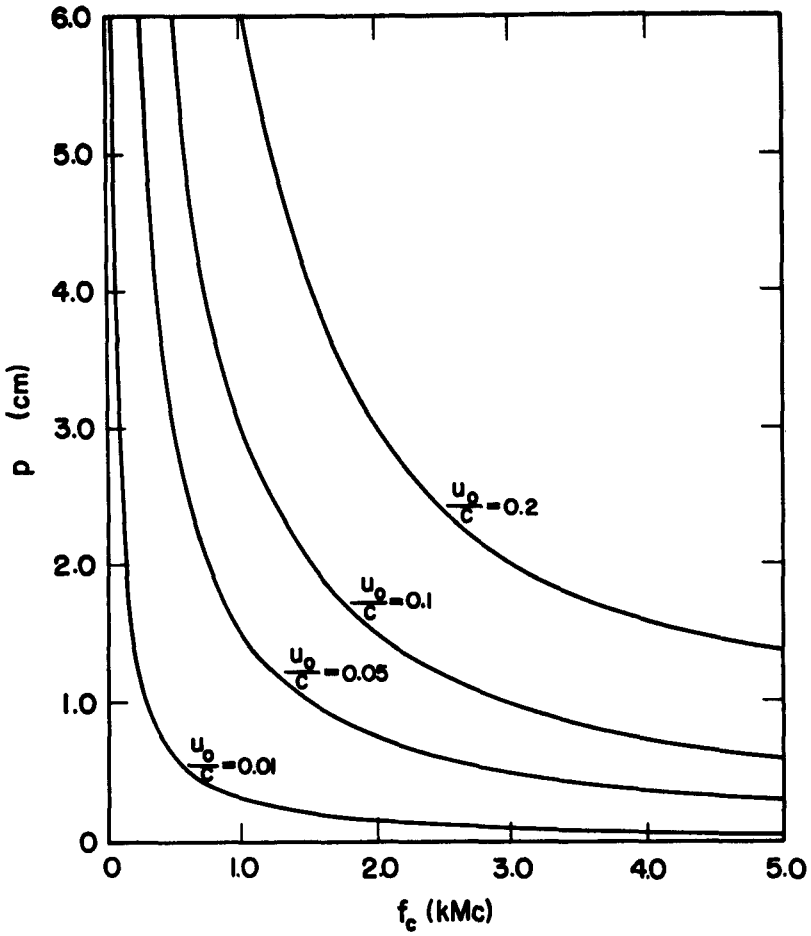

FIG. 19. THE AMPLIFYING CONDITION FOR THE CYCLOTRON-WAVE AMPLIFICATION.

experimental tube. From these curves, one finds that the pitch is decreasing as the cyclotron frequency is increasing. Therefore, the smallest realizable pitch of a quadrifilar helix actually puts an upper limit on the operating frequency of this type of amplification. It is seen from the curves of Fig. 19 that a tube using this type of amplification can be designed to operate in the millimeter range if the electrons are accelerated to near relativistic velocities.

For an operating tube, the pitch of the helix is fixed and cannot be changed easily. However the accelarating voltage of the electrons can be tuned to maintain the amplifying condition while the dc axial

magnetic field is adjusted for various cyclotron frequencies. Their relation is found to be:

$$V_a = \frac{\eta p^2}{8\pi^2} B^2 \tag{2.75}$$

where V_a is the dc beam accelerating voltage

B is the dc axial magnetic field

p is the pitch of the helix

η is the charge-to-mass ratio of electron.

Figure 20 shows this tuning characteristic between the accelerating voltage and the magnetic field using the pitch of the helix as a parameter. An operating tube can be tuned along a curve in this figure with specified pitch of the quadrifilar helix.

For design purposes, a nomograph as shown in Fig. 21 has been drawn to relate the cyclotron frequency, the dc beam velocity, the axial magnetic field, the accelerating voltage of the beam, and the pitch of the helix. Any straight line crossing these nomographs specifies the amplifying conditions for those parameters. For example, if one wants to design a cyclotron-wave amplifier by dc pumping with a quadrifilar helix having pitch equal to 1 cm immersed in an axial magnetic field of 500 gauss, then one should use an accelerating voltage V_a = 590 v determined by the line intersecting with the V_a nomograph line. Those lines can be called the lines of active pumping on cyclotron waves. One can also use this nomograph for tuning purposes in an operating tube by drawing appropriate lines through the fixed pitch value.

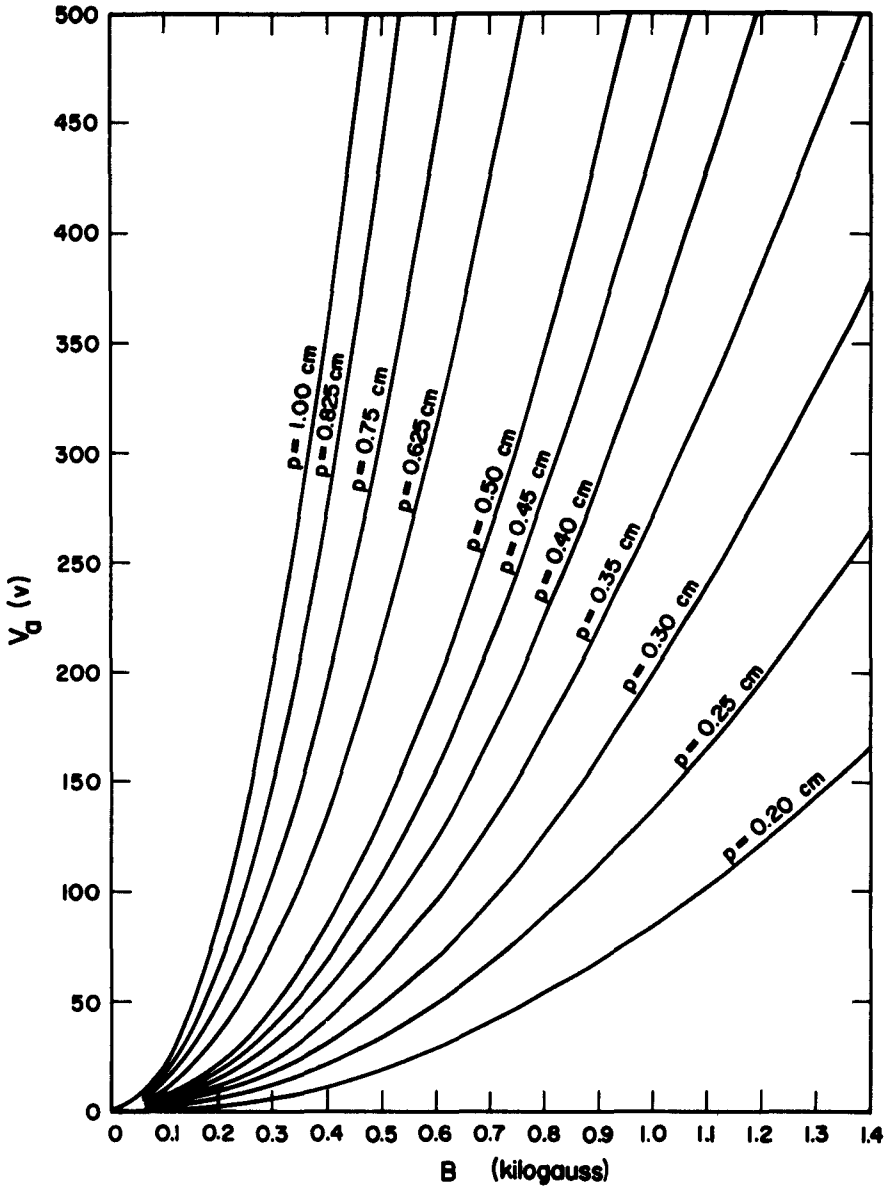

FIG. 20. THE TUNING CURVES OF THE ACCELERATING VOLTAGE AND THE MAGNETIC FIELD FOR ACTIVE DC PUMPING ON CYCLOTRON WAVES USING HELIX PITCH AS A PARAMETER.

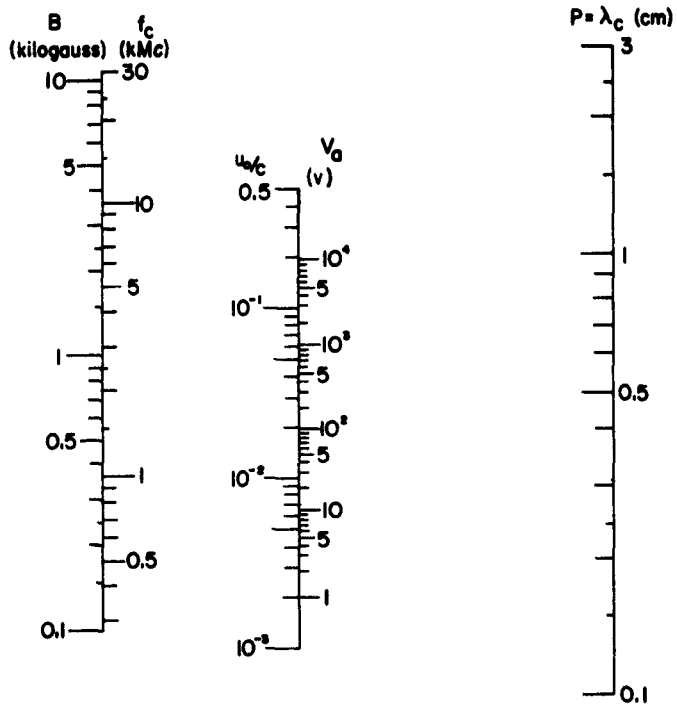

FIG. 21. NOMOGRAPH OF ACTIVE PUMPING CONDITIONS ON CYCLOTRON WAVES GIVING THE RELATIONS BETWEEN CYCLOTRON FREQUENCY, DC BEAM VELOCITY, AXIAL MAGNETIC FIELD, ACCELERATING VOLTAGE OF THE BEAM, AND PITCH OF THE QUADRIFILAR HELIX.

B. RF COUPLING IN THE QUADRIFILAR HELIX

In the dc-pumped amplifier, a quadrifilar helix is found to be useful to provide the properly twisted dc field. At the same time the helix has been used as a slow wave circuit in traveling-wave tubes for many years. The characteristics of a helix can be used equally well in transverse-wave tubes to achieve proper coupling with beam waves. Since there are four parallel-wound helices in a quadrifilar helix, there must be four independent circuit modes. By proper design of the helix, one can achieve coupling between these circuit waves and beam waves. In the following sections, this coupling will be examined in detail.

1. Normal Modes of the Quadrifilar Helix

Waves propagating along a helical structure have been studied by many workers [Refs. 28 to 36]. Here, only the case of the quadrifilar

helix will be discussed. Since there are four equally spaced helices in the quadrifilar helix, one can logically conclude that there are four and only four independent modes, which are distinguished by the relative phase of the excitation voltage on each helix at the input transverse plane.

1. In Fig. 22(a) the zero mode is excited by a source driving the four helices with same amplitude and same phase. This mode can be called the symmetric mode since its field is not only symmetric with respect to the origin but also symmetric with respect to the x- and y-axis in the input transverse plane.
2. In Fig. 22(b) the -2 mode is excited by a source driving the four helices with the same amplitude but 180 deg out of phase on adjacent helices. This mode can be called the semisymmetric mode since its field is only symmetric with respect to the origin but not symmetric with respect to the x- and y-axis in the input plane.
3. In Fig. 22(c) the -1 mode is excited by a source driving the four helices with the same amplitude but with 90-deg phase lagging on succeeding helices along the θ-direction. This mode can also be called the right-hand antisymmetric mode since its field is right-hand polarized and is not symmetric with respect to either the origin or the x- and y-axis in the input plane.
4. In Fig. 22(d) the +1 mode is excited by a source driving the four helices with the same amplitude but with 90-deg phase leading on successive helices along the θ-direction. By similar reasoning this mode can then be called the left-hand antisymmetric mode. The index number of these modes indicates the number of field variations around the circumference.

The propagation characteristics of the modes of a helix are well understood. The ω-β characteristics of the fundamental waves of each independently excitable mode for a quadrifilar helix are shown in Fig. 23. Their wave numbers are shown in Table 2.

TABLE 2. CIRCUIT WAVES ON A QUADRIFILAR HELIX

Symbol	Mode	Wave Number*	AC Energy	Polarization
A_{-2}	Semisymmetric	$\beta_o - 2\beta_q$	+	Elliptical
A_{-1}	Right-hand Antisymmetric	$\beta_o - \beta_q$	+	Right-hand
A_o	Symmetric	β_o	+	Circular
A_{+1}	Left-hand Antisymmetric	$\beta_o + \beta_q$	+	Left-hand

*$\beta_o = \frac{\omega}{c \sin \psi}$, $\beta_q = \frac{2\pi}{p}$, ψ = pitch angle, p = pitch

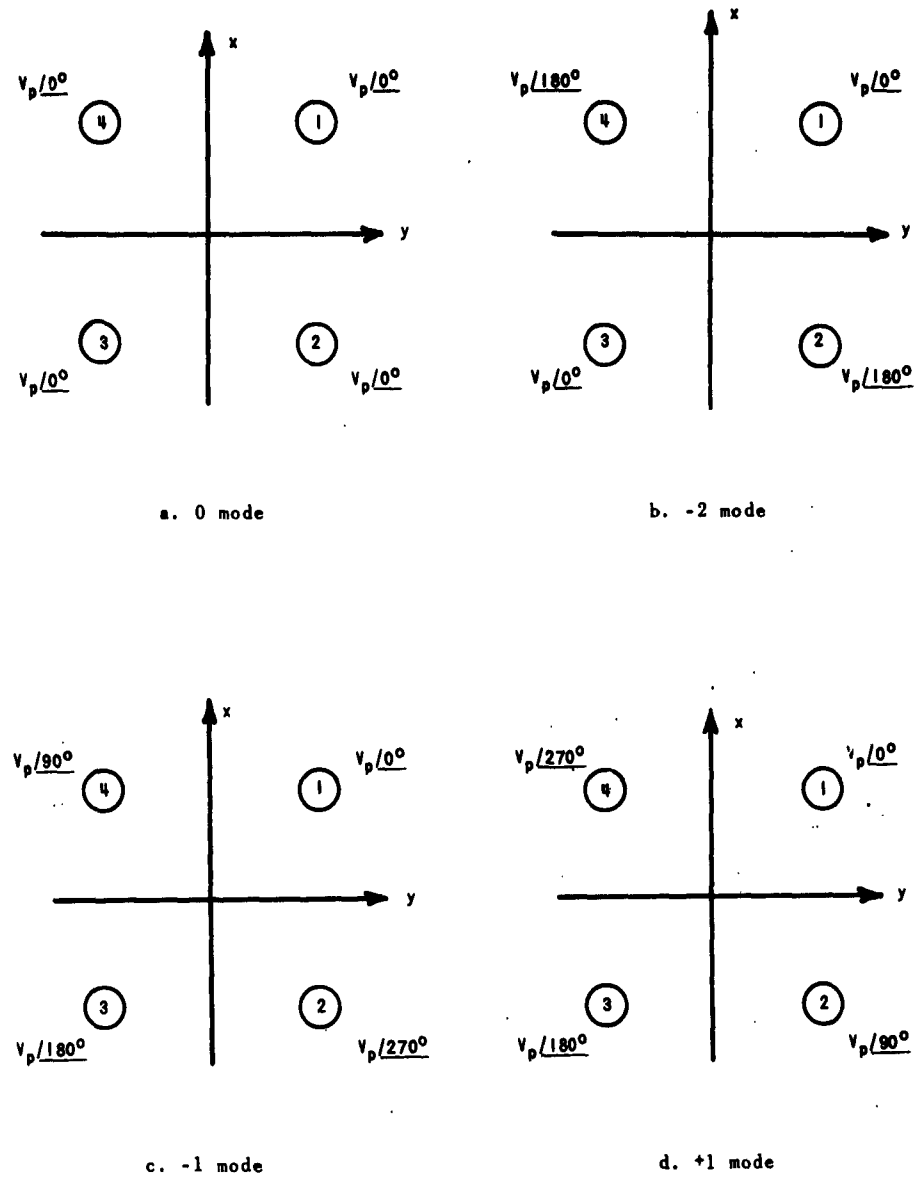

FIG. 22. THE METHODS OF EXCITING THE FOUR INDEPENDENT MODES ON THE QUADRIFILAR HELIX.

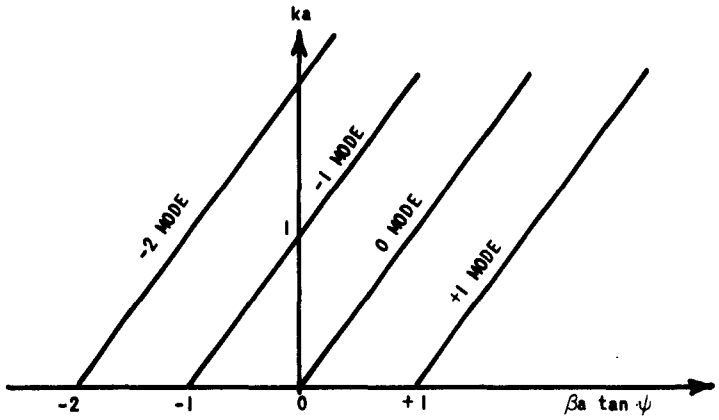

FIG. 23. THE CHARACTERISTICS OF THE FUNDAMENTAL WAVES OF THE FOUR INDEPENDENT EXCITABLE MODES ON A QUADRIFILAR HELIX.

Each mode actually contains an infinite number of spatial harmonics. These are:

$$A_m = \sum_{n=-\infty}^{\infty} A_{mn}\, e^{j\beta_{mn} z}; \qquad m = -2,\ -1,\ 0,\ +1$$

where m is the mode number; n is the order of the spatial harmonic; A_{mn} is the amplitude of the nth-order space harmonics in the m mode; and β_{mn} is the phase constant of the nth-order harmonic in the m mode, given by

$$\beta_{mn} = \beta_o + (4n + m)\, \beta_q$$

The amplitude of each space harmonic is more or less inversely proportional to the square of its own phase constant, so that high-order harmonics are small in comparison to their fundamental harmonics and can be neglected in most cases. Figure 23 shows the fundamental space harmonics of each mode only.

2. Normal Modes of the Transverse Beam Waves Carried by the Confined Electron Beam

As stated in Sec. A-1, an electron beam confined in a longitudinal dc magnetic field will carry four transverse waves. These waves are:

1. The fast cyclotron wave carrying positive energy and having right-hand polarization.
2. The slow cyclotron wave carrying negative energy and having left-hand polarization.
3. The first synchronous wave carrying positive energy and having left-hand polarization.
4. The second synchronous wave carrying negative energy and having right-hand polarization.

The characteristics of these transverse beam waves are shown in Fig. 24.

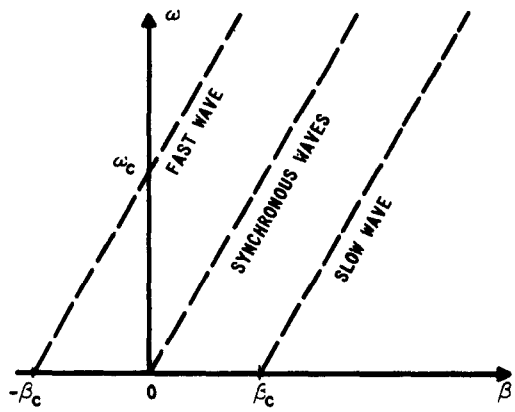

FIG. 24. THE CHARACTERISTICS OF THE TRANSVERSE WAVES CARRIED BY AN ELECTRON BEAM CONFINED IN A LONGITUDINAL DC MAGNETIC FIELD.

From this figure one can see that the fast cyclotron wave has a phase velocity faster than the dc beam velocity, the slow cyclotron wave has a phase velocity slower than the dc beam velocity, and both synchronous waves have phase velocities exactly the same as the dc beam velocity. However, all four transverse waves have the same group velocity equal to the dc beam velocity. Their various characteristics are summarized in Table 1.

These four normal modes of the transverse modulation can be more clearly interpreted physically in terms of the guiding center position and the cyclotron radius of the beam as shown in Fig. 25. From this figure one can readily notice that the radius vector $\vec{r}$ of the beam is

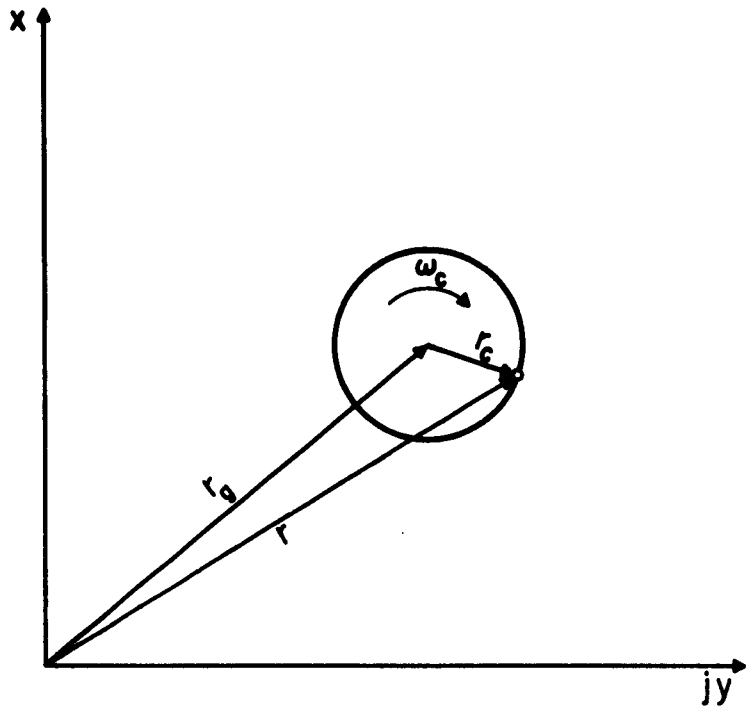

FIG. 25. ELECTRON-BEAM MOTION IN A DC MAGNETIC FIELD DIRECTED PERPENDICULARLY INTO THE PAPER.

the sum of the guiding center vector $\vec{r}_g$ and the cyclotron radius vector $\vec{r}_c$ of the beam.

$$\vec{r} = \vec{r}_g + \vec{r}_c \tag{2.76}$$

From this one can prove that the polarized components also have the same relation,

$$r_+ = r_{g_+} + r_{c_+} \tag{2.77}$$

$$r_- = r_{g_-} + r_{c_-} \tag{2.78}$$

Where the (+) and (-) subscripts represent the left-hand and right-hand polarized components of the proper vector as defined by Eq. (2.9). It can be shown from Eq. (2.1) that the following linear relation between the wave amplitudes and the polarized radius components holds:

$$\begin{bmatrix} A_f \\ A_s \\ A_1 \\ A_2 \end{bmatrix} = k\omega_c \begin{bmatrix} -r_{c_-} \\ r_{c_+} \\ -r_{g_+} \\ r_{g_-} \end{bmatrix} \tag{2.79}$$

It follows that the amplitudes of the cyclotron waves are determined by the radius of cyclotron rotational motion and are independent of the radius of the guiding center with respect to the origin of the chosen coordinates; and that the amplitudes of the synchronous waves are determined by the guiding center radius only.

3. Conditions Required for Coupling Between the Circuit Waves and the Beam Waves

A quadrifilar helix has four circuit wave modes as shown in Fig. 23, and a confined electron beam has four transverse waves as shown in Fig. 24. Carefully examining these two figures, one would notice that with the helix designed such that $ka = 1$ occurs at the cyclotron frequency and with the velocity of the fundamental circuit mode equal to the beam dc velocity, the -1 circuit mode should coincide with the fast cyclotron beam mode if one puts both ω-β diagrams of the beam and circuit together. There is then strong coupling between the fast cyclotron wave in the beam and the -1 mode wave in the helix circuit over essentially the entire range of $ka = 0.5$ to $ka = 1.5$ at fixed beam voltage. There is also a substantially weaker coupling between the slow cyclotron wave in the beam and the +1 mode circuit wave in the helix. The latter coupling is of secondary interest, in part because of its lower interaction impedance and in part because it is intended that only the -1 mode should be initially excited on the helix.

In order that $ka = 1$ occurs at the cyclotron frequency, it is required that the radius a of the helix be related to the magnetic field according to the following equation:

$$a = \frac{c}{\eta B} \tag{2.80}$$

where c is the velocity of light, B is the magnetic field, η is the charge-to-mass ratio of electron, and a is the radius of the helix. The requirement that the velocity of the fundamental circuit mode equal the dc beam velocity is:

$$\frac{\omega}{\beta_o} = u_o \tag{2.81}$$

At the cyclotron frequency, Eq. (2.81), subject to the condition of Eq. (2.80), leads to:

$$\frac{\omega_c}{\beta_q} = u_o \quad \text{or} \quad p = \lambda_c \tag{2.82}$$

where $\beta_q = 2\pi/p$ and p is the pitch of the helix.

One notices that Eq. (2.82) is exactly the same as the condition for active dc pumping on the cyclotron waves studied in Sec. A-4. Therefore the achievement of wideband rf coupling between the fast cyclotron beam wave and the -1 mode circuit wave automatically satisfies the condition for active dc pumping on both fast and slow cyclotron beam waves. In other words, if the active dc pumping condition has been achieved, then Eq. (2.80) is the only condition left for wideband rf coupling. Figures 26 and 27 are plots of this condition showing the radius a of the quadrifilar helix as a function of magnetic field and a function of cyclotron frequency, respectively.

Provided these conditions are satisfied, cyclotron-wave amplification with simultaneous rf coupling and dc pumping is possible. The ω-β diagram showing this kind of operation is plotted in Fig. 28. The analysis of this operation involving both fast and slow cyclotron waves and the -1 circuit wave will be presented in the next chapter.

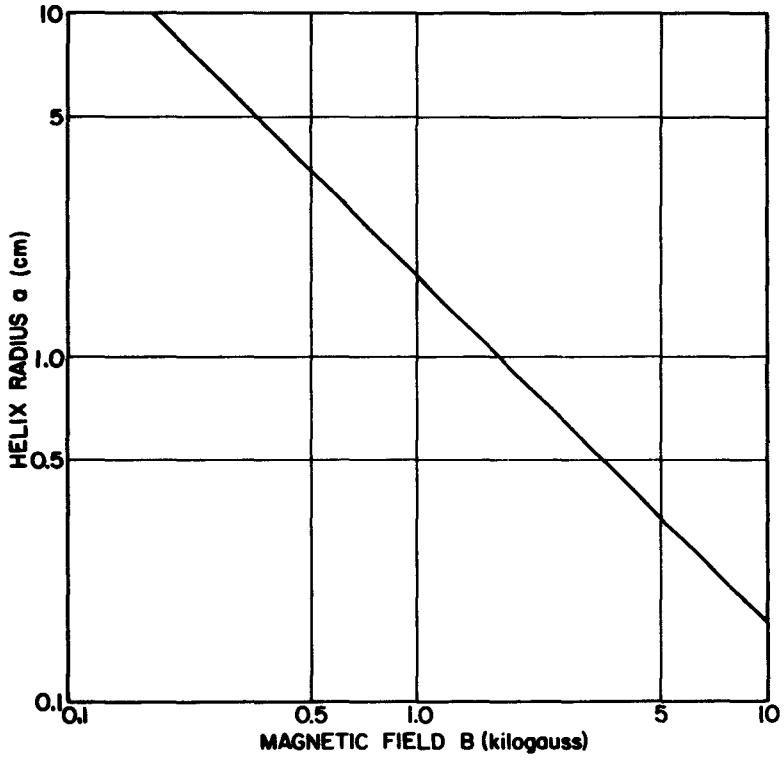

FIG. 26. THE RADIUS OF THE QUADRIFILAR HELIX AS A FUNCTION OF MAGNETIC FIELD FOR WIDEBAND COUPLING.

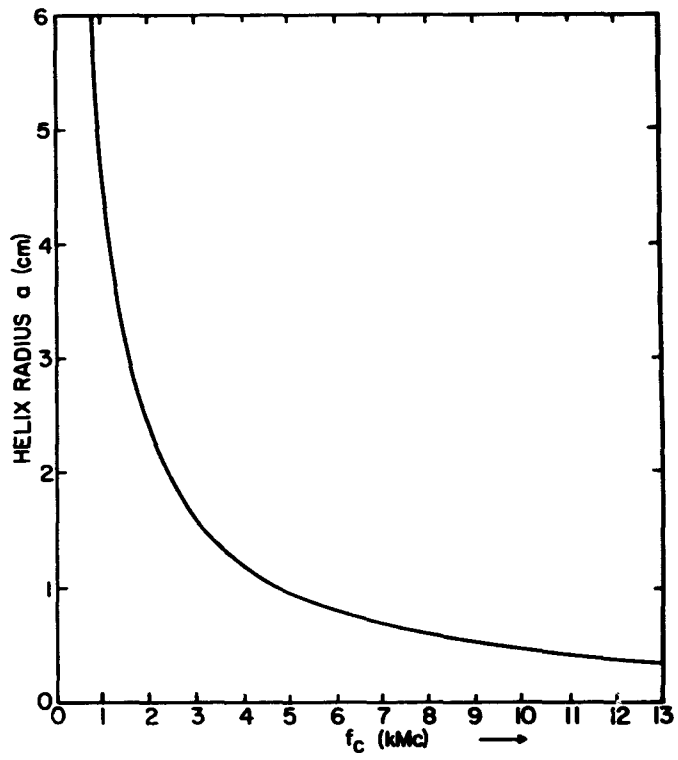

FIG. 27. THE RADIUS OF THE HELIX AS A FUNCTION OF CYCLOTRON FREQUENCY FOR WIDEBAND COUPLING.

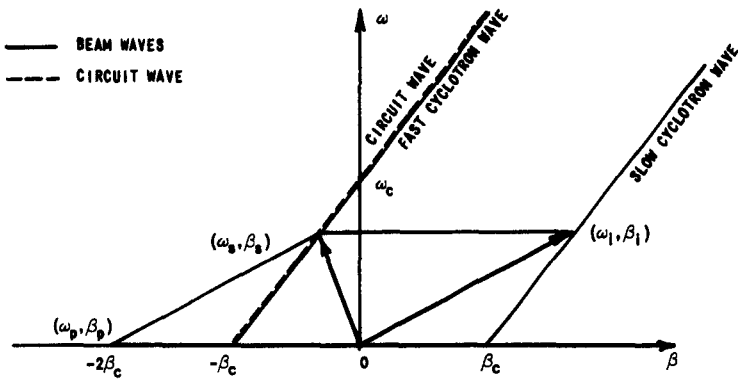

FIG. 28. THE OPERATION OF THE CYCLOTRON-WAVE AMPLIFICATION USING SIMULTANEOUS RF COUPLING AND DC PUMPING.

4. Mode Excitation of the Circuit Waves on the Quadrifilar Helix

Since there are four independent and equally spaced helices constituting the quadrifilar helix, there are four orthogonal modes or waves on the helix. These modes are independently excitable and are distinguished by the relative phase of the voltages applied on the different helices at any given cross section, as shown in Fig. 22. If the voltage excitation at the input plane is different from those shown in Fig. 22, then more than one mode of the circuit wave will be excited. Let A_o, A_{+1}, A_{-1}, A_{-2} represent voltages for the four orthogonal modes of excitation, and let V_1, V_2, V_3, V_4 be the voltages on the four different helices at any cross section. All the A's and V's are complex quantities containing voltage amplitudes and phase angles. The relations between the V's and A's can be expressed mathematically as follows:

$$\left.\begin{aligned} V_1 &= A_o + A_{+1} + A_{-1} + A_{-2} \\ V_2 &= A_o + jA_{+1} - jA_{-1} - A_{-2} \\ V_3 &= A_o - A_{+1} - A_{-1} + A_{-2} \\ V_4 &= A_o - jA_{+1} + jA_{-1} - A_{-2} \end{aligned}\right\} \qquad (2.83)$$

If written in matrix form, these become:

$$\tilde{V} = \tilde{P}\,\tilde{A} \qquad (2.84)$$

where $\tilde{P}$ is an orthogonal matrix:

$$\tilde{P} = \begin{bmatrix} 1 & 1 & 1 & 1 \\ 1 & j & -j & -1 \\ 1 & -1 & -1 & 1 \\ 1 & -j & j & -1 \end{bmatrix} \tag{2.85}$$

and

$$\tilde{V} = \begin{bmatrix} V_1 \\ V_2 \\ V_3 \\ V_4 \end{bmatrix} \qquad \tilde{A} = \begin{bmatrix} A_o \\ A_{+1} \\ A_{-1} \\ A_{-2} \end{bmatrix} \tag{2.86}$$

The inverse of P is found to be:

$$\tilde{P}^{-1} = \frac{1}{4} \begin{bmatrix} 1 & 1 & 1 & 1 \\ 1 & -j & -1 & j \\ 1 & j & -1 & -j \\ 1 & -1 & 1 & -1 \end{bmatrix} \tag{2.87}$$

So, from $\tilde{A} = \tilde{P}^{-1} \tilde{V}$, one obtains:

$$\begin{aligned} A_o &= \frac{1}{4} (V_1 + V_2 + V_3 + V_4) \\ A_{+1} &= \frac{1}{4} (V_1 - jV_2 - V_3 + jV_4) \\ A_{-1} &= \frac{1}{4} (V_1 + jV_2 - V_3 - jV_4) \\ A_{-2} &= \frac{1}{4} (V_1 - V_2 + V_3 - V_4) \end{aligned} \tag{2.88}$$

From the above equations one can evaluate the magnitude of various modes if the amplitudes and phases of voltages on different helices at a cross section are known. One can then find ways of improving the impedance matching from the source of excitation so that only the desired single mode will exist on the quadrifilar helix. From a practical viewpoint, this is one of the major technological problems in using a quadrifilar helix. One approach to this problem is discussed in a later chapter.

III. THEORY OF THE AMPLIFIER USING SIMULTANEOUS PUMPING AND COUPLING

As was pointed out in the previous chapter, we notice that both the fast and the slow cyclotron waves will be actively pumped by a properly twisted dc field. A quadrifilar helix can be designed not only to provide the active pumping with a properly twisted dc field, but also to insure that the -1 mode circuit wave will simultaneously be passively coupled with the fast cyclotron beam wave. There is actually another weaker coupling between the circuit +1 mode and the slow cyclotron beam wave. However this coupling will be neglected in the quadrifilar helix due to its relatively small transverse impedance. Longitudinal interaction is also neglected because this can be suppressed by suitable design of the circuit. In this chapter, we assume that these conditions have been fulfilled. Coupled-mode theory [Refs. 37-40] will be used to evaluate the various characteristics of this type of amplifier. In Sec. A, the complete solution of the coupled-mode equations with specified input wave amplitudes are obtained. Physical insight and interpretation of the operation of the tube is presented in Sec. B. The characteristics of gain and bandwidth are studied in Sec. C. Noise performance is studied in Sec. D.

In the case where the coupling between the +1 mode circuit wave and the slow cyclotron beam wave is not negligible, then four waves--two in the beam and two in the circuit--will be involved. The coupled-mode equations and their solutions for the four-wave case are presented in Appendix B.

A. COUPLED-MODE THEORY

The simultaneous active pumping on the cyclotron waves and the passive coupling between the circuit and beam waves lead to the following coupled-mode equations:

$$\frac{dA_-}{dz} = jk_- A_f \tag{3.1}$$

$$\frac{dA_f}{dz} = jk_- A_- + k_p A_s \tag{3.2}$$

$$\frac{dA_s}{dz} = k_p A_f \tag{3.3}$$

where all the A's are the magnitudes of the waves. The coupling coefficient and the pumping factor are:

$$k_- = \sqrt{\frac{1}{2}\frac{\omega}{\omega_c}\frac{I_o}{V_o}K_{t_-}}\,\beta_-$$

$$k_p = \frac{K}{Bu_o} = \left(\frac{P}{2\pi a}\right)^2 \frac{V_p}{2V_o}\beta_c \tag{3.5}$$

where K_{t_-} is the transverse impedance of the -1 mode circuit wave, β_- is the wave number of the -1 mode circuit wave, I_o is the dc beam current, V_o is the dc beam voltage, and all other symbols are defined as before. Here we assume that only the forward -1 mode circuit wave is excited and coupled to the beam wave; and k_p is assumed to be small compared with β_c.

The amplitudes of all the waves are constant along z if the coupling coefficient and the pumping factor are both zero--that is, the waves are uncoupled. They maintain their original amplitudes as they travel in the z-direction. The amplitudes will vary as functions of z if there is coupling between them and/or pumping upon them. We can assume that they vary in the z-direction as the exponential form:

$$A = C\,e^{\nu z}$$

where the C's and ν's are constants. Then we obtain from Eqs. (3.1), (3.2), and (3.3)

$$\left.\begin{aligned} \nu C_- - jk_- C_f + 0 &= 0 \\ -jk_- C_- + \nu C_f - k_p C_s &= 0 \\ 0 - k_p C_g + \nu C_s &= 0 \end{aligned}\right\} \tag{3.6}$$

We have changed the original simultaneous differential equations to simultaneous homogeneous algebraic equations. In order for the C's to have nontrivial solutions, it is necessary and sufficient that the determinant formed by the coefficients be zero.

$$\begin{vmatrix} \nu & -jk_- & 0 \\ -jk_- & \nu & -k_p \\ 0 & -k_p & \nu \end{vmatrix} = 0 \tag{3.7}$$

The eigenvalues of ν are found to be:

$$\left.\begin{aligned} \nu &= 0 \\ \nu_2 &= \sqrt{k_p^2 - k_-^2} \\ \nu_3 &= -\sqrt{k_p^2 - k_-^2} \end{aligned}\right\} \tag{3.8}$$

For $k_p > k_-$, the ν's are all real numbers. Let

$$\alpha = \sqrt{k_p^2 - k_-^2} \tag{3.9}$$

Then the amplitudes of the waves will have the form:

$$\left.\begin{aligned} A_- &= C_{-1} + C_{-2}\, e^{\alpha z} + C_{-3}\, e^{-\alpha z} \\ A_f &= C_{f1} + C_{f2}\, e^{\alpha z} + C_{f3}\, e^{-\alpha z} \\ A_s &= C_{s1} + C_{s2}\, e^{\alpha z} + C_{s2}\, e^{-\alpha z} \end{aligned}\right\} \tag{3.10}$$

That is, each wave contains three components; one remains constant, one is exponentially growing, and one is exponentially decaying as the waves travel down the z-direction.

Only three independent constants are determined by the input conditions. The relations between the nine constants in Eq. (3.10) can be obtained from the original coupled-mode equations as:

$$\left.\begin{aligned} C_{f1} &= 0 & & C_{s1} = -\frac{jk_-}{k_p} C_{-1} \\ C_{f2} &= \frac{\alpha}{jk_-} C_{-2} & \text{and} \quad & C_{s2} = \frac{k_p}{jk_-} C_{-2} \\ C_{f3} &= -\frac{\alpha}{jk_p} C_{-3} & & C_{s3} = \frac{k_p}{jk_-} C_{-3} \end{aligned}\right\} \tag{3.11}$$

Applying the input conditions and using C_{-1}, C_{-2}, C_{-3}. as the three independent constants, then at $z = 0$:

$$A_-(0) = C_{-1} + C_{-2} + C_{-3}$$

$$A_f(0) = 0 + \frac{\alpha}{jk_-} C_{-2} - \frac{\alpha}{jk_-} C_{-3} \tag{3.12}$$

$$A_s(0) = -\frac{jk_-}{k_p} C_{-1} + \frac{k_p}{jk_-} C_{-2} + \frac{k_p}{jk_-} C_{-3}$$

where the $A(0)$'s are the wave amplitudes at the input plane. These results can also be written in matrix form:

$$\begin{bmatrix} A_-(0) \\ A_f(0) \\ A_s(0) \end{bmatrix} = \begin{bmatrix} 1 & 1 & 1 \\ 0 & \frac{\alpha}{jk_-} & -\frac{\alpha}{jk_-} \\ -\frac{jk_-}{k_p} & \frac{k_p}{jk_-} & \frac{k_p}{jk_-} \end{bmatrix} \begin{bmatrix} C_{-1} \\ C_{-2} \\ C_{-3} \end{bmatrix} \tag{3.13}$$

From this we can easily find the inverse as

$$\begin{bmatrix} C_{-1} \\ C_{-2} \\ C_{-3} \end{bmatrix} = \begin{bmatrix} \frac{k_p^2}{\alpha^2} & 0 & -\frac{jk_-k_p}{\alpha^2} \\ -\frac{k_-^2}{2\alpha^2} & \frac{jk_-}{2\alpha} & \frac{jk_-k_p}{2\alpha^2} \\ -\frac{k_-^2}{2\alpha^2} & -\frac{jk_-}{2\alpha} & \frac{jk_-k_p}{2\alpha^2} \end{bmatrix} \begin{bmatrix} A_-(0) \\ A_f(0) \\ A_s(0) \end{bmatrix} \tag{3.14}$$

This equation combined with Eq. (3.11) gives all the nine constants in Eq. (3.10) in terms of the wave amplitudes at the input plane.

Substituting these constants into Eq. (3.10) we obtain the complete solution of the coupled-mode equations with given input amplitudes of the three waves:

$$\begin{bmatrix} A_-(z) \\ A_f(z) \\ A_s(z) \end{bmatrix} = \begin{bmatrix} g_{-,-} & g_{-,f} & g_{-,s} \\ g_{f,-} & g_{f,f} & g_{f,s} \\ g_{s,-} & g_{s,f} & g_{s,s} \end{bmatrix} \begin{bmatrix} A_-(0) \\ A_f(0) \\ A_s(0) \end{bmatrix} \tag{3.15}$$

where the elements $g_{i,j}$ give the output in wave i due to the input in wave j. In other words, the gain between the i and j waves at input and output is

$$\left.\begin{aligned}
g_{-,-} &= \frac{k_p^2}{\alpha^2} - \frac{k_-^2}{\alpha^2}\cosh \alpha z \\
g_{-,f} &= \frac{jk_-}{\alpha}\sinh \alpha z = g_{f,-} \\
g_{-,s} &= \frac{jk_pk_-}{\alpha^2}(\cosh \alpha z - 1) = g_{s,-} \\
g_{f,f} &= \cosh \alpha z \\
g_{s,s} &= \frac{k_p^2}{\alpha^2}\cosh \alpha z - \frac{k_-^2}{\alpha^2} \\
g_{s,f} &= \frac{k_p}{\alpha}\sinh \alpha z = g_{f,s}
\end{aligned}\right\} \qquad (3.16)$$

It is worth mentioning that all the gain factors are functions of tube length L, coupling coefficient k_-, and pump coefficient k_p. From these solutions, we can evaluate the gain and bandwidth characteristics, and also gain some physical insight into this type of amplification. Design parameters can be established for various applications such as attenuator, coupler, or amplifier. Noise performance can also be predicted. These characteristics are discussed in more detail in the following sections.

B. PHYSICAL INTERPRETATION OF THE OPERATION

Consider the beam as originally quiescent, i.e., with no transverse modulation on the beam so that both the fast cyclotron wave and the slow cyclotron wave are unexcited at the input terminal of the tube. This corresponds to $A_f(0) = A_s(0) = 0$. The -1 mode circuit wave is the only one excited at the input. Then from the complete solution for the coupled-mode equations as shown in the previous section, one obtains:

$$A_-(z) = \left(\frac{k_p^2}{\alpha^2} - \frac{k_-}{\alpha^2}\cosh \alpha z\right) A_-(0)$$

$$A_f(z) = \frac{jk_-}{\alpha}\sinh \alpha z\, A_-(0) \tag{3.17}$$

$$A_s(z) = \frac{jk_-k_p}{\alpha^2}(\cosh \alpha z - 1)\, A_-(0)$$

This set of equations gives the amplitudes of the various waves along the electron beam when only the -1 mode circuit wave is excited at the input or when the amplitude of both cyclotron waves is small compared with $A_-(0)$.

Figure 29 shows the amplitude of various waves as a function of z. It clearly shows that the output of the circuit wave has an amplitude much larger than the input amplitude if the tube length L is more than twice the critical length ℓ as shown in Fig. 29. The critical length, defined as the length required to couple all the signal into the beam, is a function of pump coefficient and coupling coefficient:

$$\ell = \frac{1}{\alpha}\cosh^{-1}\left(\frac{k_p}{k_-}\right)^2 = \frac{1}{\sqrt{k_p^2-k_-^2}}\log\left[\frac{k_p^2}{k_-^2}\left(1+\sqrt{1-\frac{k_-^4}{k_p^4}}\right)\right] \tag{3.18}$$

It is convenient to introduce a new quantity τ, defined as the ratio of the coupling coefficient to the pump coefficient

$$\tau \equiv \frac{k_-}{k_p} \tag{3.19}$$

Substituting the expression for k_- and k_p in Eqs. (3.4) and (3.5), one finds that τ is actually a frequency parameter if the beam current and pump voltage are fixed in an operating tube. One also finds that $1/\tau$ is actually a pump parameter if the operating frequency and beam current are fixed in an operating tube. The parameter τ can be written explicitly for a helix with center conductor as

$$\tau = \zeta\frac{\sqrt{I_o}}{V_p}\sqrt{\frac{\omega}{\omega_c}}\,\mathrm{sinc}\left(\frac{\beta_{-1}w}{2}\right) \tag{3.20}$$

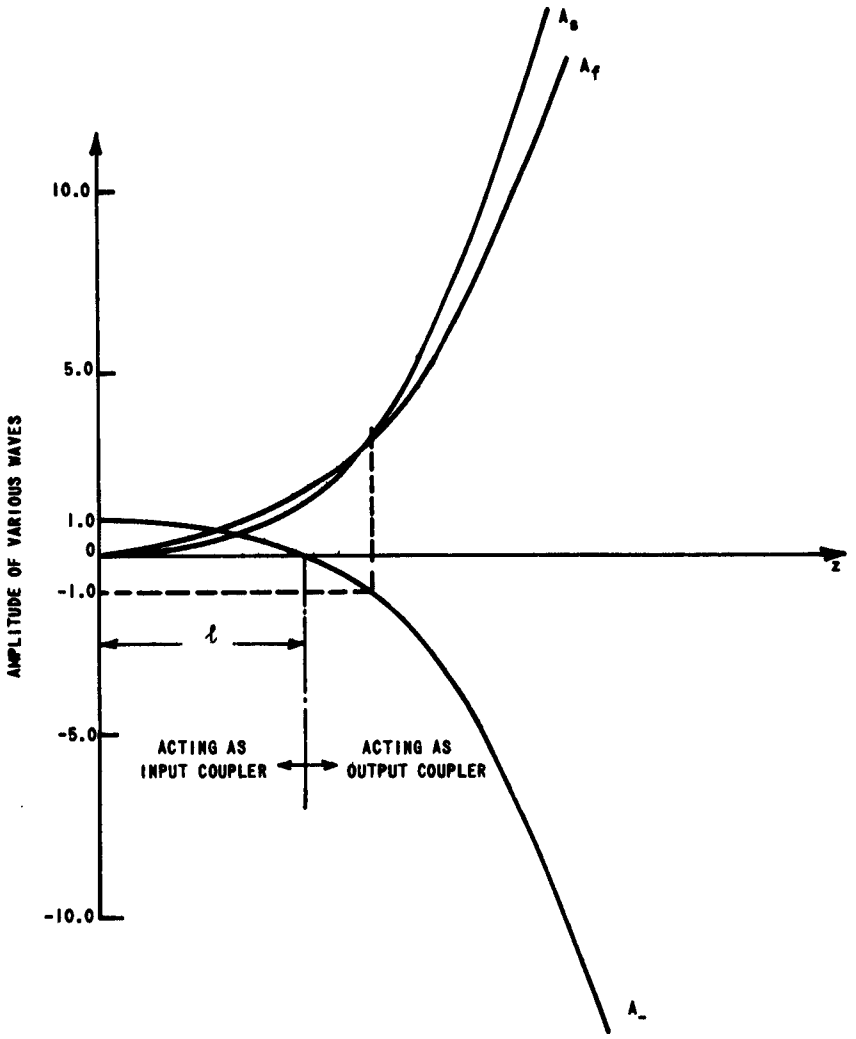

FIG. 29. THE AMPLITUDE OF VARIOUS WAVES GROWING ALONG THE z-DIRECTION IN THE QUADRIFILAR HELIX WHEN BOTH THE RF COUPLING AND DC PUMPING ARE APPLIED SIMULTANEOUSLY. (For k_p = 2.00 in.$^{-2}$, k_- = 1.20 in.$^{-1}$)

where ζ is a fixed parameter determined only by the form and dimensions of the helix. Its numerical value is of the order of 10^3 to 10^4 $v/\sqrt{amp}$ for a helix with center conductor. The dc beam current can be changed if a gun of variable perveance is used, i.e., if an additional anode or grid is used to control the beam current independent of the beam velocity.

The parameter τ will be used to plot universal curves for this type of tube. The universal curves for the critical length are plotted in Fig. 30 as $k_p\ell$ vs τ, to show the dependence on frequency with fixed pump voltage and in Fig. 31 as $k_-\ell$ vs $1/\tau$ to show the dependence on pump voltage for a fixed frequency. From these two universal curves, one notices that the critical length decreases as either the frequency or the pump voltage is increased.

Figure 29 also shows that the output of an amplified circuit wave is 180 deg out of phase with respect to the input circuit wave. Therefore this type of tube can be used as a 180-deg phase shifter when such application is necessary.

The quadrifilar helix structure with proper pump voltage could be used as an input or output coupler in a conventional parametric beam-type amplifier, but this will excite both the fast and the slow cyclotron waves. As a consequence, the noise-stripping characteristic of the Cuccia-type coupler cannot be achieved, so it is impractical for low-noise operation.

There is another characteristic length ℓ', for which the circuit wave has the same amplitude as its input but completely out of phase, and both the fast and slow cyclotron waves in the beam are equally excited. The section of the helix up to $z = \ell'$ acts as a passive section, as viewed by the circuit wave, and the helix beyond $z = \ell'$ acts as an active section. Therefore, for gain purposes a helix must be much longer than ℓ'.

If we consider a semi-infinite quadrifilar helix with both the coupling condition and the pump condition satisfied, the circuit wave will have a sinusoidal interchange of energy with the fast cyclotron beam wave if the pump field is not applied. Figure 32 is a plot of the circuit wave as a function of k_-z using the pumping coefficient k_p as a parameter. These curves show the pumping effect on the circuit wave for fixed coupling strength (i.e., fixed beam current, etc.). Two interesting features should be pointed out:

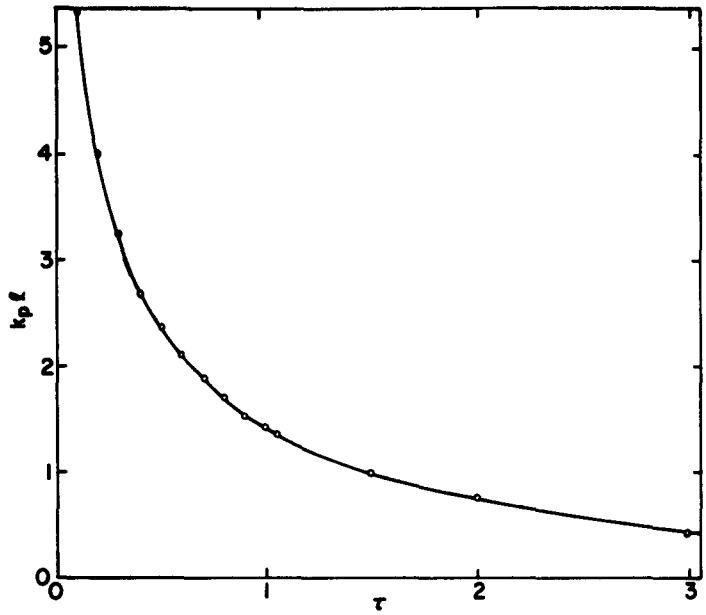

FIG. 30. UNIVERSAL CURVE FOR THE DEPENDENCE ON FREQUENCY OF THE CRITICAL LENGTH.

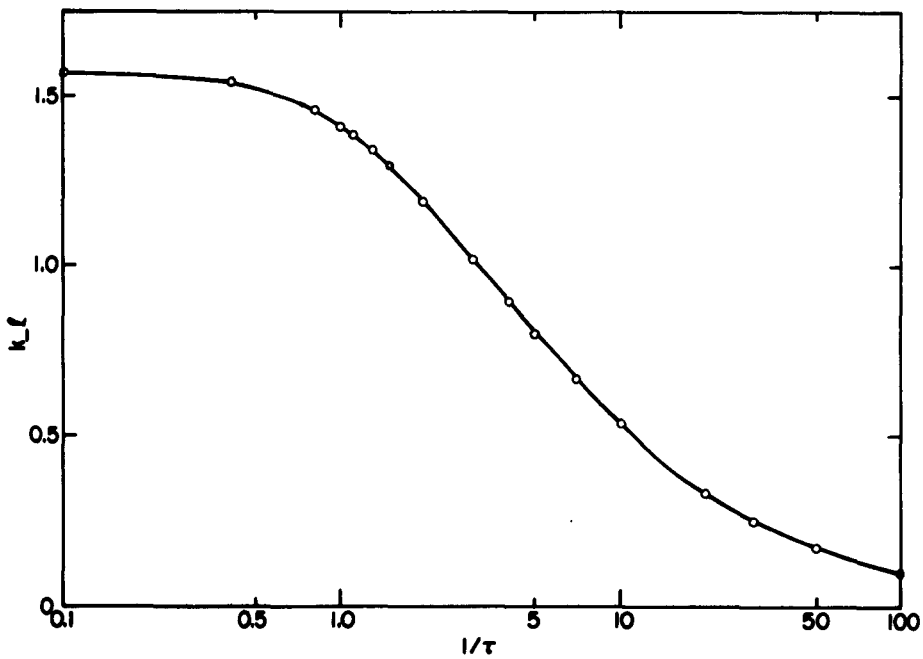

FIG. 31. UNIVERSAL CURVE FOR THE DEPENDENCE ON PUMP VOLTAGE OF THE CRITICAL LENGTH.

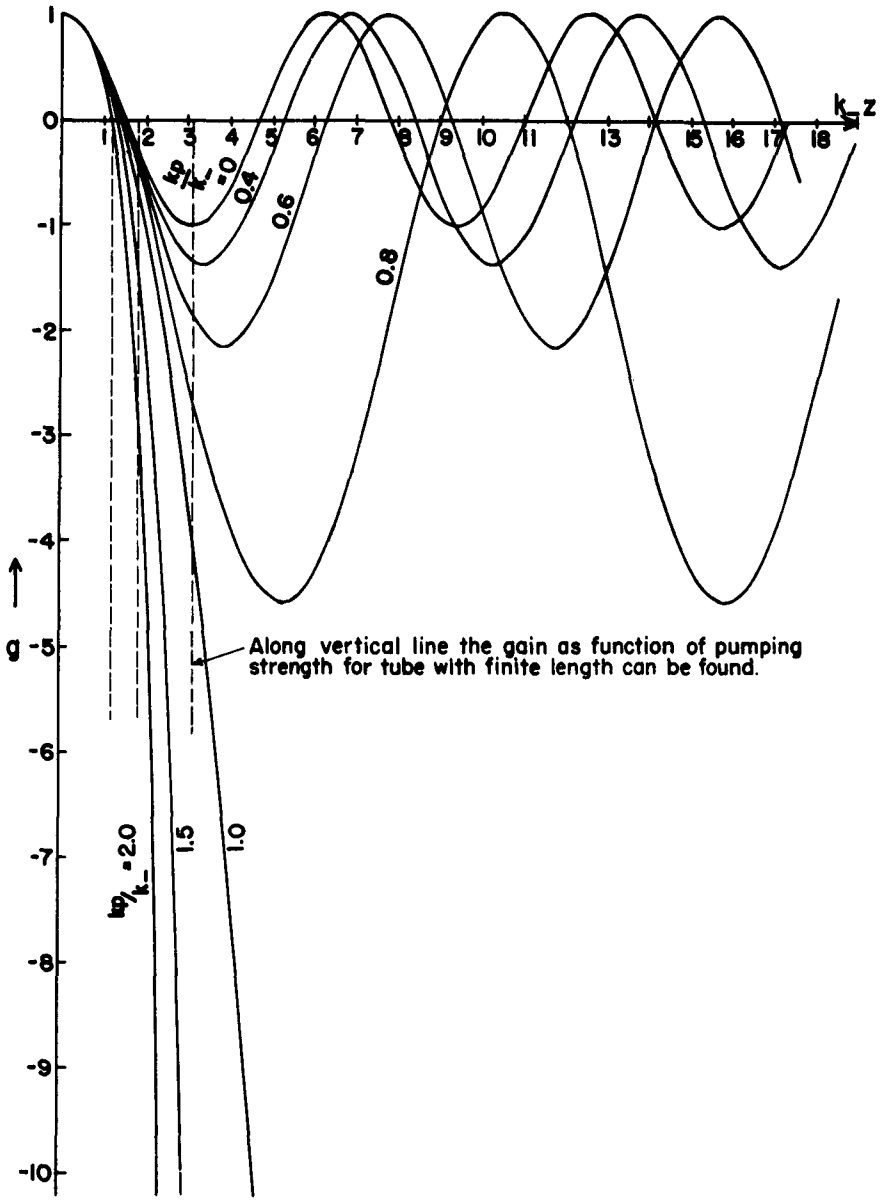

FIG. 32. THE PUMPING EFFECT ON THE CIRCUIT WAVE CARRIED BY AN INFINITELY LONG HELIX ORIGINALLY COUPLED WITH THE FAST CYCLOTRON BEAM WAVE.

1. When the pump amplitude is gradually increased, the first null of the circuit wave gradually moves closer to the input end, while all the rest of the nulls move away rapidly from the input end, reaching infinity as the pumping coefficient becomes equal to the fixed coupling coefficient.
2. Gain in the circuit wave is possible even if the circuit wave still varies sinusoidally along the helix when the pumping coefficient is smaller than the coupling coefficient.

If the helix has a finite length which is smaller than the first null of the circuit wave without pumping, that is the normalized length $k_z < \pi/2$, then the output of the circuit wave will first decrease to zero and then grow rapidly with a 180-deg phase shift, as the pump voltage is increased. This variation can be viewed on a vertical line $k_z = \text{const}$ in Fig. 32. For those helices with lengths between the first and second nulls of the circuit wave without pump, or $\pi/2 < k_z < 3\pi/2$, the circuit output is originally out of phase with respect to the input. There is one null inside the helix such that the whole circuit input is coupled into the beam at that point. The circuit wave will continually grow as the pump amplitude increases. For those helices with lengths between the second and third nulls of the circuit wave without pump, the circuit output will see only one null as the pump amplitude is increased; this is because the pumping pushes the second null outside of the helix, as mentioned before. Therefore, it is obvious that the circuit output will have $N - 1$ nulls when the pump is turned up, if there are originally N nulls inside the helix circuit. Steady growth of the circuit wave with increased pumping strength will result only after these $N - 1$ nulls are pushed outside the helix. However, if there is originally no null at all inside the helix with finite length, the pumping will then first push one null (i.e., the first null) into the helix so that the full circuit signal will be completely coupled into the beam before active pumping results.

The circuit outputs as functions of the pumping coefficient for a helix with finite length are shown in Fig. 33 using k_z as a parameter. This clearly shows the number of nulls in the circuit output depending on the coupling strength and the helix length just as in the above interpretation. The number of nulls is plotted in Fig. 34.

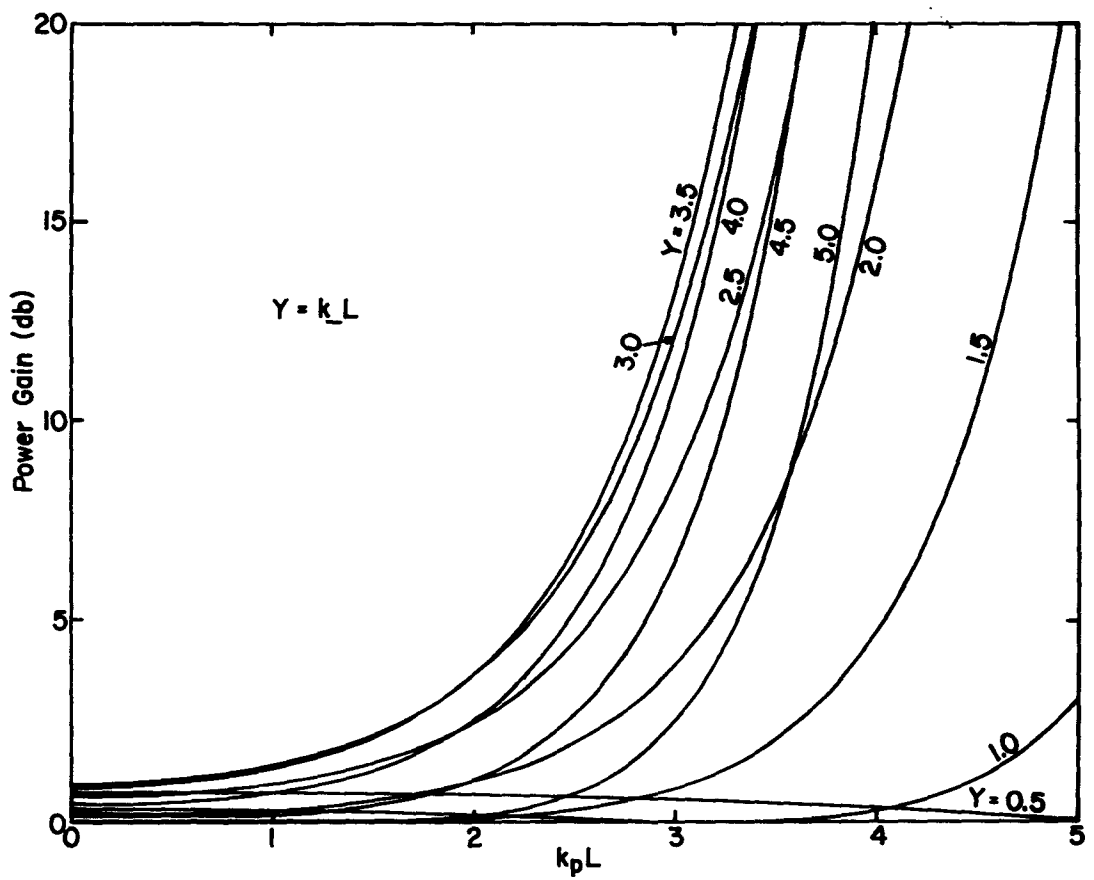

FIG. 33. THE CIRCUIT OUTPUTS OF A HELIX WITH FINITE LENGTH AS FUNCTIONS OF THE PUMPING COEFFICIENT WITH THE COUPLING COEFFICIENT AS THE PARAMETER.

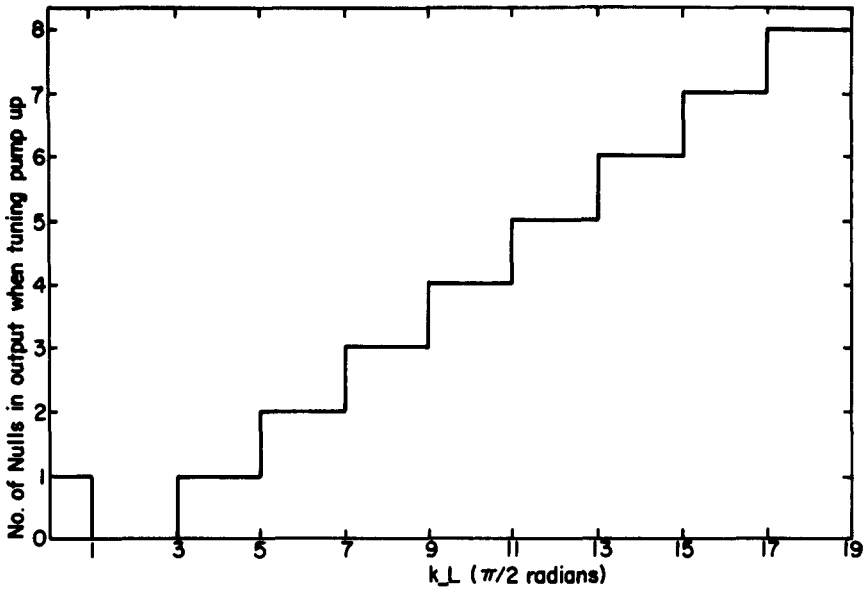

FIG. 34. THE NUMBER OF NULLS IN THE CIRCUIT OUTPUT AS A FUNCTION OF THE COUPLING COEFFICIENT AND THE CIRCUIT LENGTH.

Figure 35 is a plot of the circuit wave amplitude along the helix with the coupling coefficient k_- as a parameter. These curves show the coupling effect on the circuit wave for fixed pump strength. Starting with the coupling coefficient k_- equal to zero, the circuit wave is constant along the helix, assuming no loss. For the coupling coefficient less than the pumping coefficient, $k_- < k_p$ the circuit wave will gradually be coupled into the beam until a null is reached, after which it grows exponentially with opposite phase along the helix. For values of the coupling coefficient equal to or larger than the pumping coefficient, the circuit wave amplitude will vary sinusoidally with possible gain in the opposite phase.

For helices with finite length, the coupling effect can be viewed by following a vertical line with constant k_pL corresponding to a given pumping strength. The outputs have essentially similar variation for various pumping strengths, that is, the circuit wave output gradually decreases until a null is reached, then grows rapidly to a maximum which is a function of k_pL and always larger than one. After that, it will

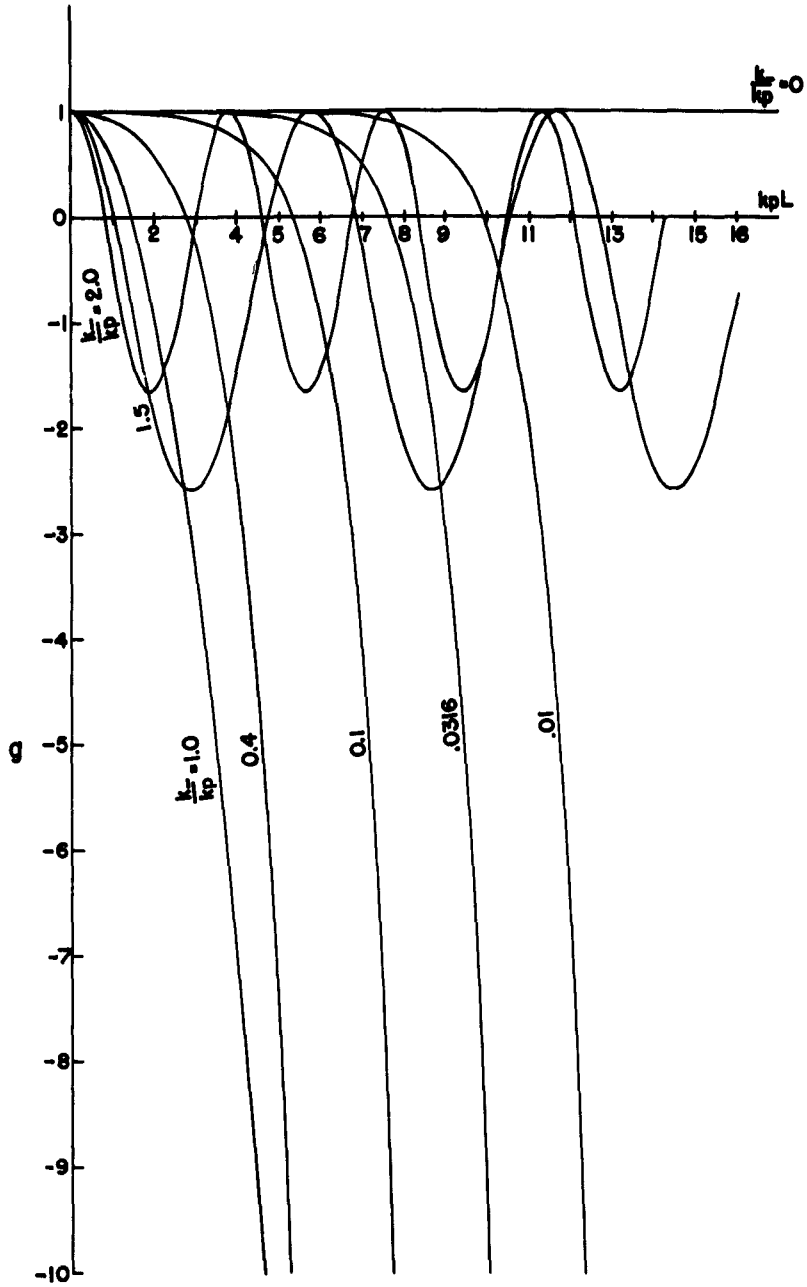

FIG. 35. THE COUPLING EFFECT ON THE CIRCUIT WAVE CARRIED BY AN INFINITELY LONG HELIX WITH THE PUMPING COEFFICIENT AS A PARAMETER.

drop again in periodic fashion as the coupling coefficient is further increased. This variation of the circuit wave output of a finite helix as a function of the coupling coefficient is shown in Fig. 36, with the pump coefficient as a parameter. Both the pumping and the coupling coefficients are normalized by the length L of the helix.

The power carried by a wave A_i is $A_i A_i^*$ and the sign of the power is determined by its parity matrix element p_{ii}. The total power carried by the three waves is then:

$$P = p_{--} A_- A_-^* + p_{ff} A_f A_f^* + p_{ss} A_s A_s^* \tag{3.21}$$

and the paraity matrix elements are:

$p_{--} = +1$, since the circuit wave carries positive power

$p_{ff} = +1$, since the fast cyclotron wave carries positive power

$p_{ss} = -1$, since the slow cyclotron wave carries negative power

Substituting the set of Eqs. (3.17) into Eq. (3.21) one then obtains:

$$\begin{aligned} P(z) &= A_-(z)\, A_-^*(z) + A_f(z)\, A_f^*(z) - A_s(z)\, A_s^*(z) \\ &= A_-(0)\, A_-^*(0) = \text{constant} \end{aligned} \tag{3.22}$$

Equation (3.22) shows that the total power carried by the three waves is an invariant along the z-direction, though the power carried by each wave does vary along the z-direction. From this result one can be sure that the twisted dc field does not supply energy to the associated waves but merely acts as a coupling mechanism to provide a path for the energy flowing from the slow cyclotron wave to the fast cyclotron wave. Since the circuit wave is coupled passively with the fast wave due to the synchronism in phase velocity, the energy is then flowing from the fast cyclotron wave to the circuit wave. It is this path of energy flow that makes the circuit wave grow along z.

Actually the energy can flow in both directions, from circuit to beam and from beam to circuit. From Fig. 29 one can notice for z smaller than the critical length that the flow of energy is dominant in the direction from circuit to beam; and for z larger than the critical length ℓ, the flow of energy is dominant in the direction from beam to circuit. Figure 37 shows that the power carried by each wave is a function of z, and also that the total power carried by the three waves is an invariant along z.

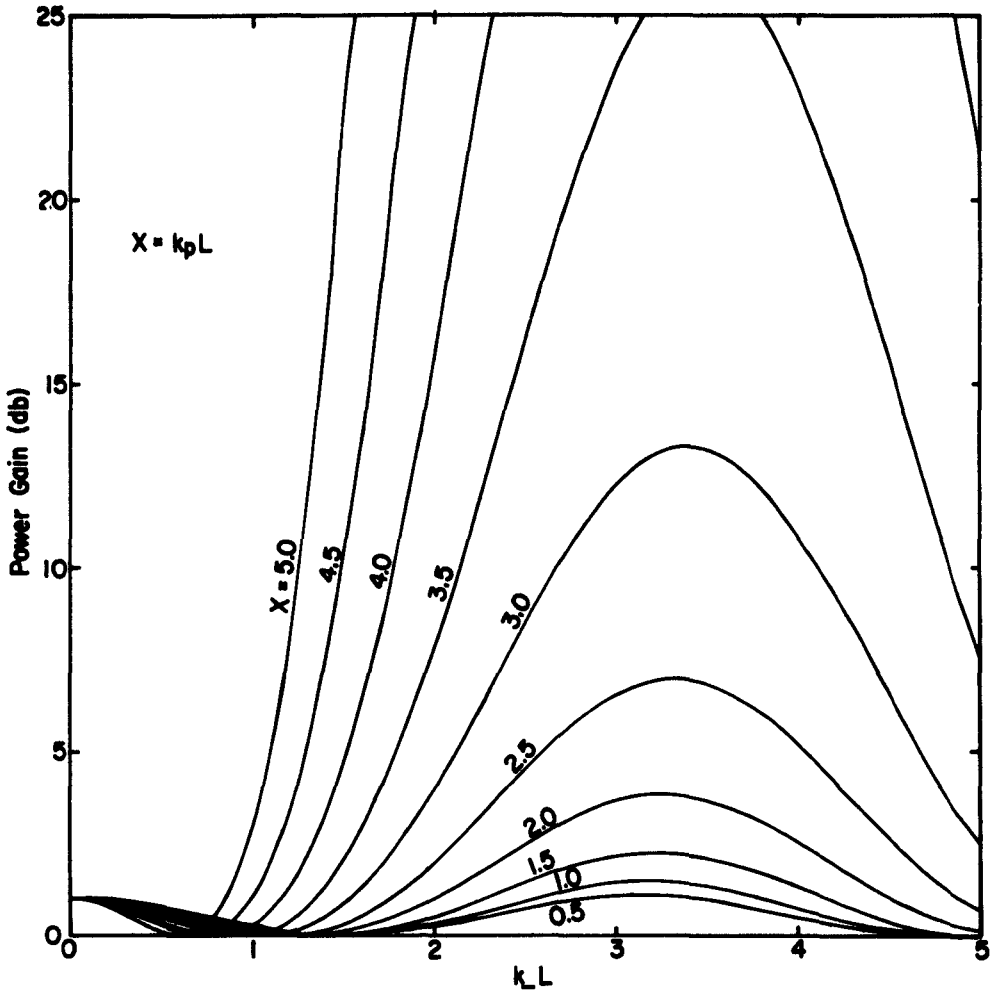

FIG. 36. THE CIRCUIT OUTPUTS OF A HELIX WITH FINITE LENGTH AS FUNCTIONS OF THE COUPLING COEFFICIENT WITH THE PUMPING COEFFICIENT AS THE PARAMETER.

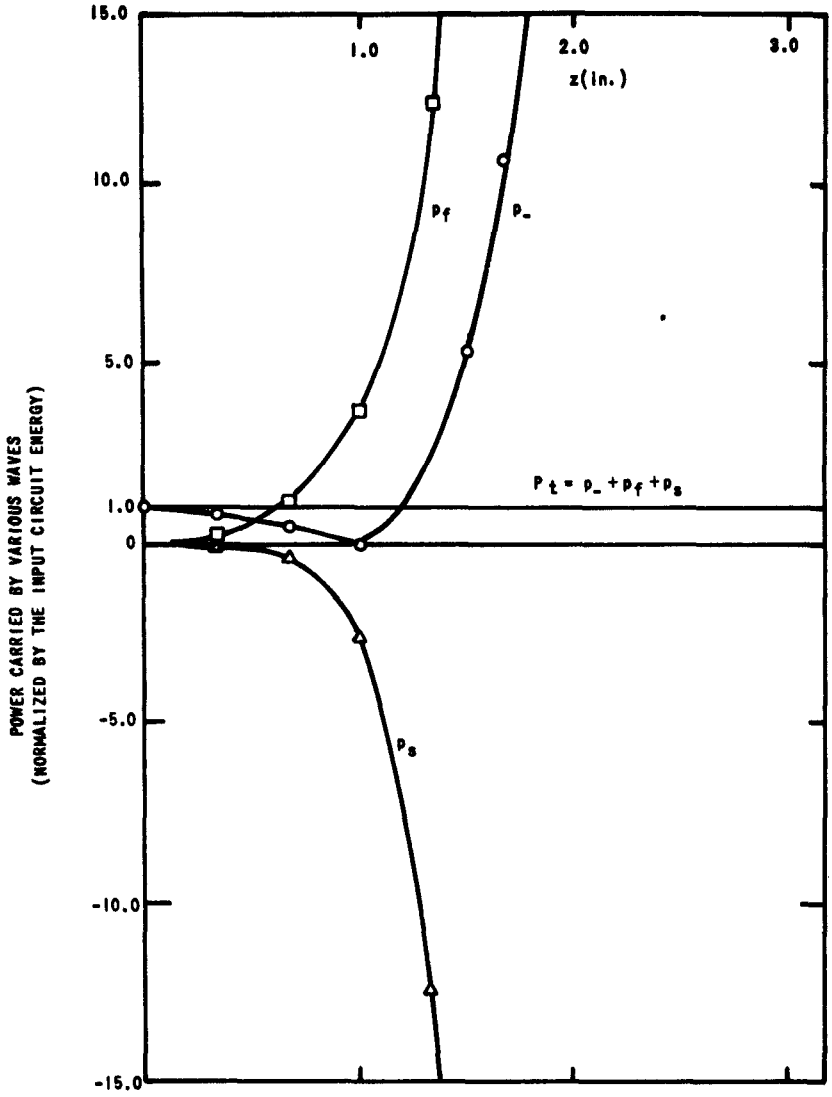

FIG. 37. THE POWER CARRIED BY VARIOUS WAVES ALONG THE z-DIRECTION IN THE QUADRIFILAR HELIX WHEN BOTH THE RF COUPLING AND THE DC PUMPING ARE APPLIED SIMULTANEOUSLY. (For $k_p = 2.00$ in.$^{-1}$, $k_- = 1.2$ in.$^{-1}$)

C. GAIN AND BANDWIDTH OF THE AMPLIFIER

The power gain of an amplifier is defined as the output signal power divided by the input signal power. In the quadrifilar helix tube the power gain can readily be obtained from the solutions of the coupled-mode equations [shown in Eq. (3.15)]:

$$G_p = g_{-1}^2 = \frac{1}{(1-\tau^2)^2}\left[1 - \tau^2 \cosh k_p L \sqrt{(1-\tau^2)}\right] \tag{3.23}$$

where L is the total length of the helix and τ is the ratio of the coupling coefficients as defined in Eq. (3.19). The power gain is plotted as a function of τ in Figs. 38 and 39 for various pump levels using G_{po} as a pump parameter, where G_{po} is the power gain of the fast cyclotron wave which would result if the coupling between the circuit wave and the beam waves were removed by some means, so that only the dc pumping action of the quadrifilar helix existed. The curves clearly show that the best operation of the tube is obtained with the pumping coefficient about twice the coupling coefficient.

The quantity G_{po} is entirely a pump parameter, involving only the pump voltage, the tube length, and the dimensions and shapes of the pump structure. Therefore, for design purposes it is a true measure of the pump strength; for a given tube it is an indication of the pump voltage. This pump-level parameter can be expressed mathematically as:

$$G_{po} = \cosh^2 k_p L \tag{3.24}$$

which is not a function of frequency, since it does not involve the only frequency-dependent factor, namely, the interaction impedance K_{-1}.

Figure 40 is a plot of the universal pump parameter G_{po} as a function of k_pL. For a tube with known helix dimensions one can readily obtain a curve of G_{po} vs pump voltage V_p from Fig. 40. The curves of gain vs τ as shown in Figs. 38 and 39 can be transformed to curves using the pump voltage as the parameter. As stated in Sec. B, τ is actually a frequency parameter for fixed pump levels; therefore, the curves of gain vs τ as shown in Figs. 38 and 39 can be readily transformed to curves of gain vs frequency for a tube with specified beam current and dimensions of the pump structure. From these data one can then obtain the bandwidth characteristic of the tube.

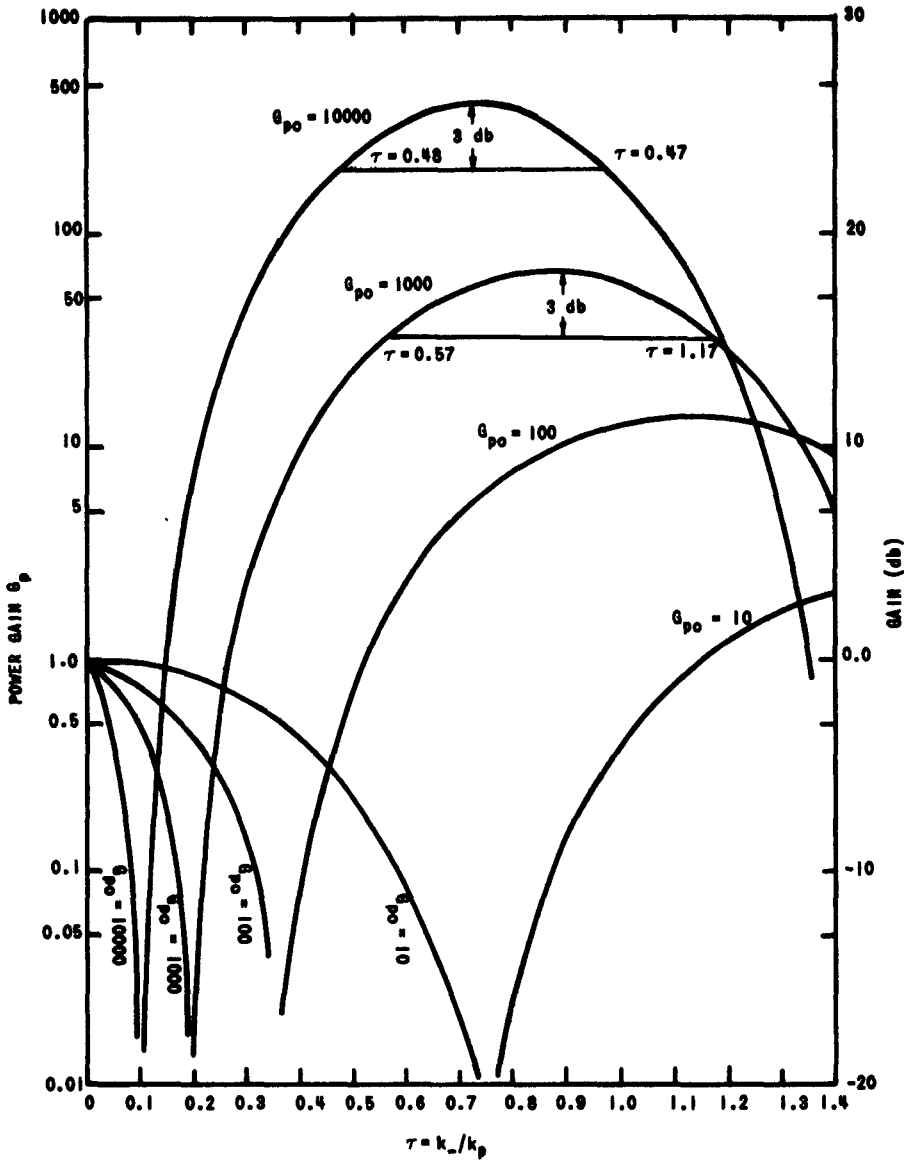

FIG. 38. POWER GAIN AS A FUNCTION OF $\tau = k_-/k_p$ USING G_{po} AS A PARAMETER.

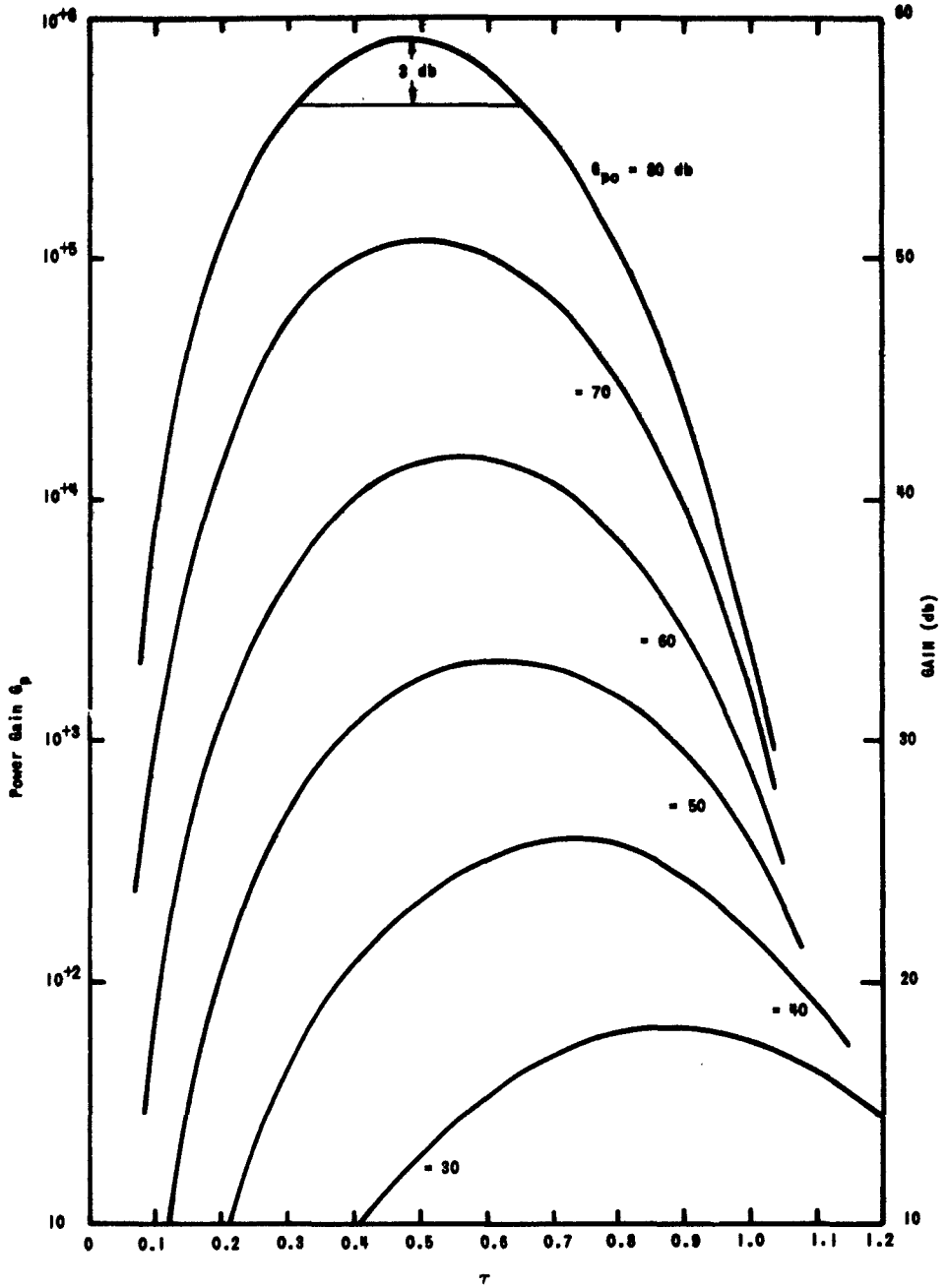

FIG. 39. POWER GAIN AS A FUNCTION OF $\tau = k_-/k_p$ FOR HIGH PUMP LEVELS.

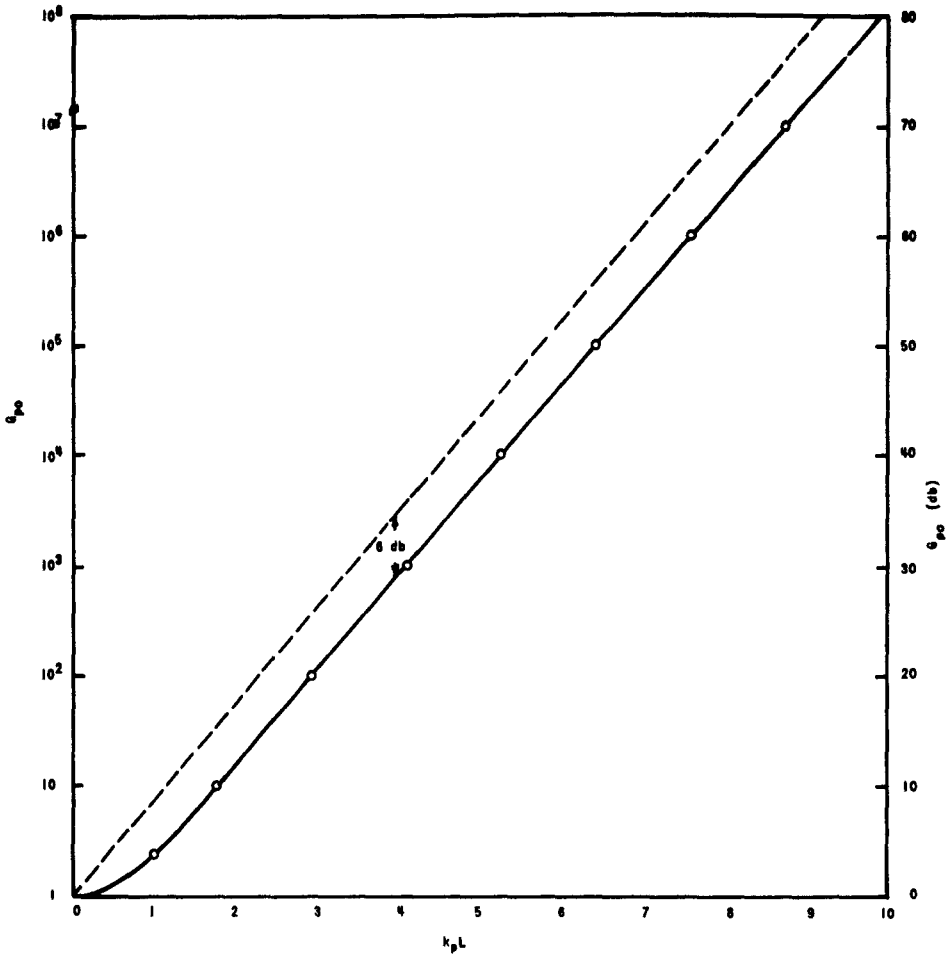

FIG. 40. UNIVERSAL CURVE OF THE PUMP PARAMETER G_{po} VS k_pL.

For a solid beam at the center of a helix, the frequency dependence is:

$$\tau^2 = \left(30\,\frac{c^2}{\eta}\right)\frac{I_o}{V_p^2}\,\frac{ka - 1}{\tan^2\psi\; I_1^2\,(ka\cot\psi)} \tag{3.25}$$

where I_o = dc beam current

V = dc pumping voltage

ψ = the pitch angle of the helix

a = the radius of the helix

k = free-space wave number

$I_1(ka\cos\psi) = -j\,J_1(jka\cot\psi)$ = Bessel function

c = velocity of light

η = charge-to-mass ratio of electron

A plot of τ as a function of ka or ω/ω_c for $I_o = 10$ ma is shown in Fig. 41 using V_p as a parameter. From the plot of power gain vs τ as shown in Fig. 38, one notices that 15 to 18 db of power gain would be obtained for values of τ between $\tau = 0.57$ and $\tau = 1.17$ for a particular pumping strength $G_{po} = 30$ db. The frequency bandwidth corresponding to the width of $\tau = 0.57$ to $\tau = 1.17$ is marked in the τ vs frequency curves as shown in Fig. 41. From these curves it is found that the bandwidth of the quadrifilar dc-pumped traveling-wave tube with 10-ma solid electron beam and 3000-Mc cyclotron field would be about 200 Mc at a center frequency of 1400 Mc for 100-v dc pumping, and about 150 Mc bandwidth at a center frequency of 1000 Mc for 1000-v dc pumping.

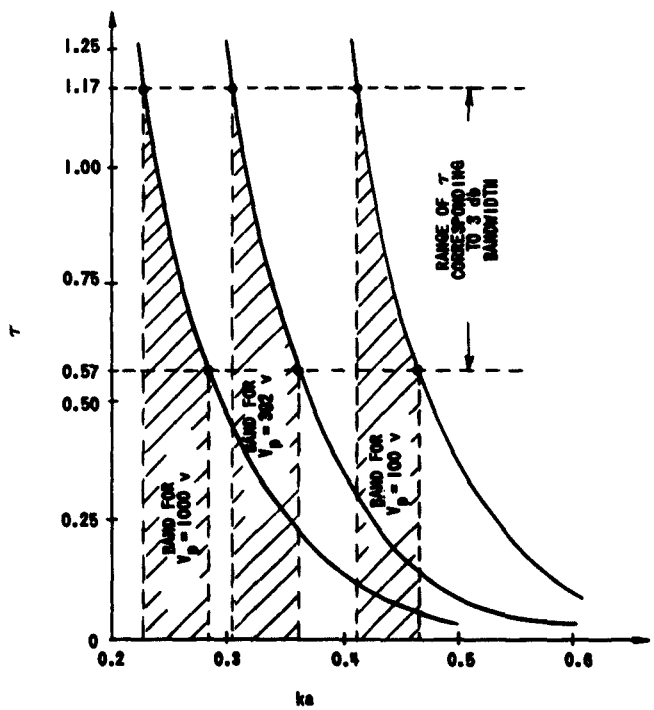

FIG. 41. THE FREQUENCY PARAMETER AS A FUNCTION OF ka FOR $I_o = 10$ ma AND $\cot\psi = 12$.

These bandwidths obtained by using a solid beam are satisfactory but not outstanding. Trial designs at higher frequencies indicate that larger bandwidths should be possible. However, the use of a hollow rather than a solid beam is found to result in much larger bandwidths and to yield various other advantages as well.

If one uses a concentric hollow beam with a center rod inside the beam, one finds that the frequency parameter is of the form:

$$\tau = \varphi \frac{\sqrt{I_o}}{V_p} \sqrt{\frac{\omega}{\omega_c}} \operatorname{sinc}\left(\frac{\beta_{-1} w}{2}\right) \tag{3.20}$$

as shown in Sec. B. In deriving this equation, the following approximate expression for the transverse impedance of a helix with center conductor is substituted into the expression of k_-,

$$K_{tn} \cong \frac{30 \; \frac{4w}{p} \; \operatorname{sinc}^2\left(\frac{\beta_n w}{2}\right)}{|\beta_n| \; (a-b) \; |n + ka|} \tag{3.26}$$

which is obtained as shown in Appendix C, where

$\beta_n = (n + ka)$

$k = \omega/c$

a = radius of the helix

b = radius of the center conductor

p = pitch of the helix

w = width of the tape that forms the helix

n = mode number of the circuit wave

$\operatorname{sinc} X \equiv \sin X/X$

The factor φ is a parameter determined by the dimensions of the helix only and is:

$$\varphi = \frac{1}{A_1} \sqrt{\frac{60}{\pi} \frac{c^2}{\eta} \frac{w}{a-b}} \; \frac{\sinh 2\beta_c (a-b)}{\sinh 2\beta_c (r_o - b)} \; (\mathrm{DLF}) \tan \psi \tag{3.27}$$

where A_1 is the amplitude factor of the fundamental mode and is close to unity, and DLF is the dielectric loading factor. All other symbols are as defined before. Thus φ can be called a helix parameter, and is found to be of the order 10^3 to 10^4 in volts/$\sqrt{\text{amp}}$ for suitable designs.

Figures 42, 43, and 44 show τ as a function of ka or ω/ω_c for different beam currents and pump levels with $\varphi = 1.8 \times 10^3$ v/$\sqrt{\text{amp}}$, using the approximation sinc $(\beta_{-1}w/2) \cong 1$. From these figures one finds that the bandwidth is attractively wide and increases as the pump level increases. But, the 3-db range of τ is found to decrease in Figs. 38 and 39 as the pump level increases. The exact bandwidth dependence on the pump level is not fully explored here.

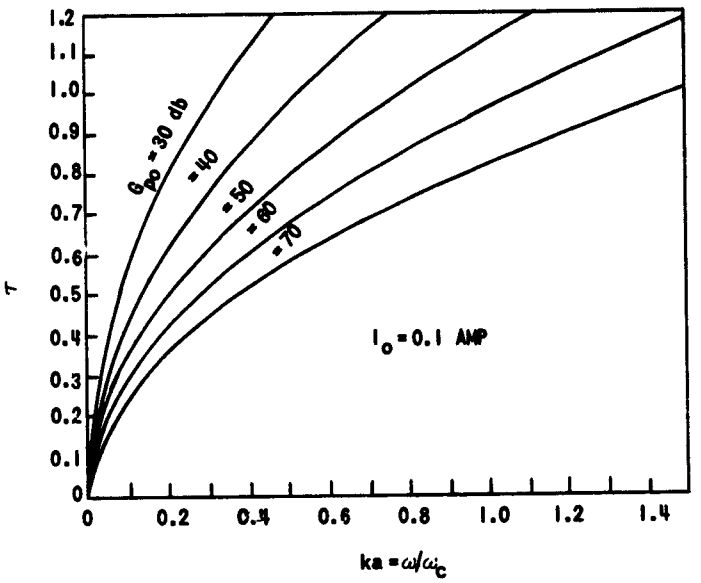

FIG. 42. THE FREQUENCY PARAMETER OF THE QUADRIFILAR HELIX WITH CENTER CONDUCTOR FOR I_o = 0.10 amp.

In order to examine in detail the bandwidth characteristics as a function of pump level, one should first notice that the value of τ at which the gain is maximum for various pump levels decreases as the pump level is increased as shown in Fig. 45. The 3-db range of τ is also decreasing when the pump level increases. Combining these facts with the curves of τ vs ω/ω_c in Figs. 42, 43, and 44, one then obtains the characteristic bandwidth curve shown in Fig. 46, where the bandwidth is expressed as the ratio of upper 3-db cutoff frequency to lower 3-db cutoff frequency. The actual bandwidth can be easily obtained as soon

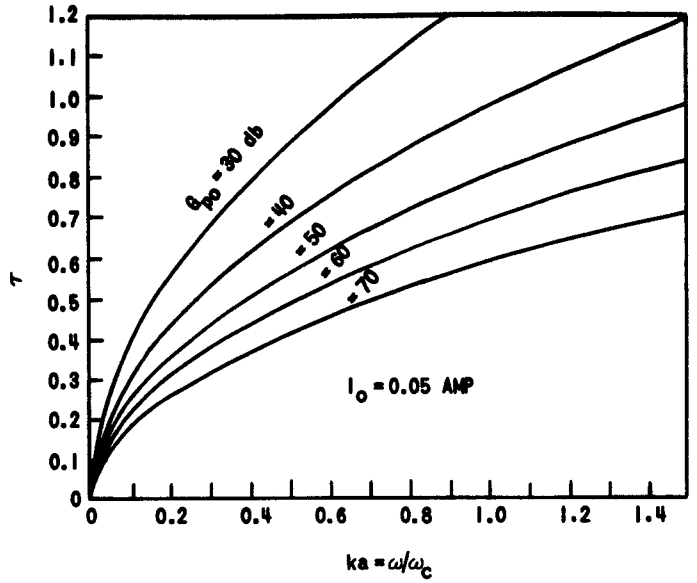

FIG. 43. THE FREQUENCY PARAMETER τ OF THE QUADRIFILAR HELIX WITH CENTER CONDUCTOR FOR $I_o = 0.05$ AMP.

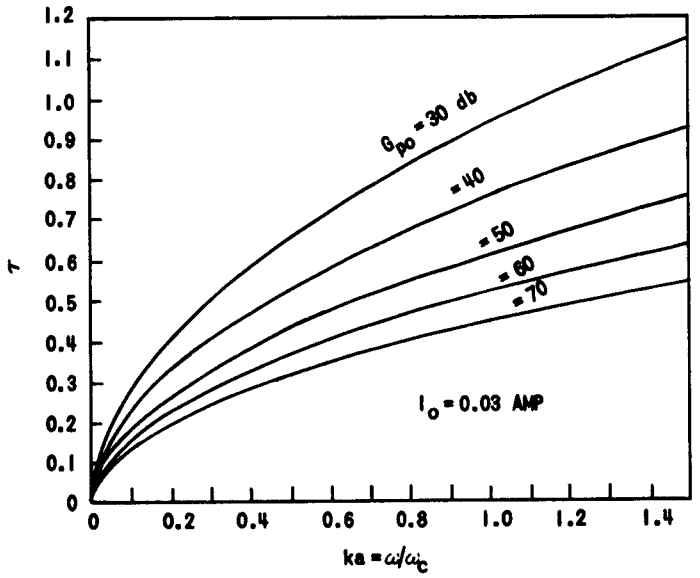

FIG. 44. THE FREQUENCY PARAMETER τ OF THE QUADRIFILAR HELIX WITH CENTER CONDUCTOR FOR $I_o = 0.03$ AMP.

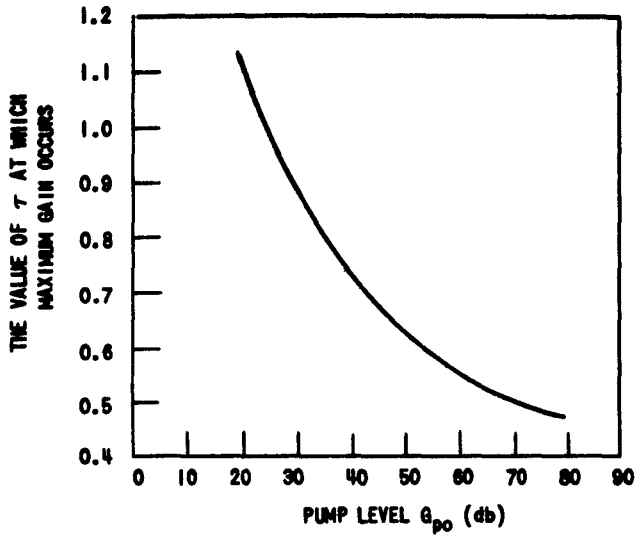

FIG. 45. THE VALUE OF τ AT WHICH MAXIMUM GAIN OCCURS AS A FUNCTION OF PUMP LEVEL.

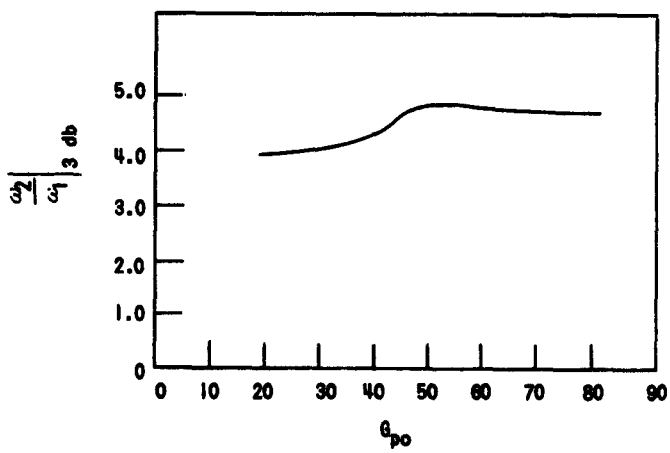

FIG. 46. BANDWIDTH CHARACTERISTIC CURVE AS A FUNCTION OF PUMP LEVEL OF THE CYCLOTRON-WAVE AMPLIFIER USING A QUADRIFILAR HELIX WITH CENTER CONDUCTOR AS A SIMULTANEOUS COUPLING AND PUMPING STRUCTURE.

as the center frequency is chosen. The center frequency can be tuned by the dc beam current as shown later. Figure 46 shows almost no bandwidth variation with pump level. An almost constant 4 to 1 bandwidth over a 50-db pump range is shown. This result is very encouraging since there are few devices that exhibit such wide bandwidth.

The tuning characteristic of the quadrifilar helix tube for hollow-beam operation can be clearly seen from Eq. (3.20) for the frequency parameter τ. One can center the gain at any specified frequency by tuning the beam current in accordance with the pump level. As shown in Fig. 47, we have tuned the current such that the maximum gain occurs at $ka = 0.8$ for three different pump levels. Since the tuning current is found to be quite insensitive to the pump level, and since the bandwidth is so wide (as shown in Fig. 47) the actual gain in decibels is still approximately linear with pump level in decibels for a fixed beam current.

Another characteristic of this type amplifier is that the gain bandwidth product is not a constant as in many other types of amplifiers. The bandwidth is almost independent of gain, and remains essentially the same as the gain or the pump level is increased, as shown in Figs. 46 and 47. This result comes about because the pump coefficient which controls the gain is independent of frequency, and the bandwidth is chiefly determined by the coupling coefficient k_- alone.

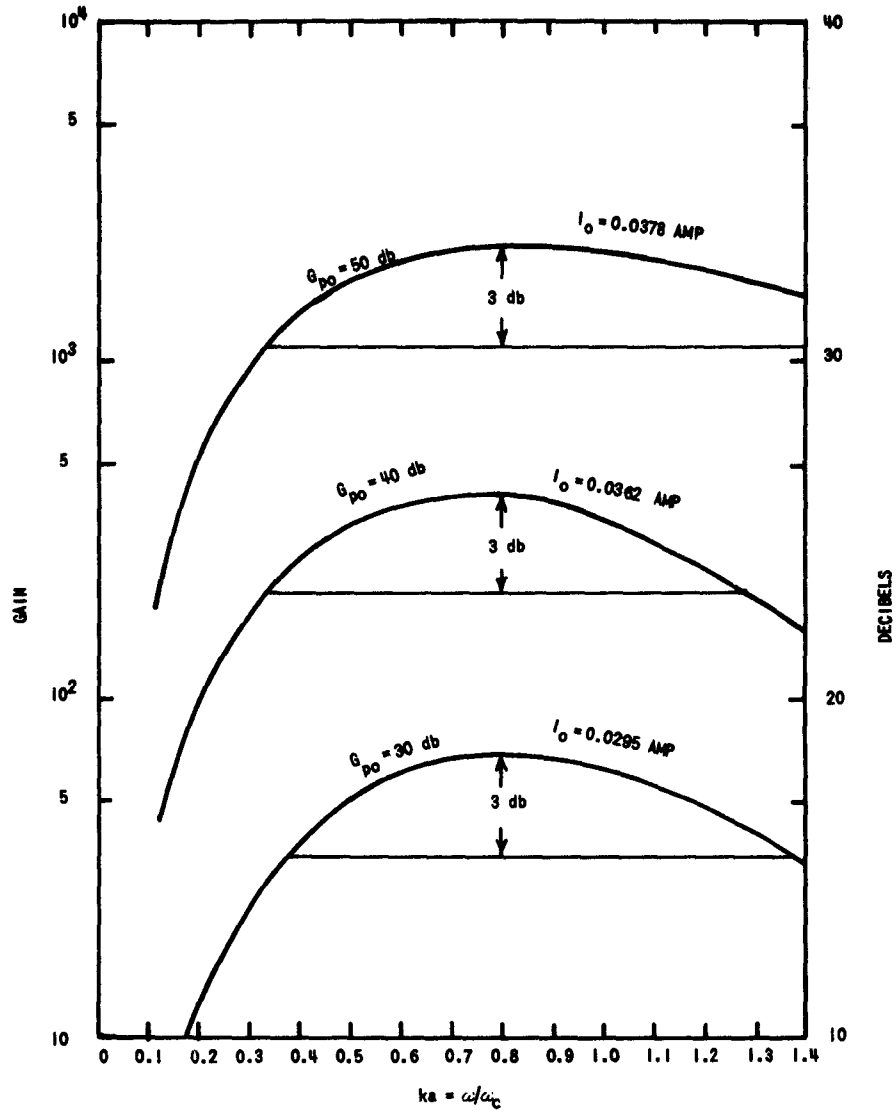

FIG. 47. FREQUENCY RESPONSE OF THE GAIN; THE MAXIMUM GAIN IS TUNED TO OCCUR AT $ka = 0.8$ FOR VARIOUS PUMP LEVELS.

D. NOISE PERFORMANCE

This type of amplification is associated with three waves, namely, the -1 mode circuit wave, the fast cyclotron wave, and the slow cyclotron wave. If no noise-stripping mechanism is applied to the beam before it enters the helical pumping and coupling region, then the beam's noise power originating at the cathode and carried along by the cyclotron waves will represent the initial cyclotron-wave noise amplitudes at the input of the helix. This beam-induced noise will be the dominant noise at the output end since the noise waves also are pumped by the dc-twisted field as shown in Eq. (3.15). Other sources of noise as considered by Lea-Wilson [Ref. 41], Adler and Wade [Ref. 15], and others [Refs. 12,42] are not comparable with the beam-induced noise at the circuit output in this type of amplifier. A few of these noise sources include:

1. Partition noise which is due to beam interception on various electrodes, sometimes caused by amplification of the thermal orbits of the electrons within the pumping and coupling region. This source introduced a noise figure of about 0.4 db in one particular case [Ref. 41].
2. Noise caused by the spread of axial velocities in the beam. In our analysis the assumption has been made that the electrons all have equal axial drift velocity. However, the axial drift velocity in actual cases will vary somewhat, due not only to space-charge depression inside the beam, but also to the axial electric field produced by the twisted dc potentials as shown in the large-signal analysis in Chapter II. The noise figure introduced by the space-charge depression in one typical case would be about 0.2 db for S-band operation, and that introduced by the axial electric field would be about 0.4 db.
3. Noise carried by the synchronous waves. This noise does not involve transverse velocity of the electron motion but rather comes from the spatial fluctuations of the center of gravity of the beam about its original axis due to the thickness of the beam. These fluctuations may induce a noise output voltage on the helix, which is proportional to the operating frequency as well as the cyclotron frequency. In comparison to the amplified cyclotron-wave noise, however, the noise from the synchronous waves is still negligible.

Noise-reduction schemes for transverse waves have been studied by Wessel-Berg and Blåtekjaer [Ref. 43]. They showed that the beam noise can be redistributed among the four waves by a proper transducer, so that the noise matrix [Haus and Robinson, Ref. 44] is diagonalized and the minimum eigenvalue is associated with the negative-energy transverse wave which is coupled or pumped by the external waves. Such schemes of noise reduction are also applicable to our case. The optimum noise

transformer would be different from the cases considered by Ref. 43, since we use both the fast cyclotron wave and the slow cyclotron wave to interact with the circuit wave. The optimum passive noise transformer, however, would make the noise temperature in our case equal the minimum noise temperature $T_{min} = (\omega/\omega_c)\, T_c$.

Our amplification scheme (simultaneous pumping and coupling) is not primarily aimed at low noise characteristics, but rather at various other advantages, such as favorable bandwidth characteristics, possibilities of high-power and high-frequency operations, etc. We will therefore only analyze the simple noise performance with the beam brought directly from the electron gun without any noise stripping or noise transformation.

In order to examine the noise performance of the tube, one starts by looking at the noise output without signal input. From solutions of the coupled-mode equation, one has the noise output circuit wave of the quadrifilar helix tube with simultaneous signal coupling and dc pumping as follows:

$$A_-(L) = \sqrt{G}\, A_-(0) + \frac{jk^*}{\alpha} (\sinh \alpha L)\, A_f(0) + \frac{jk_p k_-}{\alpha^2} \cosh \alpha L - 1)\, A_s(0) \quad (3.28)$$

where G = power gain

$A_s(0)$ = input noise magnitude of the slow wave in the beam

$A_f(0)$ = input noise magnitude of the fast wave in the beam

$A_-(0)$ = input noise magnitude of the (-1) mode circuit wave

$A_-(L)$ = output noise magnitude of the (-1) mode circuit wave

$\alpha = \sqrt{k_p^2 - k_-^2}$

k_p = coupling coefficient for dc pumping

k_- = coupling coefficient for (-1) mode

L = the length of the quadrifilar helix

The first term in Eq. (3.28) is evidently the noise output in the circuit wave from the signal source. The second term gives the noise output from the fast cyclotron wave, and the third term gives the noise output from the slow cyclotron wave.

The power spectrum of a wave A can be defined as:

$$S = \lim_{\Delta\omega \to 0} \frac{\langle A A^* \rangle}{\Delta\omega} = \text{power density spectrum}$$

$$= \text{average available power per unit bandwidth}$$

In our case, it is reasonable to assume that there is no cross-power density spectrum between the fast and the slow waves at the input. Based on this assumption and the above definition for power density spectrum, one can evaluate the noise figure of the quadrifilar helix tube with simultaneous signal coupling and dc pumping as follows:

$$NF = 1 + \frac{1}{G} \frac{k_p^2 k_-^2}{\alpha^4} (\cosh \alpha L - 1)^2 \frac{\langle A_s(0)\ A_s^*(0) \rangle}{\langle A_-(0)\ A_-^*(0) \rangle}$$

$$+ \frac{1}{G} \frac{k_-^2}{\alpha^2} (\sinh^2 \alpha L) \frac{\langle A_f(0)\ A_f^*(0) \rangle}{\langle A_-(0)\ A_-^*(0) \rangle} \tag{3.29}$$

The noise powers carried by the cyclotron waves [Ref. 42] are

$$\langle A_s(0)\ A_s^*(0) \rangle = \langle A_f(0)\ A_f^*(0) \rangle = kT_cB \frac{\omega}{\omega_c} \tag{3.30}$$

The noise power from the signal source is, as usual,

$$\langle A_-(0)\ A_-^*(0) \rangle = kT_oB \tag{3.31}$$

where k = Boltzmann constant

B = the bandwidth of the system

T_c = temperature of the cathode

T_o = temperature of the input source (usually taken to be 290°K)

Then the noise figure can be written as

$$NF = 1 + \frac{1}{G} \frac{k_-^2}{\alpha^2} \left[\frac{k_p^2}{\alpha^2} (\cosh \alpha L - 1)^2 + \sinh^2 \alpha L \right] \frac{T_c}{T_o} \frac{\omega}{\omega_c} \tag{3.32}$$

The noise figure is commonly expressed in terms of the noise temperature T_a of the tube as

$$NF = 1 + \frac{T_a}{T_o} \tag{3.33}$$

By comparison with the above equations, the noise temperature of the quadrifilar helix tube with simultaneous coupling and pumping is found in terms of the frequency parameter $\tau = k_-/k_p$:

$$T_a = \xi(\tau)\, T_c \tag{3.34}$$

where

$$\xi(\tau) = \frac{1}{G}\frac{\tau^2}{1-\tau^2}\left[\frac{1}{1-\tau^2}\left(\cosh k_pL\sqrt{1-\tau^2} - 1\right)^2 + \sinh^2 k_pL\sqrt{1-\tau^2}\right]$$

Under high gain operation, $\xi(\tau)$ can be simplified to

$$\xi(\tau) = \frac{2-\tau^2}{\tau^2} \tag{3.35a}$$

Figure 48 shows the noise ratio ξ as a function of τ with the pump level G_{po} as a parameter. It is seen that ξ is within the range of 1 to 10 and gives a noise figure of 6 to 12 db for $T_c = 870^oK$ and $\omega = \omega_c$ in the most interesting high-gain range for which $0.4 < \tau < 1.0$. Comparing these curves with those of power gain vs τ as shown in Figs. 38 and 39, one notices that the noise at the center frequency increases as the pump level increases. Figure 49 shows the noise ratio at the value of τ for which maxium gain occurs, as a function of pump level, and Fig. 50 shows the noise figure in db assuming $T_c = 870^oK$ as a function of pump level for various operating frequencies. From these curves it is evident that the noise increases with the pump level. It should be mentioned that the beam current must be adjusted such that τ_m for various pump levels occurs at the frequency chosen in following the particular curve in Fig. 50.

Figure 51 is a plot of ξ at the values of τ for which maximum gain occurs for various pump levels. It is seen that $\xi(\tau_m)$ decreases sharply at high pump levels and decreases more slowly at low pump levels.

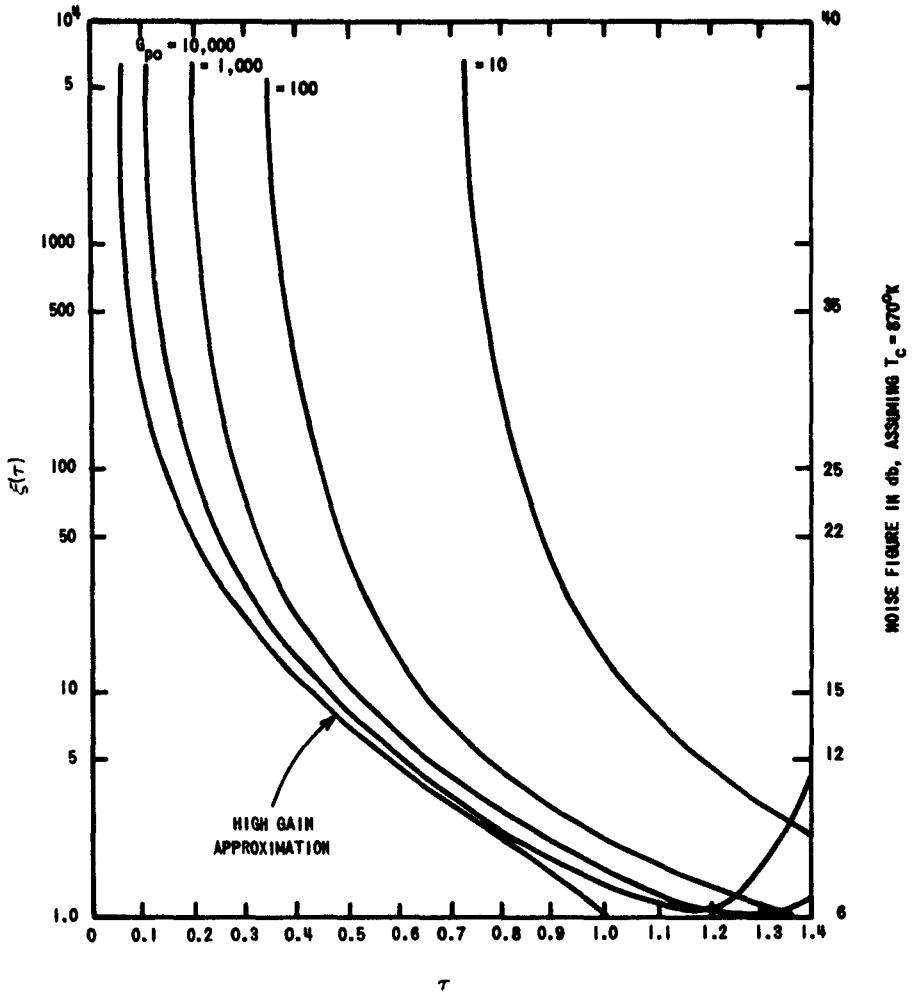

FIG. 48. NOISE CHARACTERISTIC OF VARIOUS PUMP LEVELS AS A FUNCTION OF THE FREQUENCY PARAMETER τ.

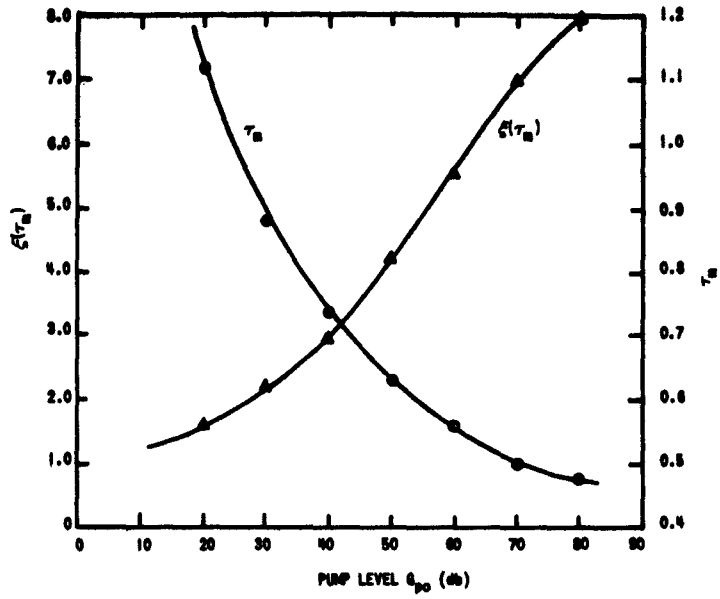

FIG. 49. THE NOISE RATIO ξ AT THE VALUE OF τ WHERE MAXIMUM GAIN OCCURS, AS A FUNCTION OF PUMP LEVEL.

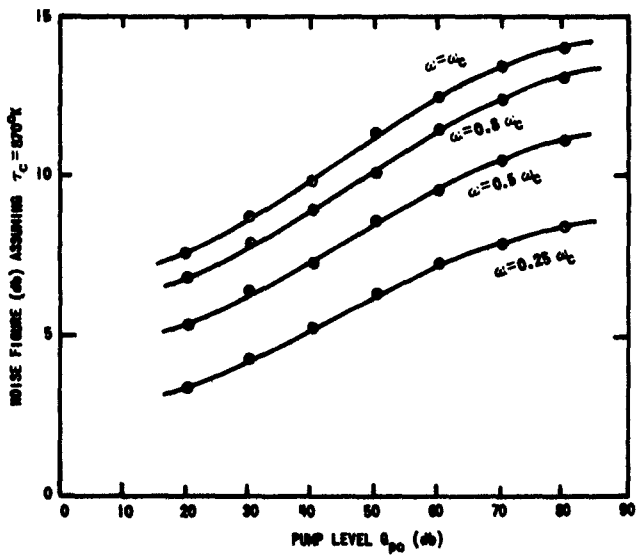

FIG. 50. NOISE FIGURE IN DECIBILS ASSUMING $T_c = 870°K$, AS A FUNCTION OF PUMP LEVEL FOR VARIOUS FREQUENCIES.

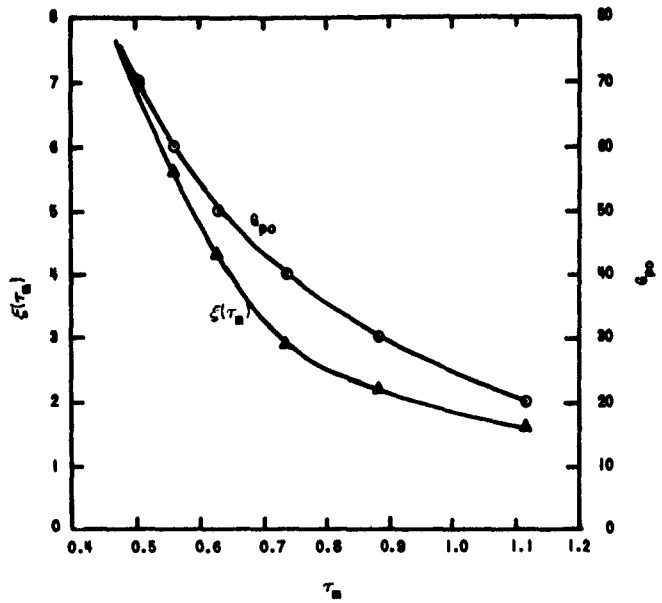

FIG. 51. THE NOISE RATIO ξ AS A FUNCTION OF THE VALUE OF τ AT WHICH THE MAXIMUM GAIN OCCURS.

In order to evaluate the noise dependence on frequency, we can substitute the expression of τ for a hollow beam as shown in Eq. (3.20) into the noise equation. Considering high gain only, so that the approximation equation for high gain can be used, then one has:

$$T_a = \frac{2 - \tau^2}{\tau^2} \frac{\omega}{\omega_c} T_c \tag{3.36}$$

From Eq. (3.20) using the approximation sinc $(\beta_{-1} w/2) \cong 1$, we find

$$T_a = \frac{2V_p^2}{\varphi^2 I_o} - \frac{\omega}{\omega_c} T_c \tag{3.37}$$

It is clear that the noise temperature of the tube decreases linearly as the frequency increases under high gain operation with fixed pump voltage and the beam current. These characteristics are shown in Fig. 52 for various conditions using the cathode temperature as a parameter. The noise figure in decibels as a function of the tube noise temperature is shown in Fig. 53.

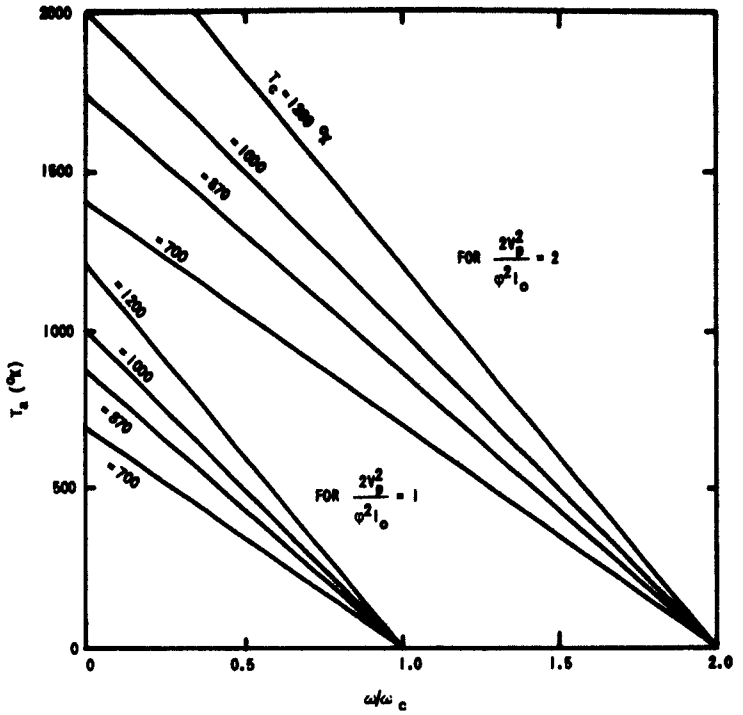

FIG. 52. THE NOISE TEMPERATURE AS A FUNCTION OF FREQUENCY FOR VARIOUS CONDITIONS USING CATHODE TEMPERATURE AS A PARAMETER.

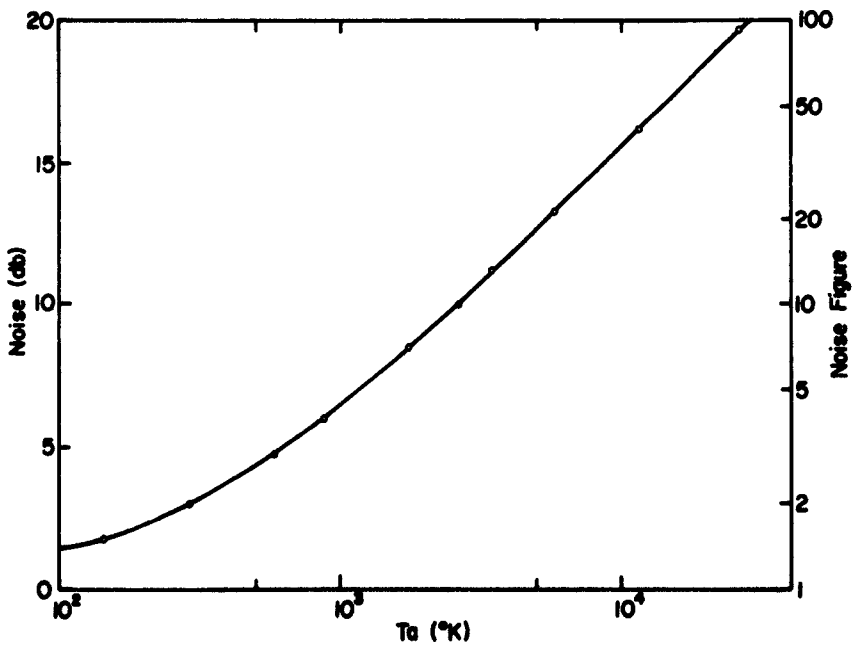

FIG. 53. NOISE IN DECIBELS AS A FUNCTION OF NOISE TEMPERATURE.

The noise figure of this type of amplifier is seen to be comparable with conventional traveling-wave tubes even if no noise-stripping mechanism is used to reduce the beam noise before the amplifying region. In view of the fact that the bandwidth is wider than the traveling-wave tube and that high-frequency and high-power operation is possible, the tube is very promising as a prospective microwave amplifier, particularly if some sort of broadband-beam noise-reduction technique can be developed in the future.

IV. DESIGN CRITERION AND THE CONSTRUCTION OF AN EXPERIMENTAL TUBE

A. DESIGN OF THE QUADRIFILAR HELIX

In designing a helix, there are two important parameters to be specified in order to achieve the proper performance: the pitch p and the diameter a of the helix. Usually one specifies a desired frequency of operation before starting to evaluate the dimensions of the structure. One can also first choose some suitable dimensions for the structure, then calculate the frequency and the performance of the structure. In the present tube we want to design a quadrifilar helix which will operate under simultaneous rf signal coupling and dc field pumping. Therefore we must choose the pitch and diameter of the helix to meet both the coupling condition and the pumping condition derived in Chapter II. After these two dimensions are chosen, one can then decide the material, the dimensions, and shape of the wire for the quadrifilar helix, from a technical point of view.

One must of course require that the pumping coefficient and the coupling coefficient have suitable values, such that a reasonable dc pumping voltage will give enough gain and a reasonable beam current will couple the signal from the circuit into the beam, and vice versa. From these data one can then decide the length of the tube for a specified gain.

From Fig. 27, one notices that the diameter of the helix for cyclotron frequencies below 10 kMc is larger than 1 cm. It is found that the pump coefficient on the helix axis for these large diameters is extremely small for reasonable pumping voltage. For example, for $u_o/c = 0.1$,

f_c (kMc)	a (cm)	k_p (V_p)
10	0.4775	0.815×10^{-4}
5	0.955	0.408×10^{-4}
3	1.59	0.244×10^{-4}
1	4.775	0.815×10^{-5}

This means that for appreciable gain the tube needs extremely high pump voltage or an unreasonable length of tube. However, the pumping coefficient can be improved considerably by using an annular hollow beam and a center conductor inside the helix. The pumping coefficient for the quadrifilar helix with a center conductor is derived in Appendix D as:

$$k_p = A_1 \frac{\sinh 2\beta_c(r_o - b)}{\sinh 2\beta_c(a-b)} \cdot \frac{|V_p|\ \beta_c}{2V_o} \tag{4.1}$$

where A_1 is the magnitude factor for the fundamental mode of the pumping field,

$$A_1 = \frac{4}{p} \int_0^{p/2} \frac{V}{|V_p|} \sin \frac{4\pi}{p} z\, dz \tag{4.2}$$

and a is the radius of the helix

b is the radius of the center conductor

r_o is the average radius of the electron beam

The ratio of the pump coefficient with center conductor to that without is found to be:

$$\Upsilon = A_1 \left(\frac{c}{u_o}\right)^2 \frac{\sinh 2\beta_c(r_o - b)}{\sinh 2\beta_c(a-b)} \tag{4.3}$$

This is called the improvement factor. Since A_1 is close to unity and the ratio of c/u_o is usually more than 10 for nonrelativistic beams, it is possible with the proper design to obtain an improvement of more than two orders of magnitude by adding the center conductor in the quadrifilar helix. The actual factor of merit is therefore the ratio of the hyperbolic sines in Eq. (4.3). This ratio has an upper limit of one if the beam is concentrated in a thin layer just next to the helix. In practice this cannot be done. However, the ratio can be made to lie in the range 0.2 to 0.5 by designing the gap between the helix and the center conductor much smaller than the helix pitch and by keeping the beam as close to the helix as possible, i.e.,

$$a - b \leq \frac{p}{2} \tag{4.4}$$

and

$$r_o \approx a \tag{4.5}$$

For example:

$(a - b) =$	$\frac{p}{2}$	$\frac{p}{2}$	$\frac{p}{4}$	$\frac{p}{4}$
$\frac{r_o - b}{a - b} =$	0.5	0.8	0.5	0.8
$\frac{\sinh 2\beta_c(r_o - b)}{\sinh 2\beta_c(a - b)} =$	0.0407	0.274	0.2	0.534

for:

$\frac{u_o}{c} = 0.1$	then	$\Upsilon =$	4.07	27.4	20	53.4
$\frac{u_o}{c} = 0.0316$		$\Upsilon =$	40.7	274	200	534

Figure 54 shows plots of the ratio of the hyperbolic sines for a quadrifilar helix with center conductor as a function of $(r_o\text{-}b/a\text{-}b)$ with $(a - b)$ as a parameter. This figure shows that one can make the gap between the helix and the center conductor larger provided the spacing between the beam and the helix is made smaller. However, the beam interception on the helix would set a limit for the beam-to-helix spacing. A compromise between the average beam radius r_o and the radius of the center conductor for a given quadrifilar helix results in a reasonable structure with substantial improvement over the helix without center conductor.

When we first designed our experimental tube for this work, the above calculation had not been completed, and we used instead a rough and overly optimistic estimate of the pumping coefficient. As a result, in our experimental tube the ratio of the hyperbolic sine is only 0.005, and the improvement factor is only 3 for $c/u_o = 26.2$. Therefore, the pump coefficient is actually much smaller (more than one order of magnitude less) than our rough, estimated value. Thus, the observed gain with a reasonable pumping strength is low in our experimental results, which we will describe later.

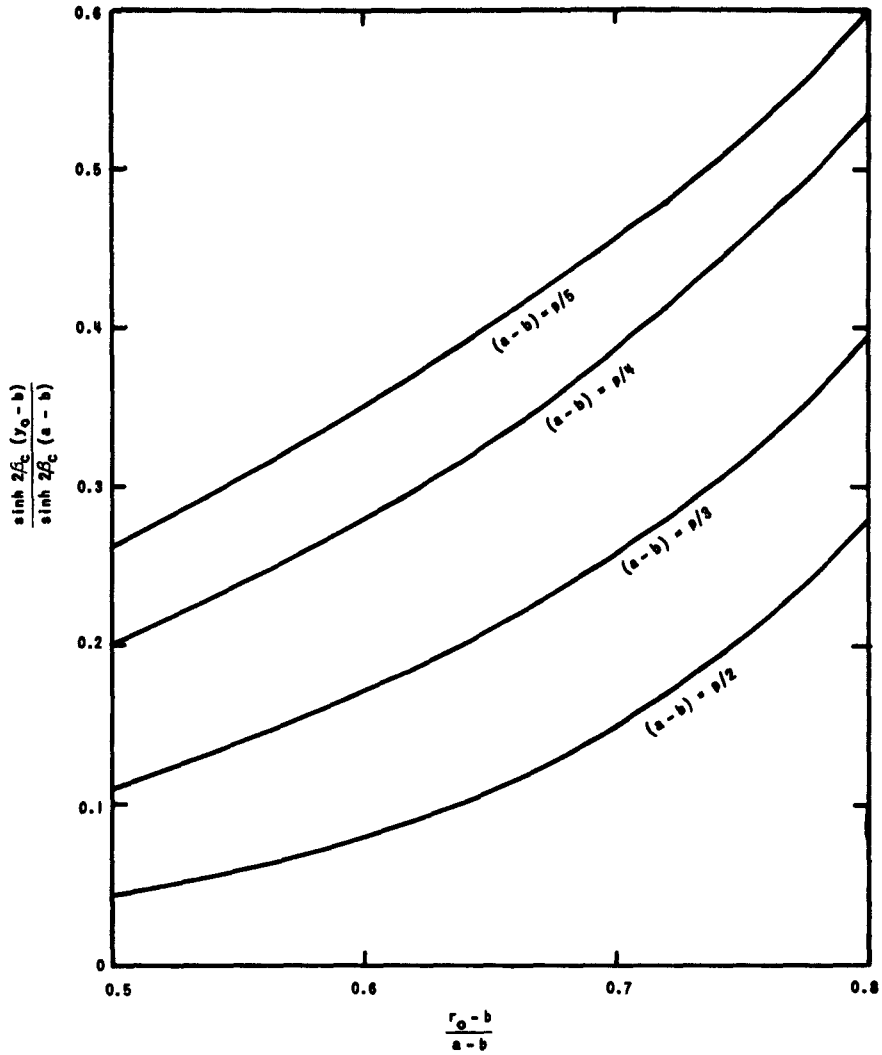

FIG. 54. THE RATIO $\frac{\sinh 2\beta_c (r_o - b)}{\sinh 2\beta_c (a - b)}$ OF A QUADRIFILAR HELIX AS A FUNCTION OF $(r_o - b)/(a - b)$ WITH $(a - b)$ AS A PARAMETER.

Three design procedures are outlined in the following paragraphs. The first and second procedures emphasize the convenience of construction and testing of the tube. The third one emphasizes the optimum design based upon the technical limit of construction.

1. Design Procedure I

In this procedure, the magnetic field and the beam voltage are first specified, from which the dimensions of the quadrifilar helix will be calculated.

1. Specify the magnetic field and the beam voltage intended to be used in the tube.
2. From the nomograph shown in Fig. 21, find the cyclotron frequency corresponding to the magnetic field. This frequency is roughly the center frequency of the operating band.
3. On the same nomograph, find the beam velocity corresponding to the beam voltage.
4. Connect the points corresponding to the magnetic field and the beam voltage in the nomograph; the intersection of this line with the pitch scale gives the pitch of the helix.
5. Find the radius of the helix corresponding to the cyclotron frequency from Fig. 27.
6. Choose either round wire or flat-tape wire to wind the helix.
7. Choose a suitable size of wire. The best choice whould be:

   w = the wire width or diameter = 1/6 p

   g = the gap between adjacent helices = 1/12 p

   This choice provides no third-space harmonic of the pumping field, and the magnitude factor of the fundamental mode is $A_1 = 1.102$. Other choices will give A_1 less than one and also provide some third-space harmonics.
8. Calculate the pumping coefficient for the helix without center conductor. If it is too small, then continue by designing a proper center conductor and using a hollow beam.
9. From Fig. 54, choose suitable radii for the center conductor and the electron beam to obtain a large improvement factor and also provide enough space for the beam to pass through without interception on the helix. Calculate the pump coefficient per volt of dc pumping voltage.
10. Specify the db gain desired for the circuit wave, then from Figs. 38 or 39 find the suitable pump parameter G_{po} and the corresponding frequency parameter τ.

11. Choose a suitable maximum pumping voltage and from Fig. 40, find the value of k_pL corresponding to the G_{pp} found in step 10. Then calculate the required length L of the helix. If the length is too long (beam spread due to space-charge force will be serious) or too short (beam spread due to dc pumping will be serious for high gain), pick a different maximum pumping voltage and determine the new L.

12. Choose a reasonable thickness for the beam and calculate the available beam area, then find the current at Brillouin flow corresponding to the specified magnetic field. Figure 55 is a set of nomographs for the current density and the current of a flat or thin hollow beam under Brillouin condition. This can be conveniently used in the design.

13. From the value of τ found in step 10, calculate the coupling coefficient required. The coupling coefficient at the cyclotron frequency of a hollow beam in the quadrifilar helix with center conductor is found by substituting the transverse impedance of Eq. (3.26) into Eq. (3.4) as follows:

$$k_-\Big|_{\text{at } \omega_c} = \sqrt{\frac{120\,\pi\, w\, I_o}{(a-b)\, p^2\, V_o}} \tag{4.6}$$

Substitute the coupling coefficient just found into the above equation, from which the required beam current can be determined.

14. Compare the necessary beam current found in step 13 with the current under Brillouin flow.

    a. If they are about the same magnitude, then a Brillouin flow gun should be used in order to have good focusing of the beam.

    b. If the necessary beam current is much smaller than the current under Brillouin flow, then an immersed Pierce gun can be used.

15. Design an electron that will provide the electron beam with proper thickness, designed average radius, required beam voltage, and enough beam current as specified in previous steps (details of gun design will be discussed later). For testing purposes it is convenient to have a variable perveance gun in which one can change the beam current without changing the beam voltage.

2. <u>Design Procedure II</u>

In this procedure, the cyclotron frequency and the slowing factor u_o/c are first specified, then the pitch and the radius of the helix as well as other dimensions are determined.

1. Specify the cyclotron frequency and the slowing factor.

2. From the nomograph of Fig. 21, find the magnetic field B corresponding to the specified cyclotron frequency; and be sure that this field strength is readily available. Otherwise, re-specify the cyclotron frequency in step 1.

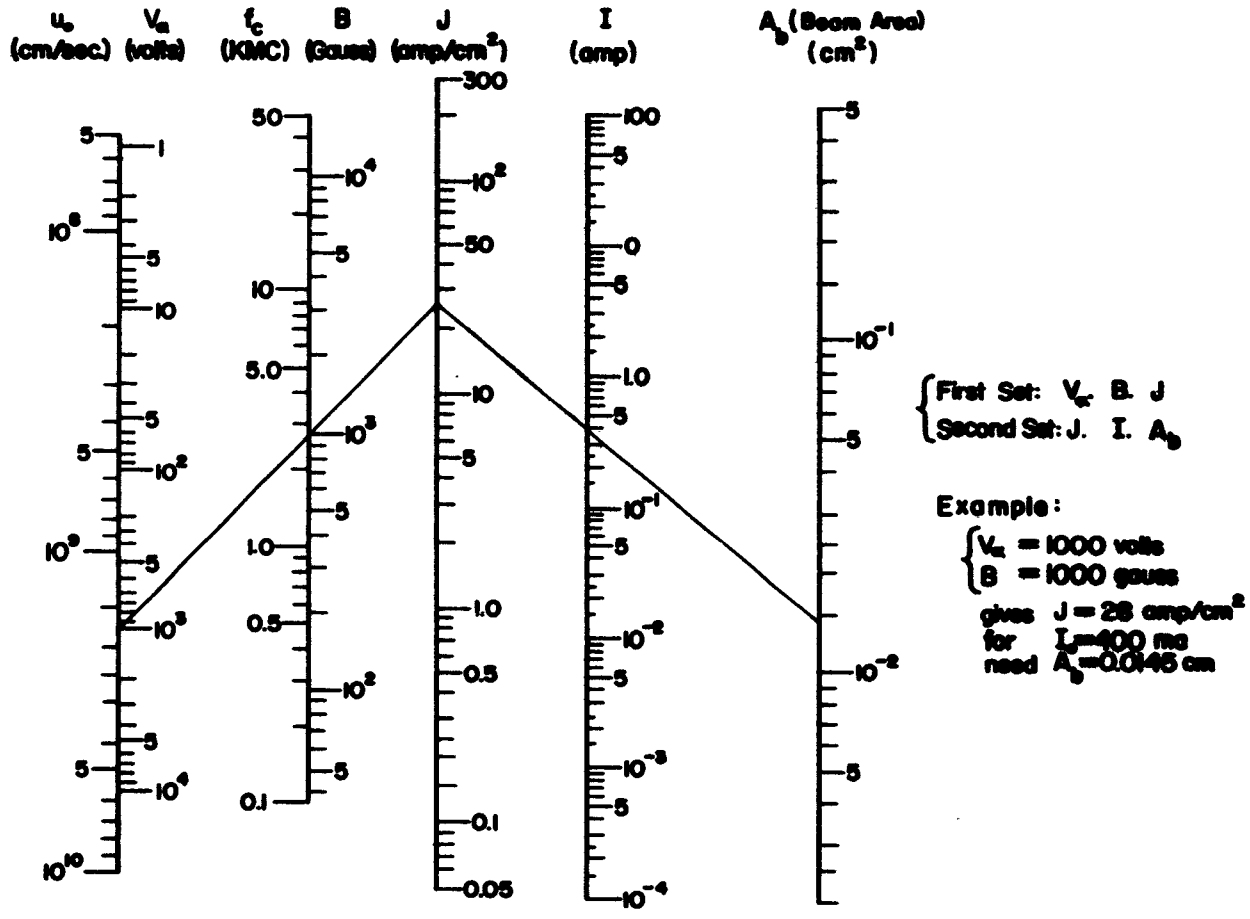

FIG. 55. THE CURRENT DENSITY AND THE CURRENT LIMIT UNDER BRILLOUIN CONDITION FOR FLAT BEAM.

3. On the same nomograph, find the beam voltage corresponding to the slowing factor.
4. Connect the points corresponding to the cyclotron frequency and the slowing factor in the nomograph. The intersection of this line with the p scale gives the pitch of the helix.
5. From Fig. 26 find the radius of the helix corresponding to the magnetic field.

6 to 15. Use the same steps as those in Procedure I.

3. Design Procedure III

In this procedure, the operating frequency is first specified, and the helix pitch then chosen equal to the smallest limit that seems reasonable from a construction point of view. Then the other parameters are calculated and/or specified. Therefore following this procedure, an optimum design is obtained.

1. From Fig. 27, find the radius of the helix by taking the operating frequency equal to some fraction, say 50 percent, of the cyclotron frequency.
2. Choose the minimum pitch that seems reasonable based on fabrication considerations.
3. Calculate the slowing factor of the beam under the pumping condition, or find this directly in the nomograph shown in Fig. 21 at the intersecting points of the slowing-factor line and the line connecting the pitch and the cyclotron frequency already specified.
4. Obtain the beam voltage at the same point.
5. Record the magnetic field corresponding to the cyclotron frequency as shown in the same nomograph.

6 to 15. Follow the same steps as those in Procedure I.

4. Sample of Helix Design; Following Design Procedure I

1. Specify $B = 1340$ gauss and $V_o = 375$ v.
2. From the nomograph shown in Fig. 56, which is the same as Fig. 21, $f_c = 3750$ Mc.
3. From the same nomograph $u_o = 1.1 \times 10^9$ cm/sec and $u_o/c = 1/26.2$.
4. Following the active pumping line determined by the magnetic field and the beam voltage, the pitch should be $p = 0.305$ cm $= 0.120$ in.
5. From Fig. 27, $a = 1.27$ cm $= 0.5$ in.
6. Flat-tape wire will be used because of large radius and small pitch of the helix.
7. Choose $w = 0.020$ in., $g = 0.010$ in, then $A_1 = 1.102$.
8. The pump coefficient of the helix without center conductor is found from Eq. (3.5), $k_p = 5 \times 10^{-5} V_p$, which is too small.

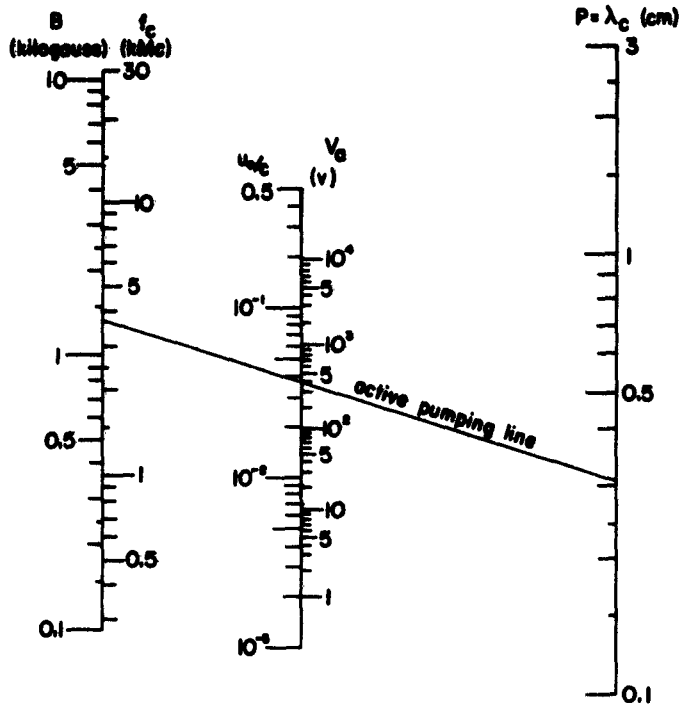

FIG. 56. THE NOMOGRAPH FOR HELIX DESIGN.

9. From Fig. 54, choose $a - b = p/4 = 0.030$ in., so $b = 0.470$ in. and $(r_o - b)/(a - b) = 0.78$, so $r_o = 0.4934$ in. Then the improving factor is, from Eq. (4.3), $\Upsilon = 1.102 \cdot (26.2)^2 \cdot 0.5 = 359$. Therefore, the pumping coefficient with center conductor is $k_p = 1.795 \times 10^{-2}\ V_p$. This is more than enough, because for a helix 10 cm long we need only about 100 v pump voltage to bring $k_pL > 10$. On the other hand, the average beam radius has only a clearance of 0.0066 in. from the helix. It seems advisable, therefore, to have more clearance in exchange for a smaller pump coefficient. So, take $(r_o - b)/(a - b) = 0.565$; $r_o = 0.487$ in. This gives 0.013-in. clearance from the helix. From Eq. (4.3) the improvement factor is now $\Upsilon = 1.102\ (26.1)^2 \cdot 0.25 = 180$. The pumping coefficient with center conductor would be $k_p = 0.9 \times 10^{-2}\ V_p\ cm^{-1}$ which is just about right.

10. Say $G_{db} = 33.3$ db is desired; then from Fig. 39, $G_{po} = 50$ db and $\tau = 0.6$.

11. From Fig. 40, k_pL is found to be 6.45, corresponding to $G_{po} = 50$ db. Say 300 v is the maximum pump voltage. Then from the pump coefficient found in step 9 we have $k_pL = 6.45 = 0.9 \times 10^{-2} \times 300\ L$. Hence, the necessary length of the helix is $L = 2.385$ cm and $L/\lambda_c = N = 7.85$ wavelength. This seems to be small. Try to specify 100 v pumping, then $L = 7.155$ cm $= 2.82$ in., and $N = 23.55$ wavelength.

12. From Fig. 55, the Brillouin current density is $J = 31$ amp/cm^2. Choose the thickness of the beam as $t = 0.010$ in.; then the beam area is $A = 2\pi r_o t = 0.0306$ in.$^2 = 0.19$ cm^2. The current under the Brillouin limit is $I_o = JA = 5.9$ amp.

13. Since $\tau = 0.6$, $k_- = \tau k_p = 0.6 \times 0.9 \times 10^{-2} \times 100 = 0.54$. From Eq. (4.6)

$$k_- = \sqrt{\frac{120\ \pi \times 0.020\ I_o}{0.030 \times (0.305)^2 \times 375}} = 2.68\ \sqrt{I_o}$$

Hence, the required I_o is

$$I_o = \left(\frac{0.54}{2.68}\right)^2 = 0.0405 \text{ amp} = 40.5 \text{ ma}$$

14. The necessary beam current found in step 13 is less than one percent of the Brillouin flow current, so an immersed Pierce gun can be conveniently used.

15. Design a Pierce gun that will deliver a thin hollow beam of 40.5 ma at 375 v with an average beam radius of 0.487 in. and a beam thickness of 0.010 in.

16. Summary of the Design:

$B = 1340$ gauss	$V_o = 375$ v
$f_c = 3750$ Mc	$c/u_o = 26.2$
$p = 0.12$ in.	$w = 0.020$ in.
$a = 0.5$ in.	$g = 0.010$ in.
$b = 0.470$ in.	$r_o = 0.487$ in.
$t = 0.010$ in.	$L = 2.82$ in.
$k_p = 0.9 \times 10^{-2}\ V_p$ cm^{-1}	$k_- = 2.68\ \sqrt{I_o}$ cm^{-1} at $f = f_c$
$I_o = 40.5$ ma	Beam power = 15.4 w

Expect about 33-db gain at cyclotron frequency with 100 v pumping.

B. DESIGN OF THE ELECTRON GUN

A two-anode gun which gives a confined-flow flat beam will be considered, since the thin hollow beam can be approximated by a flat beam. The design of the gun follows closely the analysis presented by Dunn and Luebke [Ref. 45] with slight modifications to suit present requirements. The cancellation of the lens effects at the gun apertures for the case of parallel flow beam with planar symmetry was first studied

by Pierce [Ref. 46]. He has shown that the lens effect of two anodes can be cancelled perfectly by arranging the transverse actions produced at the two anodes so that they are the same both in magnitude and in phase, but with the induced transverse velocity on the electrons in opposite direction at the two anodes because the transit time between the electrodes is one half-cyclotron wavelength. King [Ref. 47] has extended this analysis to the case of a full cyclotron wavelength between the two electrodes and with the transverse actions produced at the two anodes equal in magnitude but opposite in phase. Dunn and Luebke have generalized the principle to further include the cases of electron transits of any multiple of a half cyclotron period between the two anodes, with emphasis on the advantage of variable voltage guns.

In the present application, we need a beam in synchronism with the circuit such that the fast cyclotron wave is coupled to the -1 mode helix wave. Therefore, we want a constant voltage beam with suitable beam currents, and it is obvious that the scheme of the two-anode gun is well suited for this purpose because one can obtain a set of fixed parameters that provide perfect cancellation of the lens effect at normal operation. Also for testing purposes, the beam current can be varied by slightly changing the voltage on the first anode, while maintaining constant beam voltage. In other words, the gun can be operated as a variable perveance gun with constant beam voltage.

Figure 57 shows the dimensions and symbols used in designing the electron gun, where:

d_1 = the distance between the first anode and the cathode
d_2 = the distance between the second anode and the first anode
V_f = the voltage on the focusing electrode with respect to the cathode
V_1 = the voltage on the first anode with respect to the cathode
V_2 = the voltage on the second anode with respect to the cathode

Following the analysis of Dunn and Luebke, the following two equations should be satisfied in order to have perfect cancellation of the lens effect at the two anodes:

$$0.943 \frac{n(B/B_1)}{\sqrt{\rho}+1} = m\pi \tag{4.7}$$

and

$$\frac{\rho-1}{n}\left[1-(-1)^m \frac{1}{\sqrt{\rho}}\right] = \frac{4}{3} \tag{4.8}$$

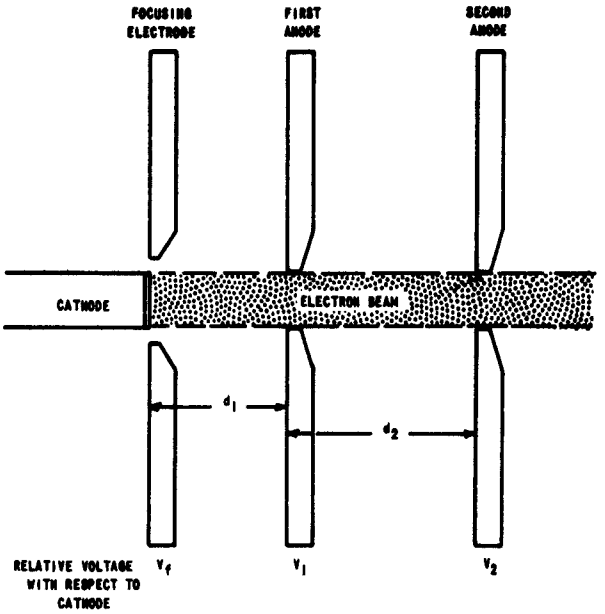

FIG. 57. THE TWO-ANODE CONFINED-FLOW STRIP BEAM GUN.

where m = the number of half cyclotron wavelengths of the distance between the first and second anodes

$n = d_2/d_1$

$\rho = V_2/V_1$

B_1 = the Brillouin magnetic field at V_1

B = the actual magnetic field used

In the present problem, we have to start with fixed voltage on the second anode and fixed beam current, obtained from the design data for the helix and the beam. Therefore Eqs. (4.7) and (4.8) can be modified to suit present design convenience by using the Brillouin magnetic field at V_2, and writing

1. m = even:

$$(B/B_2) = \frac{4.45\ m\ \rho^{3/4}}{(\sqrt{\rho} - 1)^2} \tag{4.9}$$

$$n = \frac{3}{4}\ \frac{(\sqrt{\rho} - 1)^2\ (\sqrt{\rho} + 1)}{\sqrt{\rho}} \tag{4.10}$$

2. m = odd:

$$(B/B_2) = \frac{4.45\ m\ \rho^{3/4}}{\rho - 1} \tag{4.11}$$

$$n = \frac{3}{4}\ \frac{(\sqrt{\rho} - 1)\ (\sqrt{\rho} + 1)^2}{\sqrt{\rho}} \tag{4.12}$$

where B_2 is the Brillouin magnetic field at V_2.

Figure 58 is a plot of Eqs. (4.9) to (4.12) for positive values of n, which will be useful in designing the electron gun. The design procedure is:

1. Record the beam voltage and the beam current specified in the helix and beam design.
2. Calculate the perveance of a confined-flow gun and the perveance per square P_o for the hollow beam. From practical considerations, P_o is limited to less than 0.4 $\mu a/v^{3/2}$. Otherwise, a confined flow gun cannot be used to provide the current.
3. Let the voltage on the second anode be the beam voltage, and calculate the actual current density in the beam, or find it from the nomograph shown in Fig. 55.
4. Calculate the Brillouin magnetic field at the beam voltage for a strip beam according to the following equation:

$$B_2^2 = \frac{J}{\sqrt{2}\ \epsilon\ \eta^{3/2}\ \sqrt{V_2}} \tag{4.13}$$

   where J is the current density. Or, find the Brillouin magnetic field for the strip beam from the nomograph shown in Fig. 55.
5. Calculate the ratio of the magnetic field that is actually used to that for the Brillouin flow at beam voltage.
6. From Fig. 57 find the solution of ρ, the ratio of the voltage at the second anode to that at the first anode, corresponding to the number of half cyclotron wavelengths between the two anodes.
7. Calculate the voltage of the first anode corresponding to the solution of ρ found in the previous step.
8. Determine the distance between the first anode and the cathode by Child's Law:

$$J = \frac{4\sqrt{2}}{9}\ \epsilon\ \frac{\eta^{1/2}\ V_1^{3/2}}{d_1^2}$$

   or use the nomograph shown in Fig. 59.

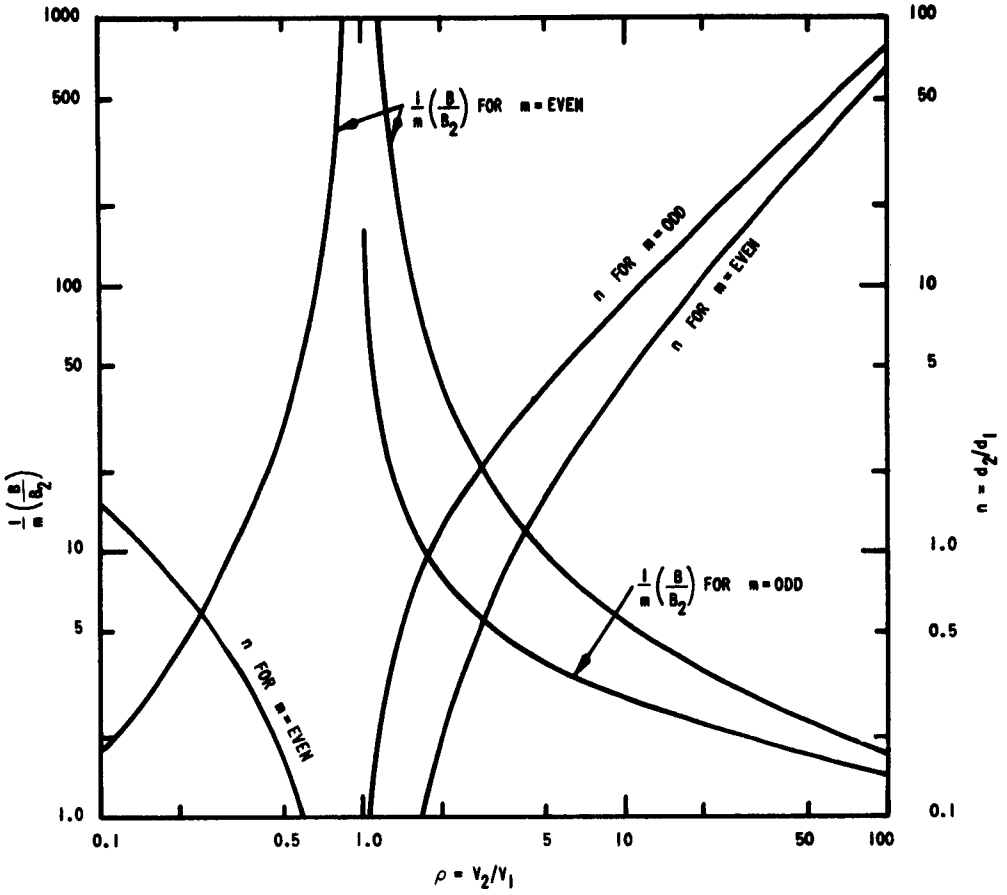

FIG. 58. THE CURVES SHOWING THE CONDITION FOR PERFECT CANCELLATION OF THE LENS EFFECT AT THE TWO ANODES.

9. Calculate the ratio $n = d_2/d_1$ from Eq. (4.10) or (4.12), or find the plot in Fig. 57, for the ρ found in step 6.
10. Calculate the distance d_2 between the first and the second anodes corresponding to the specified d_1 and n found in steps 8 and 9.

A sample gun design is:

1. From the helix and the beam design $V_2 = V_o = 375$ v and $I_o = 40.5$ ma.

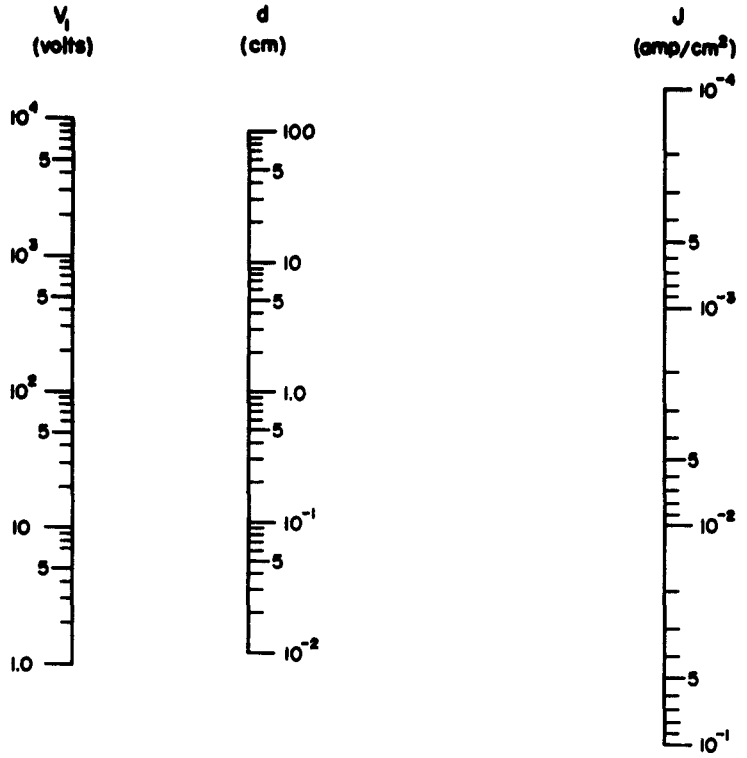

FIG. 59. NOMOGRAPH OF CHILDS LAW.

2. Let:

$$\text{Perveance} = \frac{I_o}{V_o^{3/2}} = 5.57\ \mu a/v^{3/2}$$

$$\left.\begin{array}{l}\text{No. of squares along}\\ \text{the circumference of}\\ \text{the hollow beam}\end{array}\right\} = \frac{2\pi a}{t} = 314$$

Hence $P_o = 0.0177\ \mu a/v^{3/2}$ which is less than one-tenth of the technical limit, $0.2\ \mu a/v^{3/2}$.

3. The beam area is $A_b = 2\pi at = 0.202\ cm^2$. So the current density is $J = 0.2\ amp/cm^2$.
4. From Fig. 55, $B_2 = 110$ gauss.
5. Hence $B/B_2 = 1340/110 = 12.2$.

6. From Fig. 57, the value of ρ is:

$\rho = 1.5$	for	$m = 1$
$\rho = 0.29$ or 8.6		$m = 2$
$\rho = 4.3$		$m = 3$
$\rho = 0.16$ or 26.5		$m = 2$

7. Now, $V_1 = V_2/\rho$, so:

$V_1 = 250$ v	for	$m = 1$
$V_1 = 1290$ v or 43.6 v		$m = 2$
$V_1 = 87.2$ v		$m = 3$
$V_1 = 2340$ v or 14.15 v		$m = 4$

8. From Fig. 58, we find

$d_1 = 0.215$ cm $= 0.0845$ in.	for	$m = 1$
$d_1 = 0.735$ cm $= 0.0232$ in.		$m = 2$
or		
$= 0.059$ cm $= 0.0232$ in. (too small)		
$d_1 = 0.098$ cm $= 0.0385$ in.		$m = 3$
$d_1 = 1.152$ cm $= 0.454$ in.		$m = 4$
or		
$= 0.025$ cm $= 0.0098$ in. (too small)		

9. From Fig. 55, the ratio $n = d_2/d_1$ is found to be

$n = 0.67$	for	$m = 1$
$n = 0.46$ or 3.3		$m = 2$
$n = 3.5$		$m = 3$
$n = 0.96$ or 15		$m = 4$

10. The distance d_2 is found as follows:

$d_2 = 0.0566$ in.	for	$m = 1$
$d_2 = 0.133$ in. or 0.0765 in.		$m = 2$
$d_2 = 0.135$ in.		$m = 3$
$d_2 = 0.435$ in. or 0.147 in.		$m = 4$

11. Summary:

	m = 1	m = 2		m = 3	m = 4	
Design No.	1	2	3	4	5	6
V_1 (v)	250	1290	43.6	87.2	2340	14.15
d_1 (in.)	0.0845	0.29	0.0232	0.0385	0.0454	0.0098
d_2 (in.)	0.0566	0.133	0.0765	0.135	0.435	0.147

In this design, the d_1 in No. 3 and No. 6 are too small to be constructed; and V_1 in No. 5 is too high in practice, since V_2 is only 375 v. Designs No. 1, No. 2, and No. 4 are acceptable. Each has its own advantages and disadvantages. The actual choice can be based on other considerations. For easy construction, it would be wise to choose No. 2 because of its large spacing; but it requires about three times higher voltage on the first anode than the voltage on the second anode, which is the beam voltage. Design No. 1 is good as far as construction and tube operation are concerned, but the cancellation of the lens effect is very sensitive to the anode voltages since n is small [Ref. 45]. Design No. 3 appears to be the optimum design which is within techniques for careful construction and which operates at a low voltage at the first anode. It also has a larger value of n, i.e., the spacing between the first and the second anodes is considerably larger than that between the cathode and the first anode. This fact provides a wider usable voltage range; therefore, control of the beam current by the first anode operating as a constant-voltage variable-perveance gun is more effective.

C. CONSTRUCTION OF AN EXPERIMENTAL TUBE

The design parameters for the experimental tube we constructed were:

B = 1340 gauss	V_o = 375 v
f_c = 3650 Mc	c/u_o = 26.2
p = 0.120 in.	w = 0.010 in.
a = 0.500 in.	g = 0.020 in.
b = 0.400 in.	r_o = 0.450 in.
t = 0.025 in.	L = 5.5 in.
I_o = 100 ma	Beam power = 37.5 w

The magnitude factor for the fundamental mode is:

$$A_1 = \frac{2}{\pi} = 0.636$$

The ratio of the hyperbolic sine (or figure of merit) is:

$$\frac{\sinh 2\beta_c\ (r_o - b)}{\sinh 2\beta_c\ (a-b)} = 0.006$$

The improvement factor due to the addition of the center conductor calculated from Eq. (4.3) is:

$$\Upsilon = 0.636 \times (26.2)^2 \times 0.006 = 2.52$$

This improvement factor is quite small, especially in comparison with that of the sample helix design in Sec. A of this chapter. Our design for the experimental tube is evidently not a good design for amplification, due to our early erroneous estimate of pumping strength.

Figure 60 shows the constructed quadrifilar helix. Four sapphire rods are used to support the helix and maintain its proper pitch and diameter. Tungsten tapes of 0.005-in. thickness and 0.010-in. width were used to form the helix. In constructing this fine tape helix having a large radius, difficulties arose from the large internal bending stresses which demanded considerable binding strength to hold the helix in its designed shape. We at first attempted to glaze the supporting rods to the helix, but it was found that the glaze material was not strong enough to overcome the internal bending stress of the wound helix. Several other materials were tried and also ended with failure. Finally, the rods were brazed to the helix by a thin brazing strip, and the excess conducting braze material between adjacent helices after firing was removed with a fine sharp knife. This involved much work but was very successful.

The hollow-beam electron gun was designed with the following data:

$$m = 3 \qquad \rho = 4.3 \qquad n = 3.62$$

$$V_1 = 87\ v \qquad d_1 = 0.037\ \text{in.} \qquad d_2 = 0.134\ \text{in.}$$

A spacing of three half-wavelengths between the first and second anodes was chosen to lower the first anode voltage. Since the thickness of the beam is only 0.025 in. compared with the hollow-beam mean radius

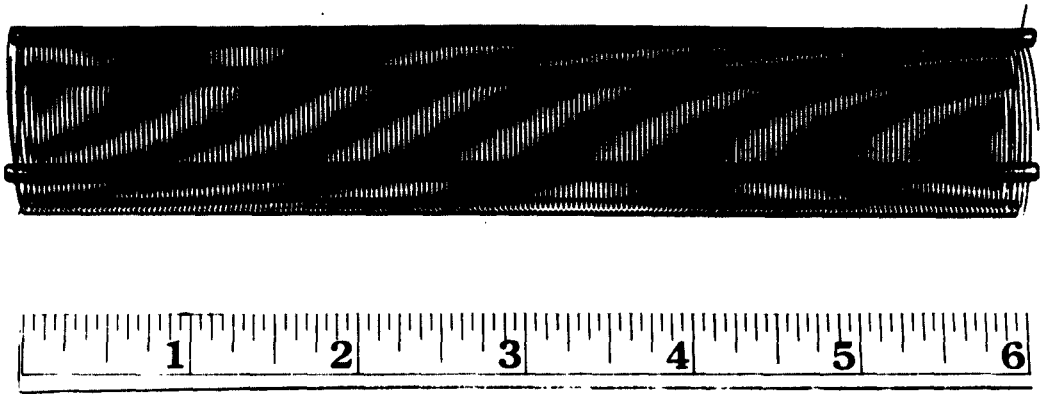

FIG. 60. THE QUADRIFILAR HELIX SUPPORTED BY FOUR SAPPHIRE RODS.

of 0.450 in., the planar beam approximation used in the design theory is justifiable. As shown in Fig. 61, a drift section is provided between the second anode and the quadrifilar helix. A supporting tube is also provided in order to support the center conducting cylinder inside the quadrifilar helix. The complete experimental tube is shown in Fig. 62.

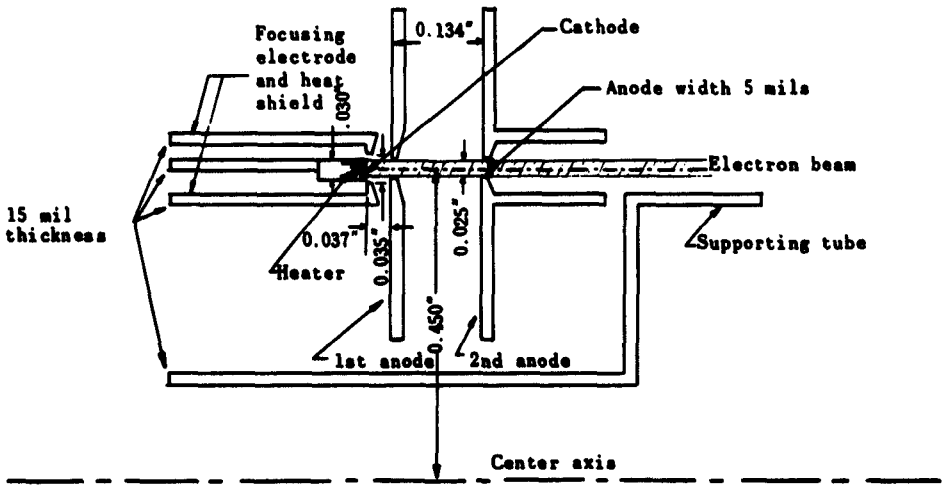

FIG. 61. HOLLOW-BEAM GUN FOR THE QUADRIFILAR DC-PUMPED TRAVELING-WAVE TUBE WITH BEAM CURRENT 100 MA AND ACCELERATING VOLTAGE 375 V.

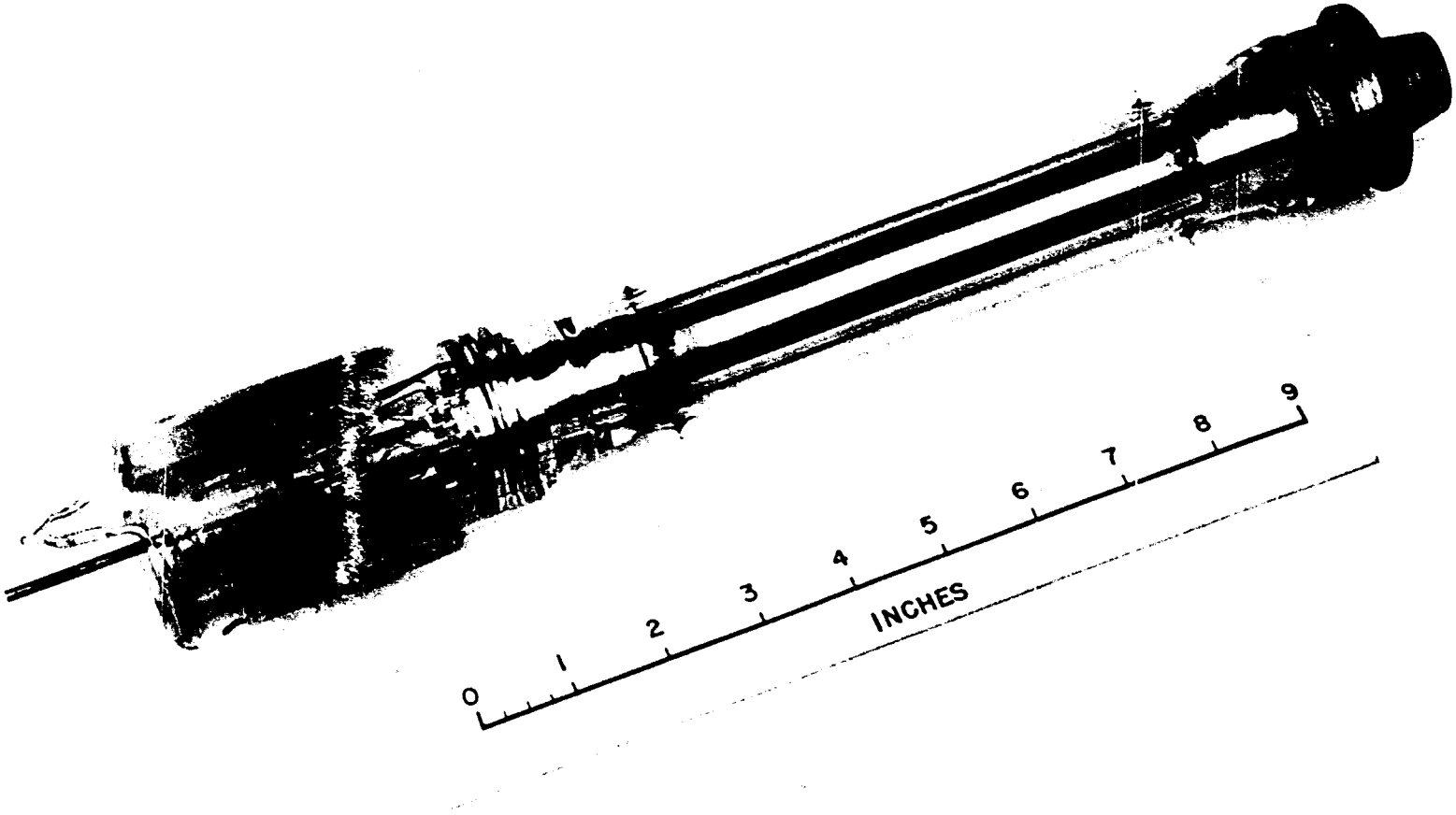

FIG. 62. THE ACTUAL EXPERIMENTAL TUBE.

The pumping coefficient and the coupling coefficient of this constructed experimental tube can be calculated from Eqs. (4.1) and (4.6) as follows:

$$k_p = 1.36 \times 10^{-4}\ V_p\ cm^{-1}$$

$$k_- = 1.04 \sqrt{I_o}\ cm^{-1} \qquad \text{at} \qquad f = f_c$$

The coupling coefficient will give the value k_-L close to $3(\pi/2)$ for $I_o = 100$ ma at the cyclotron frequency, and is in the favorable operating range as discussed in Chapter III. The pumping coefficient is, unfortunately, one order of magnitude smaller than the rough estimation originally used in specifying the dimensions for the tube construction before the detailed design theory was completed. Therefore, the gain is much smaller than the original design value for the same pumping voltage. This small pumping coefficient per volt is a direct result of the large gap between the helix and the center conducting cylinder which gives essentially no improvement upon the quadrifilar helix. It would require more than 10,000 v pump voltage to make the pumping coefficient comparable with the coupling coefficient. It is apparent that the helix cannot support this high pumping voltage because of arcing. However, it is still possible to study the operation of our tube at low pumping level to check the theory, which is the main purpose for this experimental tube. Considerable information on the operation of the tube can actually be obtained at low pumping levels. In fact, experiments at low pump levels, if carefully carried out, are a more stringent test of theory than experiments at high pump levels. This is because high-pump-level high-gain experiments depend only on the one growing wave of the system; whereas low-pump-level low-gain experiments depend on the (rather complicated) interaction of all the waves in the system. Other valuable information which can be obtained includes:

1. The transverse interaction impedance
2. The coupling coefficient as a function of the beam current and the signal frequency
3. The abrupt output pattern change before and after the Kompfner Dip coupling strength as predicted in Chapter III
4. The interaction of the various circuit modes and the different beam waves

5. Tests of other possible operations using simultaneous coupling and pumping, for example involving synchronous waves instead of one of the cyclotron waves.

The observed results from our experiments will be presented in the next chapter. In general, they do confirm the predictions of the theory, and in particular, they do verify the wide bandwidth of this amplifier.

V. EXPERIMENTAL RESULTS AND INTERPRETATION

A. COLD TESTS ON THE HELIX

The quadrifilar helix with center conductor was tested before it was assembled with the gun. The excitation of various modes on the helix was tested, and the -1 mode forbidden gap and its fast wave radiation were observed. The impedance matching to the input and output circuits was found to be acceptable, although readjustment of the matching structure at each frequency was necessary for best results. The attenuation through the helix due to ohmic and dielectric loss was also measured, and found to be acceptable. The propagation characteristics were measured by setting up a standing wave pattern on the helix and measuring the wave fields by a probe outside the helix, thereby yielding β as a function of frequency.

1. Mode Excitation on the Quadrifilar Helix

In order to excite the proper mode on the quadrifilar helix, we have to divide the signal into four branches with equal magnitudes and proper phases. A double-ridged waveguide is found useful to divide the signal equally into two branches with phase difference of 180 deg. Figure 63 is a sketch of this arrangement. The TE_{10} mode was excited

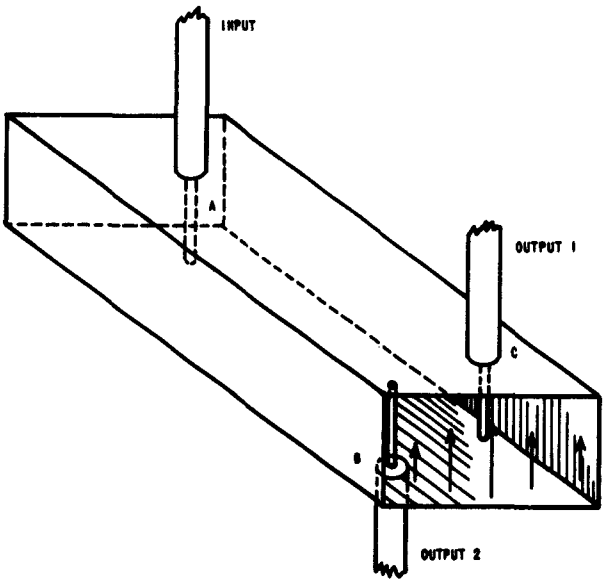

FIG. 63. WAVEGUIDE BALUN FOR DIVIDING THE SIGNAL INTO TWO BRANCHES WITH EQUAL MAGNITUDE BUT OPPOSITE PHASE.

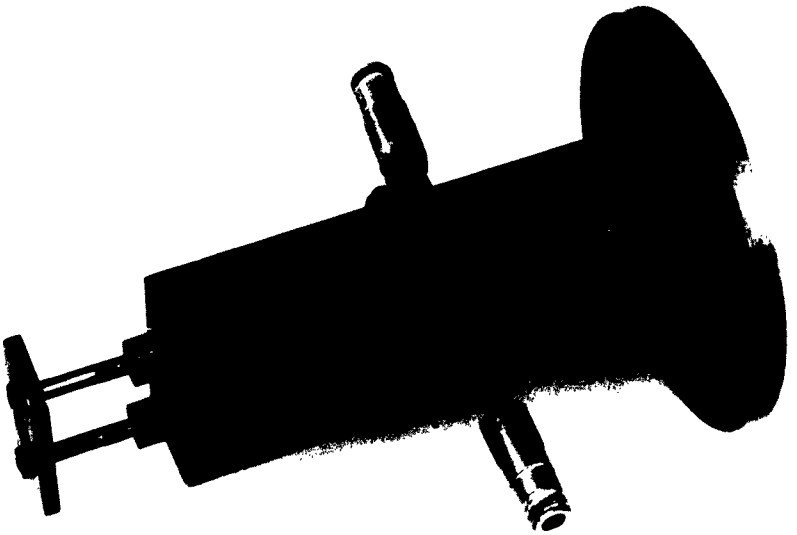

a. Exterior view

b. Interior view

FIG. 64. THE EXTERIOR AND THE INTERIOR OF THE DOUBLE-RIDGED WAVEGUIDE.

in a waveguide by a single probe shown at A. The electric field of this mode is symmetric to the center plane; therefore a pair of coaxial probes placed symmetrical to the center plane but on opposite sides couple out equal magnitudes of the field with opposite phases. The use of a double-ridged structure provides better efficiency and matching than an ordinary rectangular waveguide. Figure 64 is a photograph of the exterior and the interior of the double-ridged waveguide structure. A movable short circuit at the end is built in to adjust for best matching. Further signal division and phase shift is achieved by using 3-db directional couplers (Narda Model No. 3033). These are used to divide the S-band signal into two branches with equal magnitudes and 90-deg phase difference. Therefore, with one double-ridged waveguide and two directional couplers we can divide the signal into four branches with equal magnitudes and 90-deg phase lagging (or leading) successively as shown in Fig. 65. The actual assembly of this power divider is shown in Fig. 66. This assembly can be used either as input circuit or as output circuit.

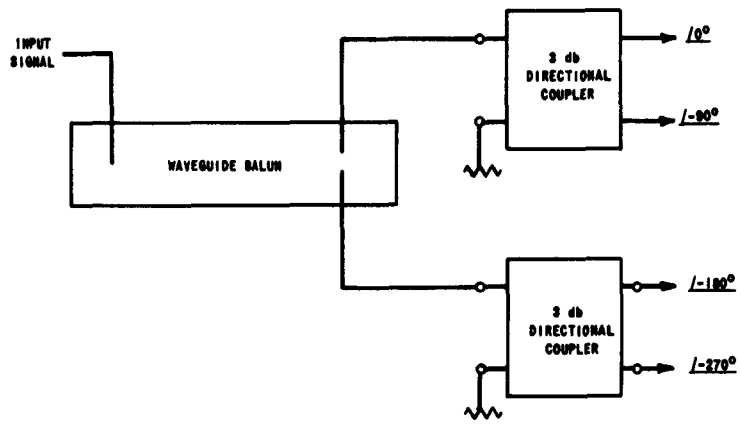

FIG. 65. THE ARRANGEMENT FOR EQUAL POWER DIVISION INTO FOUR SUCCESSIVE BRANCHES WITH 90 DEG PHASE DIFFERENCE.

The two waveguide assemblies used in the input and the output circuits were tested, and their power divisions and phase differences measured as functions of frequency, as shown in Figs. 67 and 68. Their power ratios deviate less than 1 percent from unity and their phase difference deviate less than 2 deg from 180 deg over the desired bandwidth. These results show that they are functioning satisfactorily. The Narda 3-db hybrid couplers give power ratios less than 3 percent off from unity and phase differences less than 1 deg from 90 deg over 2 to 4 kMc. They are also acceptable.

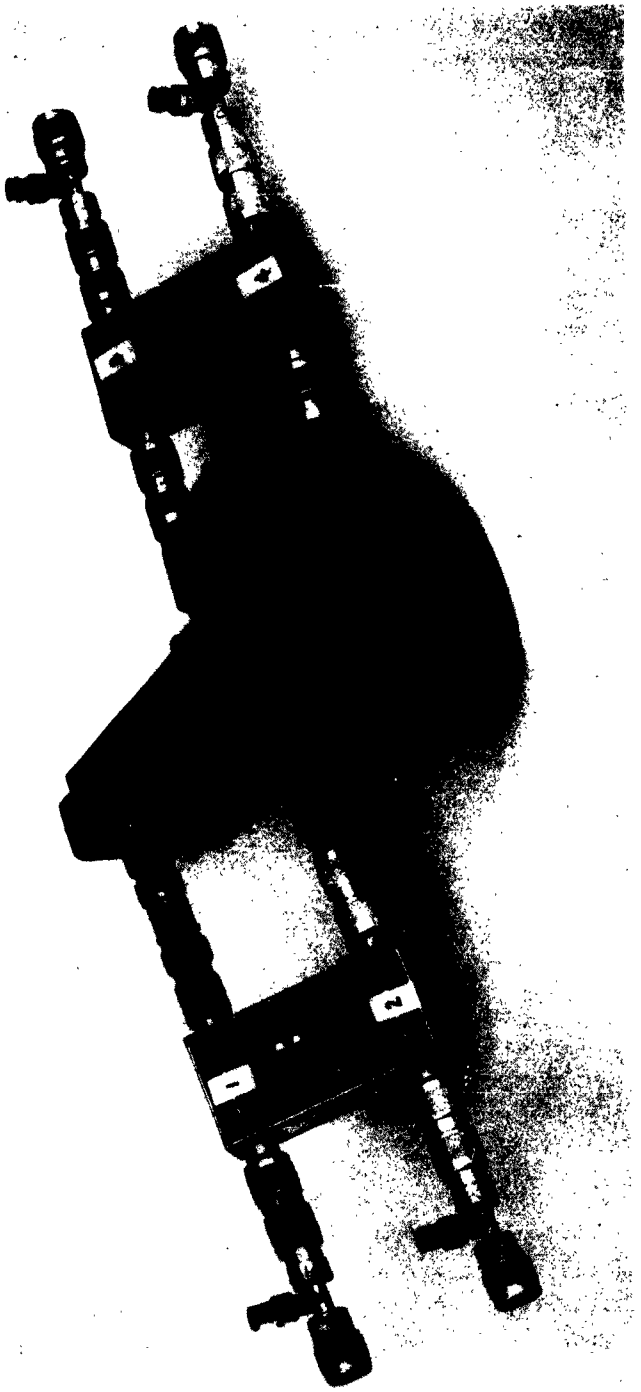

FIG. 66. THE ACTUAL ASSEMBLY OF THE INPUT OR THE OUTPUT CIRCUIT.

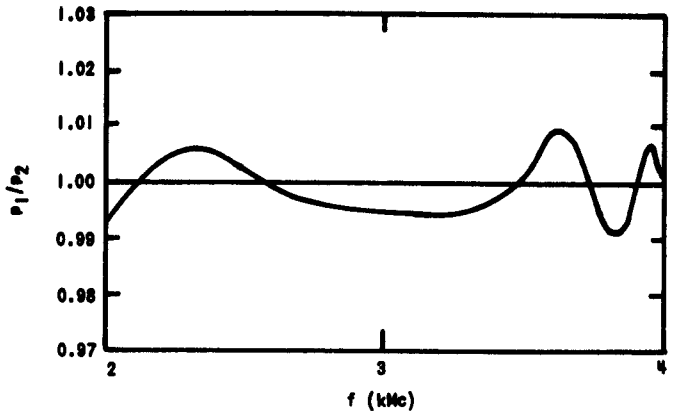

a. Power ratio of the two outputs

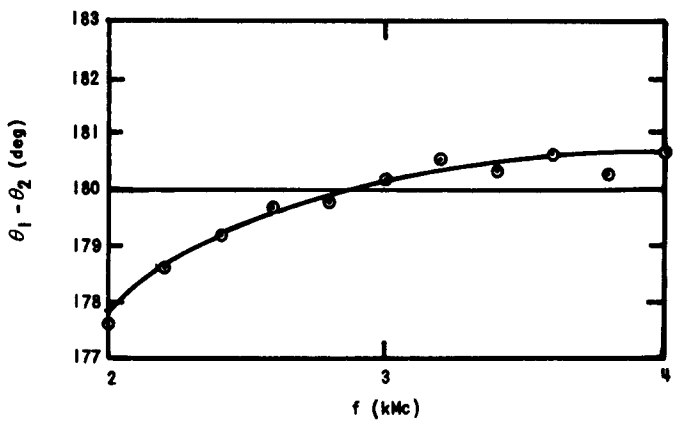

b. Phase difference at the two outputs

FIG. 67. THE MEASURED POWER RATIO AND PHASE DIFFERENCE OF THE TWO OUTPUTS OF THE INPUT WAVEGUIDE BALUN.

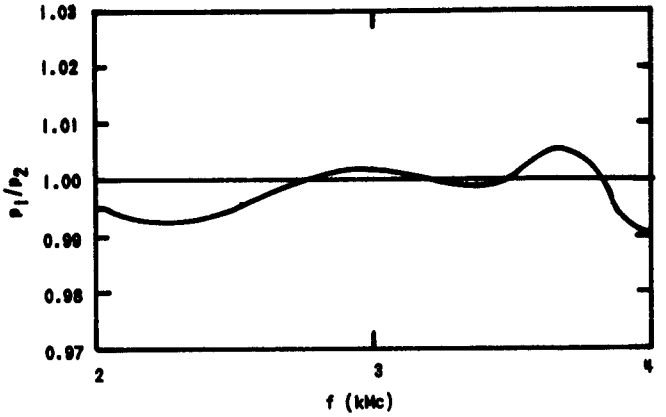

a. Power ratio of the two outputs

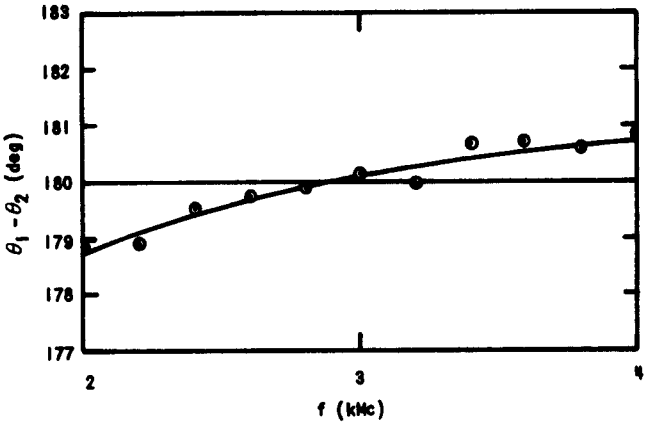

b. Phase difference of the two outputs

FIG. 68. THE MEASURED POWER RATIO AND PHASE DIFFERENCE OF THE TWO OUTPUTS OF THE OUTPUT WAVEGUIDE BALUN.

It would be possible to construct a coaxial or strip-line transducer with considerably smaller size to provide the power division with proper phase shift. It would also be possible to incorporate such a unit into the tube package. In the present research we are mainly interested in verification of the theory established in previous chapters and the testing of the operation; therefore, we will leave this possibility for future studies.

Once the proper signals in the four branches are available, one can excite only the -1 mode or only the +1 mode according to the connections to the helix, as shown in Fig. 22(c) and (d). Figure 69(a) shows the output of the circuit wave with -1 mode excitation. The forbidden gap is clearly shown in this trace. Figure 69(b) shows that the signals with frequency close to the forbidden gap or ka close to unity are eliminated by placing lossy material (for example, the hand of the experimenter) outside the glass tube which houses the helix. This is due to the fact that these signals have phase velocities very close to the velocity of light. Their energy or fields extend radially far away from the helix and can be absorbed by the lossy material outside the glass tube. This effect also identifies the circuit wave as traveling with high phase velocity and verifies the intended -1 mode excitation. Figure 70(a) is the circuit output with +1 mode excitation. This checks with the theory in that no forbidden gap exists in S-band. Figure 70(b) shows the output after adding lossy material just outside the glass tube. Essentially no change in comparison with trace (a) is observed. This identifies the circuit wave as traveling with low phase velocity, so that the field does not extend to the region outside the glass enclosure and is not affected by the existence of lossy material there. This also confirms the +1 mode excitation since the phase velocity of this mode in S-band is much slower than the velocity of light.

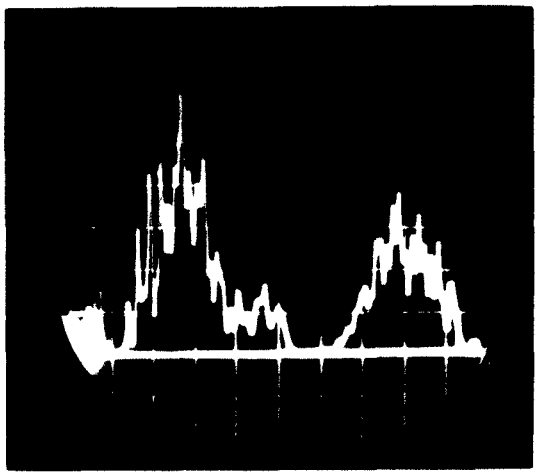

a. No lossy material outside
the glass tube

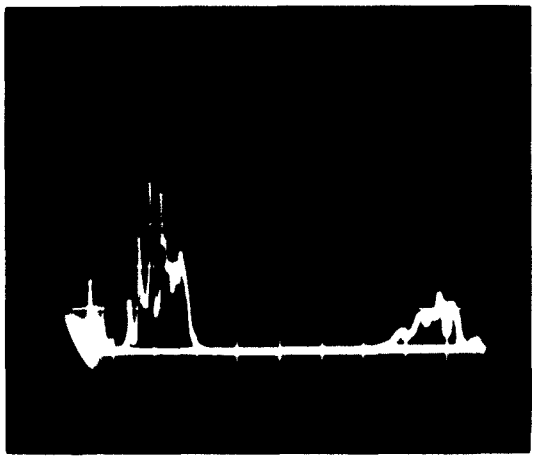

b. Lossy material outside
the glass tube

FIG. 69. THE OUTPUT OF THE QUADRIFILAR HELIX WITH -1 MODE EXCITATION.

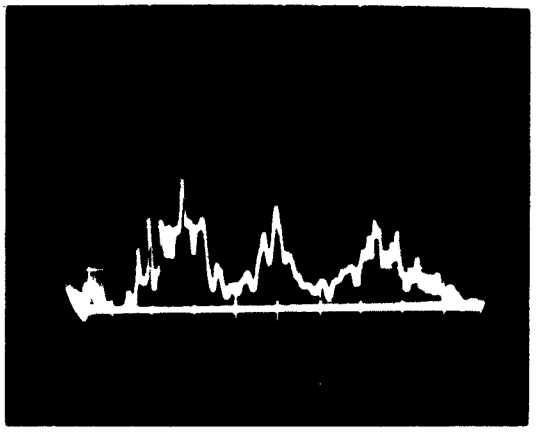

a. No lossy material outside
the glass tube

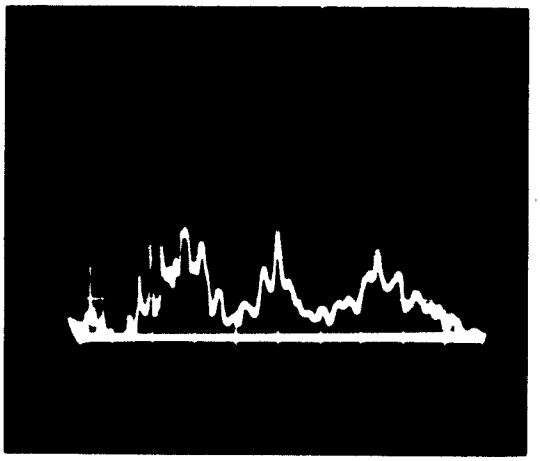

b. Lossy material outside
the glass tube

FIG. 70. THE OUTPUT OF THE QUADRIFILAR HELIX WITH +1 MODE EXCITATION.

2. Circuit Matching Measurement and Insertion Loss

The match of the transition between the helix and the coaxial cable is achieved by using adapters to provide direct contact to the pins of the helix, together with saw-tooth outer conducting sheets. It is found that a narrow adapter with short saw teeth in the outer conducting sheet will give good matching at both the input and the output terminals. An adapter with a width covering four pitches and with saw teeth covering ten more pitches is found to give the best match in S-band. The VSWR in this case is less than 1.8 over the whole band. Further adjustment can be made by adding four double-stub tuners at the output terminals. With the latter, a VSWR less than 1.5 over S-band has been measured. Caution must be observed in using the stub tuner, to insure that the -1 mode circuit wave is the only mode excited. Therefore, the offset of the phases due to the tuning should be kept as small as possible.

The insertion loss of the quadrifilar helix was measured with the best matching condition obtained. The insertion loss is in the range 10 to 14 db in the pass band of the -1 mode excitation. This loss is considered to be reasonable for the fine-tape helix.

3. Cold Measurement of the ω-β Diagram of the Quadrifilar Helix

The quadrifilar helix was assembled with a center conductor of the actual size, with both input and output pins connected to the coaxial cables by adapters as shown in Fig. 71. The measurement of the propagation characteristic of the helix was performed on the setup shown in Fig. 72. An approximate standing wave on the helix was first setup by suitable adjustment of the stub tuners at the output end of the helix. Then the standing wave pattern was measured, from which the wave number β could be calculated at each value of the signal frequency. The typical measured standing wave pattern is shown in Fig. 73 for $f = 3200$ Mc; the magnitude varies as a result of the loss along the circuit and also because of nonideal mode excitation and the presence of space harmonics. The guide wavelength is taken as the average of several measurements along the helix from which the calculated β is plotted as a function of frequency in Fig. 74. Only the -1 mode in S-band is measurable by this method, since for other cases the guide wavelength is too small to be accurately measured. In comparison with the theoretical curve, it is noticed that the group velocity of the actual wave carried by the helix is slower than the theoretical value. This is to

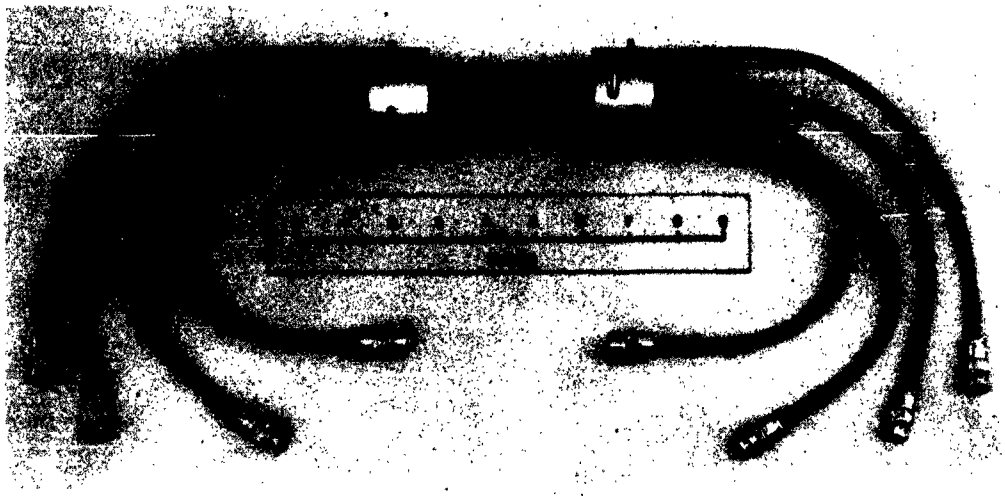

FIG. 71. THE QUADRIFILAR HELIX WITH CENTER CONDUCTOR ASSEMBLED FOR COLD TESTING.

be expected, due to the dielectric loading effect. From Fig. 74 the dielectric loading factor is found to be:

$$DLF = \frac{v_g \text{ (actual)}}{v_g \text{ (theoretical)}} = 0.92$$

This effect can be interpreted as meaning that the effective radius of the helix experienced by a wave is larger than the actual radius,

$$a \text{ (effective)} = \frac{a \text{ (actual)}}{DLF}$$

due to the dielectric supporting rods on the helix. Similar corrections apply to the required magnetic field and the beam voltage in order to have strong coupling between the fast cyclotron wave and the circuit -1 mode.

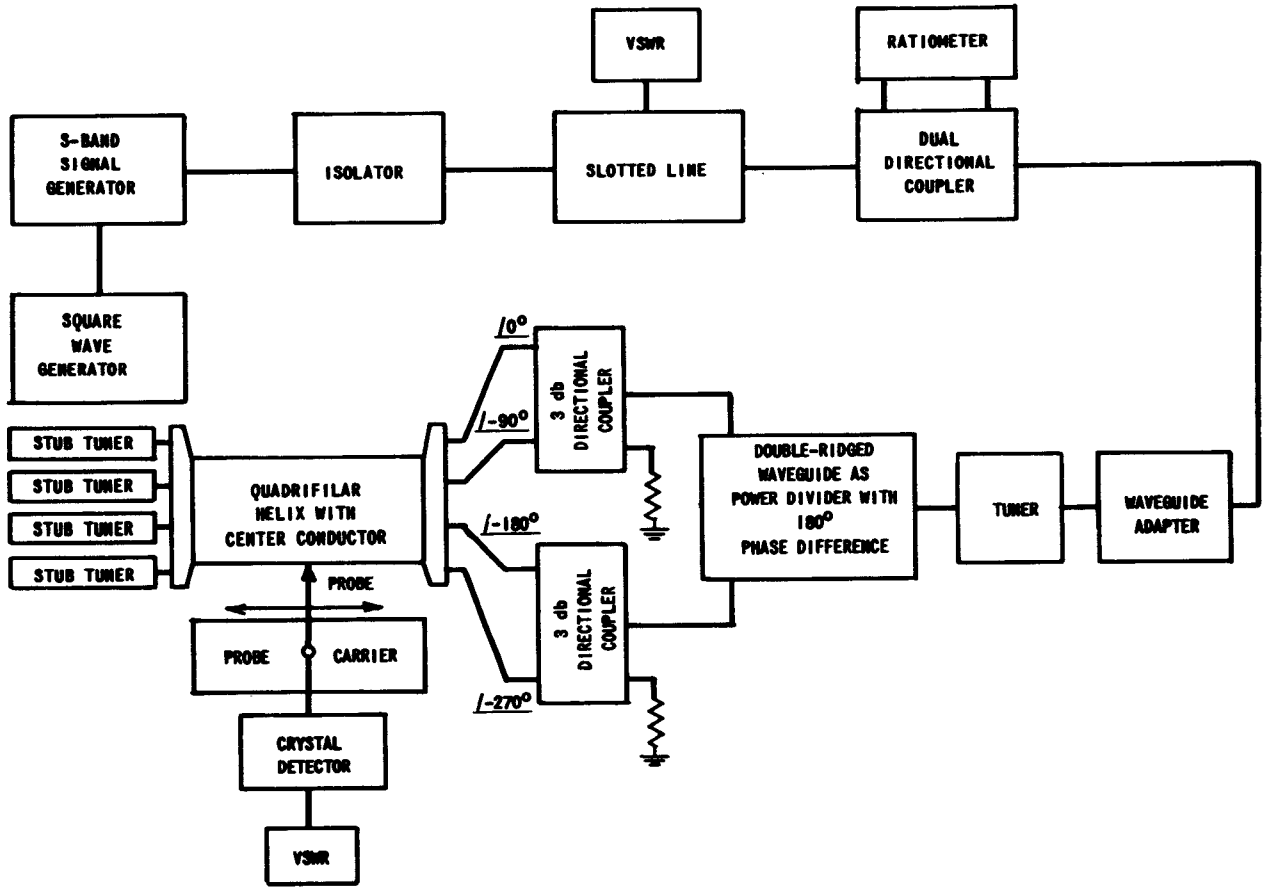

FIG. 72. BLOCK DIAGRAM FOR THE MEASUREMENT OF THE PROPAGATION CHARACTERISTIC ALONG THE HELIX.

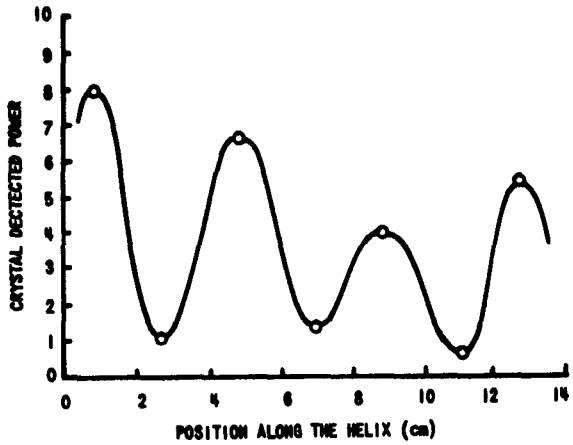

FIG. 73. THE STANDING WAVE PATTERN ALONG THE HELIX FOR f = 3200 Mc.

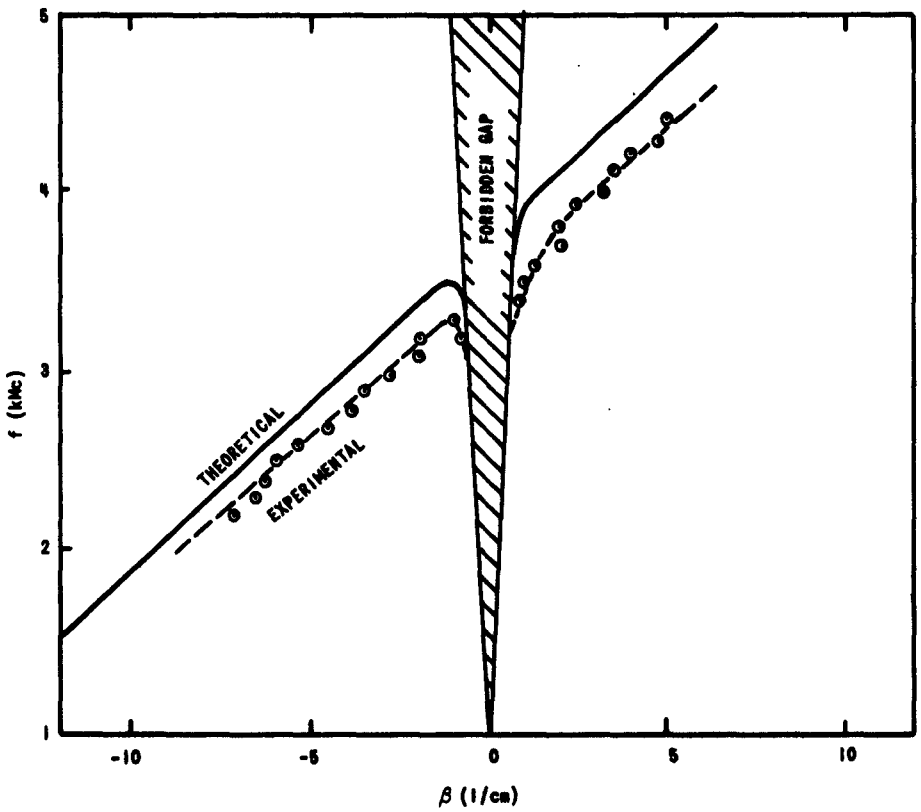

FIG. 74. THE MEASURED ω-β PROPAGATION CHARACTERISTICS OF -1 MODE HELIX WAVE.

B. DC BEAM TEST

Upon completion of the experimental tube, beam tests without rf signals were made before rf tests were attempted. The beam tests consisted of two parts; tests of gun emission and tests of beam transmission to the collector. Two tubes were actually completed. The second tube was improved in construction compared with the first tube. The first tube was found to have two electrodes shorted together after only one week of operation, due to misalignment of the inner gun electrodes after heat expansion; and the outer drift tube was found to be too heavy to be supported only at one end. In the second tube these troubles were removed by having a more rigid construction of electrodes using three alignment rods inside, together with a thinner drift tube. Better transmission was observed in the second tube, and the following results refer to the second tube.

In order to indicate the experimental setups used for various tests, a schematic representation is used for the tube. Figure 75 shows the schematic representation, as well as a listing of the connections between the pins and the various internal elements of the tube.

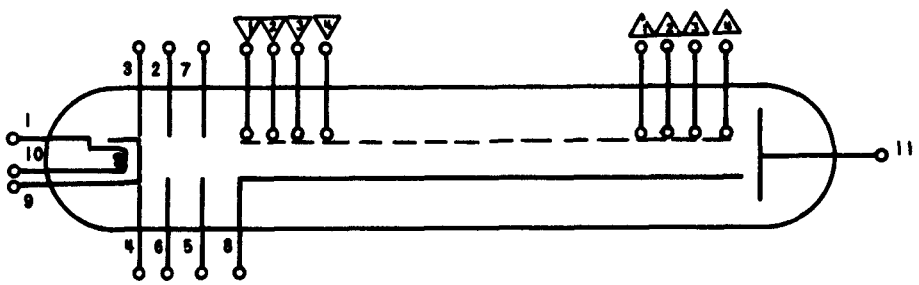

PIN NO.	TUBE ELEMENT	PIN NO.	TUBE ELEMENT
1	HEATER	8	CENTER CONDUCTING CYLINDER
2	OUTER FIRST ANODE	9	CATHODE
3	OUTER FOCUSING ELECTRODE	10	HEATER
4	INNER FOCUSING ELECTRODE	11	COLLECTOR
5	INNER SECOND ANODE	▽	HELIX INPUTS, n = 1,2,3,4
6	INNER FIRST ANODE	△	HELIX OUTPUTS, n = 1,2,3,4
7	OUTER SECOND ANODE		

FIG. 75. SCHEMATIC DIAGRAM OF THE QUADRIFILAR HELIX TUBE.

1. Tests on the Electron Gun

During the testing of the electron gun, the tube was still on the pump station so that the axial magnetic field was not applied. In order that the helix should not draw excessive current, all four helices were connected to the cathode potential. The collector and the center conductor were tied together and kept at a slightly higher potential than the second anode. The complete test setup is shown in Fig. 76. The measured temperature-limited cathode emission current as a function of heater power is shown in Fig. 77. The curve shows that the cathode is not very good. The heater power needed for normal operation would be larger than 20 w in order to have the temperature-limited current emission much larger than 100 ma. Figure 78 shows the cathode emission current as a function of the voltage on the first anode for different heater powers. It is evident from this figure that about 22 w is required for a beam current of 100 ma with the first anode voltage set at 87 w for normal operation.

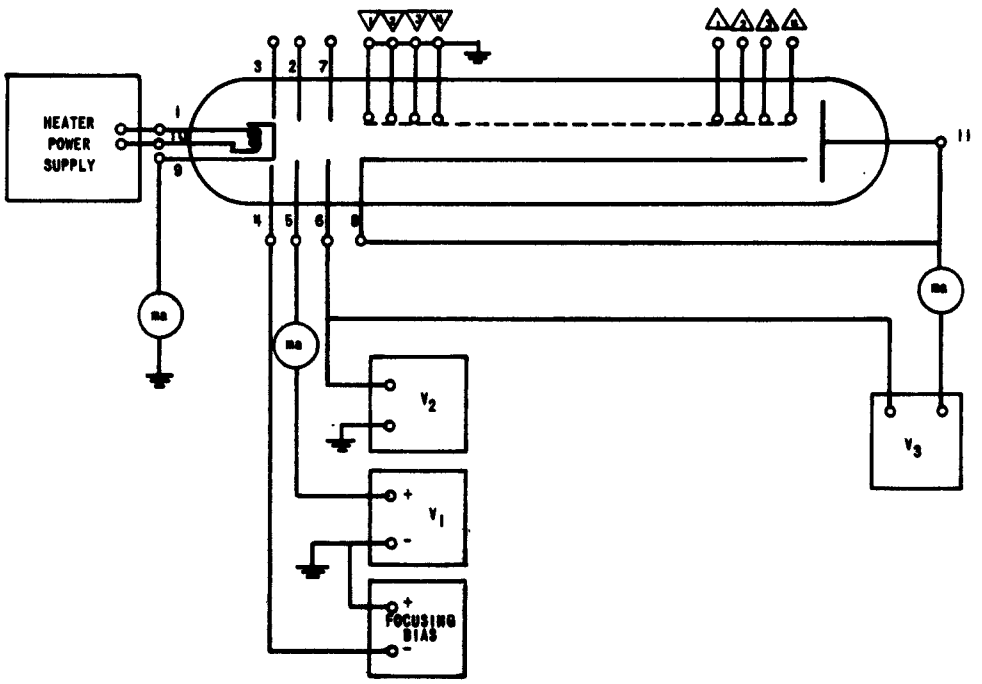

FIG. 76. TEST SETUP FOR TESTING THE ELECTRON GUN.

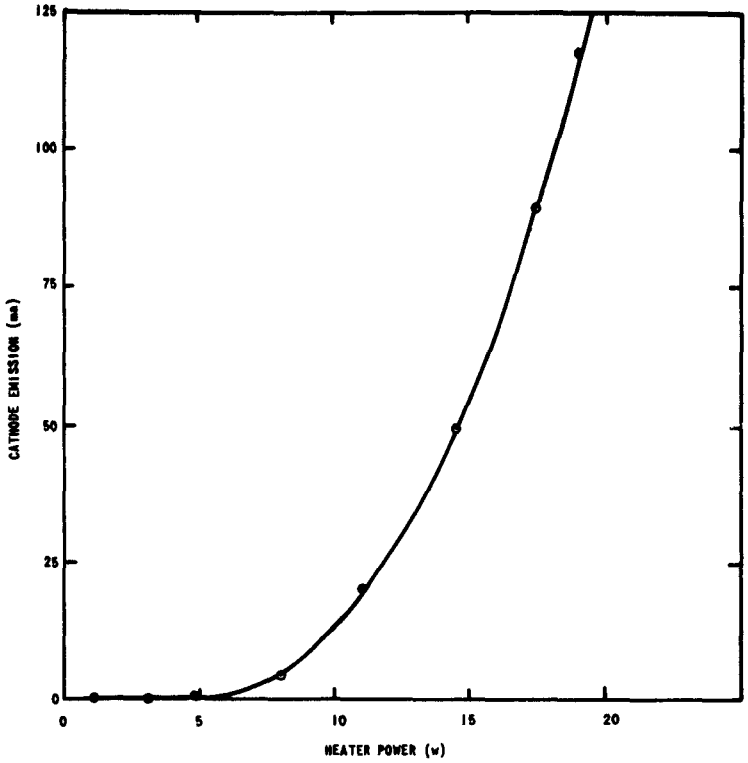

FIG. 77. THE TEMPERATURE-LIMITED CATHODE EMISSION CURRENT AS A FUNCTION OF HEATER POWER.

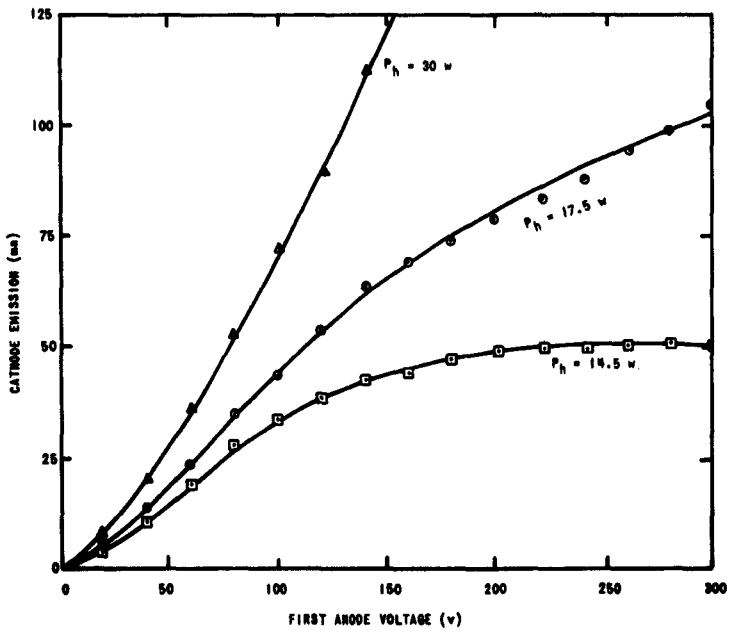

FIG. 78. THE CATHODE EMISSION CURRENT AS A FUNCTION OF FIRST ANODE VOLTAGE FOR VARIOUS HEATER POWERS.

2. Tests on the Current Transmission Through the Helix

After the tests of electron gun emission, the tube was vacuum sealed at a pressure of about 10^{-6} mm. Then the tube was inserted into the solenoid and aligned parallel to the axis. With the magnetic field applied, the beam transmission to the collector was measured. The collector, the helix, the center conductor, and the second anode were connected to the same potential, with current meters on each. The complete test setup is shown in Fig. 79. The percentage of beam current transmitted to the collector was measured as a function of magnetic field. The results are shown in Fig. 80. It is evident that the beam transmission is essentially independent of the cathode emission but is very sensitive to the magnetic field probably because the magnetic field strongly affects the cancellation of the lens effects at the two anodes.

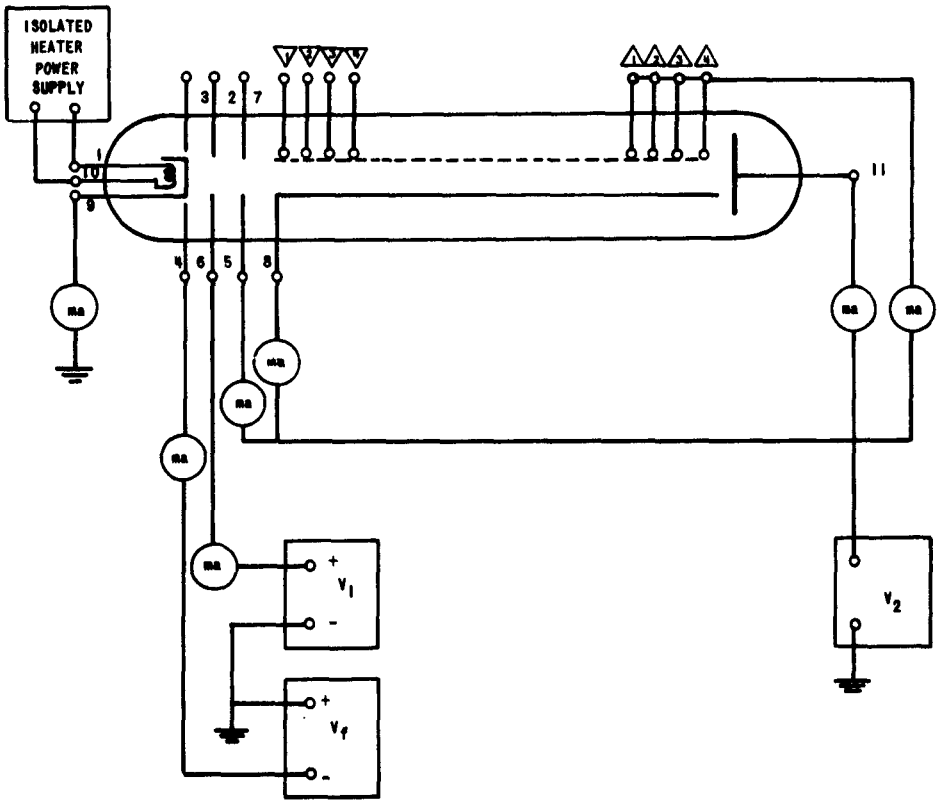

FIG. 79. TEST SETUP FOR MEASURING THE TRANSMISSION OF THE BEAM.

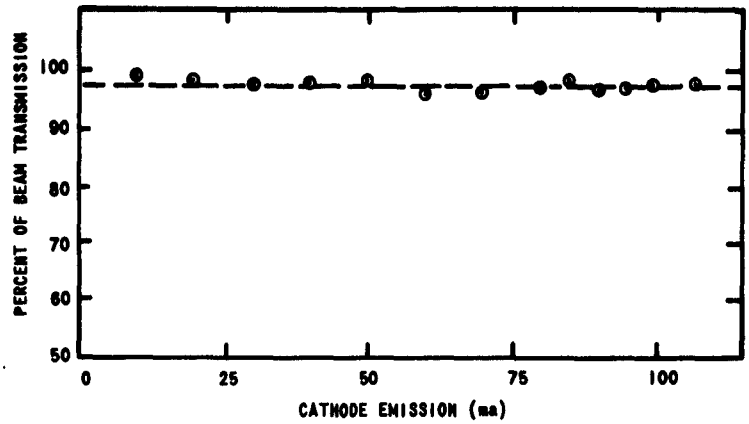

a. As a function of cathode emission current

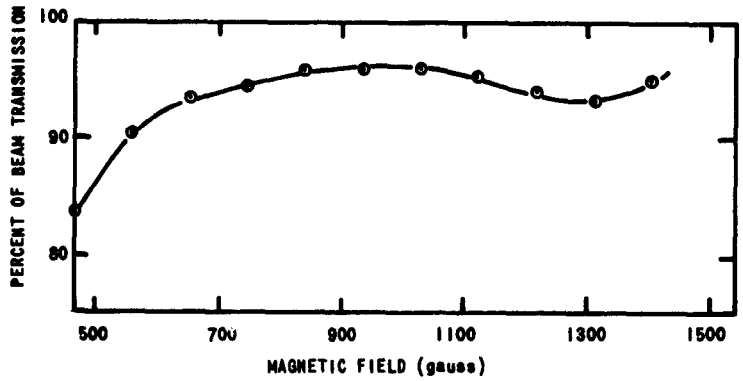

b. As a function of the axial magnetic field

FIG. 80. THE PERCENT OF BEAM CURRENT TRANSMITTED TO THE COLLECTOR.

C. RF TESTS OF THE TUBE

The rf tests of the quadrifilar helix tube consisted of three sets of measurements. The first set included measurements of the circuit behavior such as helix propagation mode, coupling coefficient, transverse impedance, etc. These measurements were made by using the interactions of the circuit waves and the beam waves. The fast cyclotron wave was especially useful in measuring the characteristics of the fast circuit wave, i.e., the -1 mode helix wave near the forbidden range.

The second set was the group of measurements of the operation under simultaneous rf coupling and dc pumping. Due to the elimination of the separate input and output couplers, the dc pumping cannot be tested without the rf coupling. It was found that the tube began oscillating in a spurious mode at a rather low beam current. Therefore, the available coupling strength was weaker than that at the designed beam current. The actual pumping strength was also not enough because of the rough estimation of pump coefficient used in designing this experimental tube. Therefore, the measurable gain was only about 4 db maximum. However, the measured results at low level were closely correlated with the theoretical results. In particular, the measured circuit output as a function of pumping strength showed the striking differences when the coupling strength was above or below the Kompfner-Dip condition, as predicted by the theory. Wide bandwidth was observed in both L- and S-bands. We are confident from these measurements that wide bandwidth with high gain can be achieved by improving the pumping structure to provide higher pumping strength per volt of dc pumping field. The sample design in the previous chapter shows that such structures can be designed with realizable dimensions.

The third set contains, as a byproduct of this work, the measurement of other possible operations using the same tube. The operation of simultaneous rf coupling and dc pumping using one cyclotron wave plus the synchronous waves was observed to give a strong amplification effect. As much as 10 db of gain was measured at only about 400 v pumping in this mode of operation. This observation presents a problem for further study.

1. Interactions of the Beam Waves and the Circuit Waves

During this test no dc pumping field was applied on the quadrifilar helix. The tube operated as a conventional traveling-wave coupler, where the circuit wave couples with transverse beam waves. Due to the

great difference in phase velocities between the fast and the slow cyclotron waves, it is relatively simple to couple to the fast or the slow cyclotron waves separately. Figure 81 presents the results of these couplings. The circuit is excited to propagate the 0 mode with signal frequency of 1200 Mc. At point A the fast cyclotron wave couples with the forward circuit wave at $V_o = 100$ v and $I_f = 0.39$ amp (the magnetic field is about 470 gauss/amp); while at point B the fast cyclotron wave couples with the backward circuit wave at $V_o = 100$ v and $I_f = 1.41$ amp. The former coupling is a co-flow type (the waves coupled together have their group velocities in the same direction); therefore Kompfner-dip type circuit loss is observed. The latter coupling is a contra-flow type (the waves coupled together have their group velocities in the opposite direction); therefore exponential-type circuit loss is observed. At point C the forward circuit wave couples to the negative-energy slow cyclotron wave; therefore, some gain rather than a Kompfner-dip is observed. It should be noted that it is impossible to have the slow cyclotron wave coupled with the backward 0-mode circuit wave.

Figure 82 shows co-flow coupling to the beam waves by the -1 mode circuit wave, with beam current as a parameter. The left side shows frequencies with $ka < 1$ and with negative phase velocity. The right side shows frequencies with $ka > 1$ and with positive phase velocity. For the same beam current, one can observe from Fig. 82 that the coupling coefficient increases as the signal frequency is increased for $ka \leq 1$ and decreases with increases in frequency for $ka > 1$. Figure 83 shows the contra-flow coupling to the fast cyclotron wave for which the exponential dip pattern was observed. At fixed beam voltage, the magnetic field which brings the fast cyclotron wave into synchronism with the -1 mode circuit wave can be measured and compared with theory. As shown in Fig. 84, good agreement with the coupled-mode theory is observed.

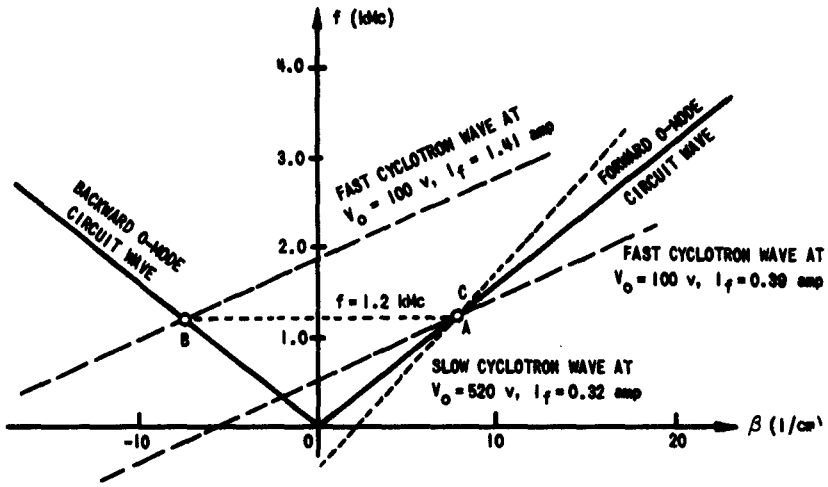

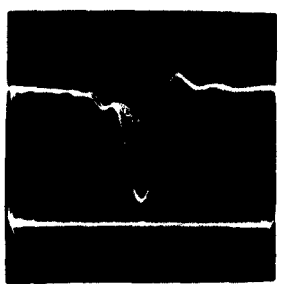

V_o

a. I_o = 2.4 ma
at Point A

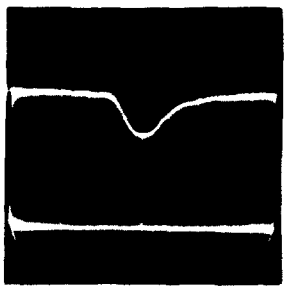

V_o

b. I_o = 3.0 ma
at Point B

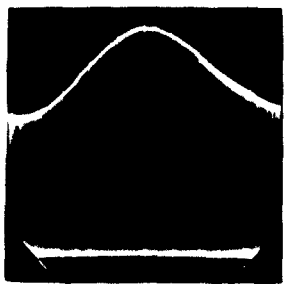

V_o

c. I_o = 3.0 ma
at Point C

FIG. 81. THE COUPLINGS BETWEEN BEAM WAVES AND THE O MODE CIRCUIT WAVE AT f = 1.2 kMc. a. Forward O mode and fast cyclotron wave. b. Backward O mode and fast cyclotron wave. c. Forward O mode and slow cyclotron wave.

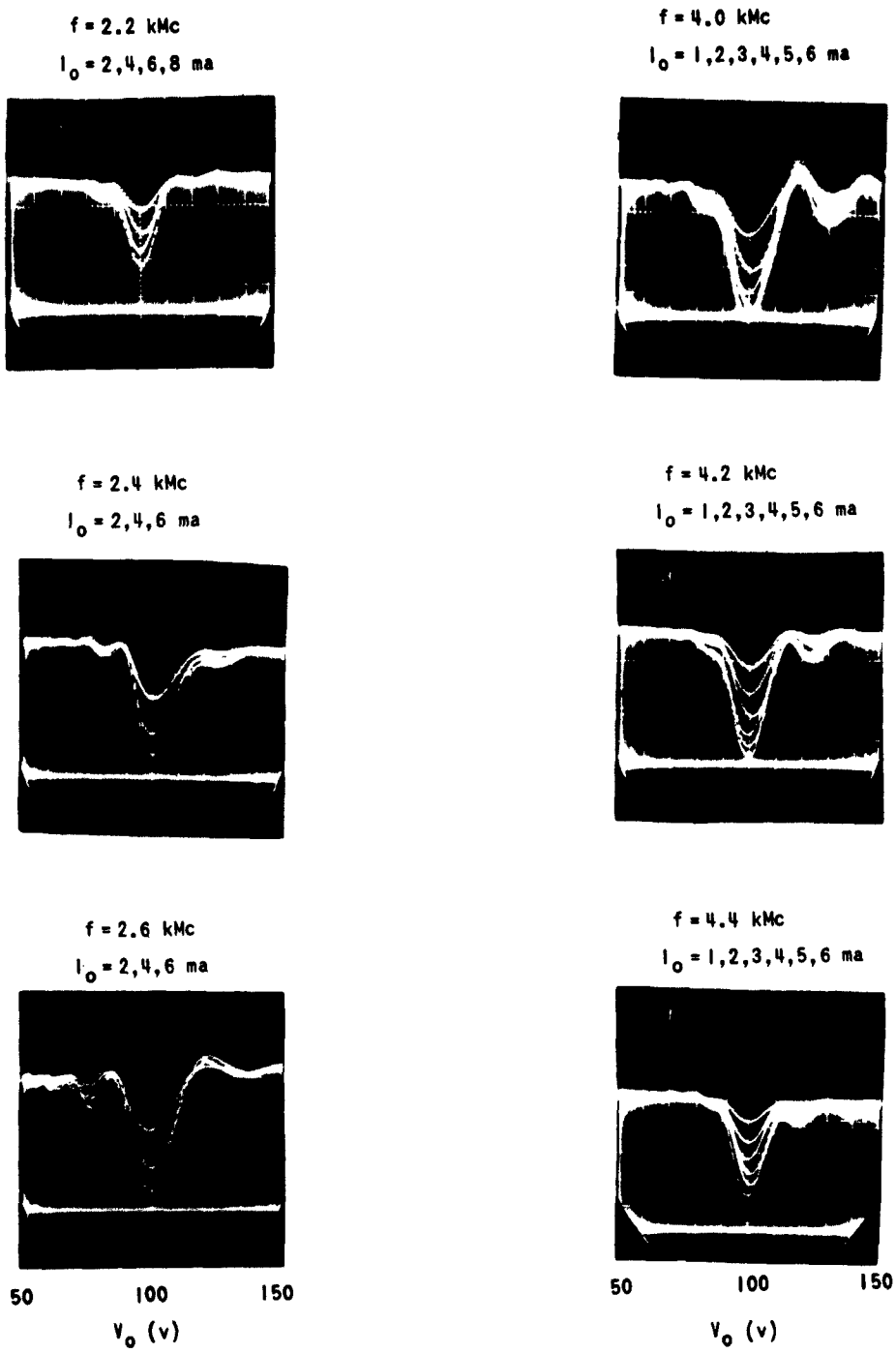

FIG. 82. THE CO-FLOW COUPLING BETWEEN THE FAST CYCLOTRON WAVE AND THE -1 MODE CIRCUIT WAVE.

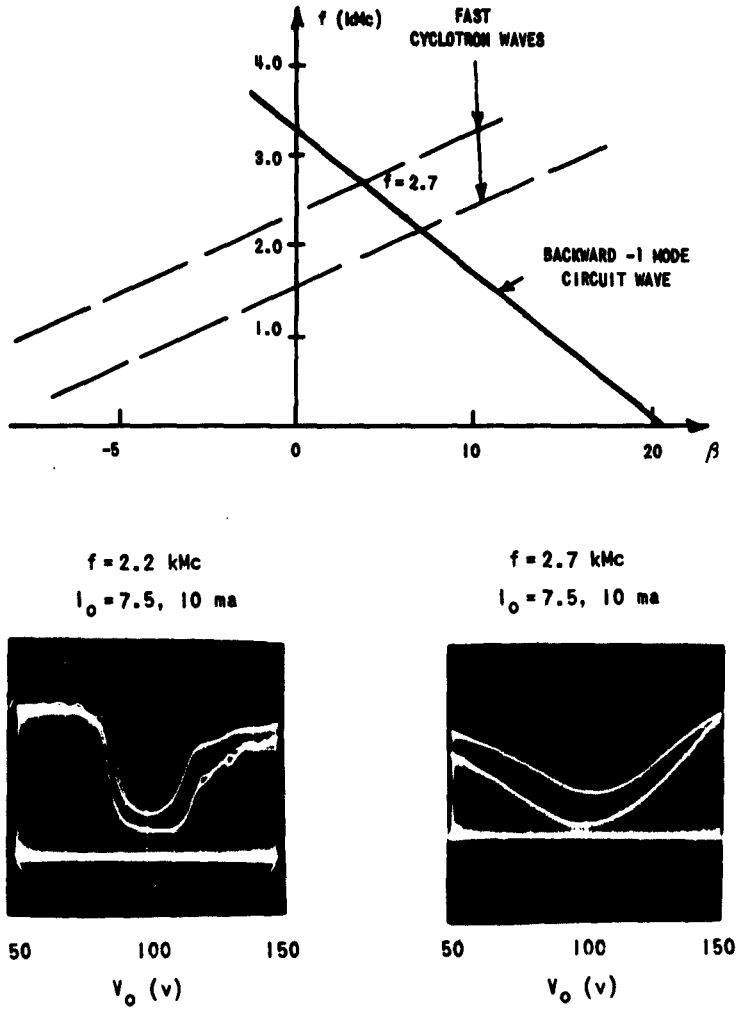

FIG. 83. THE CONTRA-FLOW COUPLING BETWEEN THE FAST CYCLOTRON WAVE AND THE -1 MODE CIRCUIT WAVE.

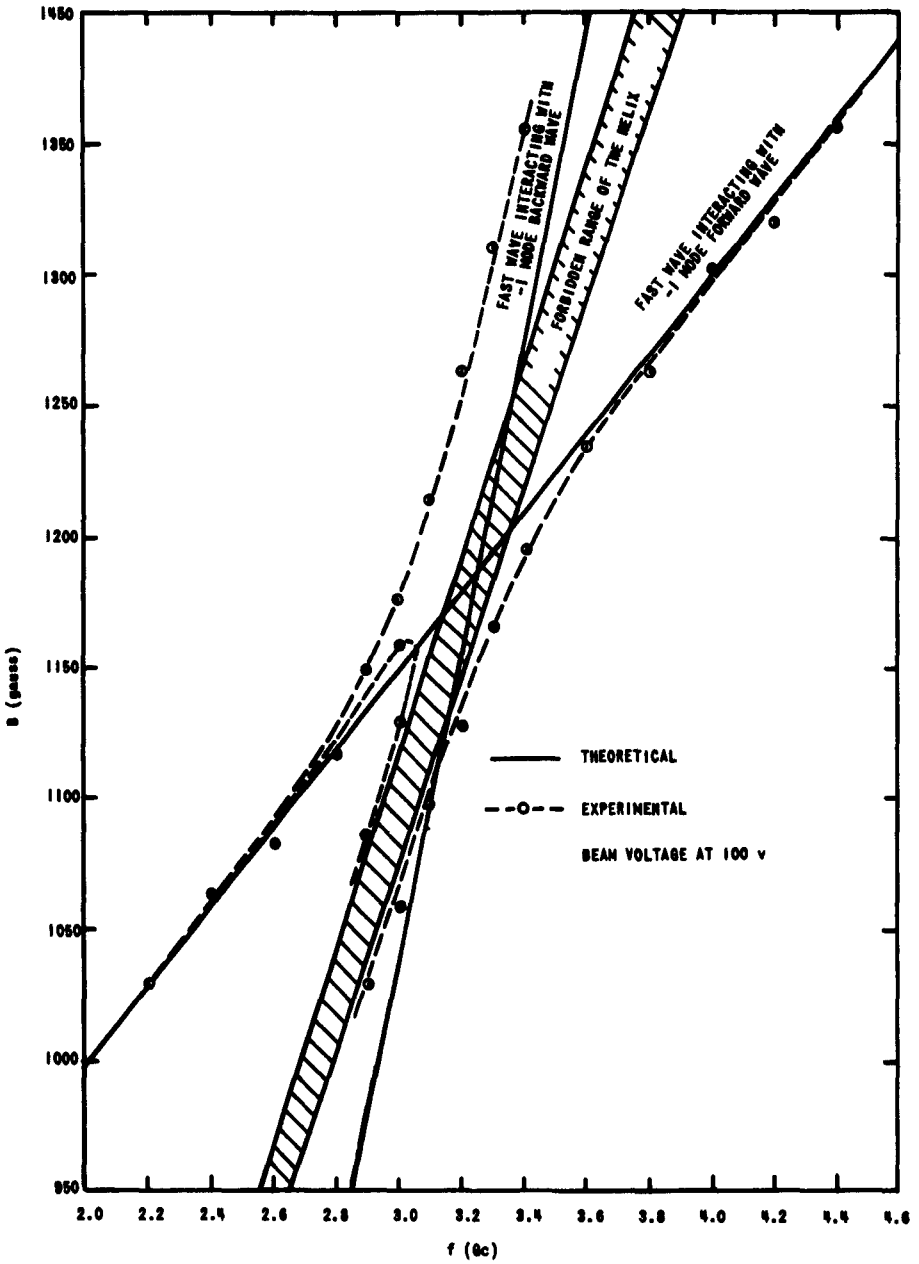

FIG. 84. THE FAST WAVE INTERACTION WITH THE -1 MODE CIRCUIT WAVE, WITH BEAM VOLTAGE FIXED AT 100 v.

2. Measurement of the ω-β Diagram of the Circuit by the Interaction with the Beam Waves

The propagation characteristic of the circuit forward 0 mode and the backward -1 mode can be measured by the interaction with the conventional longitudinal space-charge beam waves. The beam voltage at which such longitudinal interaction was observed is plotted as a function of signal frequency in Fig. 85. The wave number corresponding to any given signal frequency can then be calculated from the observed beam voltage. The plot of this wave number as a function of frequency is shown by the circled dots in Fig. 86.

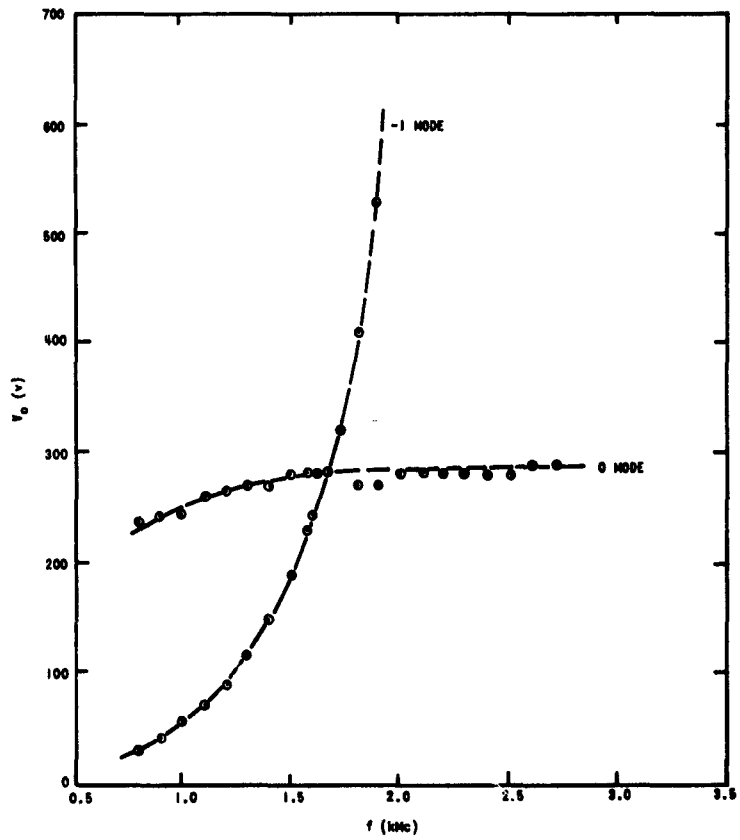

FIG. 85. THE BEAM VOLTAGE AT WHICH LONGITUDINAL INTERACTION OCCURS, AS A FUNCTION OF FREQUENCY.

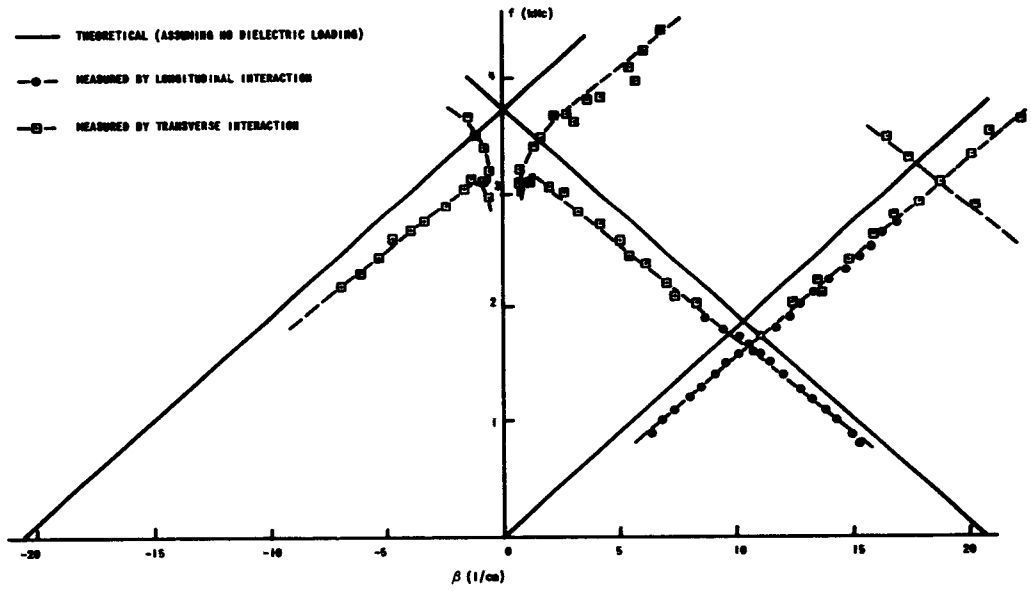

FIG. 86. THE ω-β DIAGRAM OF THE CIRCUIT MEASURED BY THE INTERACTION WITH BEAM WAVES.

The interaction with transverse beam waves can also be used to measure the ω-β characteristics. For a fixed signal frequency, the interaction can be observed by successive tuning of the beam voltage and the magnetic field. For fast cyclotron-wave interaction, if the interaction shifts to higher beam voltage as one increases the magnetic field, the wave number of the circuit mode is negative; otherwise it is positive. For slow cyclotron-wave interaction, the situation reverses; that is, if the interaction shifts to higher beam voltage as one increases the magnetic field, the wave number is positive. The slow cyclotron wave can only couple to a circuit wave with positive wave number. A plot of the square root of the beam voltage vs the magnetic field, following such an interaction, should be a straight line. The slope of this line gives the magnitude of the wave number β. Typical measured points are shown in Fig. 86 by squared dots; the behavior is indeed linear. It is found that this technique is very useful in measuring the propagation characteristic of a fast circuit wave which is not measurable by the longitudinal interaction. The dielectric loading factor of the helix in the experimental tube is found to be 0.875. This is slightly smaller than the value from the less accurate cold measurement.

3. Measurement of the Coupling Coefficient and the Transverse Impedance

The coupling coefficient is a function of the beam current and the frequency as studied in Chapter III. It can be measured as a function of current by measuring the circuit power loss when the fast cyclotron wave is coupled with the circuit. Mathematically:

$$k_{-}L = \cos^{-1}\sqrt{\frac{P_c}{P}} = C\sqrt{I_o}$$

where P_c = power output under coupling conditions and P = power output without coupling. Therefore, a plot of $(\cos^{-1}\sqrt{P_c/P})^2$ vs I_o should be a straight line. The slope of this line will give the coupling coefficient for fixed beam current. The transverse impedance can be calculated from this slope as follows:

$$\text{slope} = C^2$$

$$K_t = \frac{2V_o}{\beta^2} \times \frac{\omega_c}{\omega} \times \text{slope}$$

Measurements of $(\cos^{-1}\sqrt{P_c/P})^2$ vs I_o for various signal frequencies are shown in Fig. 87 for the -1 mode circuit wave and in Fig. 88 for the 0 mode. The results check with the theory and form a set of straight lines. From the slopes of these straight lines the transverse impedances at various frequencies were calculated and plotted vs (ka + n) in Fig. 89 for both the -1 mode and the 0 mode. The measured impedances are quite close to the theoretical curve, but the values are a small amount lower than the theoretical curve. This is thought to be due to the fact that the beam is not concentrated on one thin layer but is distributed over a range of 0.025 in. in thickness.

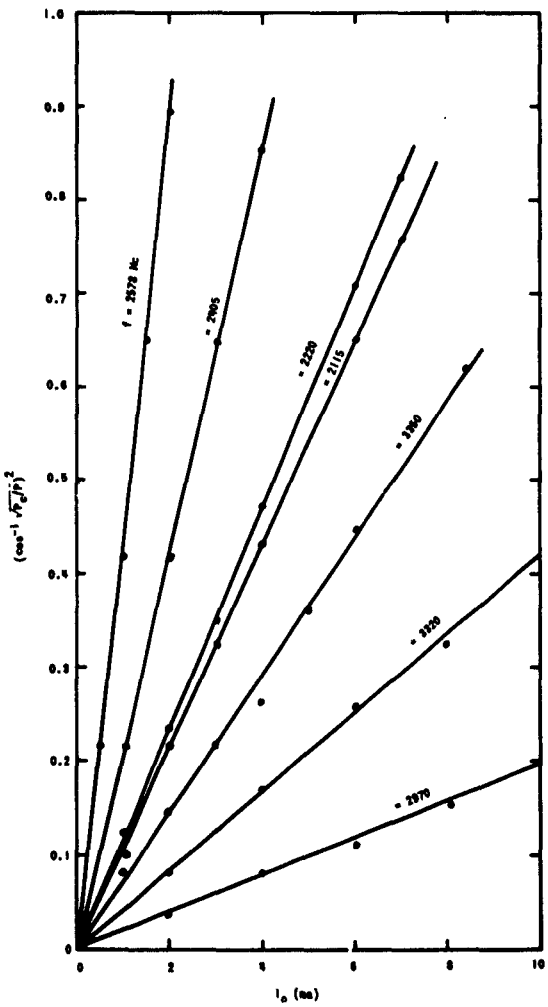

FIG. 87. THE MEASURED $(\cos^{-1}\sqrt{P_c/P})^2$ OF THE -1 MODE VS I_o FOR VARIOUS FREQUENCIES.

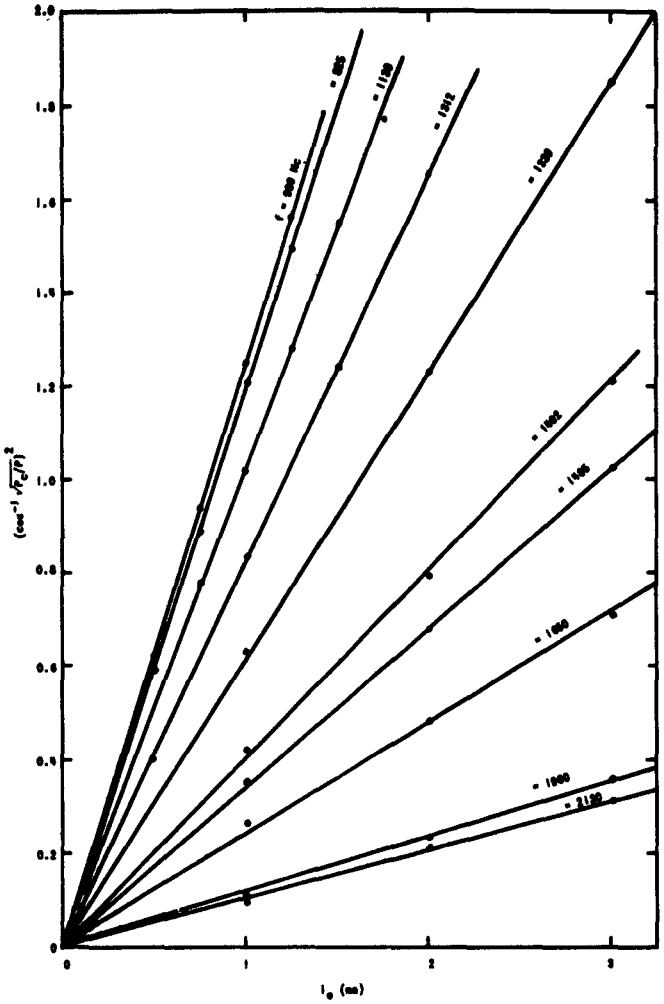

FIG. 88. THE MEASURED $(\cos^{-1}\sqrt{P_c/P})^2$ OF THE O MODE VS I_o FOR VARIOUS FREQUENCIES.

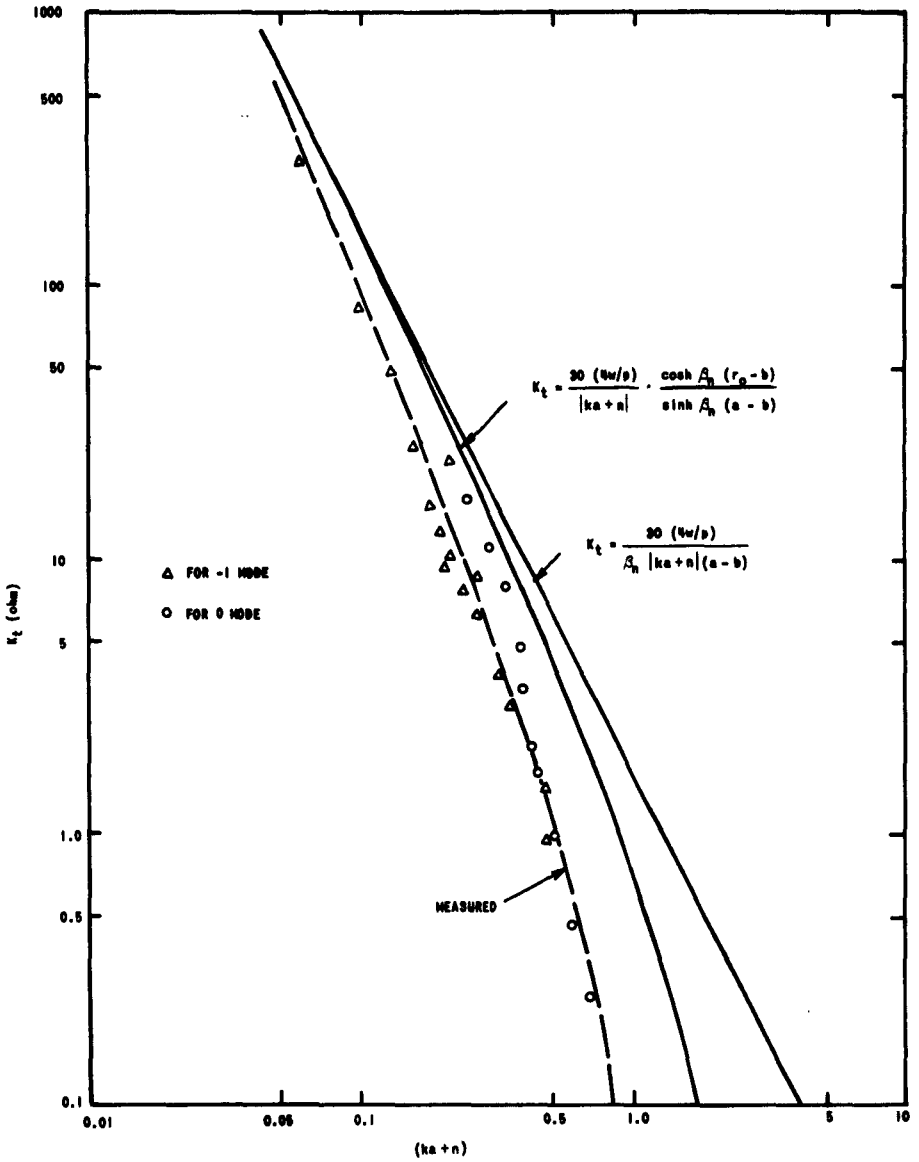

FIG. 89. THE MEASURED TRANSVERSE IMPEDANCE VS (ka + n) IN COMPARISON WITH THE THEORETICAL VALUE.

4. Measurements of the Operation of Simultaneous rf Coupling and dc Pumping on Cyclotron Waves

As discussed in Chapter IV, this tube does not represent a good design for amplification. However, some pumped gain under simultaneous coupling can be observed. For example, in Fig. 90, the circuit output shows fast wave coupling when the pump voltage is off, and some gain when the pump is on. The tube performance is further hampered by the fact the tube exhibits a spurious oscillation in the gun region above about 3 ma of beam current. Various methods were tried in order to eliminate this oscillation. With the best arrangement the tube could be operated up to about 6 ma without oscillation. By sweeping the pump voltage to large amplitudes, we were able to observe various output pattern changes as predicted in Chapter III. Figure 91 shows oscilloscope traces of the observed output. The pump voltage is zero on the left side of the curves and increases toward the right. As the beam current is increased on subsequent curves, one first observes the Kompfner dip, followed by a rapid exponential increase in output. The Kompfner dip with zero pump voltage ($k_- L = \pi/2$) occurs at about 4 ma. Below this current, increasing the

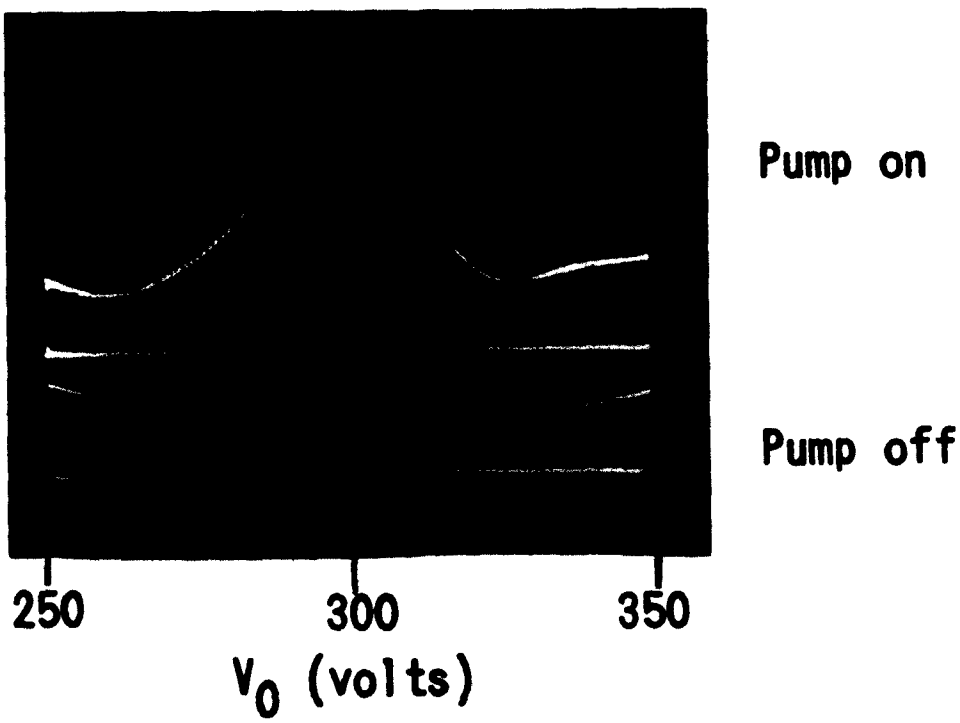

FIG. 90. THE PUMPED GAIN OF THE CIRCUIT WAVE.

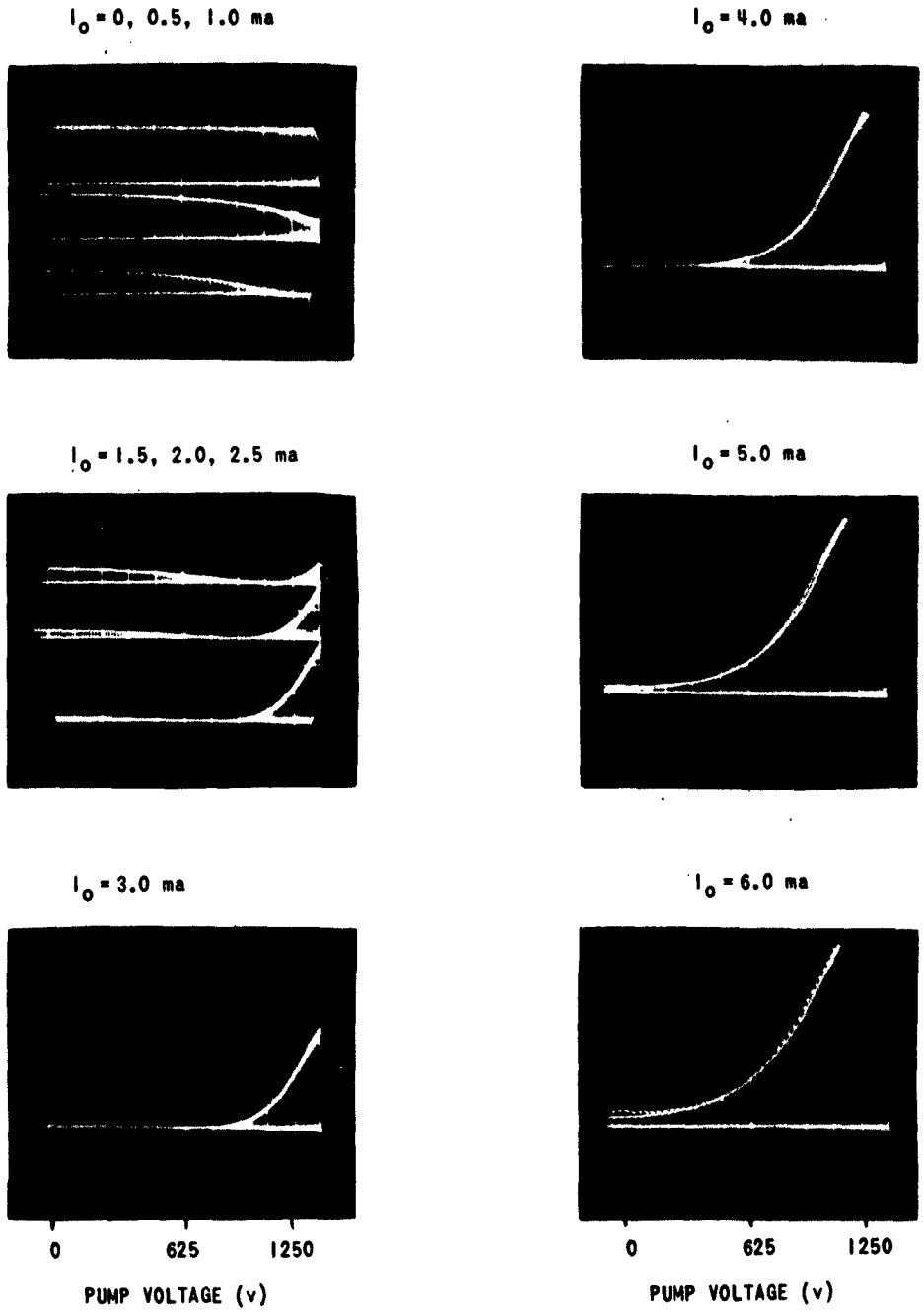

FIG. 91. THE OUTPUT AS A FUNCTION OF PUMPING VOLTAGE AT f = 3700 Mc WITH BEAM CURRENT AS A PARAMETER. (Oscilloscope gain is the same in all traces.)

pump voltage causes first a null, and then exponential gain. Above this current, there is no null point and the circuit output continually increases as one turns up the pump voltage. This strongly confirms the theory of this scheme of operation. The observed output as a function of pump voltage is plotted for some typical cases in Fig. 92 and compared with the theoretical values. Good agreement is shown.

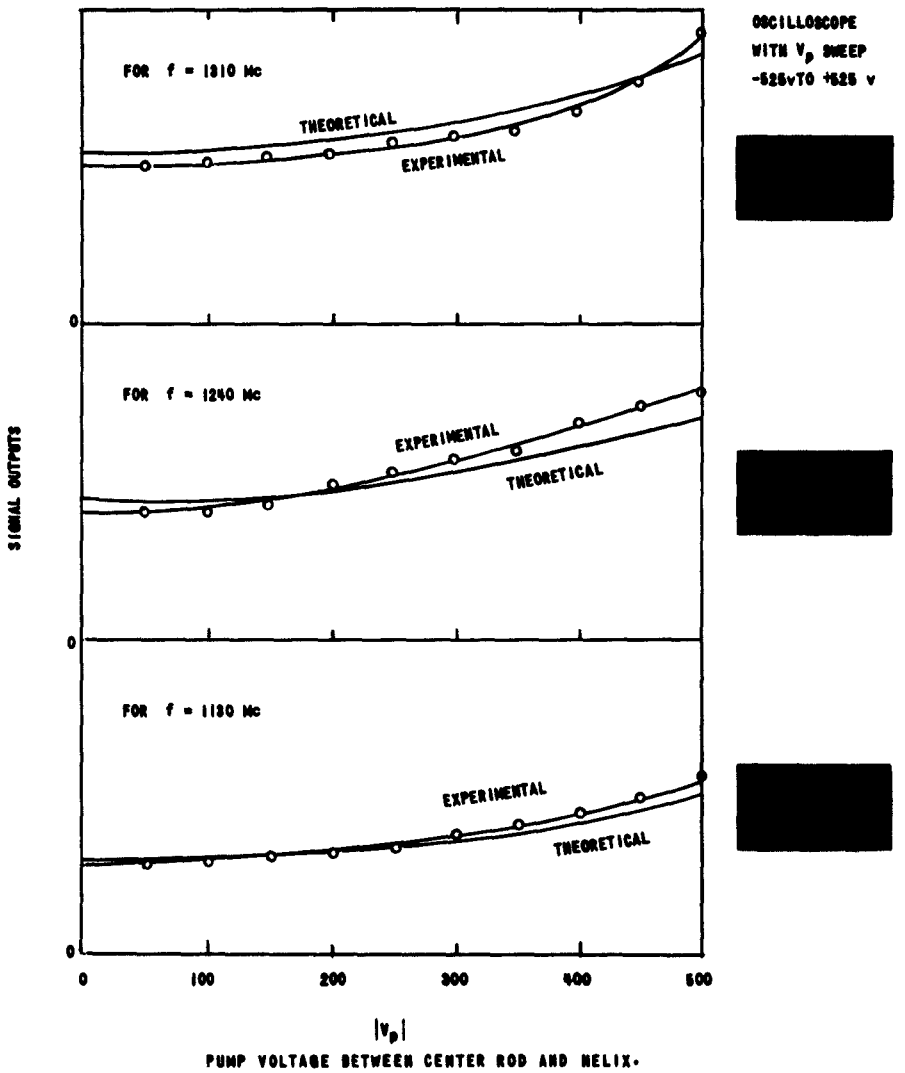

FIG. 92. THE COMPARISON OF THE OBSERVED AND CALCULATED OUTPUT VS PUMPING VOLTAGE.

5. Measured Gain and Bandwidth

Gain was measured at various frequencies in both L- and S-bands. The highest gain observed was about 4 db at $f = 3.7$ kMc. Figure 93 shows the gain measured at various frequencies with 1000 v pumping and 6 ma beam current. The solid line is the theoretical calculated curve. It is noted that the greatest discrepancy between the theoretical curve and the measured points happens close to the forbidden gap of the helix at $ka = 1$ or $f = 3.3$ kMc. All other points show good agreement with theory. Note that these points were measured with all voltages and currents fixed, although the impedance matches were optimized at each frequency. The bandwidth is extremely large and actually covers both L- and S-bands except for the forbidden gap in the center. If the helix had no stop band, the gain would continue through this region.

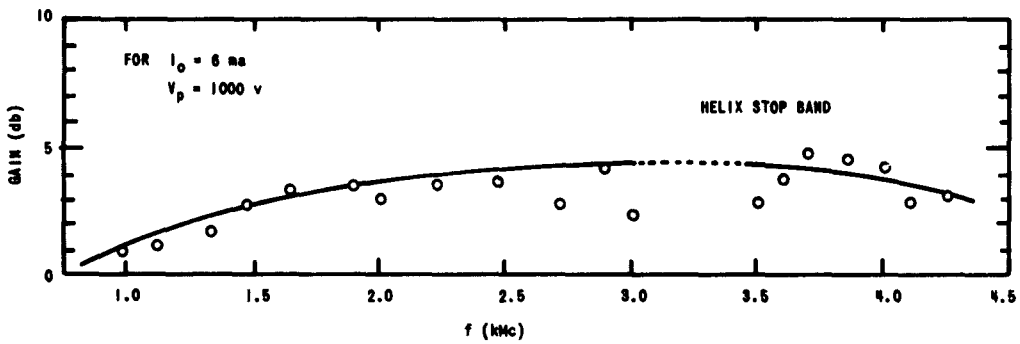

FIG. 93. THE MEASURED GAIN AT VARIOUS FREQUENCIES FOR SYNCHRONOUS ELECTRON BEAM UNDER + - + - DC PUMPING.

6. Sensitivity to dc Beam Voltage, Magnetic Field, and the Lens Effect

The gain was found to be very sensitive with respect to the dc beam voltage and the magnetic field, but insensitive with respect to the anode voltage. Figure 94 shows the variation of the output as a function of the percentage change in these parameters. The curves indicate that for stable operation, well-regulated power supplies are required for control of the beam voltage and magnetic field.

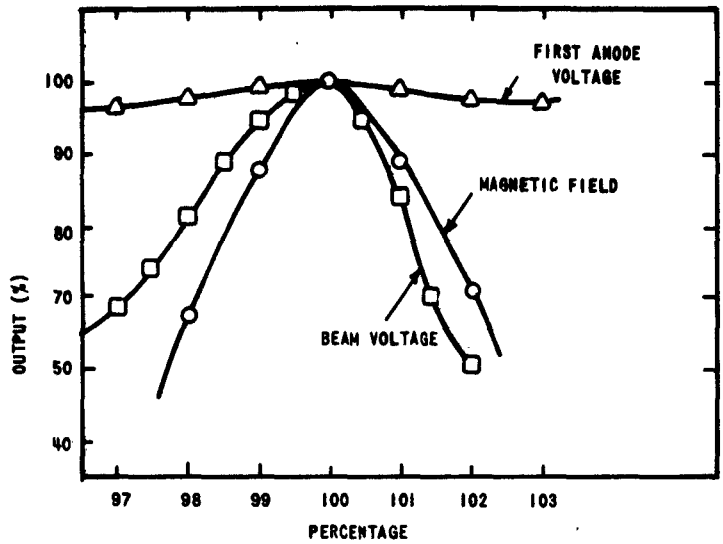

FIG. 94. THE SENSITIVITY OF THE OPERATION TO DC BEAM VOLTAGE, MAGNETIC FIELD, AND THE LENS EFFECT.

7. Observation of High-Gain Operation Under Other Arrangements

We were surprised during the experimental program to observe high-gain operation for dc pumping of one synchronous wave and one cyclotron wave. Two sets of experimental conditions leading to this situation were observed, both resulting in high gain. In the first experiment, the beam voltage was lowered and hence the electron beam slowed down such that the electrons rotated two cyclotron cycles within one pitch of the helix, or one cyclotron cycle within one period of the dc electrostatic pumping field. With this arrangement the electron beam experiences a pumping field with wave number $\beta_p = -4\pi/p = -\beta_c$. This operation is clearly shown in the ω-β diagram in Fig. 95, together with the measured gain vs pumping voltage at a particular frequency of 3700 Mc. About 10 db gain is observed with only 400 v pumping. Current interception on the helix starts at about 420 v, and the gain drops rapidly above this point as shown in Fig. 95. This mode of operation has a narrow bandwidth for fixed beam voltage and magnetic field. However, it has a wide tuning range with suitable tuning of the magnetic field and the beam voltage such that β_c remains $4\pi/p$.

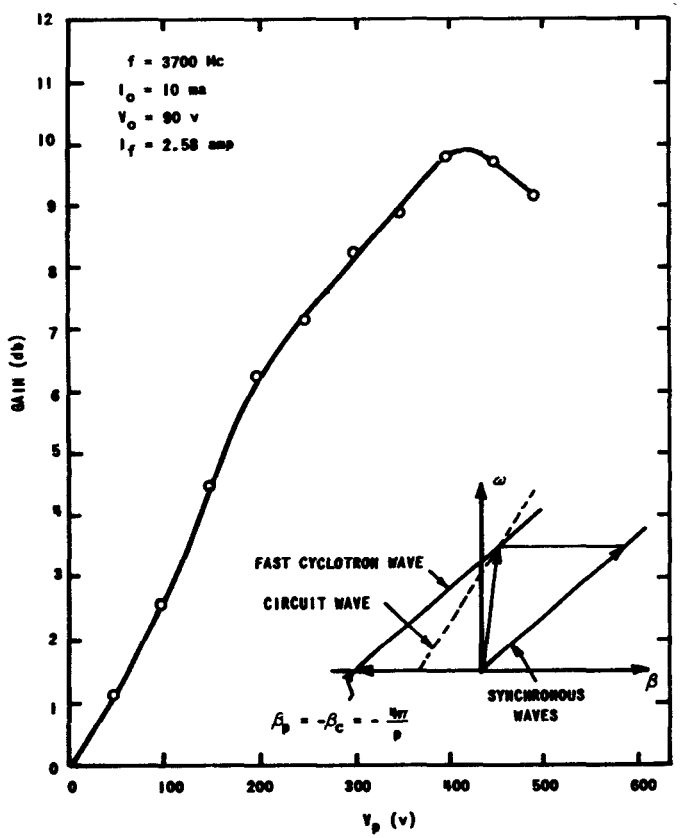

FIG. 95. THE OPERATION WITH SLOWED ELECTRON BEAM UNDER + - + - DC PUMPING.

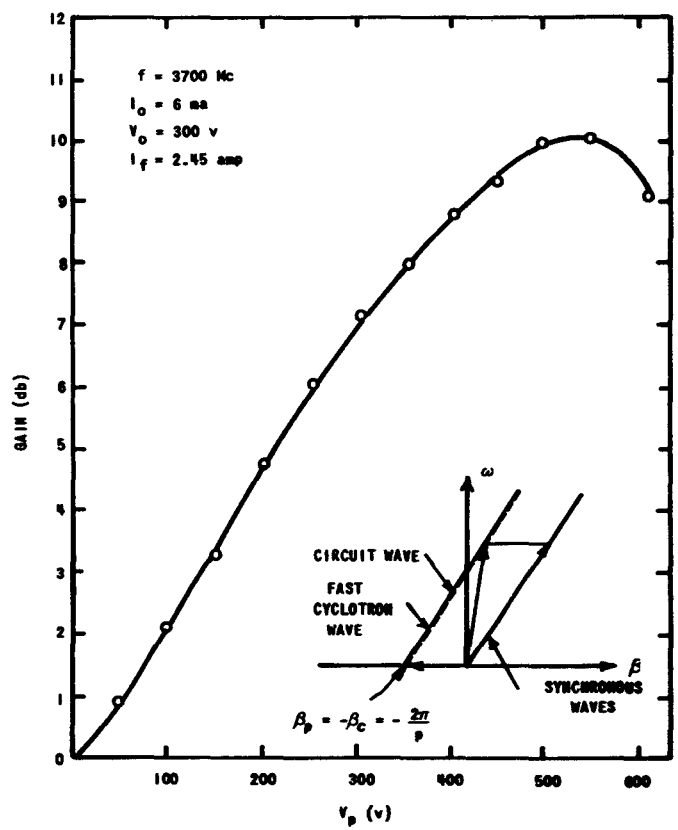

FIG. 96. THE OPERATION WITH SYNCHRONOUS ELECTRON BEAM UNDER + + - - DC PUMPING.

The second unexpected observation of high gain was made using axial antisymmetrical pumping instead of axial symmetrical pumping, i.e., connecting + + - - dc pump voltages to successive helices instead of the usual + - + - connections. In essence, the quadrifilar helix is operated as a bifilar helix with two adjacent helices at a positive potential and the remaining two helices at the same negative potential, relative to the center conductor. This pumping field has a wave number exactly half that of the normal mode of operation, because the period along the z-axis is twice as large. The wave number of the pumping field is $\beta_p = -2\pi/p = -\beta_c$. The electron beam is operated at its normal synchronous velocity. The ω-β diagram explaining this operation is presented in Fig. 96. From this diagram one can see that this arrangement has a potentiality for wideband operation.

It should be pointed out that the first and the second arrangements both have the pumping-wave number equal to the cyclotron wave number. This tells us they are essentially similar operations. Figure 96 shows the measured gain in db as a function of pump voltage at the frequency 3700 Mc for the second case, with the beam voltage at 300 v and the beam current at 6 ma. High gain requires a higher pump voltage compared with the results measured under the first arrangement. This is because a lower beam current is used in the second arrangement which has the beam velocity in synchronism with the circuit fundamental mode. To keep the tube below oscillation, the current is limited to 6 ma. In the first arrangement our experimental tube could be operated at a higher beam current without oscillation. However, saturation occurs at about the same gain level of 10 db in both cases at the same frequency.

Our original theory in Chapter II predicts no amplification under this pumping condition, namely, $\beta_p = \beta_c$. This discrepancy is believed to come from the fact that we used the field expression of a simple quadrifilar helix without center conductor in the analysis in Chapter II, whereas we actually used a complicated quadrifilar helix with center conductor in the experimental tube. If one goes back to the mathematics and takes into account the effect that is due to the existence of the center conductor inside the helix, it is found that these operations actually involve all four beam waves and can yield linear gain. This essentially opens a new subject for further studies; a detailed analysis of these new modes of operation will not be presented here.

VI. CONCLUSION AND RECOMMENDATIONS FOR FURTHER STUDIES

In this study, a complete theory of the amplification of cyclotron waves using simultaneous rf coupling and dc pumping is established. Detailed design criteria are also presented. For most operating frequencies, a hollow beam in a helix with center conducting rod appears to be an optimum structure, in part because of the improved pumping strength, and in part because of the comparatively small frequency dependence of the coupling coefficient. Though the bandwidth in practice is somewhat narrowed by the rapid drop in actual interaction impedance compared with the theoretical curve used in arriving at the original prediction, it is conservative to say that the bandwidth would be double that of conventional traveling-wave tubes because in this operation more than twice as large a range of ka can be used. The experimental results from the tube tested are in good correlation with the theoretical predictions and calculations. The low gain obtained is essentially due to an overestimation of pumping strength in the original design. The tube has been tested throughout the L- and S-bands, and very wide bandwidths are observed. These results would be interesting for applications where large bandwidths are required.

An unexpected observation of high-gain operation for dc pumping with phase number equal to the cyclotron phase number ($\beta_p = -\beta_c$) raises further problems for theoretical and experimental study, in order to gain full understanding of this type of operation and to explore all other possible types of operations, if any.

Since the radius of the helix under our mode of operation (namely, the simultaneous rf coupling and dc pumping) is about 5 to 10 times larger than that of the conventional traveling-wave tube operating at the same frequency, this provides a larger available beam area (somewhat mitigated by the use of hollow beams). Thus, the power capability in this mode of operation may be higher. It seems qualitatively that this mode of operation may also offer higher frequency limits from the fabrication point of view, due to the larger size of helix employed. However, because a quadrifilar (possibly bifilar) helix is required instead of a single helix, the construction is more complicated. Structures other than helices which can possibly be used for this operation are flat helices, interdigital lines with ground plane, two interspaced meander lines with ground plane, and any other structure which can propagate a wideband circuit wave and support an active dc pumping field. All these possibilities would be of interest for further explorations and quantitative studies.

APPENDIX A. THE POTENTIAL DISTRIBUTION INSIDE THE QUADRIFILAR HELIX WITH AXIALLY SYMMETRIC DC PUMPING

The potential distribution inside the quadrifilar helix with axially symmetric dc pumping as shown in Fig. 6 can be derived by solving Laplace's equation:

$$\frac{1}{r}\frac{\partial}{\partial r}\left(r\frac{\partial V}{\partial r}\right) + \frac{1}{r^2}\frac{\partial^2 V}{\partial \phi^2} + \frac{\partial^2 V}{\partial z^2} = 0 \tag{A.1}$$

The solution may be assumed in product form, $RZ\Phi$, where R is a function of r alone, Z of z alone, and Φ of ϕ alone. In matching the boundary conditions of the quadrifilar helix, Z has solutions in sinusoidal function with spatial periodicity $p/2$; Φ also has solutions in sinusoidal form with circumferential periodicity π; and R has solutions of the Bessel type. Since the center axis of the helix is included in the solution, the Bessel solution of the second kind will not appear in the result, in order that it be finite at the center. By going through the mathematics, one can readily find that the solution that satisfies the present boundary situation is of the following form:

$$V = A\, J_2\,(kr) \cdot \sin\,(2\phi - 2\beta_q z) \tag{A.2}$$

This can be simplified for small kr by taking only the smallest order term in the series expansion as an approximation of the Bessel function

$$V = \frac{Kr^2}{2} \sin\,(2\phi - 2\beta_q z) \tag{A.3}$$

where $\beta_q = 2\pi/p$, k and A are constants, $K = Ak^2$. Expanding the sine factor, one can easily obtain

$$V = \frac{K}{2}\,[2xy \cos 2\beta_q z - (x^2 - y^2) \sin 2\beta_q z] \tag{A.4}$$

as introduced in Eq. (2.4).

APPENDIX B. FOUR-WAVE ANALYSIS

As analyzed in Chapter III, a quadrifilar helix can be used as a simultaneous rf coupling and dc pumping structure for cyclotron-wave amplification. We obtained the complete solution for the case where the coupling coefficient for the +1 mode circuit wave is negligibly small. In that case, the +1 mode circuit can be considered as uncoupled, so that only three waves are involved within this structure. The fast cyclotron wave is passively coupled with the -1 mode circuit wave by circuit design, and the fast cyclotron wave is also actively coupled with the slow cyclotron wave by means of dc pumping. Because of these couplings, all three waves will grow exponentially with distance along the beam. As a consequence, this amplifier does not possess low-noise characteristics such as the Adler-Wade tube does. As shown in Fig. 46, this amplifier may have a large bandwidth over a 50-db pump range. This novel characteristic leads to an interest in finding the effect of the +1 mode circuit wave when the coupling to this mode is not negligible. In this case we will add one more coupling into the problem, i.e., the +1 mode circuit wave coupled with the slow cyclotron wave in the beam. The coupled-mode equations for the four-wave case are:

$$\frac{dA_s}{dz} = jk_+ A_o^{(+1)} + k_p A_f$$

$$\frac{dA_f}{dz} = jk_- A_o^{(-1)} + k_p A_s$$

$$\frac{dA_o^{(+1)}}{dz} = -jk_+^* A_s$$

$$\frac{dA_o^{(-1)}}{dz} = +jk_-^* A_f$$

where k_+ = coupling coefficient for +1 mode

k_- = coupling coefficient for -1 mode

k_p = coupling coefficient for dc pumping

$A_o^{(+1)}$ = magnitude of +1 mode on the circuit

$A_o^{(-1)}$ = magnitude of -1 mode on the circuit

A_s = magnitude of slow wave in the beam

A_f = magnitude of fast wave in the beam.

By Laplace transformation we have the Laplacian solution for the coupled-mode equations as:

$$\begin{bmatrix} a_s(s) \\ a_f(s) \\ a_o^{(+1)}(s) \\ a_o^{(-1)}(s) \end{bmatrix} = \frac{1}{\Delta} \begin{bmatrix} s(s^2+k_-^2) & s^2k_p & jk_+(s^2+k_-^2) & jk_pk_-s \\ s^2k_p & s(s^2-k_+^2) & jk_pk_+s & jk_-(s^2-k_+^2) \\ -jk_+^*(s^2+k_-^2) & -jk_pk_+^*s & s(s^2-k_p^2+k_-^2) & k_pk_-k_+^* \\ jk_pk_-^*s & jk_-^*(s-k_+^2) & -k_pk_-^*k_+ & s(s^2-k_p^2-k_+^2) \end{bmatrix} \begin{bmatrix} A_s(0) \\ A_f(0) \\ A_o^{(+1)}(0) \\ A_o^{(-1)}(0) \end{bmatrix}$$

where

$$\Delta = s^4 - (k_p^2 + k_+ - k_-^2)\ s^2 - k_+^2\ k_-^2$$
$$= (s^2 - s_1^2)\ (s^2 - s_2^2)$$

and

$$s_1 = \alpha,\ s_2 = j\beta$$

$$\begin{Bmatrix} \alpha \\ \beta \end{Bmatrix} = \left[\frac{1}{2} \sqrt{(k_p^2 + k_+^2 - k_-^2) + 4k_+^2\ k_-^2} \pm \frac{1}{2}\ (k_p^2 + k_+^2 - k_-^2) \right]^{1/2}$$

It is evident that α gives exponentially growing components and β gives sinusoidally nongrowing components.

The complete solution can be written as:

$$\begin{bmatrix} A_s(z) \\ A_f(z) \\ A_o^{(+1)}(z) \\ A_o^{(-1)}(z) \end{bmatrix} = \begin{bmatrix} g_{s,s} & g_{s,f} & g_{s,+} & g_{s,-} \\ g_{f,s} & g_{f,f} & g_{f,+} & g_{f,-} \\ g_{+,s} & g_{+,f} & g_{+,+} & g_{+,-} \\ g_{-,s} & g_{-,f} & g_{-,+} & g_{-,-} \end{bmatrix} \begin{bmatrix} A_s(0) \\ A_f(0) \\ A_o^{(+1)}(0) \\ A_o^{(-1)}(0) \end{bmatrix}$$

where

$$g_{s,s} = \frac{1}{\alpha^2+\beta^2}\left[(\alpha^2 + k_-^2)\cosh \alpha z + (\beta^2 - k_-^2)\cos \beta z\right]$$

$$g_{f,f} = \frac{1}{\alpha^2+\beta^2}\left[(\alpha^2 - k_+^2)\cosh \alpha z + (\beta^2 + k_+^2)\cos \beta z\right]$$

$$g_{+,+} = \frac{1}{\alpha^2+\beta^2}\left[(\alpha^2 - k_p^2 + k_-^2)\cosh \alpha z + (\beta^2 + k_p^2 - k_-^2)\cos \beta z\right]$$

$$g_{-,-} = \frac{1}{\alpha^2+\beta^2}\left[(\alpha^2 - k_p^2 - k_+^2)\cosh \alpha z + (\beta^2 + k_p^2 + k_+^2)\cos \beta z\right]$$

$$g_{s,f} = \frac{k_p^2}{\alpha^2+\beta^2}\left[\alpha \sinh \alpha z + \beta \sin \beta z\right]$$

$$g_{s,+} = -\frac{k_+}{k_+^*}\, g_{+,s} = \frac{jk_+}{\alpha^2+\beta^2}\left[\alpha\left(1 + \frac{k_-^2}{\alpha^2}\right)\sinh \alpha z + \beta\left(1 - \frac{k_-^2}{\beta^2}\right)\sin \beta z\right]$$

$$g_{s,-} = \frac{k_-}{k_-^*}\, g_{-,s} = \frac{jk_pk_-}{\alpha^2+\beta^2}\left[\alpha \sinh \alpha z + \beta \sin \beta z\right]$$

$$g_{f,+} = -\frac{k_+}{k_+^*}\, g_{+,f} = \frac{jk_pk_+}{\alpha^2\beta^2}\left[A \sinh \alpha z + \beta \sin \beta z\right]$$

$$g_{f,-} = \frac{k_-}{k_-^*}\, g_{-,f} = \frac{jk_-}{\alpha^2\beta^2}\left[(\alpha^2 - k_+^2)\cosh \alpha z + (\beta^2 + k_-^2)\cos \beta z\right]$$

$$g_{+,-} = \frac{k_-k_+^*}{k_-^*k_+}\, g_{-,+} = \frac{k_pk_-k_+^*}{\alpha^2\ \ ^2}\left[\frac{1}{\alpha}\sinh \alpha z - \frac{1}{\beta}\sin \beta z\right]$$

For gain studies, the most interesting terms are the power gains of the circuit waves with a tube length L. They can be expressed in a form useful for calculation as follows:

$$G_{-,-} = (g_{-,-})^2 = \frac{1}{4}\,[(1 - C_-)\cosh \alpha'\,(k_pL) + (1 + C_-)\cos \beta'\,(k_pL)]^2$$

$$G_{+,+} = (g_{+,+})^2 = \frac{1}{4}\,[(1 - C_+)\cosh \alpha'\,(k_pL) + (1 + C_+)\cos \beta'\,(k_pL)]^2$$

and

$$G_{+,-} = G_{-,+} = \frac{1}{D^2}\,[\beta' \sinh \alpha'\,(k_pL) - \alpha' \sin \beta'\,(k_pL)]^2$$

where

$$D = \sqrt{(1 + \tau_+^2 - \tau_-^2)^2 + 4\tau_+^2\,\tau_-^2}$$

$$\begin{matrix}\alpha' \\ \beta'\end{matrix} = \left[\frac{1}{2}\,D \pm \frac{1}{2}\,(1 + \tau_+^2 - \tau_-^2)\right]^{1/2}$$

$$C_- = \frac{1 + \tau_+^2 + \tau_-^2}{D}$$

$$C_+ = \frac{1 - \tau_+^2 - \tau_-^2}{D}$$

$$\tau_+ = \frac{k_+}{k_p}$$

$$\tau_- = \frac{k_-}{k_p}$$

k_pL = the pump level.

Let us consider a special case such that the coupling coefficient for the +1 mode equals that of the -1 mode, i.e., $\tau_+ = \tau_- = \tau$. Then we have

$$D = 2\tau^2\sqrt{1 + \frac{1}{4\tau^4}}$$

$$\begin{matrix}\alpha' \\ \beta'\end{matrix} = \sqrt{\frac{1}{2}(D \pm 1)}$$

$$C_- = \frac{1 + 2\tau^2}{D}$$

$$C_+ = \frac{1 - 2\tau^2}{D}$$

The gains for this special case are plotted as functions of τ in Fig. 97 for the pump level G_{po} = 20 db; in Fig. 98 for G_{po} = 40 db; and in Fig. 99 for G_{po} = 60 db. Referring to the curves of the frequency parameter vs $ka = \omega/\omega_c$, as shown in Figs. 42, 43, and 44, one can notice the bandwidth is essentially unlimited. There is no upper limit on the value of τ as in the three-wave case. Therefore, the four-wave coupling operation might give even better bandwidth than the three-wave coupling operation in this case.

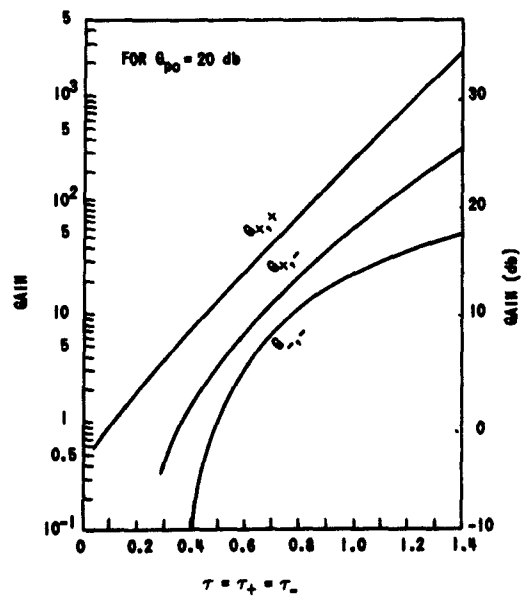

FIG. 97. THE GAINS OF THE CIRCUIT WAVES PLOTTED AS FUNCTIONS OF τ AT PUMP LEVEL G_{po} = 20 db.

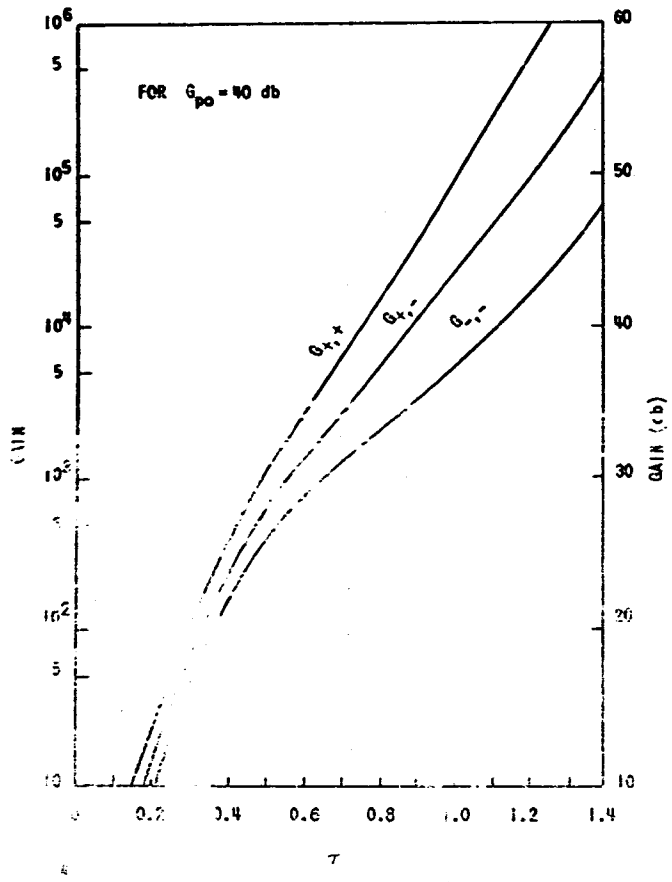

FIG. 98. THE GAINS OF THE CIRCUIT WAVES PLOTTED AS FUNCTIONS OF τ AT PUMP LEVEL G_{po} = 40 db.

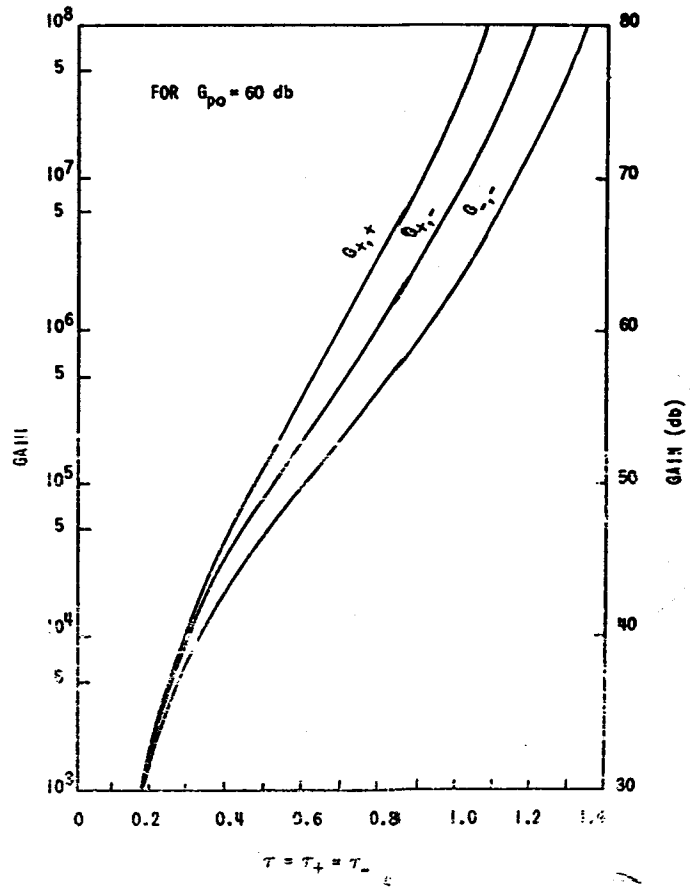

FIG. 99. THE GAINS OF THE CIRCUIT WAVES PLOTTED AS FUNCTIONS OF τ AT PUMP LEVEL G_{po} = 60 db.

Best Available Copy

APPENDIX C: THE TRANSVERSE IMPEDANCE OF HELICES WITH CENTER CONDUCTOR

The transverse impedance of a quadrifilar helix with center conductor close to the helix as shown in Fig. 100 can be derived from the simplified transverse E field as follows:

$$
E_t(z) = \begin{cases}
\dfrac{V_1}{a-b} & \text{for} \quad 0 < z < w \\[2ex]
0 & \text{for} \quad w < z < w + \delta = \dfrac{p}{4} \\[2ex]
\dfrac{V_4 \exp(-j\beta z)}{a-b} & \text{for} \quad \dfrac{p}{4} < z < \dfrac{p}{4} + w \\[2ex]
0 & \text{for} \quad \dfrac{p}{4} + w < z < \dfrac{p}{2} \\[2ex]
\dfrac{V_3 \exp(-j\beta z)}{a-b} & \text{for} \quad \dfrac{p}{2} < z < \dfrac{p}{2} + w \\[2ex]
0 & \text{for} \quad \dfrac{p}{2} + w < z < \dfrac{3p}{4} \\[2ex]
\dfrac{V_2 \exp(-j\beta z)}{a-b} & \text{for} \quad \dfrac{3p}{4} < z < \dfrac{3p}{4} + w \\[2ex]
0 & \text{for} \quad \dfrac{3p}{4} + w < z < p
\end{cases}
\tag{B.1}
$$

where the V's are the excitation voltage on each helix at the input plane ($z = 0$) and are linear combinations of the four independent modes as shown in Eq. (2.8) and where β is the phase delay in a full pitch, $\beta = \frac{2\pi}{p} = 2\pi k$. We assume that:

$$
E_t(z) = \sum_n E_{tn}\, e^{-j\beta_n z} \tag{B.2}
$$

where

$$
\beta_n = \beta_0 + n\frac{2\pi}{p} = (ka + n)\frac{2\pi}{p} \tag{B.3}
$$

Best Available Copy

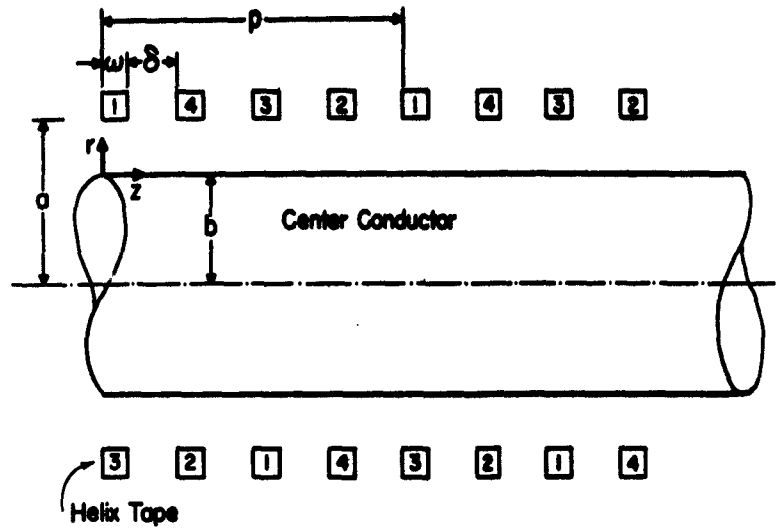

FIG. 100. THE DIMENSIONS OF A QUADRIFILAR HELIX WITH CENTER CONDUCTOR.

Then:

$$E_{tn} = \frac{1}{p} \int_{o}^{p} E_t(z)\, e^{j\beta_n z}\, dz \tag{B.4}$$

This integration consists of four intervals, and the solution is found to be:

$$E_{tn} = \frac{w \exp(j \frac{1}{2} \beta_n w)}{p(a-b)} \operatorname{sinc}\left(\frac{1}{2} \beta_n w\right) \left\{ V_1 + V_4 \exp\left[j \frac{1}{4}\left(\beta_n p - \theta\right)\right] \right.$$

$$\left. + V_3 \exp\left[j \frac{1}{2}\left(\beta_n p - \theta\right)\right] + V_2 \exp\left[j \frac{3}{4}\left(\beta_n p - \theta\right)\right] \right\} \tag{B.5}$$

where $\operatorname{sinc} x = \frac{(\sin x)}{x}$ since

$$\beta_n p - \theta = (ka + n)\, 2\pi - 2\pi ka = 2\pi m \tag{B.6}$$

and note:

$$\exp[j(\pi/2)] = j \tag{B.7}$$

so:

$$E_{tn} = \frac{\exp(j\,\frac{1}{2}\,\beta_n w)}{(a-b)}\,\mathrm{sinc}\left(\frac{1}{2}\,\beta_n w\right)\,[V_1 + (j)^n\,V_4 + (-1)^n\,V_3 + (-j)^n\,V_2] \tag{B.8}$$

Substituting the normal modes of Eq. (2.83) into Eq. (B.8), we have:

$$E_{tn} = \frac{w\,\exp(j\,\frac{1}{2}\,\beta_n w)}{p(a-b)}\,\mathrm{sinc}\left(\frac{1}{2}\,\beta_n w\right)\,\{A_o[1 + (j)^n + (-1)^n + (-j)^n]$$

$$+ A_{+1}[1 - j(j)^n - (-1)^n + j(-j)^n] + [A_{-1}[1 + j(j)^n - (-1)^n - j(-j)^n]$$

$$+ A_{-2}[1 - (j)^n + (-1)^n - (-j)^n]\} \tag{B.9}$$

The power flow in the quadrifilar helix is:

$$P = \frac{1}{2Z_o}\,(V_1V_1^* + V_2V_2^* + V_3V_3^* + V_4V_4^*) \tag{B.10}$$

Substituting the normal modes of Eq. (2.83) into Eq. (B.10) and approximating the characteristic impedance Z_o as that of a strip line above a ground plane,

$$Z_o = \sqrt{\frac{\mu}{\epsilon}}\,\frac{a-b}{w} \tag{B.11}$$

then:

$$P = \frac{2(A_oA_o^* + A_{+1}A_{+1}^* + A_{-1}A_{-1}^* + A_{-2}A_{-2}^*)}{\sqrt{\frac{\mu}{\epsilon}}\,\frac{a-b}{w}} \tag{B.12}$$

Therefore from the definition of K_t as shown in Siegman's paper [Ref. 2]:

$$K_{tn} = \frac{E_{tn}E_{tn}^{*}}{4\beta_n^2 p} = \frac{\frac{1}{4}\,\frac{4w}{p}\sqrt{\frac{\mu}{\epsilon}}\,\mathrm{sinc}^2\left(\frac{1}{2}\,\beta_n w\right)}{|\beta_n|\,(a-b)\,|ka+n|} \tag{B.13}$$

or:

$$K_{tn} = \frac{30\,\frac{4w}{p}\,\mathrm{sinc}^2\left(\frac{1}{2}\,\beta_n w\right)}{|\beta_n|\,(a-b)\,|ka+n|} \tag{B.14}$$

For the helix made of wide tape with small gap, i.e., $\delta \ll w$, one can approximate $4w \simeq p$; and for small β_n's, sinc $(1/2\ \beta_n w)$ is approximately unity. The transverse impedance is then approximately

$$K_{tn} = \frac{30}{|\beta_n|\,(a-b)\,|ka+n|} \tag{B.14a}$$

APPENDIX D. THE PUMPING COEFFICIENT OF A QUADRIFILAR HELIX WITH CENTER CONDUCTING ROD

The large-radius and small-pitch-angle quadrifilar helix with center conductor close to the helix can be developed to form a two-dimensional structure as shown in Fig. 101. This structure provides a two-dimensional electrostatic field with periodicity in the z-direction. In the x-direction, the structure is considered wide enough so that no end effects need be taken into consideration (i.e., $2\pi a \gg a - b$). By solving the Laplace equation and matching the boundary conditions, one can readily find that the potential distribution within this structure is

$$V = V_o + |V_p| \sum_n A_n \frac{\sinh \beta_n (y - b)}{\sinh \beta_n (a - b)} \sin \beta_n z \qquad \text{(D.1)}$$

where V_o is the base potential on the ground plane developed from the center conductor, V_p is the pump voltage, the A_n's are constants chosen to match the boundary conditions, and $\beta_n = (2n - 1)\, 4\pi/p$.

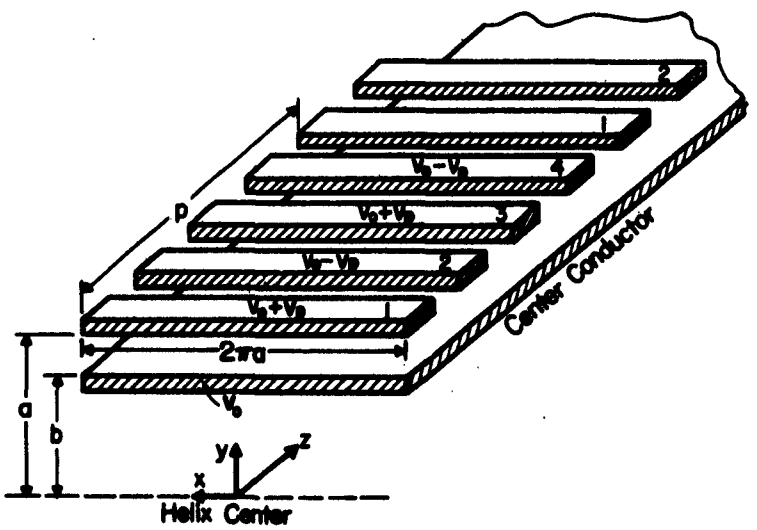

FIG. 101. A DEVELOPED QUADRIFILAR HELIX WITH CENTER CONDUCTOR CLOSE TO THE HELIX.

Substituting this potential distribution into the equation of motion of an electron and considering only the predominant fundamental variation of the fields, i.e., n = 1, one obtains

$$\frac{d^2y_1}{d\theta^2} + y_1 - \frac{u}{\beta_1} \cosh \beta_1 (y_o + y_1 - b) \sin \beta_1 z = 0 \tag{D.2}$$

where y_o is the electron position without pumping, y_1 is the deviation of the electron position from y_o, and

$$\theta = \omega_c t$$

$$\beta_1 = \frac{4\pi}{p} = 2\beta_q = \beta_p \tag{D.3}$$

$$u = \frac{\eta |V_p| \; A_1 \; \beta_1^2}{\omega_c^2 \sinh \beta_1 (a - b)}$$

For small pumping strength, the axial velocity of the electrons can be considered as a constant. Then one can transfer the electron moving frame to the laboratory frame by:

$$\theta - \theta_o = \beta_c z \tag{D.4}$$

and one can also make the following approximations

$$\cosh \beta_1 y_1 \cong 1 \qquad \text{and} \qquad \sinh \beta_1 y_1 \cong \beta_1 y_1 \tag{D.5}$$

Then the differential equation for y_1 becomes

$$\frac{d^2y_1}{dz^2} + \beta_c^2 y_1 - 4\beta_c\left(\frac{c}{\beta_1} + s y_1\right) \sin \beta_1 \; z = 0 \tag{D.6}$$

where

$$c = \frac{u\beta_c}{4} \cosh \beta_1 (y_o - b) \tag{D.7}$$

$$s = \frac{u\beta_c}{4} \sinh \beta_1 (y_o - b) \tag{D.8}$$

Since y_1 is a linear combination of the four transverse waves

$$y_1 = j\left[A_f\, e^{j\beta_c z} + A_s\, e^{-j\beta_c z} - A_1 - A_2\right] \tag{D.9}$$

Substituting this relation into Eq. (D.6), one obtains the key equation that shows the interaction among the beam waves due to the pumping field with varying helix pitch,

$$\left[\frac{d^2A_f}{dz^2} + j2\beta_c \frac{dA_f}{dz}\right] e^{j\beta_c z} + \left[\frac{d^2A_s}{dz^2} - j2\beta_c \frac{dA_s}{dz}\right] e^{-j\beta_c z}$$

$$- \left[\frac{d^2A_1}{dz^2} + \beta_c^2 A_1\right] - \left[\frac{d^2A_2}{dz^2} + \beta_c^2 A_2\right]$$

$$= -j2\beta_c \left[\frac{c}{j\beta_1} + s\left(A_f\, e^{j\beta_c z} + A_s\, e^{-j\beta_c z} - A_1 - A_2\right)\right]\left(e^{j\beta_1 z} - e^{-j\beta_1 z}\right) \tag{D.10}$$

For the case that the electron travels one pitch in one cyclotron period, that is, $\beta_1 = 2\beta_c$, one finds that the fast and the slow cyclotron waves are coupled, due to this pumping field, in the form

$$\frac{d^2A_f}{dz^2} + j2\beta_c \frac{dA_f}{dz} = -j2\beta_c\, s\, A_s \tag{D.11}$$

$$\frac{d^2A_s}{dz^2} - j2\beta_c \frac{dA_s}{dz} = +j2\beta_c\, s\, A_f \tag{D.12}$$

Assume the magnitudes of the waves vary as $e^{\nu z}$. Then the eigenvalues of ν must satisfy the following equation

$$\begin{vmatrix} \nu^2 + j2\beta_c\nu & j2\beta_c s \\ -j2\beta_c s & \nu^2 - j2\beta_c\nu \end{vmatrix} = 0 \tag{D.13}$$

These eigenvalues are

$$\begin{matrix}\nu_1 \\ \nu_2\end{matrix} = \pm\, \alpha \qquad \begin{matrix}\nu_3 \\ \nu_4\end{matrix} = \pm\, j\beta \tag{D.14}$$

where

$$\alpha = \sqrt{2\beta_c^2\left(\sqrt{1 + \frac{s^2}{\beta_c^2}} - 1\right)} \cong s \tag{D.15}$$

$$\beta = \sqrt{2\beta_c^2\left(\sqrt{1 + \frac{s^2}{\beta_c^2}} + 1\right)} \cong 2\beta_c\sqrt{1 + \frac{s^2}{4\beta_c^2}} \tag{D.16}$$

Hence the exponentially growing pumping coefficient is

$$k_p = s = A_1 \frac{\sinh 2\beta_c(y_o - b)}{\sinh 2\beta_c(a - b)} \cdot \frac{|V_p|\beta_c}{2V_o} \tag{D.17}$$

REFERENCES

1. A. H. W. Beck, *Space Charge Wave and Slow Electromagnetic Waves*, Pergamon Press, New York, 1958.
2. A. E. Siegman, "Waves on a Filamentary Electron Beam in a Transverse-Field Slow-Wave Circuit," *J. Apply. Phys.*, *31*, Jan 1960, pp. 17-26.
3. W. H. Louisell and C. F. Quate, "Parametric Amplification of Space Charge Waves," *Proc. IRE*, *46*, Apr 1958, pp. 707-716.
4. A. Ashkin, "Parametric Amplification of Space Charge Waves," *J. Appl. Phys.*, *29*, Dec 1955, pp. 1646-1651.
5. J. S. Cook and W. H. Louisell, "Fast Longitudinal Space Charge Wave Parametric Amplifiers," *IRE WESCON Conv. Rec.*, Part 3, Aug 1959, p. 77.
6. H. Sobol, "Extension of Longitudinal-Beam Parametric Amplifier Theory," *Proc. IRE* (Correspondence), *48*, Apr 1960, pp. 792-793.
7. R. Adler, G. Hrbek, and G. Wade, "A Low-Noise Electron-Beam Parametric Amplifier," *Proc. IRE*, *46*, Oct 1958, pp. 1756-1757.
8. R. Adler, G. Hrbek, and G. Wade, "The Quadrupole Amplifier, a Low-Noise Parametric Device," *Proc. IRE*, *47*, Oct 1959, pp. 1713-1727.
9. A. Ashkin, "A Low Noise Microwave Quadrupole Amplifier," *Proc. IRE*, *49*, Jun 1961, pp. 1016-1019.
10. T. E. Everhart, "Space Charge Effect in a Quadrupole Pump," *Proc. Internatt. Mikrowellen Tagung, Munich, June 7-11, 1960.* Friedr. Vieweg and Sohn, Braunschweig, Germany, Aug 1961, pp. 350-352.
11. C. P. Lea-Wilson, "Some Possible Causes of Noise in Adler Tubes," *Proc. IRE* (Correspondence), *48*, Feb 1960, pp. 225-256.
12. E. I. Gordon, "Noise in Beam-Type Parametric Amplifiers," *Proc. IRE*, *49*, 7, Jul 1961, p. 1208.
13. F. N. H. Robinson and R. N. Franklin, "The Transverse Electric Noise from an Electron Beam," *J. Elec. and Control*, *10*, 4, Apr 1961, p. 277.
14. P. A. H. Hart, "On Cyclotron Wave Noise Reduction," *Proc. IRE* (Correspondence), *50*, 2, Feb 1962, pp. 227-228.
15. R. Adler and G. Wade, "Beam Refrigeration by Means of Large Magnetic Fields," *J. Appl. Phys.*, *31*, 7, Jul 1960, pp. 1201-1203.
16. E. I. Gordon, S. J. Buchsbaum, and J. Feinstein, "A Transverse Field Amplifier Employing Cyclotron Resonance Interaction," Paper presented at the 17th Conference on Electron Tube Research, Mexico City, Mexico, Jun 1959.
17. E. I. Gordon, Private Communication, Bell Telephon Laboratories, Murray Hill, N. J.
18. A. E. Siegman and S. Mao, "Wave Analysis of the d-c Pumped Quadrupole Amplifier," Paper presented to the Conference on Electron Tube Research, Seattle, Wash., 30 Jun 1960.
19. A. E. Siegman, "The d-c Pumped Quadrupole Amplifier--A Wave Analysis," *Proc. IRE*, *48*, Oct 1960, pp. 1750-1755.

20. T. Wessel-Berg, "Transverse-Field Couplers for Electron Beams," Tech. Note No. 1, Contract A.F. 61(052)-531. Internal Report No. IR-R-97, Norwegian Defense Research Establishment, Bergen, Norway, Jul 1961.

21. T. Wessel-Berg and K. Blötekjaer, "Some Aspects of Cyclotron Wave Interaction in Time Periodic and Space Periodic Fields," *Record of the International Congress on Microwave Tubes, Munich, June 1960.* Friedr. Vieweg and Sohn, Braunschweig, Germany, 1961, pp. 372-382.

22. Kjelt Blötekjaer, "Transverse Wave Amplification in Periodic Electrostatic and Magnetic Fields," Paper presented at the NATO Conference on Microwave Techniques, Paris, Mar 1962.

23. J. C. Bass, "Microwave Amplification in Electrostatic Ring Structures," *Proc. IRE* (Correspondence) *49*, Sept 1961, pp. 1424-1425.

24. J. C. Bass, "A d-c Pumped Amplifier with a Two Dimensional Field Structure," *Proc. IRE* (Correspondence), *49*, Dec 1961, pp. 1957-1958.

25. G. Wade, K. Amo, and D. Watkins, "Noise in Transverse-Field Tubes," *J. Appl. Phys.*, *35*, 12, Dec 1954, pp. 1514-1520.

26. P. A. Sturrock, "Parametric Refrigeration--A Mechanism for Removal of Noise from the Slow Wave of an Electron Beam," Internal Memo. No. 656, Microwave Laboratory, Stanford University, Stanford, Calif., Oct 1959.

27. H. A. Haus, "Noise on One-Dimensional Beams," *J. Appl. Phys.*, *26*, May 1955, p. 560.

28. S. Sensiper, "Electromagnetic Waves Propagation on Helical Conductors," Report No. 194, MIT Research Lab. of Elec., 16, May 1951.

29. P. K. Tien, Private Communication, Bell Telephone Laboratories, Murray Hill, N. J.

30. G. W. C. Mathers and G. S. Kino, "Some Properties of a Sheath Helix with a Center Conductor or External Shield," TR No. 65, Stanford Electronics Laboratories, Stanford, Calif., Contract N6onr-251(07), 17 Jun 1952.

31. J. R. Pierce and P. K. Tien, "Coupling of Modes in Helices," *Proc. IRE*, *42*, Sep 1954, pp. 1389-1396.

32. D. A. Watkins and A. E. Siegman, "Helix Impedance Measurements Using an Electron Beam," *J. Appl. Phys.*, *24*, Jul 1953, pp. 917-922.

33. H. R. Johnson, T. E. Everhart, and A. E. Siegman, "Wave Propagation on Multifilar Helices," *IRE Trans.*, *ED-3*, Jan 1956, p. 18.

34. J. S. Cook, R. Kompfner, and C. F. Quate, "Coupled Helices," *Bell Sys. Tech. J.*, *35*, Jan 1956, pp. 127-178.

35. D. G. Dow, "Modified Multifilar Helices for Use in Wide Band Traveling Wave Tubes," TR No. 37, Stanford Electronics Laboratories, Stanford, Calif., Contract Nonr-225(24), May 1958.

36. C. M. Chu, "Propagation of Waves in Helical Waveguides," *J. Appl. Phys.*, *37*, Jan 1958, p. 88.

37. J. R. Pierce, "Coupling Modes of Propagation," *J. Appl. Phys.*, *25*, Feb 1954, pp. 178-183. Also, "The Wave Picture of Microwave Tubes," *Bell Sys. Tech. J.*, *33*, 1954, pp. 1343-1372.

38. W. H. Louisell, *Coupled Mode and Parametric Electronics*, John Wiley and Sons, Inc., New York, 1960.

39. R. W. Gould, "A Coupled Mode Description of B.W.O. and the Kompfner Dip Conditions," *Proc. IRE*, *43*, Jul 1955, p. 874.

40. J. R. Pierce, *Traveling-Wave Tubes*, D. Van Norstrand Co., Inc., New York, 1950.

41. C. P. Lea-Wilson, "Some Possible Causes of Noise in Adler Tubes," *Proc. IRE* (Correspondence), *48*, Feb 1960, pp. 255-256.

42. R. Adler, G. Hrbek, and G. Wade, "The Noise Behavior of Quadrupole Parametric Amplifiers," Paper presented at the Conference on Electron Tube Research, Mexico City, Mexico, 26 Jun 1959.

43. T. Wessel-Berg and K. Blötekjaer, "Noise Reduction Schemes in Transverse Modulation Tubes," Paper presented at the AGARD Low Noise Symposium, Oslo, Aug 1961. Internal Report No. IR-R-103, Norwegian Defence Research Establishment, Bergen, Norway, Nov 1961. *IRE Trans.*, *ED-9*, Sep 1962.

44. H. A. Haus and F. N. H. Robinson, "The Minimum Noise Figure of Microwave Beam Amplifier," *Proc. IRE*, *43*, Aug. 1955, pp. 981-991.

45. D. A. Dunn and W. R. Luebke, "Beam Perturbations in Confined Flow Electron Beams with Planar Symmetry," *IRE Trans.*, *ED-4*, 3, Jul 1957, pp. 265-270.

46. J. R. Pierce, *Theory and Design of Electron Beams*, 2nd ed., D. Van Nostand Co., Inc., New York, 1954.

47. P. G. R. King, "Electron Guns for Traveling-Wave Tubes," *S.E.R.L. Tech. J.*, (England), *4*, Feb 1954.

ELECTRON DEVICES DISTRIBUTION LIST

April 1963

GOVERNMENT

Commanding Officer, USAELRDL
Ft. Monmouth, N.J.
1 Attn: SIGRA/SL-PRM
1 Attn: SIGRA/SL-PA
2 Attn: SIGRA/SL-SC
1 Attn: SIGRA/SL-XS, H. Cohen
1 Attn: TDC Bldg. No. 27
1 Attn: H. Brett
1 Attn: Dr. E. M. Reilley, Dir. Inst. for Explor. Res.
1 Attn: SIGRA/SL-ADT-E
1 Attn: SIGRA/SL-ADT
2 Attn: Dir. Commun. Dept.

U.S. Army Signal Material Support Agency
Ft. Monmouth, N.J.
1 Attn: SIGMS-ADJ
1 Attn: Engr. Proc edures Br. Millard Rosenfeld

Electronic Warfare Div., USASCS
Ft. Monmouth, N.J.
1 Attn: H. Allem

Director of Research, USAELRDL
Ft. Monmouth, N.J.
1 Attn: Harold A. Zahl

Marine Corps Liaison Office
1 Ft. Monmouth, N.J.

Corps of Engr. Liaison Office
1 Ft. Monmouth, N.J.
1 Attn: SIGRA/SL-LNE

Army Liaison Office
1 Lexington, Mass.

U.S. Army Engr. R and D Lab
Ft. Belvoir, Va.
1 Attn: Tech. Doc. Ctr.

Signal Corps Liaison Office
Cambridge, Mass.
1 Attn: A. D. Bedrosian

Commanding General
U.S. Army Ordnance Missile Command
Redstone Arsenal, Alabama
1 Attn: ORDXM-RFE, Mr. Lindberg
1 Attn: Technical Library

Commanding Officer, Frk.Rd.Asnel.
Philadelphia 37, Pa.
1 Attn: ORDBA 1520
1 Attn: Library Br., 0270

Commanding Officer
Watertown Arsenal
Watertown, Mass.
1 Attn: OMRO

Ballistics Research Lab
Aberdeen Proving Ground, Md.
1 Attn: V. W. Richard, BRL

Commanding Officer
White Sands Missile Range, N.M.
1 Attn: SIGMS-MEW

Commanding General
U.S. Army Electr. Proving Ground
Ft. Huachuca, Arizona
1 Attn: Tech. Library

Chief of Naval Research
Dept. of the Navy
Washington 25, D.C.
1 Attn: Code 427

Commanding Officer
ONR Branch Office
1000 Geary St.
1 San Francisco 9, Calif.

Chief Scientist, ONR Branch Office
1030 E. Greene St.
1 Pasadena, Calif.

Commanding Officer, ONR Branch Off.
John Crerar Library Bldg.
86 E. Randolph St.
1 Chicago 1, Ill.

Commanding Officer, ONR Branch Off.
207 W 24th St.
1 New York 11, N.Y.

New York Naval Shipyard
Material Lab Library, Bldg. 291
Brooklyn, N.Y.
1 Attn: Code 913.5, M. Rogofsky

Officer-in-Charge, ONR
Navy No. 100, Box 39, Fleet P.O.
16 New York, N.Y.

U.S. Naval Research Lab
Washington 25, D.C.
6 Attn: Code 2000
1 Attn: Code 2027
1 Attn: Code 5200
1 Attn: Code 5240
1 Attn: Code 5260
1 Attn: Code 5260
1 Attn: Code 5300
1 Attn: Code 5400
1 Attn: Code 5430

Chief, Bureau of Ships
Washington 25, D.C.
1 Attn: Code 691A1
3 Attn: Code 670B

Chief, Bureau of Naval Weapons
Washington 25, D.C.
1 Attn: Code RAAV-6
1 Attn: Code RREN-3
1 Attn: Code RAAV-44

Chief of Naval Operations
Navy Dept.
Washington 25, D.C.
1 Attn: Code Op 94T - Pentagon 4C717
1 Attn: Code Op 352

Commanding Officer and Director
U.S. Navy Electronics Lab
1 San Diego 52, Calif.

U.S. Naval Post Graduate School
Monterey, Calif.
1 Attn: Tech. Reports Librarian

Weapons System Test Division
Patuxent River, Md.
1 Attn: Library

Commander U.S. Naval Missile Ctr
Pt. Mugu, Calif.
1 Attn: N 3232

U.S. Naval Weapons Lab
Dahlgren, Va.
1 Attn: Tech. Library

Commanding Officer
U.S. Naval Air Dev't. Ctr.
Johnsville, Pa.
1 Attn: NADC Library

U.S. Naval Avionics Facility
Indianapolis 18, Indiana
1 Attn: Station Library

Commanding Officer
U.S. Army Research Office
Durham, N.C.
3 Attn: CRU-AAIP

Department of the Army
Washington 25, D.C.
1 Attn: Research Support Div.

Chief, Research and Dev't Div.
Office of the Chief Signal Officer
Washington 25, D.C.
1 Attn: SIGRD-9A

Commanding General
U.S. Army Electronics Command
Ft. Monmouth, N.J.
3 Attn: AMSEL-AD

Chief, Library Branch
Dept. of the Army
Office of the Chief of Engineers
1 Washington 25, D.C.

OASD (R and E); Rm. 3C-128
The Pentagon
Washington 25, D.C.
1 Attn: Tech. Library

Hq., USAF
Washington 25, D.C.
1 Attn: Mr. Harry Milkey

Chief of Staff, USAF
Washington 25, D.C.
1 Attn: AFDRT-ER

U.S. Army Signal Liaison Office
Aeronautical Systems Division
Wright-Patterson AFB, Ohio
1 Attn: ASDL-9

Commander, ASD
Wright-Patterson AFB, Ohio
1 Attn: ASNPRO
1 Attn: ASRNCF-1
1 Attn: ASRNEB, Mr. D. R. Moore
1 Attn: ASRNCE-3
1 Attn: ASRNRD
1 Attn: ASRNCC-1
1 Attn: ASAPRL
1 Attn: ASRNEM-2

Commander, AF Inst. of Technology
Wright-Patterson AFB, Ohio
1 Attn: MCLI-Library

Executive Director
AF Office of Scientific Res.
Washington 25, D.C.
1 Attn: SRYA

School of Aerospace Medicine
Brooks AFB, Ohio
1 Attn: SMAP

Air Proving Ground
Eglin AFB, Fla.
1 Attn: APGTRI, Tech. Library

Commander
Holloman AFB, New Mexico
1 Attn: MER

AF Special Weapons Center
Kirtland AFB, New Mexico
1 Attn: SWOI

Director, Air University Library
Maxwell AFB, Ala.
1 Attn: CR 4582

AF Missile Test Center
Patrick AFB, Florida
1 Attn: AFMTC Tech. Library, MU-135

Commanding General, RADC
Griffiss AFB, Rome, N.Y.
2 Attn: RCRW
1 Attn: RAWCL
1 Attn: Document Library, RAALD
1 Attn: RAWED/L. Sues
1 Attn: RALS/J. Fallik
1 Attn: RAWEC, T. J. Domurat
1 Attn: RAWE, Haywood Webb

Commander, AFCRL
Bedford, Mass.
1 Attn: CRTOTT-2, Electronics
1 Attn: CRXL, Scientific Lib.
1 Attn: Elec. Res. Lab. (CRR)
1 Attn: CRRCPV
1 Attn: CRRCP, Phys. Elec. Br.

Commander, AF Ballistics
Missile Division
Los Angeles, Calif.
1 Attn: WDLPM-1-TDC

Hq., AFSC Andrews AFB
Washington 25, D.C.
1 Attn: SCEI
1 Attn: SCTAE

Director, R and D
Hq., USAF
Washington 25, D.C.
1 Attn: AFRDR-NU (Lt. Col. Booth)

Assistant Secy. of Defense(R and D)
Washington 25, D.C.
1 Attn: Technical Library

Office of Director of Defense
R and E
1 Washington 25, D.C.

Office of Assistant Sec'y. of Def.
Washington 25, D.C.
1 Attn: AE

Department of Defense
Washington 25, D.C.
1 Attn: Code 121A, Tech. Lib.

Institute for Defense Analyses
1666 Connecticut Ave.
Washington 6, D.C.
1 Attn: W. E. Bradley

Director
Weapons System Evaluation Group
1 Washington 25, D.C.

Central Intelligence Agency
Washington 25, D.C.
1 Attn: OCR Standard Dist.

U.S. Coast Guard
Washington, D.C.
1 Attn: EEE

Advisory Group on Electron Devices
New York 13, N.Y.
2 Attn: Harry Sullivan

Commander, ASTIA
Arlington 12, Va.
20 Attn: TISIA

Advisory Group on Reliability of
Electronic Devices
The Pentagon
1 Washington 25, D.C.

Office of Technical Services
1 Washington 25, D.C.

NASA, Langley Res. Ctr.
Hampton, Va.
1 Attn: C. L. Fricke, IRD-CRS

Commanding Officer
Diamond Ordnance Fuze Labs
Washington 25, D.C.
1 Attn: T. M. Liimatainen
2 Attn: ORDTL 930, Dr. R. Young
1 Attn: ORDTL-450-638-R. A. Comyn

Director
U.S. National Bureau of Standards
Washington 25, D.C.
1 Attn: Sec. 14.1, G. Shapiro

U.S. Department of Commerce
National Bureau of Standards
Boulder, Colo.
1 Attn: Central Radio Prop. Lab.
1 Attn: Library
2 Attn: Miss J. V. Lincoln, Chief
Radio Warning Service Sec.

Director
National Security Agency
Ft. George G. Meade, Md.
1 Attn: R 31
1 Attn: R 304, W. R. Boenning
2 Attn: C3/TDL, Rm. 2c087
1 Attn: R 42
1 Attn: C15

Chief
U.S. Army Security Agency
2 Arlington 12, Va.

UNIVERSITIES

University of Arizona
Tucson, Arizona
1 Attn: Dr. D. J. Hamilton

California Institute of Technology
Pasadena, Calif.
1 Attn: Prof. L. M. Field
1 Attn: Documents Library

University of California
Berkeley, Calif.
1 Attn: R. M. Saunders, Chm. EE Dept.
1 Attn: Prof. J. R. Singer
1 Attn: Dr. R. K. Wakerling, Rad. Lab.

University of California
Livermore, Calif.
1 Attn: Tech. Info. Div.

University of California
Los Angeles 24, Calif.
1 Attn: C. T. Leondes, Prof. of Eng.

Laboratories for Applied Sciences
University of Chicago
Chicago 37, Ill.
1 Attn: Library

Cornell University
1 Ithaca, N.Y.

Drexel Institute of Technology
Dept. of EE
Philadelphia 4, Pa.
1 Attn: F. B. Haynes

DePaul University
1036 W. Beldon Ave.
Chicago 14, Ill.
1 Attn: Dr. J. J. Hupert

University of Florida
1 Gainesville, Fla.
1 Attn: Prof. W. E. Lear
1 Attn: M. J. Wiggins, Engr.

George Washington University
Washing 6, D.C.
1 Attn: N. T. Grissmore
Principal Investigator

Georgia Institute of Technology
Atlanta, Georgia
1 Attn: Mrs. H. Crosland, Librarian
1 Attn: ; F. Dixon, Engr. Exp. St.

Harvard University
Cambridge 30, Mass.
2 Attn: Mrs. E. Farkas, Librarian

Illinois Institute of Technology
Chicago 16, Ill.
1 Attn: Dr. Paul C. Yuen

University of Illinois
Urbana, Ill.
1 Attn: Paul D. Coleman
1 Attn: Antenna Lab
1 Attn: Wm. Perkins
1 Attn: Prof. D. Alpert
1 Attn: Library Serials Dept.

Johns Hopkins University
Silver Spring, Md.
1 Attn: A. W. Nagy
1 Attn: N. H. Choksy

Carlyle Barton Lab
Johns Hopkins University
Charles and 34th Streets
Baltimore 18, Md.
1 Attn: Librarian
1 Attn: J. M. Minkowski

Linfield Research Institute
McMinnville, Oregon
1 Attn: G. N. Hickok, Director

Marquette University
Milwaukee, Wisconsin
1 Attn: Arthur C. Moeller

MIT
Research Lab of Electronics
Cambridge 39, Mass.
1 Attn: Document Rm. 26-327
1 Attn: John E. Ward

MIT
Electronic Systems Lab
1 Lexington 73, Mass.
1 Attn: Library A-229
1 Attn: Dr. W. I. Wells

Director
Cooley Electronics Lab, N. Campus
University of Michigan
1 Ann Arbor, Michigan

University of Michigan
Ann Arbor, Michigan
1 Attn: Elec. Phys. Lab.
1 Attn: Prof. J. E. Rowe
1 Attn: Tech. Doc. Service

University of Minnesota
Minneapolis 14, Minn.
1 Attn: Prof. A. Van der Ziel
1 Attn: W. M. Munn, Jr.

University of Nevada
Reno, Nevada
1 Attn: Dr. R. A. Manhart

New York University
New York 53, N.Y.
1 Attn: R. F. Cotellessa

Northwestern University
Evanston, Ill.
1 Attn: W. S. Toth

University of Notre Dame
South Bend, Indiana
1 Attn: Eugene Henry

Ohio State University
1 Columbus 10, Ohio
1 Attn: Prof. E. M. Boone

Ohio University
Athens, Ohio
1 Attn: R. C. Quisenberry

Oregon State University
Corvallis, Oregon
1 Attn: H. J. Oorthuys

Polytechnic Institute
Brooklyn, N.Y.
1 Attn: Leonard Shaw
1 Attn: Dept. of EE

Polytechnic Institute
Route 110
Farmingdale, N.Y.
1 Attn: Librarian

Princeton University
Dept. of EE
1 Princeton, N.J.

Purdue University
Lafayette, Indiana
1 Attn: Library

Rensselaer Polytechnic Institute
1 Troy, N.Y.

University of Rochester
Rochester 20, N.Y.
1 Attn: Dr. G. H. Cohen

Rose Polytechnic Institute
Dept. of EE
Terre Haute, Indiana
1 Attn: Dr. C. C. Rogers

Rutgers University
Newark 2, N.J.
1 Attn: Dr. Charles Pine

Stanford Research Institute
Menlo Park, Calif.
1 Attn: External Reports G-037

University of Texas
1 Austin, Texas

Texas Technological College
EE Dept.
Lubbock, Texas
1 Attn: Prof. Harold Spuhler

University of Utah
Salt Lake City, Utah
1 Attn: Richard W. Grow

Villanova University
Villanova, Pa.
1 Attn: Thos. C. Gabriele, Asst.Prof.

University of Virginia
Charlottesville, Va.
1 Attn: Alderman Library

University of Washington
Seattle 5, Wash.
1 Attn: A. E. Harrison

Yale University
Engineering Library
New Haven, Conn.
1 Attn: Sloane Physics Lab
1 Attn: Dept. of EE
1 Attn: Dunham Lab

INDUSTRY

Admiral Corp.
Chicago 47, Ill.
1 Attn: E. N. Roberson, Librarian

Airborne Instruments Lab
Deer Park, L.I., N.Y.
1 Attn: J. N. Dyer, VP and Tech. Dir.

Amperex Corp.
Hicksville, L.I., N.Y.
1 Attn: A. Barbasso, Proj. Engr.

Argonne National Lab
Argonne, Ill.
1 Attn: Dr. O. C. Simpson, Director
Solid State Science Div.

Autonetics
Downey, Calif.
1 Attn: Tech. Lib. 3040-3

Bell Telephone Labs
Murray Hill, N.J.
1 Attn: Dr. J. K. Galt
1 Attn: Dr. J. R. Pierce
1 Attn: Dr. M. Sparks
1 Attn: J. W. Fitzwilliam
1 Attn: Mr. J. A. Morton
1 Attn: Dr. R. M. Ryder

Bendix Corp.
Southfield, Detroit, Michigan
1 Attn: A. G. Peifer

Bendix Corp.
North Hollywood, Calif.
1 Attn: Engr. Library

Boeing Scientific Res. Lab
Seattle 24, Wash.
1 Attn: G. L. Hollingsworth

Bomac Laboratories
Beverly, Mass.
1 Attn: Research Library

Baird Atomic
33 University Rd.
Cambridge 38, Mass.
1 Attn: Dr. Hornig

Columbia Radiation Lab
1 New York 27, N.Y.

Convair-A Div. of Gen. Dynamics
San Diego 12, Calif.
1 Attn: Engr. Library

Cook Research Labs
1 Morton Grove, Ill.

Cornell Aeronautical Labs., Inc.
Buffalo 21, N.Y.
2 Attn: Library
1 Attn: D. K. Plummer

Eitel-McCullough, Inc.
San Carlos, Calif.
1 Attn: Res. Library
1 Attn: W. R. Lusbke

Electronic Communication, Inc.
1 Timonium, Md.

Emerson Research Labs
Silver Spring, Md.
1 Attn: S. Rattner

Evan Knight Corp.
East Natick, Mass.
1 Attn: Library

Fairchild Semiconductor Corp.
Palo Alto, Calif.
1 Attn: Dr. V. H. Grinich

Geisler Labs
P.O. Box 252
Menlo Park, Calif.
1 Attn: Librarian

General Electric Co.
Cornell U. Defense Elec. Div.-LMED
Ithaca, N.Y.
1 Attn: Library
VIA: Commander
Wright-Patterson AFB,
Ohio, Attn: WCLGL-4

General Electric Co.
Johnson City, N.Y.
1 Attn: A. C. Warrick

General Electric TWT Product Sec.
Palo Alto, Calif.
1 Attn: Tech. Library
1 Attn: D. H. Goodman, Mgr.
Manufacturing Operations

General Electric Co.
Schenectady, N.Y.
1 Attn: Dr. P. M. Lewis

General Electric Co.
Syracuse, N.Y.
1 Attn: Document Library

General Electric Co.
Auburn, N.Y.
1 Attn: Mr. G. C. Huth

General Electric Co.
Schenectady 5, N.Y.
1 Attn: G. E. Feiker
1 Attn: E. D. McArthur

General Precision, Inc.
Link Division
1451 Calif. Ave.
Palo Alto, Calif.
1 Attn: Miss S. R. Field, Librarian

General Telephone and Electronic
Labs., Inc.
Bayside 60, N.Y.
1 Attn: L. R. Bloom

Gilfillan Brothers
Los Angeles, Calif.
1 Attn: Engineering Library

Goddard Space Flight Center
Greenbelt, Md.
1 Attn: Code 611

Hallicrafters Co.
Chicago 24, Ill.
1 Attn: Wm. Frankart

Hewlett-Packard Co.
1 Palo Alto, Calif.

Hoffman Electronics Corp.
1 Los Angeles 7, Calif.

HRB Singer, Inc.
State College, Pa.
1 Attn: Tech. Info. Ctr.

Hughes Aircraft Co.
Culver City, Calif.
1 Attn: Tech. Documents Ctr.

Hughes Aircraft Co.
Newport Beach, Calif.
1 Attn: Library

Huggins Lab
1 Sunnyvale, Calif.

IBM Corporation
San Jose, Calif.
1 Attn: Dr. Mih Yin
1 Attn: Miss M. Griffen

IBM Corporation
Technical Reports Center
Space Guidance Center
Federal Systems Division
1 Owego, N.Y.

ITT Federal Labs
Nutley 10, N.J.
1 Attn: Librarian, Mr. Ellis Mount
1 Attn: J. J. Golden
1 Attn: A. W. McEwan
1 Attn: J. LeGrand

ITT Labs
San Francisco, Calif.
1 Attn: C. V. Stanley

Jansky and Bailey
Washington 7, D.C.
1 Attn: Mr. J. Renner

Laboratory for Electronics, Inc.
Boston 15, Mass.
1 Attn: Library

LEL, Inc.
Copiague, L.I., N.Y.
1 Attn: Mr. R. S. Mautner

Lenkurt Electric Co.
San Carlos, Calif.
1 Attn: M. L. Waller, Librarian

Librascope
Glendale 1, Calif.
1 Attn: Engr. Library

Litton Industries
San Carlos, Calif.
1 Attn: Tech. Librarian

Lockheed Aircraft Corp.
Marietta, Ga.
1 Attn: Dept. 72-15

Lockheed Aircraft Corp.
Sunnyvale, Calif.
1 Attn: Dr. W. M. Harris

Lockheed Missile and Space Co.
P.O. Box 504
Sunnyvale, Calif.
1 Attn: Dept. 67-33, Bldg. 524
G. W. Price

Lockheed Electronics Co.
Plainfield, N.J.
1 Attn: C. L. Opitz

Loral Electronics Corp.
11844 Mississippi Ave.
1 Los Angeles 25, Calif.

Loral Electronics Corp.
New York 72, N.Y.
1 Attn: Louise Daniels, Librarian

The Martin Co.
SCI-Tech. Library, Mail J 398
1 Baltimore 3, Md.

The Maxson Electronics Corp.
New York 1, N.Y.
1 Attn: M. Simpson

Melpar, Inc.
Falls Church, Va.
1 Attn: Librarian

Microwave Associates, Inc.
Burlington, Mass.
1 Attn: Library

Microwave Associates, Inc.
Burlington, Mass.
1 Attn: Dr. Kenneth Mortenson

Microwave Electronics Corp.
Palo Alto, Calif.
1 Attn: Stanley F. Kaisel
1 Attn: M. C. Long

Minneapolis-Honeywell Regulator Co.
1 Riviera Beach, Fla.

Minneapolis-Honeywell Regulator Co.
Aeronautical Division
1915 Armacost Ave.
Los Angeles 25, Calif.
1 Attn: Tech. Library

Monsanto Research Corp.
Dayton 7, Ohio
1 Attn: Mrs. D. Crabtree

Monsanto Chemical Co.
St. Louis 66, Mo.
1 Attn: Mr. E. Orban, Mgr. of
Inorganic Development

Motorola, Inc.
Chicago 51, Ill.
1 Attn: Jo Goldyn, CMC Librarian
VIA: Motorola, Inc. Security
Officer, Chicago 51, Ill.

Motorola, Inc.
Scottsdale, Arizona
1 Attn: Dr. J. W. Welch, Jr.
1 Attn: Military Electronics Div.
1 Attn: John Cacheris, Mgr.
1 Attn: Paul Stancik

Norden Division of
United Aircraft Corp.
Norwalk, Conn.
1 Attn: Alice Ward, Librarian

Nortronics, Inc.
Palos Verdes Research Park
1 Paloc Verdes Estates, Calif.

North American Aviation, Inc.
1 Columbus 16, Ohio

Pacific Semiconductors, Inc.
Lawndale, Calif.
1 Attn: H. Q. North

Philco Corp., W.D.L.
Palo Alto, Calif.
1 Attn: B. Herzog

Philco Corp.
Philadelphia 34, Pa.
1 Attn: F. R. Sherman, Mgr. Ed.

Philco Corp.
Blue Bell, Pa.
1 Attn: Dr. J. R. Feldmeier
1 Attn: C. T. McCoy, Res. Div.

Polarad Electronics Corp.
Long Island City 1, N.Y.
1 Attn: A. H. Sonnenschein

PRD Electronics, Inc.
Brooklyn 1, N.Y.
1 Attn: R. Casiana, Adv. Assit.

Radiation, Inc.
Melbourne, Fla.
1 Attn: Librarian

RCA
Harrison, N.J.
1 Attn: Microwave Tube Dev. Lab.
Bldg. 55
1 Attn: V. Valva

RCA
1 Moorestown, N.J.

RCA Labs
Princeton, N.J.
1 Attn: Harwick Johnson

RCA Labs
New York 13, N.Y.
1 Attn: M. C. Myers, Jr., Mgr.

RCA
Woburn, Mass.
1 Attn: Library

Ramo-Wooldridge
Canoga Park, Calif.
1 Attn: Tech. Info. Services

The Rand Corp.
Santa Monica, Calif.
1 Attn: Helen J. Waldron, Lib.

Raytheon Co.
Burlington, Mass.
1 Attn: Librarian, Microwave and
Power Tube Div.

Raytheon Co.
Bedford, Mass.
1 Attn: Mrs. I. Britton, Lib.

Raytheon Co.
1 Santa Barbara, Calif.
1 Attn: Librarian

Raytheon Co.
Waltham 54, Mass.
1 Attn: Res. Div. Lib.
1 Attn: Dr. H. Scharfman

Revere Copper and Brass, Inc.
Brooklyn, N.Y.
1 Attn: Vincent B. Lane

Sandia Corp.
Albuquerque, New Mexico
1 Attn: Mr. B. R. Allen, Lib.

S.F.D. Labs, Inc.
1 Union, N.J.
1 Attn: Dr. J. Sloom

Socony Mobil Oil Co.
Dallas 21, Texas
1 Attn: Librarian

The STL Tech. Library
1 Redondo Beach, Calif.

Sperry Gyroscope Co.
Great Neck, N.Y.
1 Attn: Leonard Swern (M.S. 3T 105)

Sperry Microwave Electronics Co.
Clearwater, Fla.
1 Attn: J. E. Pippin, Res. Sec. Head

Sperry Electron Tube Div.
1 Gainesville, Fla.

Sperry Gyroscope Co.
Great Neck, L.I., N.Y.
1 Attn: R. L. Wathen
1 Attn: T. D. Sege
1 Attn: K. Barney, Engr. Dept.

Sylvania Electric Products, Inc.
P.O. Box 997
Mt. View, Calif.
1 Attn: Tech. Library
1 Attn: J. B. Gaenzle, MTL

Commanding Officer
U.S. Army Signal Electronics
Research Unit
P.O. Box 205
1 Mt. View, Calif.

Sylvania Electronics Products
Waltham, Mass.
1 Attn: Librarian
1 Attn: John Donner
1 Attn: Mr. E. E. Hollis

Technical Research Group
1 Syosset, L.I., N.Y.

Texas Instruments, Inc.
Dallas 22, Texas
1 Attn: M. E. Chun
1 Attn: Dr. W. Adcock

Tektronix, Inc.
Beaverton, Oregon
4 Attn: Dr. Jean F. DeLord, Dir.
of Research

TUCOR, Inc.
Wilton, Conn.
1 Attn: Mrs. Marion E. Osband

Varian Associates
Palo Alto, Calif.
1 Attn: Tech. Lib.

Watkins-Johnson Co.
Palo Alto, Calif.
1 Attn: Dr. H. R. Johnson

Westinghouse Elec. Corp.
Baltimore 3, Md.
1 Attn: Eng. Dept.
H. B. Smith, Mgr.
1 Attn: Tech. Info. Ctr.
Mrs. A. E. Battaglia, Supv.
1 Attn: G. Ross Kilgore, Mgr.
Applied Res. Dept.

Westinghouse Elec. Corp.
Elmira, N.Y.
1 Attn: C. Miller
Elec. Tube Div.

Westinghouse Elec. Corp.
Pittsburgh 22, Pa.
1 Attn: Dr. G. C. Sziklai

Westinghouse Elec. Corp.
Pittsburgh 35, Pa.
1 Attn: J. G. Castle, Jr. 401-1B5
2 Attn: R. E. Davis

Zenith Radio Corp.
Chicago 39, Ill.
1 Attn: J. Markin